

**Non-Invasive Assessment of Intraventricular and Arterial Haemodynamics:
Tools to Guide Diagnosis and Therapy in Patients
with Heart Failure with Preserved Ejection Fraction**

**Niet-invasieve bepaling van de intraventriculaire en arteriële hemodynamica:
hulpmiddelen voor diagnose en therapie bij patiënten
met hartfalen met bewaarde ejection fraction**

Francisco Javier Londoño Hoyos

**Promotoren: prof. dr. ir. P. Segers, prof. dr. J. Chirinos Medina
Proefschrift ingediend tot het behalen van de graad van
Doctor in de ingenieurswetenschappen: biomedische ingenieurstechnieken**



**UNIVERSITEIT
GENT**

**Vakgroep Elektronica en Informatiesystemen
Voorzitter: prof. dr. ir. K. De Bosschere
Faculteit Ingenieurswetenschappen en Architectuur
Academiejaar 2019 - 2020**

ISBN 978-94-6355-350-6

NUR 954

Wettelijk depot: D/2020/10.500/27

Supervisors:

Prof. dr. ir. Patrick Segers
Prof. dr. MD. Julio A. Chirinos

Research lab:

Institute Biomedical Technology
Biofluid, Tissue and Solid Mechanics for Medical Applications (bioMMeda)
Ghent University
Corneel Heymanslaan 10 - Blok B (entrance 36)
B-9000 Gent
BELGIUM

Members of the exam committee:*Chairman:*

Prof. dr. ir. Filip De Turck Faculty of Engineering and Architecture,
UGent

Secretary:

Prof. dr. ir. Sofie Van Hoecke Faculty of Engineering and Architecture,
UGent

Reading committee:

Prof. dr. ir. Sofie Van Hoecke Faculty of Engineering and Architecture,
UGent

Prof. dr. MD. Ernst Rietzschel Faculty of Medicine and Health Sciences,
UGent

Prof. dr. ir. Jef Vandemeulebroucke Faculty of Engineering,
Vrije Universiteit Brussel,
Belgium

Prof. dr. Alun Hughes Faculty of Population Health Sciences,
University College London, UK

Prof. dr. ir. Nikolaos Stergiopoulos Institute of Bioengineering,
Laboratory of Hemodynamics
and Cardiovascular Technology,
Ecole Polytechnique Fédérale
de Lausanne (EPFL),
Lausanne, Switzerland

Other members:

Prof. dr. ir. Patrick Segers Faculty of Engineering and Architecture,
UGent

Prof. dr. MD. Julio A. Chirinos Perelman School of Medicine,
University of Pennsylvania,
Philadelphia (PA), USA

To my Dad

PREFACE

« At school you are engaged not so much in acquiring knowledge as in making mental efforts under criticism. A certain amount of knowledge you can indeed with average faculties acquire so as to retain; nor need you regret the hours you spent on much that is forgotten, for the shadow of lost knowledge at least protects you from many illusions. But you go to a great school not so much for knowledge as for arts and habits; for the habit of attention, for the art of expression, for the art of assuming at a moment's notice a new intellectual position, for the art of entering quickly into another person's thoughts, for the habit of submitting to censure and refutation, for the art of indicating assent or dissent in graduated terms, for the habit of regarding minute points of accuracy, for the art of working out what is possible in a given time, for taste, for discrimination, for mental courage, and for mental soberness. »

William Johnson – Cory

I must confess I don't know anything else about the author of these lines, but the spirit of these words transcends the person behind them and, in my case, describes perfectly my experience during the PhD. I enjoyed so much each step of my path, each difficulty, each accomplishment, each moment of lucidity, everything that pushed me to improve. The big moments and the small ones, everything was worth it, every single struggle, every single achievement. All was an immense sea of wisdom and learning. An epiphany of mental soberness.

Through this path, there were so many people who helped me in their own unique way. Thanks to the colleagues at Medisip to share with us not only a space but nice moments. Thanks to my colleagues at bioMMeda, their company, help and conversations were not only stimulating but also fresh air when things became difficult. Thanks to Inge and Jurgen for their kind help and support. To Saskia who was an incredible support in moments of need with gentle words and a smile. To the friends I met at the lab and out, it was always a pleasure to share with them and to find their support. Thanks to the people at MEDES and Verhaert, it was an amazing experience to work with them all. Thanks to Prof. Van Bortel and his team, especially to Jelle and Dr. De Backer, they were always so helpful and patient. Thanks for all

their advice and help. Thanks to Dr. Chirinos and his team, my experience at UPenn was incredibly productive, it helped me so much to grow as a professional learning from all the team and their experiences. Thanks to Patrick for this amazing opportunity, for the advice, for his support and patience, especially during difficult moments. Thanks for this opportunity that changed my life so positively. I am also grateful for the people I found in Gent, at the bank, at the offices, I always found a helpful advice from someone, and this made my adventure in Belgium even more special.

« José Arcadio Buendía soñó esa noche que en aquel lugar se levantaba una ciudad ruidosa con casas de paredes de espejo. Preguntó qué ciudad era aquella, y le contestaron con un nombre que nunca había oído, que no tenía significado alguno, pero que tuvo en el sueño una resonancia sobrenatural: Macondo. »

Cien años de Soledad. Gabriel García Márquez

“Macondo” is the imaginary place where I was born. And Macondo has always the resonance of the word family. And my family was a corner stone to culminate my experience. They have always been a great support in my life. Thank you my family for everything. Thanks to my mom and my dad. My dad, a spirit full of joy, full of wisdom, full of light. You are my best friend. I will always miss you and I hope that this achievement, which is your achievement as well, makes you proud. Thanks mom for your courage, support and company. I love you so much and I am so glad I can share this moment with you.

Finally, one great lesson during this experience, especially during these last couple of years, was that, rarely, things in life go the way we want, expect or plan. And Time inexorably passes and transforms everything. Facing the construction of this manuscript and the experiences I was having, I connected deeply with an author that remarkably expressed these emotions, and I decide to let his lucid words express my closure thoughts for this experience:

« Enfin cette idée du Temps avait un dernier prix pour moi, elle était un aiguillon, elle me disait qu’il était temps de commencer, si je voulais atteindre ce que j’avais quelquefois senti au cours de ma vie, dans de brefs éclairs, du côté de Guermantes, dans mes promenades en voiture avec Mme de Villeparisis, et qui m’avait fait considérer la vie comme digne d’être vécue. Combien me le semblait-elle davantage, maintenant qu’elle me semblait pouvoir être éclaircie, elle qu’on vit dans les ténèbres, ramenée au vrai de ce qu’elle était, elle qu’on fausse sans cesse, en somme réalisée dans un livre ! Que celui qui pourrai écrire un tel livre serait heureux, pensais-je, quel labeur devant lui ! Pour en donner une idée, c’est aux arts les plus élevés et les plus différentes qu’il faudrait emprunter

des comparaisons ; car cet écrivain, qui d'ailleurs pour chaque caractère en ferait apparaître les faces opposés, pour montrer son volume, devrait préparer son livre, minutieusement, avec de perpétuels regroupements de forces, comme une offensive, le supporter comme une fatigue, l'accepter comme une règle, le construire comme une église, le suivre comme un régime, le vaincre comme un obstacle, le conquérir comme un amitié, le suralimenter comme un enfant, le créer comme un monde sans laisser de côté ces mystères qui n'ont probablement leur explication que dans d'autres mondes et dont le pressentiment est ce qui nous émeut le plus dans la vie et dans l'art. Et dans ces grands livres-là, il y a des parties qui n'ont eu le temps que d'être esquissés, et qui ne seront sans doute jamais finies, à cause de l'ampleur même du plan de l'architecte. Combien de grandes cathédrales restent inachevées ! On le nourrit, on fortifie ses parties faibles, on le préserve, mais ensuite c'est lui qui grandit, qui désigne notre tombe, la protège contre les rumeurs et quelque temps contre l'oubli. Mais pour en revenir à moi-même, je pensais plus modestement à mon livre, et ce serait même inexact que de dire en pensant à ceux qui liraient, à mes lecteurs. »

Le Temps retrouvé. À la recherche du temps perdu VII. Marcel Proust

A book to end and to start.

Francisco J. Londono Hoyos
La Judea (Santa Rosa de Osos), 7 de enero de 2020

TABLE OF CONTENTS

| | |
|--|--------------|
| Preface | ix |
| Table of contents | xiii |
| Abbreviations and symbols | xix |
| Samenvatting | xxiii |
| Summary | xxix |
| Introduction | xxxv |
| | |
| I Fundamentals | 1 |
| <hr/> | |
| 1 The Cardiovascular System | 3 |
| 1.1 Functional cardiovascular anatomy | 4 |
| 1.1.1 Cardiac anatomy | 4 |
| 1.1.2 Vascular anatomy | 5 |
| 1.2 Principles of cardiovascular physiology | 7 |
| 1.2.1 Cardiac physiology | 8 |
| 1.2.1.1 Cardiac cycle | 8 |
| 1.2.1.2 Function of the heart | 12 |
| 1.2.2 Physiology of the vascular system | 17 |
| 1.2.2.1 Regulation of blood flow | 17 |
| 1.2.3 Autonomic nervous system in cardiac function . . . | 21 |
| 1.3 Pathophysiology of the cardiovascular system | 22 |
| 1.3.1 Heart failure | 22 |
| 1.3.1.1 Heart failure classification and stages . . . | 24 |
| 1.3.1.2 Mechanisms of heart failure | 24 |
| 1.3.1.3 Heart failure treatment | 26 |
| 1.3.2 Atherosclerosis | 30 |
| 1.3.3 Aging | 31 |

| | | |
|----------|--|-----------|
| 2 | Non-invasive techniques for cardiovascular assessment | 35 |
| 2.1 | Non-invasive arterial pressure wave measurement | 36 |
| 2.2 | Cardiovascular imaging | 38 |
| 2.2.1 | Principles of imaging | 38 |
| 2.2.1.1 | Basic concepts | 38 |
| 2.2.2 | Echocardiographic imaging | 39 |
| 2.2.2.1 | Principles | 40 |
| 2.2.2.2 | Echocardiography | 44 |
| 2.2.2.3 | Applications of echocardiography | 47 |
| 2.2.2.4 | Additional considerations of echocardiographic imaging | 55 |
| 2.2.3 | Cardiovascular magnetic resonance imaging | 56 |
| 2.2.3.1 | Basic principles of MRI | 57 |
| 2.2.3.2 | Applications of MRI | 62 |
| 2.2.3.3 | Additional considerations of MRI | 63 |
| 3 | Modelling and Processing Methodologies | 65 |
| 3.1 | Cardiac function | 66 |
| 3.1.1 | Fluid dynamics of intraventricular flow | 66 |
| 3.1.2 | Intraventricular pressure difference estimation | 68 |
| 3.1.2.1 | Colour M-Mode based estimation | 68 |
| 3.1.2.2 | MRI based estimation | 69 |
| 3.1.3 | Computational fluid dynamics model of the left ventricle | 69 |
| 3.2 | Vascular function | 71 |
| 3.2.1 | Haemodynamic analysis | 71 |
| 3.2.1.1 | Carotid flow profile - implementing Womersley theory | 76 |
| 3.2.2 | Wave power analysis | 77 |
| 3.2.2.1 | Forward and backward components of pressure, flow, and hydraulic power | 77 |
| 3.3 | Dedicated tools for the assessment of arterial health | 81 |
| 3.3.1 | Wall tracking algorithm based on RF ultrasound data | 81 |
| 3.3.2 | Signal alignment using a correlation method | 82 |
| 3.3.3 | Wave speed determination | 83 |
| 3.3.4 | Wave separation | 85 |
| 3.3.5 | Reflection magnitude | 86 |

II Novel Cardiovascular Research **87**

| | | |
|----------|---|-----------|
| 4 | Cardiac Function | 89 |
| 4.1 | Background and rationale of IVPD estimation | 90 |
| 4.1.1 | Introduction | 90 |
| 4.1.2 | IVPGs/IVPDs: basic concepts | 92 |
| 4.1.3 | Non-invasive assessment of IVPG/IVPD: ultrasound and MRI | 94 |
| 4.1.4 | Conclusions | 103 |
| 4.2 | Assessment of methodologies to calculate IVPDs | 104 |
| 4.2.1 | Introduction | 104 |
| 4.2.2 | Methods | 104 |
| 4.2.2.1 | Computational fluid dynamics model of the left ventricle | 105 |
| 4.2.2.2 | IVPD curve characterisation | 108 |
| 4.2.2.3 | In vivo application: MRI- and ultrasound- based IVPD calculation and comparison . | 111 |
| 4.2.2.4 | Statistical analysis | 113 |
| 4.2.3 | Results | 114 |
| 4.2.3.1 | CFD model processing results | 114 |
| 4.2.3.2 | In vivo processing results: calculation of pressure curves from a HFpEF population | 115 |
| 4.2.4 | Discussion | 118 |
| 4.2.4.1 | CFD model data | 118 |
| 4.2.4.2 | In vivo data | 120 |
| 4.2.5 | Limitations of the study | 121 |
| 4.2.6 | Conclusions | 122 |
| 4.3 | <i>In vivo</i> assessment of MRI-based IVPDs estimation | 123 |
| 4.3.1 | Introduction | 123 |
| 4.3.2 | Methods | 123 |
| 4.3.2.1 | Doppler echocardiography | 124 |
| 4.3.2.2 | 2D Phase Contrast imaging acquisition and processing | 124 |
| 4.3.2.3 | Image processing and computation of IVPDs | 124 |
| 4.3.2.4 | Statistical analysis | 125 |
| 4.3.2.5 | Reproducibility and repeatability assessment | 127 |
| 4.3.2.6 | Echocardiographic/MRI correlation assessment | 127 |
| 4.3.3 | Results | 127 |
| 4.3.3.1 | Diastolic IVPDs | 128 |
| 4.3.3.2 | Systolic IVPDs | 131 |
| 4.3.3.3 | Reproducibility and repeatability assessment | 131 |

| | | | |
|----------|---|--|------------|
| | 4.3.3.4 | Echocardiographic/MRI correlation assessment | 131 |
| | 4.3.4 | Discussion | 133 |
| | 4.3.5 | Conclusions | 136 |
| 5 | Vascular Function | | 137 |
| 5.1 | Haemodynamics effects of nitrates in HFpEF | | 138 |
| 5.1.1 | Introduction | | 138 |
| 5.1.2 | Methods | | 139 |
| | 5.1.2.1 | Study population | 139 |
| | 5.1.2.2 | Study protocol | 140 |
| 5.1.3 | Pressure–flow analyses | | 142 |
| | 5.1.3.1 | Statistical analysis | 144 |
| 5.1.4 | Results | | 144 |
| 5.1.5 | Discussion | | 148 |
| 5.1.6 | Conclusions | | 152 |
| 5.2 | Nitrate effects on cerebrovascular pulsatile power in HFpEF | | 153 |
| 5.2.1 | Introduction | | 153 |
| 5.2.2 | Methods | | 153 |
| | 5.2.2.1 | Wave power analysis | 154 |
| 5.2.3 | Results | | 155 |
| 5.2.4 | Discussion | | 157 |
| 5.2.5 | Conclusions | | 160 |
| 6 | Dedicated tools | | 161 |
| 6.1 | Carotid haemodynamics assessment during stress conditions | | 162 |
| 6.1.1 | Introduction | | 162 |
| 6.1.2 | Methods | | 163 |
| | 6.1.2.1 | Subjects | 163 |
| | 6.1.2.2 | Protocol instrumentation and setup | 165 |
| | 6.1.2.3 | Protocol implementation | 165 |
| | 6.1.2.4 | Signal processing | 167 |
| | 6.1.2.5 | Carotid pulse wave velocity and reflection magnitude | 168 |
| | 6.1.2.6 | Statistical analysis | 169 |
| 6.1.3 | Results | | 169 |
| 6.1.4 | Discussion | | 171 |
| 6.1.5 | Limitations | | 174 |
| 6.1.6 | Conclusions | | 175 |
| 6.2 | Assessment of arterial stiffness relative to reference values | | 176 |
| 6.2.1 | Introduction | | 176 |
| 6.2.2 | Methods | | 177 |

| | | |
|-----------------------------|---|------------|
| 6.2.3 | Results | 180 |
| 6.2.4 | Conclusions | 183 |
| 6.3 | Continuous physiological and medical monitoring | 184 |
| 6.3.1 | Introduction | 184 |
| 6.3.2 | Methods | 185 |
| 6.3.2.1 | Sample population | 185 |
| 6.3.2.2 | CPMM protocol | 185 |
| 6.3.2.3 | Tonometry measurements | 185 |
| 6.3.2.4 | Ultrasound measurements | 187 |
| 6.3.2.5 | Ultrasound image processing | 187 |
| 6.3.2.6 | SAHC measurements | 188 |
| 6.3.3 | Results | 188 |
| 6.3.3.1 | Sphygmomanometer measurements | 188 |
| 6.3.3.2 | Tonometry measurements | 190 |
| 6.3.3.3 | Ultrasound measurements | 191 |
| 6.3.3.4 | SAHC measurements | 191 |
| 6.3.4 | Conclusions | 191 |
| III Closure Thoughts | | 193 |
| <hr/> | | |
| 7 | Conclusions | 195 |
| | Bibliography | 203 |

ABBREVIATIONS AND SYMBOLS

The following list summarizes the most commonly used abbreviations and symbols in this thesis.

Abbreviations

| | |
|---------|---|
| 1D | One-dimensional |
| 2D | Two-dimensional |
| 3D | Three-dimensional |
| 4D | Four-dimensional |
| ACC/AHA | American college of cardiology/American heart association |
| ACE | Angiotensin-converting enzyme |
| Aix | Augmentation index |
| ANS | Autonomic nervous system |
| AP | Augmented pressure |
| ARB | Angiotensin II receptor blockers |
| ASE | American Society of Echocardiography |
| AV | Atrioventricular |
| BB | Beta-blockers |
| BMI | Body mass index |
| BP | Blood pressure |
| BSA | Body surface area |
| cf-PWV | Carotid to femoral pulse wave velocity |
| CFD | Computational fluid dynamics |
| CMM | Colour M-Mode |
| CNN | Convolutional neural network |
| CO | Cardiac output |
| CPMM | Continuous physiological and medical monitoring |
| CPT | Cold pressor test |
| CSA | Cross-sectional area |
| CW | Continuous-wave |
| DBP | Diastolic blood pressure |
| DC | Distensibility coefficient |

ABBREVIATIONS AND SYMBOLS

| | |
|------------------------------|--|
| DICOM | Digital imaging and communications in medicine |
| DT | Deceleration time |
| EACVI | European Association of Cardiovascular Imaging |
| ECG | Electrocardiogram |
| echo-PIV | Echocardiographic particle image velocimetry |
| EDD | End-diastolic diameter |
| EDP | End-diastolic pressure |
| EDV | End-diastolic volume |
| EEG | Electroencephalography |
| EF | Ejection fraction |
| EMG | Electromyography |
| ESA | European Space Agency |
| ESD | End-systolic diameter |
| ESP | End-systolic pressure |
| ESV | End-systolic volume |
| FCW | Forward compression wave |
| FEW | Forward expansion wave |
| FID | Free induction decay |
| fMRI | Functional magnetic resonance imaging |
| FOV | Field of view |
| HF | Heart failure |
| HFpEF | Heart failure with preserved ejection fraction |
| HFrEF | Heart failure with reduced ejection fraction |
| HGT | Hand grip test |
| HR | Heart rate |
| HRV | Heart rate variability |
| IMT | Intima-media thickness |
| IVPD | Intraventricular pressure difference |
| IVRT | Isovolumetric relaxation time |
| KNN | k-nearest neighbours |
| LA | Left atrium |
| LBNP | Lower body negative pressure |
| LV | Left ventricle |
| LVOT | Left ventricular outflow tract |
| MAP | Mean arterial pressure |
| MEDES | Institute for Space Medicine and Physiology |
| MRI | Magnetic resonance imaging |
| MSE | Mean squared error |
| MSNA | Muscle sympathetic nerve activity |
| MVC | Maximal voluntary contraction |
| NO | Nitric oxide |
| NO ₂ ⁻ | Nitrite |

| | |
|------------------------------|-----------------------------------|
| NO ₃ ⁻ | Nitrate |
| NTG | Nitroglycerin |
| NYHA | New York Heart Association |
| PCA | Principal components analysis |
| PP | Pulse pressure |
| PW | Pulsed-wave |
| PWT | Posterior wall thickness |
| PWV | Pulse wave velocity |
| RA | Right atrium |
| RF | Radio frequency |
| RV | Right ventricle |
| RVOT | Right ventricular outflow tract |
| SAHC | Short arm human centrifuge |
| SAN | Sinoatrial node |
| SBP | Systolic blood pressure |
| SD | Standard deviation |
| SV | Stroke volume |
| SVM | Support vector machine |
| SVR | Systemic vascular resistance |
| SWT | Septal wall thickness |
| TD | Time domain |
| TDI | Tissue Doppler imaging |
| TE | Echo time |
| TEE | Transoesophageal echocardiography |
| TOF | Time of flight |
| TR | Repeat time |
| TVI | Time velocity integral |
| VFI | Vector flow imaging |
| V _p | Propagation velocity |
| WIA | Wave intensity analysis |
| WPA | Wave power analysis |

Symbols

| | | |
|-----------|-------------------------|--------------------------------------|
| α | Attenuation coefficient | [cm ⁻¹] |
| Γ | Reflection coefficient | [-] |
| γ | Gyromagnetic constant | [MHz/T] |
| λ | Wavelength | [m] |
| μ | Viscosity | [mPa · s] |
| ν | Kinematic viscosity | [10 ⁻⁶ m ² /s] |
| ω | Angular frequency | [rad/s] |

ABBREVIATIONS AND SYMBOLS

| | | |
|----------------|---|--|
| Π | Hydraulic power | [W] |
| ρ | Density | [kg/m ³] |
| τ | Myocardial relaxation | [ms] |
| θ | Angle | [°] |
| v | Velocity | [m/s] |
| ε | Strain | [%] |
| c | Speed of sound propagation | [m/s] |
| f | Frequency | [Hz] |
| G | Gradient field | [T/m] |
| K | Elastic modulus | [Pa] |
| Z_A | Acoustic impedance | [10 ⁴ kg/m ² s] |
| Z_c | Characteristic impedance of the proximal aorta | [10 ⁶ Pa · s/m ³] |
| Z_{in} | Input impedance | [10 ⁶ Pa · s/m ³] |
| A | Late diastolic mitral flow caused by atrial contraction | [cm/s] |
| a' | Late diastolic mitral annulus motion with atrial contraction | [cm/s] |
| B | Magnetic field | [T] |
| C | Total arterial compliance | [ml/mmHg] |
| D | Diameter | [cm] |
| E | Early diastolic mitral flow | [cm/s] |
| e' | Early diastolic mitral annulus motion | [cm/s] |
| I | Intensity | [W/m ²] |
| P | Pressure | [mmHg] |
| Pb | Backward pressure wave | [mmHg] |
| Pf | Forward pressure wave | [mmHg] |
| Q | Flow | [cm ³ /s] |
| S | Systolic (aortic) outflow | [cm/s] |
| S' | Systolic mitral annulus motion | [cm/s] |
| T ₁ | Time when 63% of the longitudinal magnetization has recovered | [ms] |
| T ₂ | Time when 63% of the transverse magnetization has decayed | [ms] |
| U | Flow velocity | [m/s] |
| V _p | Propagation velocity | [cm/s] |

SAMENVATTING

INLEIDING

Hart- en vaatziekten (CVD's) vormen wereldwijd een belangrijke doodsoorzaak, waarbij in het bijzonder hartfalen (HF) een sterke opmars kent in de verouderende bevolking. HF verschilt enigszins van andere belangrijke CVD's en omvat een globaal en complex ziekteproces, eerder dan een precies definieerbare ziekte die met één enkele behandeling kan worden behandeld. De wereldwijd toenemende incidentie en prevalentie van HF is oorzaak van toename van morbiditeit en mortaliteit, verminderde levenskwaliteit en toenemende zorgkosten. Ongeveer de helft van de patiënten met symptomen van HF hebben een bewaarde linker ventrikel (LV) ejectiefractie (HFpEF), en het zijn in het bijzonder deze patiënten die moeilijk te behandelen zijn, en voor wie er momenteel geen bewezen effectieve farmacologische therapieën zijn. Om deze therapieën te kunnen ondersteunen en ontwikkelen is er nood aan een beter inzicht in de pathofysiologie van deze ziekte en bijgevolg aan een verbeterde diagnostiek. We denken hierbij in de eerste plaats aan niet-invasieve en adequaat gevalideerde methodieken en technieken voor het nauwkeurig kwantificeren van cardiovasculaire functie en hemodynamica, en meer specifiek aan methoden voor het begroten van intra-ventriculaire drukverschillen (IVPD's) en gradiënten (IVPG's), de ventriculo-vasculaire interactie en energetische aspecten van de hart- en vaatfunctie. Dergelijke hulpmiddelen zijn essentieel voor de ondersteuning van op wetenschappelijk bewijs gestoelde (evidence-based) geneeskunde en de verwezenlijking van richtlijnen voor de behandeling van patiënten met hartfalen (in het bijzonder HFpEF).

De algemene doelstelling van dit doctoraatsproject is de ontwikkeling, validatie en implementatie van niet-invasieve methoden voor de beoordeling van de cardiovasculaire functie, waarbij we drie concrete doelstellingen hebben geformuleerd: 1) Het ontwikkelen en valideren van een niet-invasieve methode voor de schatting van IVPD's, waarbij de techniek zal worden gebruikt voor het karakteriseren van de intraventriculaire hemodynamiek in patiënten met hartfalen met bewaarde en verminderde ejectiefractie (HFpEF); 2) Evaluatie

van de differentiële effecten van organische en anorganische nitraten in de vasculaire functie van patiënten met HFpEF; 3) Ontwikkelen van aanvullende methodieken voor het niet-invasief begroten van cardiovasculaire functie voor een aantal verschillende toepassingen.

Om de realisatie van deze doelstellingen overzichtelijk en nader toe te lichten, is het manuscript verdeeld in drie grote delen. Deel I - Fundamenten verschaft de lezer de nodige achtergrond in o.a. de anatomie en fysiologie van hart- en bloedvaten, de pathofysiologie van hartfalen, diagnostiek en beeldvorming en methodologische concepten die worden gehanteerd binnen het cardiovasculair onderzoek en geneeskunde. Deel II - Nieuw Cardiovasculair Onderzoek presenteert de resultaten van origineel onderzoek en studies die gericht zijn op het onderzoeken van de haalbaarheid, accuraatheid en de toegevoegde waarde van nieuwe analyses en indices die de hart- en vaatfunctie kwantificeren. In Deel III – Eindbeschouwing, wordt gestart met een algemeen overzicht van de resultaten, de beperkingen en belangrijkste besluiten van het voorgestelde cardiovasculair onderzoek. Hierop aansluitend wordt een aantal suggesties geformuleerd voor een verdere verbetering van de vooropgestelde diagnostische methoden. Tot slot wordt een persoonlijk perspectief met betrekking van dit promotieproject geschetst.

DEEL I - FUNDAMENTEN

Dit deel omvat de anatomische, (patho-) fysiologische en technische basisprincipes ter inleiding en ondersteuning van het originele onderzoek dat aan bod komt in Deel II - Nieuw cardiovasculair onderzoek.

Hoofdstuk 1 - Het cardiovasculaire systeem

Dit hoofdstuk gaat van start met een beknopte beschrijving van de functionele anatomie van het hart- en bloedvatenstelsel, om aansluitend de basisprincipes van de cardiovasculaire fysiologie (hartcyclus en hartfunctie) te behandelen. Hierbij wordt gefocust op het linker ventrikel (LV) waarbij de hartfunctie, conform de benadering in de cardiologie, wordt opgesplitst in de systolische (lediging) en diastolische (vulling) functie. Systolische functie wordt beschreven in termen van de mechanica van contractie, met aandacht voor de determinanten van de contractie van het linker ventrikel en het meten van de systolische functie. Wat de vulling van het hart betreft bekijken we de hemodynamische fasen van diastole, de eigenschappen van het LV in diastole en niet-invasieve methoden voor de evaluatie van de LV diastolische functie. Aansluitend wordt de fysiologie van het perifere vaatstelsel behandeld,

met een bijdrage omtrent de regulerende rol van het autonome zenuwstelsel in cardiovasculaire functie. Het laatste deel van het hoofdstuk onderzoekt de pathofysiologie van het cardiovasculaire systeem, met als voornaamste ziektebeelden atherosclerose en hartfalen. Het gebruik van organische en anorganische nitraten bij de behandeling van cardiovasculaire ziekte wordt kort toegelicht. Ook de impact van veroudering op de cardiovasculaire gezondheid komt aan bod in dit laatste deel.

Hoofdstuk 2 - Niet-invasieve technieken voor het meten van cardiovasculaire functie

Dit hoofdstuk introduceert de technische principes van de (voor deze doctoraatsthesis) meest relevante niet-invasieve beeldvormingsmodaliteiten en methoden voor het meten van fysiologische signalen in cardiovasculair onderzoek.

Het hoofdstuk begint met de beschrijving van drukgolfmetingen voor de beoordeling van de arteriële stijfheid en hemodynamica. Vervolgens worden de principes van echocardiografie en magnetische resonantie beeldvorming (MRI), twee belangrijke cardiovasculaire beeldvormingsmodaliteiten, in detail uitgelegd, samen met de belangrijkste cardiovasculaire toepassingen.

Hoofdstuk 3 - Toelichting bij gebruikte methoden voor modellering en signaalverwerking

In een eerste deel (dat de lezer voorbereidt op hoofdstuk 4) wordt aandacht besteed aan basisprincipes van de vloeistofdynamica, intra-ventriculaire stroming en de schatting van IVPG's en IVPD's uit echocardiografie of cardiale MRI. Het computermodel van bloedstroming in het linker ventrikel, dat verderop wordt gebruikt voor de validatie van ontwikkelde methoden, wordt in dit deel wat meer in detail toegelicht.

Het tweede deel van het hoofdstuk (ter ondersteuning van hoofdstuk 5) introduceert methoden voor de beoordeling van vasculaire functie door bepalen van de impedantie en hemodynamische analyse (met splitsing van drukgolven in hun voorwaartse en gereflecteerde componenten) en behandelt het concept van “wave power” en het hydraulisch vermogen. Er wordt toegelicht hoe de Womersley theorie wordt toegepast voor een verbeterde benadering van de debietgolf in de halsslagader.

Het laatste deel van het hoofdstuk behandelt het theoretische en methodologische kader van hoofdstuk 6, waarin specifiek ontwikkelde hulpmiddelen

voor de beoordeling van arteriële gezondheid in niet-routinematige omstandigheden worden voorgesteld. Deze initiatieven omvatten verschillende signaal- en beeldverwerkingsmethoden, zoals het tracken van de verplaatsing van de arteriële wand op basis van RF-ultrasone gegevens, signaaluitlijning op basis van correlatie-technieken en methoden voor het bepalen van de golfsnelheid en inschatten van de sterkte van golfreflecties.

DEEL II - NIEUW CARDIOVASCULAIR ONDERZOEK

In dit deel worden de resultaten van eigen origineel onderzoek toegelicht. Deze resultaten zijn gepubliceerd in peer-reviewde wetenschappelijke tijdschriften.

Hoofdstuk 4 - Hartfunctie

Dit hoofdstuk herneemt kort het theoretische vloeistof-dynamische kader dat aan de grondslag ligt van de analyse van de intra-ventriculaire stroming en de afgeleide drukschattingen (IVPD's) uit echocardiografie en MRI. De ontwikkelde methoden worden eerst gevalideerd op basis van een vloeistof-dynamisch computermodel van het linker ventrikel, waarbij gesimuleerde snelheidsdata worden gebruikt als pseudo-MRI/ultragegeluid data waarna de nauwkeurigheid van de schattingen van IVPD's uit dergelijke snelheidsdata kan worden ingeschat. De gunstige resultaten van de op MRI gebaseerde methode motiveerden verder onderzoek naar een grotere steekproef, inclusief proefpersonen zonder HF, en patiënten met HF_rEF en HF_pEF. De studie leverde interessante resultaten op met betrekking tot de karakterisering van HF-subtypen door het gebruik van IVPD-parameters, maar verder onderzoek is noodzakelijk om de bevindingen te bevestigen en de toepassing van de methode te verbeteren.

Hoofdstuk 5 - Vasculaire functie

Dit hoofdstuk focust op het inschatten van de effecten van organische en anorganische nitraten, een vasodilaterend medicijn en gebruikt bij de farmacologische behandeling van patiënten met hartfalen, op de vaatfunctie. Er wordt gebruik gemaakt van data gemeten in een steekproefpopulatie van patiënten met HF_pEF. Er wordt in het bijzonder gefocust op effecten van de medicatie op de hemodynamica in de halsslagader als toegang tot de cerebrale circulatie.

“Conventionele” hemodynamische analyse toont aan dat behandeling met organische nitraten leidt tot een inconsistente vermindering van arteriële golfreflecties, cerebrovasculaire weerstand en impedantie van de halsslagader, en dit in tegenstelling tot een behandeling met anorganische nitraten. Verdere analyse van de door de hemodynamische golven gegenereerde energie en vermogen geeft aan dat organische nitraten de penetratie van hydraulisch vermogen vanuit de aorta naar de halsslagader verhogen, terwijl anorganische nitraten geen significante veranderingen in deze parameters veroorzaakten.

Deze analyses vormen een mechanistische basis voor een aantal bekende en gedocumenteerde bijwerkingen van organische nitraten zoals hoofdpijn, duizeligheid en hypotensie bij patiënten met HFpEF. Bovendien bieden de in dit hoofdstuk besproken resultaten aanvullend bewijs ter ondersteuning van een effectieve behandeling van patiënten met HFpEF op basis van anorganische nitraten.

Hoofdstuk 6 - Specifiek ontwikkelde hulpmiddelen

Dit hoofdstuk bundelt drie aanvullende toepassingen van cardiovasculair onderzoek die in de loop van het doctoraatsonderzoek in meer of mindere mate zijn bestudeerd geweest.

In een eerste studie werden niet-invasieve technieken geëvalueerd voor de studie van de interactie tussen hemodynamica en cardiovasculaire functiemodulatie door het autonoom zenuwstelsel. Hiertoe werden stresstests uitgevoerd bij (vermoedelijk) gezonde vrijwilligers, waarbij bloeddruk- en echocardiografische metingen werden verkregen. Resultaten onthullen de specifieke fysiologische respons van het autonome cardiovasculaire systeem om elke stressstimulus adequaat te regelen.

In een tweede deel wordt een webgebaseerde applicatie voorgesteld met als doel de standaardisatie van parameters voor arteriële stijfheid (gekwantificeerd als de voortplantingssnelheid van de intra-arteriële drukgolf) te bevorderen. Ondanks het feit dat het algemeen aanvaard is dat arteriële stijfheid een sterk voorspellende waarde heeft bij de beoordeling van cardiovasculair risico, wordt een wijdverspreid gebruik van deze parameter gehinderd door de afwezigheid van methodologische standaardisatie om afgeleide parameters te bepalen. De ontwikkelde toepassing maakt een gemakkelijke beoordeling mogelijk van een gegeven gemeten waarde van arteriële stijfheid, waarbij een percentielscore wordt meegegeven voor die specifieke parameter die wordt begroot op basis van bestaande referentie databanken.

Een derde project werd uitgevoerd in een samenwerking met het bedrijf Verhaert, binnen een project gefinancierd door de Europese

ruimte-organisatie ESA. Deze heeft een bijzondere interesse in de aanpassing van het cardiovasculaire systeem in extreme ruimte-omstandigheden. Momenteel zijn de beschikbare apparaten om de cardiovasculaire toestand van astronauten te evalueren relatief beperkt. Doelstelling van ESA was om nieuwe methoden te exploreren die potentieel kunnen worden ingezet voor een meer nauwkeurige opvolging van de adaptatie van het cardiovasculair systeem bij langer verblijf in de ruimte. Wij ontwikkelden een systeem dat tonometrie en ultrasone metingen integreert, en onderzochten de functie van het systeem bij gezonde personen onder verschillende omstandigheden, waarbij proefpersonen werden gekanteld, werden blootgesteld aan onderdruk van het onderlichaam of terwijl proefpersonen werden onderworpen aan centrifugaal krachten tijdens testen in de korte arm centrifuge. Over het algemeen werden bemoedigende resultaten bekomen met het ontwikkelde systeem.

DEEL III - EINDBESCHOUWING

Hoofdstuk 7 - Conclusies

In dit hoofdstuk wordt gestart met een overzicht van de behaalde resultaten, een bespreking van de beperkingen, en formulering van een aantal conclusies. Vervolgens wordt wat dieper ingegaan op een aantal suggesties voor vervolgonderzoek voor een verdere verbetering van de vooropgestelde methodieken. Hierbij denken we vooral aan actuele relevante technieken zoals machinaal en diep leren. Het werk wordt afgesloten met een persoonlijk perspectief op het voorliggende promotieproject.

SUMMARY

INTRODUCTION

Cardiovascular diseases (CVDs) are a leading cause of death globally with heart failure (HF) showing a critical progress among the population and differing from other major CVDs since it is considered a disease process rather than a precise illness that can be treated with a single form of therapy. The increasing incidence and prevalence of HF worldwide is responsible for a large burden of morbidity and mortality, poor quality of life, and healthcare costs. Although approximately half of patients with HF have a preserved left ventricular (LV) ejection fraction (HFpEF), there are currently no proven effective pharmacological therapies to improve patient outcomes. Consequently, evidence-based and sustainable strategies to gain a better understanding of the pathophysiological process, to enhance diagnostic tools and, ultimately, to find an effective treatment should be encouraged, considering that non-invasive diagnostic procedures constitute a desirable (and feasible) advantage. Therefore, the validation of diagnostic strategies based on non-invasive data analysis for cardiovascular assessment is essential to define evidence-based medicine and to accomplish helpful guidelines. Indeed, non-invasive assessment of cardiovascular function using non-invasive data is feasible through different approaches, such as the estimation of intraventricular pressure gradients (IVPGs) and differences (IVPDs), the calculation of haemodynamic parameters, the application of wave power analysis, among others.

Hence, the general aim of this PhD project is to develop non-invasive methodologies for the assessment of cardiovascular function. This aim is break down into three concrete goals: 1) To develop and to validate a non-invasive processing tool for the estimation of IVPDs in order to characterise patients without HF, and with HF and reduced ejection fraction (HFrEF) or HFpEF; 2) To evaluate the differential effects of organic and inorganic nitrates in the vascular function of HFpEF patients; 3) To propose and to develop additional strategies for improving cardiovascular medicine in different applications.

To elaborate on these goals, the manuscript is divided in three major parts. Part I - Fundamentals establishes essential concepts of cardiovascular research and medicine, providing the basis for novel research proposals. Part II - Novel Cardiovascular Research presents results of studies aiming to explore the value of novel analyses and indices quantifying cardiac and vascular function in various settings. Part III - Closure Thoughts develops the final remarks regarding the manuscript, starting with a general overview of the results, limitations and conclusions of the proposed cardiovascular research, followed by suggestions concerning potential future work to improve these diagnostic methodologies. Finally, a personal perspective outlines the general conclusions of this PhD project.

PART I - FUNDAMENTALS

This part sets the basic anatomical, physiological and technical principles to support the novel cardiovascular research proposed in Part II.

Chapter 1 - The Cardiovascular System

This chapter contains a general description of the basic anatomy, physiology and pathophysiological processes and adaptations of the cardiovascular system.

First, the chapter presents a concise description of the functional cardiovascular anatomy. The second portion of the chapter presents the basic principles of cardiovascular physiology, such as cardiac cycle and heart function. Heart function is considered as systolic and diastolic function. The former is discussed in terms of mechanics of contraction, determinants of LV contraction and physiologic measurements of LV systolic function. The later deals with haemodynamic phases of diastole, LV diastolic properties and non-invasive evaluation of LV diastolic function. Following, the physiology of the peripheral vascular system is addressed. Lastly, the regulation role of the autonomic nervous system (ANS) in cardiac function is shortly revised. The last portion of the chapter examines the pathophysiology of the cardiovascular system, focusing on HF and atherosclerosis. Finally, the chapter addresses the impact of aging on cardiovascular health.

Chapter 2 - Non-invasive techniques for cardiovascular assessment

This chapter introduces the technical principles of relevant non-invasive signalling and imaging methodologies in cardiovascular medicine.

The chapter begins with the description of pressure wave measurements to support the assessment of arterial stiffness. Following, the chapter introduces the main principles and concepts common to all cardiovascular imaging methodologies, and then, echocardiography and magnetic resonance imaging (MRI), two major cardiovascular imaging modalities, are explained in detail. Both sections concerning echocardiography and MRI define basic principles of each technique, major cardiovascular applications and additional considerations.

Chapter 3 - Modelling and Processing Methodologies

This chapter revises concepts related to cardiovascular function and completes the fundamental theory to support Part II.

The first section of the chapter formulates basic principles of cardiac function assessment further developed in Chapter 4, comprising fluid dynamics of intraventricular flow and the estimation of IVPGs and IVPDs through imaging methodologies, such as echocardiography or cardiac MRI. Additionally, a validation strategy consisting in a computational fluid dynamics model of the LV is introduced.

The second section of the chapter, associated with Chapter 5, encompasses vascular function assessment through haemodynamic and wave power analysis. This section develops relevant concepts on the Womersley flow profile, the calculation of forward and backward components of pressure, the determination of hydraulic power, and other suitable approaches.

The last section of the chapter deals with the theoretical framework of Chapter 6, in which dedicated tools for the assessment of arterial health in non-routine conditions are presented. These initiatives involve different signal/image processing methods, such as arterial wall tracking based on RF ultrasound data, signal alignment through correlation, wave speed determination, wave separation and the calculation of the reflection magnitude.

PART II - NOVEL CARDIOVASCULAR RESEARCH

This part of the manuscript presents the novel cardiovascular research proposed.

Chapter 4 - Cardiac Function

The chapter presents the theoretical framework of fluid dynamic principles applied to the analysis of intraventricular flow and derived pressure estimations.

Considered approaches calculate parameters using non-invasive flow data from standard imaging techniques, such as echocardiography and MRI. Furthermore, the relevance of IVPGs and IVPDs for a proper cardiac function is established, thereby supporting the selection of IVPDs related parameters to assess cardiac function in HF patients and, potentially, to support the characterisation of HF subtypes.

Several methods have been proposed for non-invasive IVPDs estimation, but comparison has been hampered by technical difficulties. Therefore, a CFD model is proposed to perform the evaluation of echocardiographic and MRI based approaches. The favourable results of the MRI-based method motivated further research on a larger sample, including subjects without HF, and patients with HFrEF and HFpEF. The study provided interesting results regarding the characterisation of HF subtypes by the use of IVPD parameters but further research is warranted to confirm the findings and improve the application of the method.

Chapter 5 - Vascular Function

Throughout the chapter, different approaches are proposed to assess the impact of treatment based on nitrates in vascular function, particularly in a sample population with HFpEF.

Traditional haemodynamic analysis show that the treatment with organic nitrates produces an inconsistent reduction in arterial wave reflections, cerebrovascular resistance and carotid characteristic impedance, in contrast to inorganic nitrates treatment. Furthermore, a novel analysis based on wave power transmission is also implemented, indicating that organic nitrates increase power penetration from the aorta into the carotid whereas inorganic nitrates did not produce significant changes in wave power parameters.

Such analyses may relate the changes in cerebrovascular circulation induced by organic nitrates to their (documented) poorly tolerance and side effects like headache, dizziness and hypotension in patients with HFpEF. Moreover, results discussed in this chapter provide additional evidence to support further research for an effective HFpEF treatment using inorganic nitrates.

Chapter 6 - Dedicated tools

The chapter introduces three supplementary applications of cardiovascular research in precise fields of interest, each contributing to the understanding of

cardiovascular function. The first study focuses on the haemodynamic assessment of the cardiovascular function modulation by the ANS. To achieve this goal, stress testing is performed in (presumably) healthy volunteers and blood pressure and echocardiographic measurements are obtained. Results reveal specific physiological response of the autonomous cardiovascular system to regulate adequately each stress stimulus.

The second proposal presents the implementation of a web-based application to promote the standardization of arterial stiffness parameters. Undoubtedly, arterial stiffness has been identified as a crucial parameter for the assessment of cardiovascular risk although a wider implementation has been hampered by the lack of established reference values and the absence of methodological standardization to determine derived parameters. Thus, the proposed application allows the easy assessment of a given measured value of arterial stiffness, providing the percentile reference associated with that specific value.

A third project was carried out in collaboration with the company Verhaert, within a project funded by the European Space Agency (ESA), to analyse cardiovascular adaptation in extreme conditions. Currently, the devices available to evaluate the cardiovascular status of astronauts are relatively limited. The objective of ESA was to explore new methods that could potentially be used for a more accurate follow-up of the adaptation of the cardiovascular system during a longer stay in space. We developed a system that integrates tonometry and ultrasonic measurements, and investigated the function of the system in healthy individuals under different conditions, where test subjects were tilted, exposed to lower body pressure or subjected to centrifugal forces at the short arm human centrifuge. In general, encouraging results were obtained with the developed system.

These applications evidence that different fields of research can contribute to gain insights into cardiovascular function from dissimilar and complementary perspectives. This chapter concludes Part II, describing innovative contributions in biomedical engineering to cardiovascular research.

PART III - CLOSURE THOUGHTS

Chapter 7 - Conclusions

This chapter elaborates the final remarks of the PhD project. First, a general overview of the results, limitations and conclusions of the proposed cardiovascular research is stated. Next, the chapter develops on suggestions concerning potential future work to improve these diagnostic methodologies, including current relevant subjects such as machine and deep learning.

Finally, a personal perspective outlines the general conclusions of this PhD project.

INTRODUCTION

RATIONALE

The global burden of cardiovascular diseases (CVDs) has reached pandemic proportions and continues to rise. Not only do CVDs lack geographic, gender, or socioeconomic boundaries, but their major contributory causes show an increasing trend, among which stand out the aging of the world population, lifestyle changes due to urbanization, progressive industrialization and burgeoning globalization. Indeed, CVDs are the leading cause of death worldwide and proper strategies must be proposed to face effectively this epidemic and the entailed parallel augmentation in health care and social costs, considering specific factors, such as the demographic, economic, social, nutritional and epidemiological context.

Particularly, heart failure (HF) shows a critical progress among the population and differs from other major CVDs since it is considered the common final path of various disease processes, rather than a distinct illness that can be treated with a single form of therapy. In fact, HF involves the development of several pathological adaptations and complex interactions, affecting both cardiac and vascular function. Moreover, HF has a wide spectrum of dysfunction, in which two major subtypes have been identified, based on whether or not the ventricle maintains its ability to eject a sufficiently large proportion of its end-diastolic volume with each heart beat: HF with reduced ejection fraction (HFrEF) and with preserved ejection fraction (HFpEF). Even if systolic and diastolic dysfunction manifest in both subtypes in different degrees, HFrEF is generally related to systolic dysfunction whereas HFpEF is associated with diastolic dysfunction. In contrast to HFrEF, an effective treatment for HFpEF is still elusive while its incidence and prevalence continue to rise, largely due to an increasingly aging population and to the obesity epidemic.

With this perspective, specific strategies to tackle HFpEF should be encouraged, first searching for a deeper understanding of the pathological adaptations involved, then identifying proper parameters and tools to support diagnosis and, finally, finding an effective treatment. Nonetheless, any

suggested strategy must be supported by evidence to produce and consolidate useful clinical practice guidelines for the improvement of patient care and decision-making, considering the context and the sustainability of the proposal in terms of costs. Additionally, practicality and cost/effectiveness are two essential conditions for the successful application of any approach in the clinical setting. Consequently, non-invasive diagnostic procedures constitute not only a desirable advantage but also a feasible one because of the current availability of advanced signalling and imaging technologies.

NON-INVASIVE DIAGNOSTIC METHODOLOGIES FOR CARDIOVASCULAR RESEARCH

The validation of diagnostic strategies based on non-invasive data analysis for cardiovascular assessment remains a fundamental research necessity and a crucial step to define evidence-based medicine and to accomplish helpful guidelines. Therefore, the strategies developed through this document for non-invasive assessment of cardiovascular function encompass an explicit or an implicit validation scheme to support the results, the discussion and, particularly, the conclusions extracted from each project. Concretely, validation was accomplished by using *in silico* models, contrasting results between different sample populations or, implicitly, by applying methods that are extensively validated.

Furthermore, non-invasive data were obtained using established signalling and imaging techniques, such as applanation tonometry in combination with sphygmomanometry to measure blood pressure, ultrasound (or echocardiography) and MRI to measure blood flow and image structures, the latter two being well-established imaging techniques in clinical cardiovascular medicine. Non-invasive assessment of cardiac and vascular function using these data is feasible through different approaches, which include the estimation of intraventricular pressure gradients (IVPGs) and differences (IVPDs), the calculation of haemodynamic parameters, the application of wave power analysis, among others. Moreover, these approaches employ data already obtained from common clinical procedures in cardiovascular medicine or from slightly modified protocols, improving practicality and avoiding excessively long or additional protocols.

However, non-invasive approaches are facing also new challenges. For instance, in terms of feasibility of the approaches, digitalization is a milestone of cardiovascular medicine and a pivotal attribute of cardiovascular imaging, although the increasing amount of available data is often exceeding the processing capacity, which is generally manual, thus leading to errors. It is clear,

then, that better processing tools must be developed to address these challenges and to improve cardiovascular medicine supporting evidence-based guidelines and clinical decision making.

CARDIOVASCULAR RESEARCH

The major focus of the research studies presented throughout this manuscript is related to the non-invasive assessment of cardiac and vascular functions in CVD states, particularly in patients with HF. These chapters elucidated the need not only to improve the comprehension of underlying mechanics of an adequate cardiovascular function and pathophysiological process and adaptations, including age related changes, and the involvement of other systems for proposing effective treatment, but also the urgency to develop better diagnostic tools for identifying subjects at risk and implementing prevention strategies towards the general population. Hence, this manuscript includes also research proposals in this regard, aiming to tackle the CVD epidemic at different levels and stages.

RESEARCH OBJECTIVES

Briefly, the general aim of this PhD project is the development of non-invasive methodologies for the assessment of cardiovascular function, which can be broken down into three concrete goals:

Goal 1 - To develop and to validate a non-invasive processing tool for the estimation of IVPDs in order to characterise patients without HF, and with HFrEF or HFpEF.

Goal 2 - To evaluate the differential effects of organic and inorganic nitrates in the vascular function of HFpEF patients.

Goal 3 - To propose and to develop additional strategies for improving cardiovascular medicine in different applications.

The technical development of non-invasive algorithms for signal and image processing is supported on and aligned with investigation conducted at the bioMMeda research group of Ghent University, including biomedical ultrasound research, cardiovascular mechanics and other research tools (<https://www.biommeda.ugent.be/research>). Moreover, the medical component of the research is carried out in partnership with the arterial

haemodynamics and cardiovascular core lab of the University of Pennsylvania (<https://www.med.upenn.edu/accl/>).

Specific studies to achieve the listed goals are additionally supported by other institutions or work teams involved in cardiovascular research projects, which include the Asklepios Study, Reference Values for Arterial Stiffness' Collaboration, the company Verhaert, the Institute for Space Medicine and Physiology (MEDES), the European Space Agency (ESA), among others.

STRUCTURE

The manuscript is divided in three major parts.

Part I - Fundamentals establishes essential concepts of cardiovascular research and medicine, providing the basis for novel research proposals. First, Chapter 1 provides an overview of the cardiovascular system anatomy, a brief discussion of the principles of cardiovascular physiology and a concise review of relevant pathophysiological conditions, current clinical treatment and the impact of the aging process on cardiovascular structure and function. Then, Chapter 2 introduces non-invasive techniques to measure and image the cardiovascular system, focusing on two major cardiovascular imaging modalities: ultrasound (or echocardiography) and MRI. Finally, Chapter 3 expands and revises concepts related to cardiovascular function and its assessment, such as intracardiac fluid dynamics, *in silico* simulations, haemodynamic analysis and signal/image processing algorithms.

Part II - Novel Cardiovascular Research presents results of studies aiming to explore the value of novel analyses and indices quantifying cardiac and vascular function in various settings. This part is divided in three chapters, each addressing one of the formulated goals for this PhD project. Chapter 4 focuses on the assessment of cardiac function through non-invasive flow data to calculate IVPGs and IVPDs. The chapter starts providing a review on the non-invasive assessment of IVPGs and IVPDs, and their potential role in the characterisation of patients with HF. Then, the chapter deals with the assessment of methodologies to estimate IVPDs, in which an echocardiographic and an MRI approach are evaluated with the use of a computational fluid dynamics (CFD) model of the left ventricle (LV). These results supported the implementation and feasibility assessment of an MRI-based processing algorithm to estimate IVPDs noninvasively in subjects without HF, with HF_rEF or with HF_pEF. Chapter 5 entails the assessment of vascular function implementing conventional and novel haemodynamic analyses to compare the effects of organic and inorganic nitrates in a HF_pEF population. The first section of the chapter introduces the evaluation of vascular function

through classical haemodynamic assessment in time and frequency domains, and the second section describes the implementation of a novel analysis to evaluate wave power transmission into the cerebrovascular circulation. In Chapter 6, further dedicated tools to assess the cardiovascular system are explored. This chapter starts with the discussion of a study concerning the influence of the autonomic nervous system (ANS) in adjustments of the cardiovascular function under stress conditions. Next, the second section introduces a web-based application to support the standardization of vascular stiffness parameters and to promote their widespread use in common clinical practice. Finally, the third section is an exploratory feasibility study of a continuous physiological and medical monitoring system, based on tonometry and ultrasound measurements, with potential applications in space science.

Part III - Closure Thoughts presents the final remarks regarding the manuscript, starting with a general overview of the results, limitations and conclusions of the proposed cardiovascular research, followed by suggestions concerning potential future work to improve these diagnostic methodologies. Finally, a personal perspective outlines the general conclusions of this PhD project.

LIST OF PUBLICATIONS

First author in peer-reviewed papers and conference contributions

Peer-reviewed papers

- F. Londono-Hoyos, P. Segers, Z. Hashmath, G. Oldland, M. R. Koppula, K. Javaid, R. Miller, R. Bhuvva, I. Vasim, A. Tariq, W. Witschey, S. Akers and J. A. Chirinos, 'Non-invasive intraventricular pressure differences estimated with cardiac mri in subjects without heart failure and with heart failure with reduced and preserved ejection fraction', *Open Heart*, vol. 6, no. 2, 2019.
- F. J. Londono-Hoyos, A. Swillens, J. Van Cauwenberge, B. Meyers, M. R. Koppula, P. Vlachos, J. A. Chirinos and P. Segers, 'Assessment of methodologies to calculate intraventricular pressure differences in computational models and patients', *Medical & biological engineering & computing*, vol. 56, no. 3, pp. 469–481, 2018.
- F. Londono-Hoyos, P. Zamani, M. Beraun, I. Vasim, P. Segers and J. A. Chirinos, 'Effect of organic and inorganic nitrates on cerebrovascular pulsatile power transmission in patients with heart failure and

preserved ejection fraction', *Physiological measurement*, vol. 39, no. 4, p. 044 001, 2018.

- J. A. Chirinos, F. Londono-Hoyos, P. Zamani, M. Beraun, P. Haines, I. Vasim, S. Varakantam, T. S. Phan, T. P. Cappola, K. B. Margulies *et al.*, 'Effects of organic and inorganic nitrate on aortic and carotid haemodynamics in heart failure with preserved ejection fraction', *European journal of heart failure*, vol. 19, no. 11, pp. 1507–1515, 2017.
- F. Londono, T. S. Klopmeijer, D. Georgakopoulos, E. G. Lovett, L. Van Bortel and P. Segers, 'Carotid haemodynamics during sympathetic nervous system stimulation via handgrip and cold pressor testing in young healthy subjects: A feasibility study', *Artery Research*, vol. 8, no. 4, pp. 178–188, 2014.

Conference contributions

- F. Londono, J. Bossuyt, L. Engelen, C. Stehouwer, I. Ferreira, S. Laurent, P. Boutouyrie, P. Segers and L. Van Bortel, '4d. 01: A simple calculator for the assessment of measurements of carotid-femoral pulse wave velocity and local arterial stiffness relative to the reference values database', *Journal of hypertension*, vol. 33, e60, 2015.
- F. J. Londono Hoyos, J. Bossuyt, P. Segers and L. Van Bortel, 'An easy and intuitive web interface for the assessment of measurements of carotid-femoral pulse wave velocity and local arterial stiffness relative to the reference values database', in *Artery 15, Artery research*, vol. 12, 2015, pp. 43–43.
- F. Londono, B. Uytterhaegen, R. Kassel, R. VanRaemdonck, A. Beck, B. Comet, A. Runge and P. Segers, '8a. 03: Continuous monitoring of hemodynamics in the short arm human centrifuge a feasibility study', *Journal of hypertension*, vol. 33, e104–e105, 2015.
- F. J. Londono Hoyos, B. Meyers, P. Vlachos, J. Chirinos and P. Segers, 'Effect of organic nitrates on intraventricular pressure gradients in heart failure patients with preserved ejection fraction', in *Artery 14*, vol. 8, 2014, pp. 147–147.
- F. J. Londoño, P. Segers, P. Shiva kumar, P. Konda, P. Zamani, R. Bhuva, A. Dunde, V. Ferrari and J. A. Chirinos, 'MRI assessment of diastolic and systolic intraventricular pressure gradients in heart failure', *Circulation*, vol. 130, no. suppl_2, A20360–A20360, 2014.

-
- F. J. Londono Hoyos, P. Shiva-Kumar, S. Peddireddy, J. Chirinos and P. Segers, 'Sublingual nitroglycerin in patients with heart failure and preserved ejection fraction: Impact on central and regional carotid and radial input impedance and hemodynamics', in *Artery* 14, vol. 8, 2014, pp. 147–147.
 - F. J. Londono Hoyos, A. Swillens, B. Trachet and P. Segers, 'Wall tracking for the assessment of aortic distensibility during a follow up of 49 days in angiotensin ii-infused apoe^{-/-}-mice', in *ARTERY* 12, Elsevier, vol. 6, 2012, pp. 181–181.

Co-author in peer-reviewed papers

- S. Jain, F. J. Londono, P. Segers, T. C. Gillebert, M. De Buyzere and J. A. Chirinos, 'MRI assessment of diastolic and systolic intraventricular pressure gradients in heart failure', *Current heart failure reports*, vol. 13, no. 1, pp. 37–46, 2016.
- T. S. Phan, F. Londono, J. A. Chirinos and J. K. Li, 'Augmentation index is blind to early-systolic effects of arterial wave reflections', *Journal of the American Society of Hypertension*, vol. 10, no. 4, e34, 2016.
- B. Trachet, R. A. Fraga-Silva, F. J. Londono, A. Swillens, N. Stergiopulos and P. Segers, 'Performance comparison of ultrasound-based methods to assess aortic diameter and stiffness in normal and aneurysmal mice', *PloS one*, vol. 10, no. 5, e0129007, 2015.

I

Fundamentals

CHAPTERS

| | | |
|----------|--|-----------|
| 1 | The Cardiovascular System | 3 |
| 2 | Non-invasive techniques for cardiovascular assessment | 35 |
| 3 | Modelling and Processing Methodologies | 65 |

THE CARDIOVASCULAR SYSTEM

This chapter presents an overview of the cardiovascular system, starting with a succinct description of basic anatomy followed by a brief discussion of physiological principles to finish with a concise review of relevant pathophysiological conditions, current clinical treatment and the impact of the aging process on cardiovascular structure and function.

It is important to highlight that this chapter is based, extracted, adapted and/or edited from different textbooks with the most relevant sources: *Hurst's the heart* book of Fuster [16], *Mayo Clinic Cardiology: Concise Textbook* of Murphy [17], *Textbook of cardiovascular medicine* of Topol and Califf [18], *Braunwald's heart disease: a textbook of cardiovascular medicine* of Libby [19], *Vascular surgery* book of Rutherford [20], *Grossman & Baim's cardiac catheterization, angiography, and intervention* book of Moscucci [21], *Introduction to vascular ultrasonography* book of Zwiebel and Pellerito [22], *Heart failure in children and young adults: from molecular mechanisms to medical and surgical strategies* book of Chang and Towbin [23], *Cirugía vascular* book of Martínez [24], and *The heart as a muscle-pump system and the concept of heart failure* article of Weber and Janicki [25].

1.1 FUNCTIONAL CARDIOVASCULAR ANATOMY

1.1.1 Cardiac anatomy

The heart lies within a resilient sac, the pericardium, composed of two layers: fibrous and serous. The former, a collagenous and inelastic tissue, encases the heart and extends onto the great vessels wall. The latter, a delicate mesothelial layer, lines the inner surface of the fibrous (parietal) pericardium and the outer lining of the heart and intrapericardial great vessels (visceral pericardium or epicardium). The pericardium houses the pericardial cavity, which is filled by a serous fluid (the pericardial fluid) secreted by the serous layer. The ascending aorta, pulmonary artery, portions of both venae cavae and all pulmonary veins are intrapericardial [16].

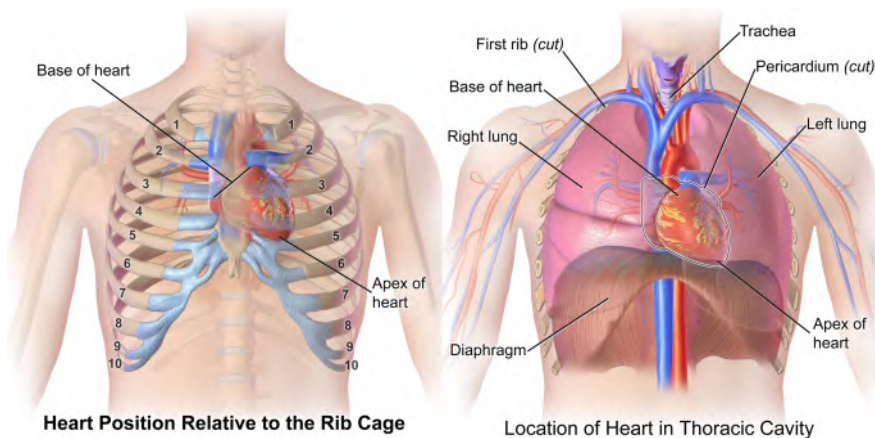


Figure 1.1: Illustration of the heart position within the thorax. Adapted from https://commons.wikimedia.org/wiki/File:Blausen_0458_Heart_ThoracicCavity.png and https://commons.wikimedia.org/wiki/File:Blausen_0467_HeartLocation.png. By Blausen.com staff (2014). "Medical gallery of Blausen Medical 2014". WikiJournal of Medicine 1 (2). DOI:10.15347/wjm/2014.010. ISSN 2002-4436. [CC BY 3.0 (<https://creativecommons.org/licenses/by/3.0/>)], from Wikimedia Commons.

The heart itself is a hollow muscular structure with a pyramidal geometry (a base, three surfaces and an apex). It lies within the rib cage (or thoracic cavity) in the middle of its central compartment, the mediastinum (see figure 1.1). The three surfaces of the heart are the anterior or sternocostal, the inferior or diaphragmatic and the posterior (base). The heart has an internal division in two halves, right and left, by a longitudinal and obliquus septum (see figure 1.2); each half has an (upper) atrium that receives blood and a (lower)

ventricle that ejects blood into the corresponding circulation system. The ventricles constitute the apex of the heart whereas the atria, lying opposite to the ventricles, form the base and receive the venae cavae and the pulmonary veins [16].

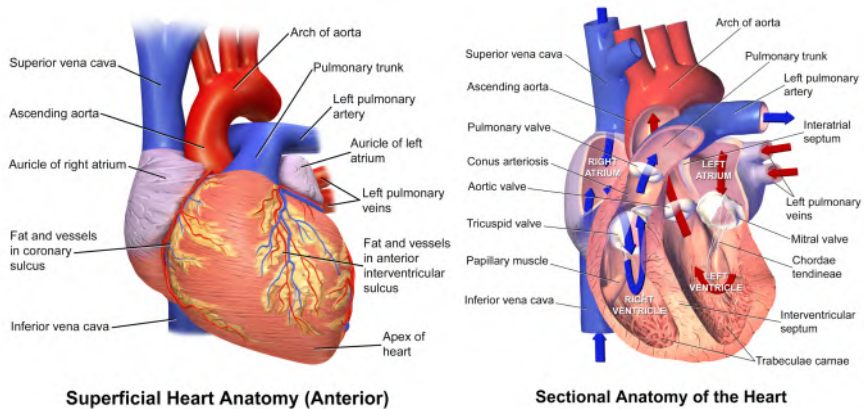


Figure 1.2: Illustration of the (anterior) heart anatomy. Adapted from <https://commons.wikimedia.org/w/index.php?curid=26986391> and <https://commons.wikimedia.org/w/index.php?curid=26986380>. By Blausen Medical Communications, Inc. - Donated via OTRS, see ticket for details, CC BY 3.0.

The venous return from the venae cavae and coronary sinus flows into the right atrium (RA) (see figure 1.2) and passes to the right ventricle (RV) crossing the tricuspid valve. Then, blood streams through the pulmonary valve to the pulmonary arterial circulation, where it is distributed to the lungs. Next, the oxygenated blood arrives to the left atrium (LA) through the pulmonary veins, it passes to the left ventricle (LV) throughout the mitral valve and, finally, during ejection, the aortic valve opens to let the blood flows into the aorta and the systemic circulation [16].

The atria and the ventricles are separated by the atrioventricular (AV) groove, which is well defined posteriorly but interrupted in the anterior portion by the aorta and the pulmonary trunk; the AV groove encases the coronary sinus, the right coronary artery and the left coronary artery termination (see figure 1.2).

1.1.2 Vascular anatomy

Veins are elastic vessels that transport blood from tissues to the heart. Most veins present valves with cusps directed toward the heart and covered by endothelium. These valves have muscular bundles at their base that actively participate in their opening and closure (see figure 1.3). The venous return

system is a complex network of venules and small and great veins, subdivided in two parts: 1) the systemic venous return that transports deoxygenated blood from tissues and organs to the RA; and 2) the pulmonary venous system that transports oxygenated blood from the pulmonary circulation to the LA. The systemic venous return presents two central structures: the venae cavae. The superior and the inferior vena cava drain blood into the RA from the upper and the lower half of the body, respectively [16].

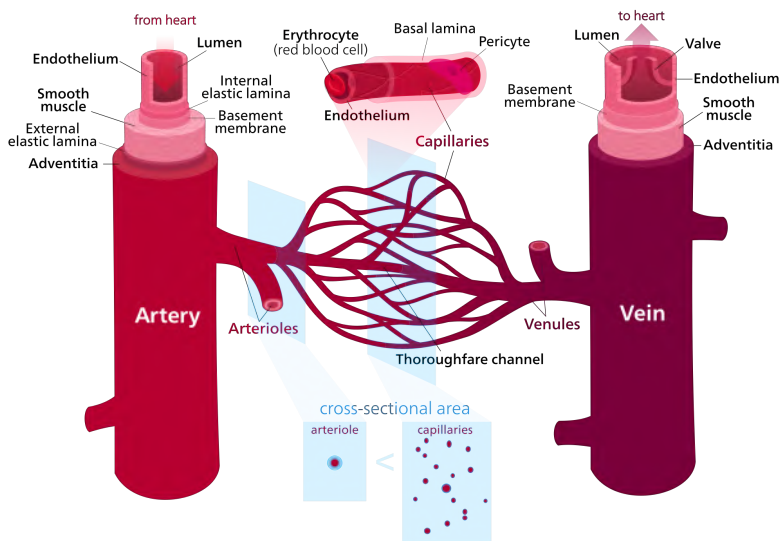


Figure 1.3: Illustration of the major components of the vascular system. Adapted from [https://commons.wikimedia.org/wiki/File:Blood_vessels_\(retouched\)_-en.svg](https://commons.wikimedia.org/wiki/File:Blood_vessels_(retouched)_-en.svg). By Kelvinsongderivative work: Begoon [CC BY-SA 3.0 (<https://creativecommons.org/licenses/by-sa/3.0/>)].

Arteries are membranous conducts, with divergent ramifications, in charge of the distribution of the blood expelled in each cardiac systole to all body tissues. To accomplish their tasks, arteries are designed to tolerate pressure. They have thick walls consisting in: 1) an intima layer, provided with very active endothelial cells that respond to different constrict or dilatatory stimuli; 2) a medial layer formed by smooth muscle cells and elastin; and 3) an adventitia layer composed of fibrocellular connective tissue [19], [20]. Closer to the heart, arteries are more elastic than muscular while the proportion of smooth muscle is higher in median calibre arteries. A graphical overview of these components is presented in figure 1.3. The arterial system is an intricate network of high-pressure, thick walled vessels (arteries, arterioles and capillaries). Arteries are more than simple passive conduits for transporting blood to tissues, arteries are biomechanical structures adapted to execute their functions, both metabolic and mechanic, under different

stress conditions, either in the short or long term, for ensuring continuous optimal blood flow [20]. While the great vessels of the arterial system move away from the origin, they branch to proportionate adequate irrigation to all organic territories. The arterial system is subdivided in two circulation systems: systemic and pulmonary. At the heart, two voluminous trunks arise from each ventricle: the aorta (left) and the pulmonary arteries (right) [16].

The aorta, which is the major arterial structure in the human body, is in charge of the distribution of oxygenated blood through the systemic circulation. The aorta begins at the aortic valve annulus and has four major segments: ascending aorta, aortic arch, descending aorta, and abdominal aorta. The three leaflets of the aortic valve are connected to a sinus (of Valsalva), of which the right and left sinuses give rise to the right and left coronary arteries, respectively [16], [18]. From the aortic arch, the innominate (or brachiocephalic), left common carotid, and left subclavian arteries emerge (in that order). From the innominate artery, the right subclavian artery arises. Both subclavian arteries (left and right) originate both axillary arteries, which provide the upper limbs with oxygenate blood, and continue as brachial arteries at the (upper) arm. Later, brachial arteries bifurcate to form the radial and ulnar arteries which run down the forearm [16], [20]. The descending thoracic aorta borders the LA, oesophagus, and vertebral column. The abdominal aorta is the final portion of the artery before it ends at the aortic bifurcation, from which the left and right common iliac arteries arise and, posteriorly, branch into different structures, being the femoral artery (at each side) of high importance for the lower limbs circulation [16], [19], [20].

The pulmonary trunk (or main pulmonary artery) is a major vessel of the human heart that emanates from the RV. Its function is to transport deoxygenated blood to the pulmonary circulation. The pulmonary artery branches into left and right pulmonary arteries before arriving to the lungs [16], [20].

1.2 PRINCIPLES OF CARDIOVASCULAR PHYSIOLOGY

The cardiovascular system is composed of two separate circulations to accomplish its main functions (see figure 1.4). The (low resistance and high capacitance) pulmonary circulation performs bidirectional gas exchange with the environment. The (relatively high resistance) systemic circulation supplies essential molecules, such as oxygen and nutrients, to the tissues and extracts CO_2 and waste products for transporting them to organs in charge of their removal (lungs, kidneys, liver). The heart pumps blood through both circulations by the action of its chambers at each side: the thin-walled atrium

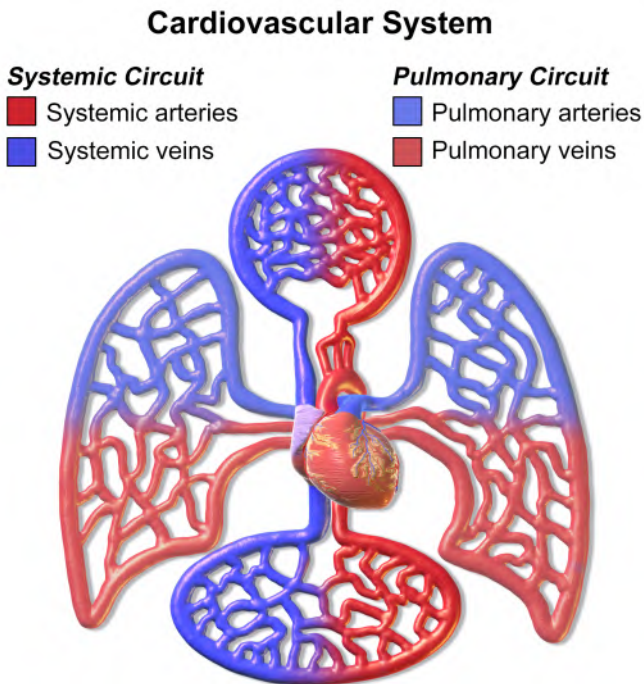


Figure 1.4: Diagram of the cardiovascular system. The diagram presents the heart at the centre of the cardiovascular system and depicts the separation of the pulmonary and systemic circulations. Adapted from https://commons.wikimedia.org/wiki/File:Blausen_0168_CardiovascularSystem.png. By Blaussen Medical Communications, Inc. [CC BY 3.0 (<https://creativecommons.org/licenses/by/3.0/>)], via Wikimedia Commons.

receives blood and has a booster pump function, and the thicker-walled ventricle pumps the blood to its respective circulation [16].

The cardiovascular system must adjust to function under different demands. During exercise, extreme conditions, and even during respiration, adaptation mechanisms should be in place to guarantee a proper cardiac function. Thus, this section reviews the general mechanisms to accomplish these tasks [16].

1.2.1 Cardiac physiology

1.2.1.1 Cardiac cycle

The cardiac cycle (i.e., the temporal sequence of events taking place during a single heartbeat) starts with an electrical signal transmitted by specialised

conduction tissue. These conduction cells provide an adequate sequence of activation for maximizing filling and contraction efficiency. Furthermore, the conduction tissue regulates the heart rate (HR) in response to various influences, particularly from the autonomic nervous and neuroendocrine systems. The electrocardiogram (ECG) represents the electrical activity of the specialised conduction tissue and the spread of the electric impulse [16].

Located in the RA, a group of conduction cells, known as the sinus node or sinoatrial node (SAN), operates as the natural pacemaker of the heart. Thereupon, the electric signal begins at the SAN and then travels throughout both atria, generating an atrial contraction (P wave). Next, the electrical signal courses the junctional region between interatrial and interventricular septa, first passing through the AV node and then through the His bundle. Conduction is slow at the AV node and, consequently, there is a delay between atrial contraction and ventricular depolarisation (PR interval) that facilitates the synchronization between atria and ventricles, enhancing their function. Instead, the conduction velocity increases after the His bundle, from which the electrical signal propagates through bundle branches and Purkinje fibres with several ventricular ramifications favouring preferential current flow. Accordingly, this stage of the cardiac cycle presents a fast-ventricular depolarisation (QRS complex) followed by the subsequent ventricular repolarisation (T wave). In brief, the electrical activation of the heart follows a specific (efficient) path of coordinated events, which results in the ejection of blood by the ventricles into the systemic and pulmonary circulations [16]. This process is summarised graphically in figure 1.5.

By convention, ventricular end diastole establishes the onset of the mechanical cycle. At that moment, there is an abrupt and quick intraventricular pressure increment until ventricular pressure exceeds atrial pressure and forces the closure of the AV valves. During this phase, ventricular volume is fixed (isovolumic contraction) and ventricular pressures continue to rise rapidly. When aortic and pulmonary arterial pressures are exceeded, both semilunar valves open and the phase of rapid ejection begins. In addition to pressure gradients across semilunar valves, arterial elastic properties influence the rate of ejection, which is pivotal on the left side of the heart since the systemic circulation is submitted to higher pressure and systolic expansion. Throughout ejection, ventricular and aortic/pulmonary arterial pressures rise to a peak and then fall together with the rate of ejection of blood (phase of reduced ejection) [16]. A reduced blood flow is maintained by blood inertia and arterial recoil (the windkessel model effect [26]) until the pressure in the outflow tracts surpasses the falling pressure in the ventricle and, soon after, semilunar valves close and ejection ends, an event signalled by the dicrotic notch of the respective arterial pressure waveforms.

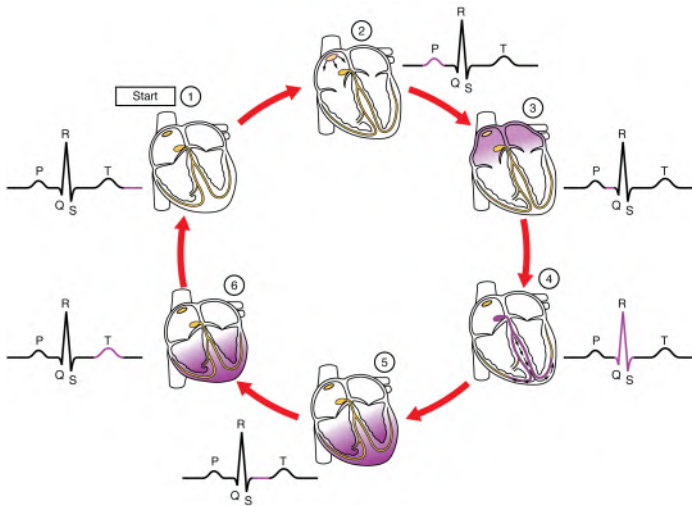


Figure 1.5: Diagram of the cardiac cycle and its phases. 1) After ventricular contraction, a period of relaxation starts in which no electrical signal is generated by cardiac tissue. 2) The cardiac electric signal begins at the sinoatrial node and then travels throughout both atria (P wave), 3) generating an atrial contraction. 4) Then, the signal passes through the atrioventricular node and from there to the His bundle, from which the electrical signal propagates through bundle branches and Purkinje fibres with several ventricular ramifications favouring preferential current flow (QRS complex). 5) A fast-ventricular depolarisation is triggered 6) and followed by the subsequent ventricular repolarisation (T wave), after which ventricular relaxation begins, marking a new cardiac cycle. Adapted from https://commons.wikimedia.org/wiki/File:2023_ECG_Tracing_with_Heart_ContractionN.jpg. By OpenStax College [CC BY 3.0 (<https://creativecommons.org/licenses/by/3.0>)].

The following phase, the isovolumic (constant volume) relaxation, is an active energy-dependent process. This phase starts with the closure of the semilunar valves and extends until intraventricular pressure drops below atrial pressure and the AV valves open. With this opening, early diastolic filling of the ventricles begins, accounting for most of the ventricular filling (~ 75 – 80%), and then pressures in the atrium and ventricle equalize and filling slows or even stops. This period is named diastasis and is followed by atrial contraction, which re-establishes the AV gradient and additional blood is pumped into the ventricle without an excessive increase in atrial pressure. Concretely, the LV filling pattern is the result of the transmitral pressure produced by elastic recoil (suction), the rate of myocardial relaxation, chamber compliance, LA pressure, and HR [16]. A Wiggers diagram showing temporal relationships between relevant parameters at the LV is presented in figure 1.6.

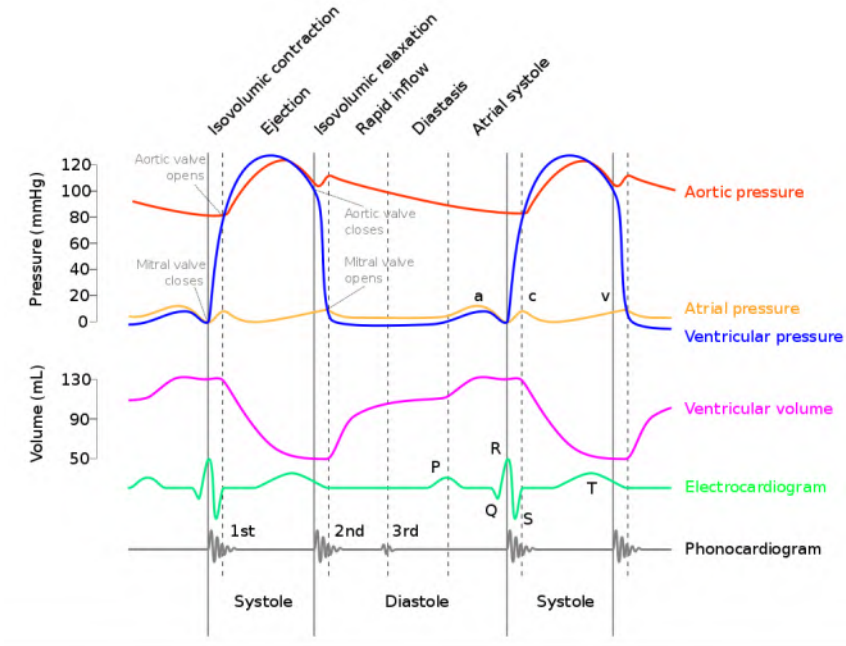


Figure 1.6: Wiggers diagram. Temporal relationships between: aortic (orange line), LV (blue line) and LA (yellow line) pressures; LV volume (magenta line); ECG (green line); and phonocardiogram (grey line). The diagram marks the systolic and diastolic periods (bottom) and the phases of the cardiac cycle (top). Additionally, opening and closure of mitral and aortic valves are shown together with characteristic features of atrial pressure curves, in which wave "a" reflects atrial contraction, wave "c" corresponds to an increase in atrial pressure after mitral closure, and wave "v" evidences the atrial early filling. The ECG tracing shows three main components: the P wave (atrial contraction), the QRS complex (ventricular depolarisation) and the T wave (ventricular repolarisation). Moreover, heart sounds are indicated as 1st and 2nd due to the reverberation of blood from the sudden closure of the mitral and aortic valves, respectively, and 3rd rarely heard in young or athletic people, but may also be a sign of serious cardiac problems. Adapted from https://commons.wikimedia.org/wiki/File:Wiggers_Diagram_2.svg. By adh30 revised work by DanielChangMD who revised original work of DestinyQx; Redrawn as SVG by xavax [CC BY-SA 4.0 (<https://creativecommons.org/licenses/by-sa/4.0>)], via Wikimedia Commons.

Even if volume variations and pressure waveforms during filling are comparable in both sides of the heart, the thick-walled LV generates a much higher filling pressure (up to $7 - 8\text{mmHg}$) than the RV, which is a reflection of the high-resistance systemic vascular bed, while mean LA pressure is also (normally) higher than RA pressure. Comparatively, pressure and filling patterns exhibit concrete differences at both sides of the heart due to intrinsic properties of the cardiac chambers and their associated circulation, whether systemic or pulmonary [16].

1.2.1.2 *Function of the heart*

Ventricular pump performance, or the proper blood supply to the tissues at adequate filling pressures, can be evaluated through function curves relating filling pressure to mechanical output estimations, such as stroke volume (SV, the volume ejected per beat), cardiac output (CO, the volume ejected per minute), stroke work (the product of mean ejection pressure and SV), among others. Such curves demonstrate the Frank-Starling mechanism of the heart, which states that the SV of the heart proportionally relates to the end-diastolic volume (EDV) [16]. EDV (preload) or surrogated quantities of volume, such as pulmonary capillary wedge and LV end-diastolic pressure (EDP) are used to generate the curves for describing the Frank-Starling mechanism (see figure 1.7). Shifts of the function curves are related to changes in intrinsic contractile performance, but effects caused by altered diastolic compliance cannot be differentiated from those caused by altered contractile performance [16], [17]. Contractile function is the intrinsic property of the cardiac muscle to contract independently of changes in loading conditions (preload, which is the load present at the end of diastole before the beginning of systolic contraction, or afterload, which is the systolic load on the LV after systolic contraction starts). Contractile function relates the rate of contraction with the peak force of the cardiac muscle and, often, with the rate of relaxation (the lusitropic effect) [16], [17].

Although both aspects of heart performance, systolic (myocardial contraction) and diastolic (relaxation and filling) function, overlap and interact, in practice, it is convenient to analyse them separately [16].

Systolic function

Myocardial contraction or systole can be defined as the period between the isovolumic contraction and the end of the ejection phase. The SV is the volume of blood pumped from the heart during ejection and the CO is calculated by multiplying SV and HR [16].

According to the Frank-Starling mechanism or Starling's law of the heart, the initial muscle fibre length regulates the contraction force (at any given tension). Based on this premise, experiments introduced the concepts of preload, afterload and contractility as mechanical determinants of cardiac function [17].

Preload can be defined as ventricular end-diastolic wall stress, which is related to muscle sarcomere length and venous filling pressure. Corresponding to Starling's law, SV and wall shortening extent and velocity are proportional to preload, while systolic wall stress and SV present an inverse relation at a constant preload. Alterations in preload are a crucial factor of ventricular performance and length-function curves. Indeed, the capacity to increase preload in stress situations is a functional reserve to maintain LV systolic performance in many disease states [16], [17].

Afterload, a major determinant of SV, is characterised as the tension (force or wall stress) on the LV fibres after shortening starts, which is basically the arterial pressure. With a constant preload, a rise in LV ejection impedance induces a fibre shortening and an LV SV decline. In a healthy heart, SV can be preserved by augmenting LV EDV and EDP, i.e., an afterload increase is met by a preload increase. In contrast, the diseased heart (such as in heart

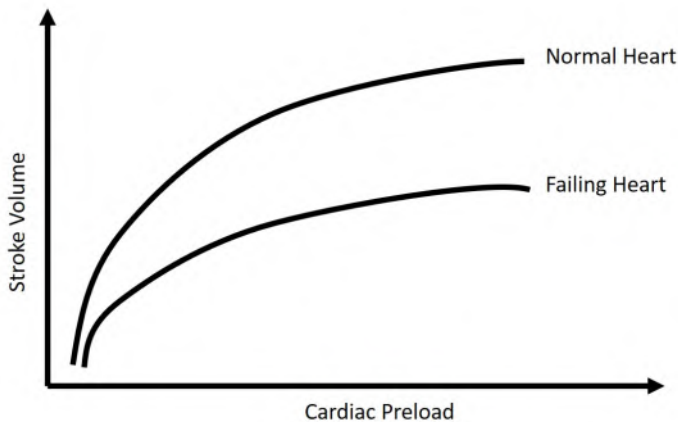


Figure 1.7: Frank-Starling curves. The Frank-Starling law characterises the correlation between the contraction force and the initial length of muscle cells. The failing heart curve shows a decreased slope indicating that higher cardiac preload is required to maintain adequate stroke volume, i.e., contractile force. Adapted from the reference: Optimal perioperative fluid management: What is the strategy? - Scientific Figure on ResearchGate. Available from: https://www.researchgate.net/figure/Frank-Starling-curves-of-ventricular-contractility_fig2_306088064 [accessed 20 Oct, 2019] via license: Creative Commons Attribution 4.0 International [27].

failure) or the intact heart during acute conditions (such as hypovolemia) has limited preload reserve and, thus, cannot increase sufficiently to maintain the SV [16], [17].

Contractility is the generic term to express the intrinsic strength of myocardial contraction, and thus it has been related to the inotropic state, although it has not a straightforward quantitative definition. With constant preload and afterload (loading conditions), cardiac performance is related to contractility, which in turn is affected by different factors as sympathetic neural activity. Responses of the LV contraction to alterations in preload, afterload, and contractility are assessed through the analysis of the LV pressure-volume relationship (functional curves) [16], [17].

Physiologic measurements of LV systolic function

LV ejection fraction (EF) is the most well-accepted expression of global LV function, indicating how much EDV is ejected from the LV with each contraction. Various imaging approaches are used to measure EF, being echocardiography the standard (see Chapter 2). Accuracy depends on the limitations of the method and, therefore, magnetic resonance imaging (MRI) has been proposed as a quality alternative to improve EF estimation (see Chapter 2) [17]. For the EF calculation, LV EDV and end-systolic volume (ESV) are obtained, and the following equation is applied:

$$LVEjection\ Fraction\ (EF) = \frac{(LV\ EDV - LV\ ESV)}{LV\ EDV} = \frac{SV}{EDV} \quad (1.1)$$

Maximal ventricular elastance is another common parameter to assess systolic function. End-systolic pressure-volume intercepts form a straight line on the pressure-volume curve for a given degree of contractility, and the slope of this line is the maximal elastance (see figure 1.8), which is directly proportional to contractility. This approach involves the development of pressure-volume curves and the control of either preload or afterload [17].

Diastolic function

Diastolic function is the filling capacity of the heart to reach an adequate EDV at appropriate blood pressures.

Determinants of LV diastolic performance vary in their importance and interaction during the four diastolic phases, which are isovolumic relaxation,

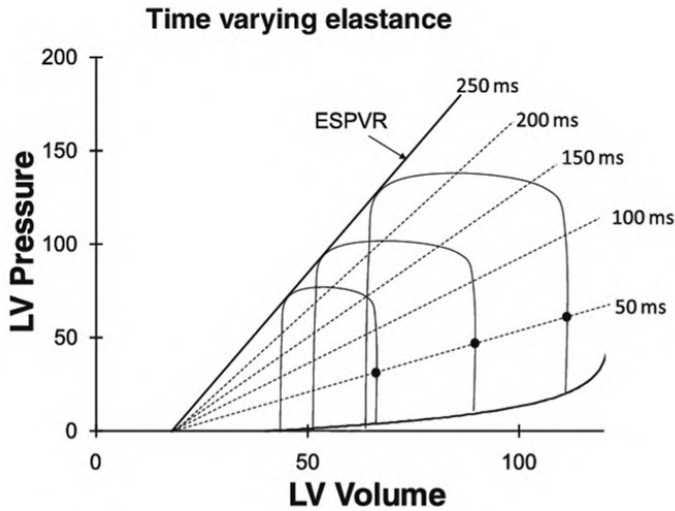


Figure 1.8: Estimation of the maximum elastance. Three differently loaded cardiac cycles. The end-systolic pressure–volume points all lie on a line termed the end-systolic pressure–volume relationship (ESPVR). The slope of the ESPVR is maximum elastance (E_{max}). At any time during systolic contraction (e.g., 50ms time points are shown as filled circles) a line can be drawn connecting pressure–volume points from each of the differently loaded contractions defining elastance ($\Delta P/\Delta V$) at that time point. Ventricular systolic contraction can therefore be regarded as a time-varying elastance. Adapted from the reference: Left ventricular function: Time-varying elastance and left ventricular aortic coupling - Scientific Figure on ResearchGate. Available from: https://www.researchgate.net/figure/Three-differently-loaded-cardiac-cycles-The-end-systolic-pressure-volume-points-all-lie_fig1_307959220 [accessed 20 Oct, 2019] via license: Creative Commons Attribution 4.0 International [28].

early LV filling, diastasis, and filling at atrial contraction. This division is only a convention to facilitate the description of LV diastolic properties since it has been difficult to understand LV diastolic function due to: 1) the complex interaction between factors through all phases (particularly in disease states), 2) the additional factors that influence LV diastolic properties, such as systolic function, pericardial restraint, among others, and 3) the overlap of the effects of these factors on the different phases of diastole [16], [17].

LV diastolic properties

During systole, the compression of elastic cardiac components produces elastic recoil, which in turn results in an LV suction effect by active relaxation during the early filling phase. This effect increases the pressure gradient between LA and LV, thus enhancing early diastolic filling and producing a

normal LV filling pattern. Abnormalities in relaxation generate lower transmitral gradients and an anomalous LV filling pattern with greater proportion of filling at atrial contraction. Under stress conditions, such as exercising, this pattern hampers the ability of the heart for an optimal filling [16], [17]. The $-dP/dt_{max}$ curve and τ (the time constant of relaxation) are calculated invasively as estimations of the rate of isovolumic relaxation. These methods present several limitations that restrict its application, hence other indices of isovolumic relaxation has been proposed using echocardiography and tissue Doppler measurements (see Chapter 2). Nonetheless, the best method to assess LV relaxation is still under research [16], [17].

Myocyte/myocardial and LV chamber compliance are less energy-dependent properties that govern the LV filling after relaxation. The former is determined by collagen fibres and sarcomeric proteins while the latter is determined by external elements, e.g., the pericardium and pulmonary airway pressure. Stress-strain relationship curves are used to evaluate myocardial compliance, yet *in vivo* measurements are impractical, so pressure-volume loops are determined during diastasis to characterise the combined effects of myocardial and chamber compliance and external forces, such as LV relaxation and viscoelastic properties. Chamber compliance, or its reciprocal (stiffness), is assessed with the slope of a tangent to the pressure-volume relationship, in which a steeper slope indicates a stiffer LV (see figure 1.8). However, this approach has several restraints, and its application has limited to experimental studies [17].

LV relaxation and chamber compliance are critical determinants of transmitral pressure gradient and LV filling. During diastole, the transmitral pressure gradient ensures competent LV filling whereas normal SV is preserved by an adequate LV EDP such that the myocardium volume is optimal (Frank-Starling mechanism). Changes in ventricular stiffness induce adjustments in LV EDPs to maintain filling. A slower LV relaxation causes a reduction of early diastolic transmitral gradient and a greater proportion of filling at atrial contraction. A compensatory increase of atrial pressure might be present in either case. At young age, diastole shows an efficient early filling whilst, in the aging heart, a slower LV relaxation produces a higher filling at atrial contraction. During exercise, a healthy heart shows a faster LV relaxation rate and a shorter PR interval, reducing diastolic filling time to preserve both early and late filling without raising atrial pressure [16], [17].

Non-invasive evaluation of LV diastolic function

For practical reasons, non-invasive methods for calculating LV filling patterns have been developed to assess indirectly LV diastolic function. The current

gold standard technique is echo-Doppler, and age-related values has been established for transmitral flow velocities (Chapter 2). The assessment of diastolic function is complemented with the calculation of additional parameters, such as maximal LA volume, LV filling in response to preload reduction (the Valsalva manoeuvre) and mitral annular motion assessed by tissue Doppler imaging (TDI) (see Chapter 2).

1.2.2 Physiology of the vascular system

Vascular function modulates total and peripheral resistance to control blood flow by regulating arterial vasculature tone and venous capacitance and return. Fast adaptation of blood flow to different physiological conditions, even daily routine activities as standing up or exercising, is crucial to an appropriate distribution of blood flow along the circulation system to preserve adequate pressures and metabolic tissue needs [18], [19]. Elastic arteries, such as the aorta or the common carotid arteries, have a relevant task in the distribution of CO since they act as a reserve of blood and energy to keep flow during diastole, when the ejection ceases. This phenomenon is known as the windkessel effect [26] and it helps to damp the pulsatility of pressure in smaller vessels and capillaries (see figure 1.9).

1.2.2.1 Regulation of blood flow

Vascular tone is inversely proportional to arterial size, being highest in the smaller, muscular arteries and arterioles, which are major determinants of peripheral resistance and local blood flow. Several physiological mechanisms influence the level of vascular tone and, hence, lumen diameter and resistance. All these mechanisms eventually focus on the modulation of vascular smooth muscle responding to modifications of the mechanical forces at the vascular wall or the release of neurotransmitters or metabolites by surrounding tissues. Particularly, myogenic tone is the intrinsic ability of vascular smooth muscle to constrict in response to pressure or stretch. On the other hand, the endothelium releases vasoactive factors that influence vascular tone [16], [20].

Although myogenic responses in arteries, arterioles and veins are reported, the mechanisms behind this effect are still elusive. On the other hand, endothelium influences vascular tone by releasing vasoactive molecules, such as nitric oxide (NO), peptide endothelin and dilator and constrictor prostaglandins (see figure 1.10), either through cholinergic, physical or chemical stimulation. An important example of physical stimulation is shear stress

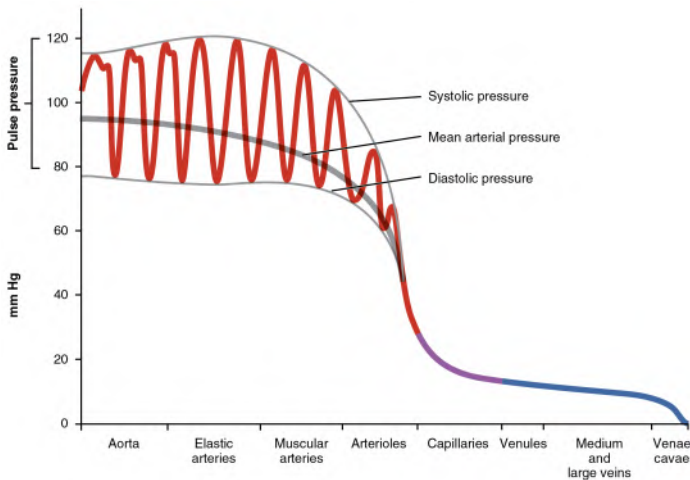


Figure 1.9: Graphical depiction of blood pressure values and changes throughout the vascular system. Blood pressure in the arterial tree is pulsatile due to the pump function of the heart and arterial mechanical properties. At this portion of the vascular system, systolic, diastolic, mean and pulse pressure are identified (pulsatile red line). Blood pressure is reduced in arterioles (straight red line) and capillaries (purple line) and pulsatility ceases. Blood pressure continues to decrease through the venous return system (blue line) until blood reaches the right atrium of the heart. Adapted from https://commons.wikimedia.org/wiki/File:2109_Systemic_Blood_Pressure.jpg. By OpenStax College [CC BY 3.0 (<https://creativecommons.org/licenses/by/3.0>)].

that acts on the vascular endothelium as a stimulant for vascular tone regulation in the short term and arterial remodelling in the long term, according to tissue blood flow demand [16], [20].

Regarding the control of peripheral blood flow and resistance, another important factor to consider is autonomic regulation. Arterial pressure is partly controlled by direct sympathetic innervation. Sympathetic efferent activity is dictated by sophisticated interactions from different portions of the nervous system and feedback signals from cardiovascular mechano- and chemoreceptors localised in the heart, the aortic arch and the carotid sinuses. During sympathetic activation (i.e., the “fight or flight reaction”), blood pressure (BP) rockets, venous return raises and, thus, CO is redistributed. In contrast, parasympathetic activity typically generates opposite responses: vascular relaxation and reduced cardiac rate and output. However, the role of the parasympathetic system is considered secondary in peripheral vascular regulation [16], [17], [19].

Moreover, sympathetic vasoconstrictor and vasodilator fibres respond to emotional stress and/or to postural changes and are involved in the regulation

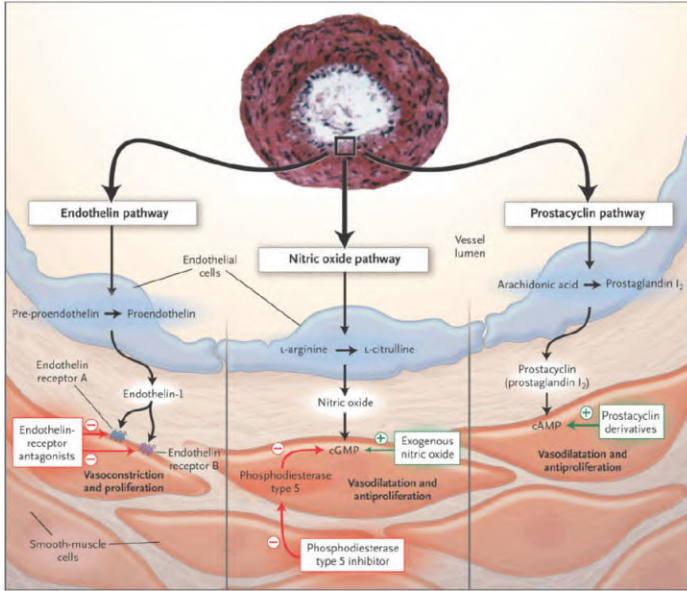


Figure 1.10: Postulated pathways of vasodilation. There are three relevant vasodilation pathways: The endothelin pathway involving peptides known as endothelins that constrict blood vessels and promote platelet aggregation; The nitric oxide (NO) pathway in which NO is produced in endothelial cells from the amino acid L-arginine modulating vasodilation and adhesion of both platelets and monocytes to the vascular wall; The prostacyclin pathway, which involves the synthesis of a prostaglandin (derived from the arachidonic acid) that is an effective vasodilator and inhibits blood platelet activation. cAMP: cyclic adenosine monophosphate; cGMP: cyclic guanosine monophosphate. Adapted from the reference: Reprinted from Humbert M, Sitbon O, Simonneau G. 2004. Treatment of pulmonary arterial hypertension. *N Engl J Med*, 351:1425-36. Copyright © 2004 with permission from Massachusetts Medical Society. Adapted from the reference: A review of pulmonary arterial hypertension: Role of ambrisentan - Scientific Figure on ResearchGate. Available from: https://www.researchgate.net/figure/Postulated-pathways-in-the-pathobiology-of-pulmonary-arterial-hypertension-PAH-and-drug_fig1_6254474 [accessed 20 Oct, 2019] via license: Creative Commons Attribution-NonCommercial 4.0 International [29].

of body temperature. Notably, local metabolites produced during exercise or ischemia have a powerful vasodilator effect in vessels within skeletal muscle. Not only these metabolites stimulate the release of endothelial factors (NO and prostacyclin) but their incremental effect in flow operates as a (shear stress) stimulus for the further release of endothelial vasoactive substances. However, metabolic regulation is only one of several mechanisms, including neural, myogenic and humoral/endothelial, for peripheral blood flow control, since it concerns a complex interaction determined partly by ambient conditions [17], [19], [20].

The ability of most vascular beds to maintain a constant blood flow over a range of systemic arterial pressures is known as autoregulation, and it is determined by the capability of the resistance vessels to constrict in response to a pressure increase and to dilate due to a pressure fall. Autoregulation is especially well developed in cerebral, coronary, and renal circulations [19], [20].

Pressure-Flow waveforms

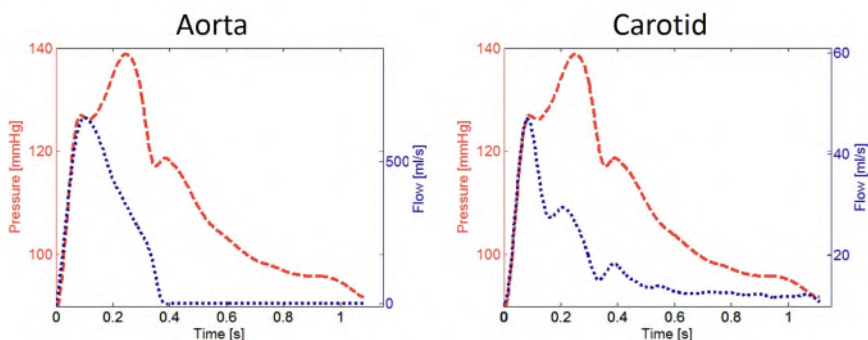


Figure 1.11: Graphical description of pressure (red) and flow (blue) waves alignment to perform Fourier analysis. At the aorta (left) and carotid (right) arteries. Adapted from F. Londono-Hoyos, P. Zamani, M. Beraun, I. Vasim, P. Segers and J. A. Chirinos, 'Effect of organic and inorganic nitrates on cerebrovascular pulsatile power transmission in patients with heart failure and preserved ejection fraction', *Physiological measurement*, vol. 39, no. 4, p. 044001, 2018 [3].

Peripheral resistance also impacts arterial flow and pressure waves. During systole, the compliant aorta stores a portion of the SV that is pushed forward by elastic recoil during diastole. When the blood arrives to the high resistance arterioles, a part is transmitted while other part is reflected to the arterial tree. In terms of flow, the reflected wave subtracts from the forward wave, producing a short period of reversal flow in early diastole unless peripheral resistance is low [20]. Instead, the pressure reflected wave adds to

the forward wave, producing an upward deflection on the downslope of the pressure pulse. This effect accounts for the systolic pressure amplification, diastolic pressure reduction and pulse pressure widening observed as blood flows from the aorta to the peripheral arteries. Even if wave reflections occur through all the arterial tree at vessel branches, bifurcations and narrowing, high-resistance vessels are a pivotal factor [20]. Moreover, waveform modifications due to reflections are more evident in peripheral arteries [20]. Fourier analysis of pressure and flow waveforms delivers supplementary information about the peripheral cardiovascular system (see figure 1.11 and Chapters 3 and 5).

1.2.3 Autonomic nervous system in cardiac function

The sympathetic and parasympathetic components of the autonomic nervous system influence the cardiovascular function, and their interaction modulates cardiac function through direct effects on heart's contractility and/or vascular tone in response to a variety of conditions. The parasympathetic system reduces BP through a fall in HR and, in a lower degree, contractility. In contrast, sympathetic activation increases BP by elevating total peripheral resistance and CO through a rise in cardiac contractility, HR, venoconstriction, and arterial vasoconstriction [16]–[18]. In normal physiological conditions, parasympathetic activity dominates via active sensors known as baroreceptors, which are stretch-dependent mechanoreceptors that sense pressure changes and transmit via afferents to the nucleus tractus solitarius and, ultimately, to the vasomotor centre of the brain. A sudden raise in BP stretches the baroreceptors and results in an increased firing of the frequency action potentials, producing an inhibition of the sympathetic drive and a stimulation of (parasympathetic) vagal tone. By contrast, a drop in pressure generates lower wall tension and, thus, lower firing of impulses, causing a disinhibition of sympathetic activity and a reduction of vagal tone. This inverse coupling of sympathetic and parasympathetic systems boosts the control of BP levels [16]–[18].

The baroreflex is a fast response mechanism to maintain BP and includes a collection of reflexes such as arterial baroreceptors (high pressure receptors) and cardiopulmonary receptors (low pressure receptors). The most sensitive sensors are the arterial baroreceptors, which are located in the carotid sinuses, aortic arch, and at the origin of the right subclavian artery. These baroreceptors present a set point above which they are activated. This set point depends largely on endogenous factors and disease states although in normal physiological conditions, baroreceptors are activated at a mean arterial pressure (MAP) above 70mmHg , whereas below this threshold they

become “silent”. After nearly one day, hypertension or hypotension resets the baroreceptors to the new blood pressures levels [16], [18], [19].

Arterial baroreceptors placed at the carotid sinuses react to both increases or decreases in arterial pressure, whilst baroreceptors at the aortic arch are sensitive only to increments in arterial pressure. Cardiopulmonary receptors are located in the heart and large veins, such as venae cavae. Unlike arterial baroreceptors, low pressure receptors respond primarily to changes in volume and/or chemical stimuli, contributing to BP modulation through the regulation of body fluid volume. Finally, chemoreceptors are chemical sensors that regulates sympathetic activation. They are divided in two components: central, which are found in the brainstem and respond to abnormally elevated carbon dioxide (CO_2) levels in the blood (hypercapnia), and peripheral, which are placed in the carotid bodies and respond to abnormally low levels of oxygen (O_2) in the blood (hypoxemia). Thus, hypercapnia and hypoxemia activate the sympathetic system [17]–[19].

1.3 PATHOPHYSIOLOGY OF THE CARDIOVASCULAR SYSTEM

1.3.1 Heart failure

Heart failure (HF) has become one of the major causes of death worldwide with increasing prevalence and incidence as the population ages. Despite this, there is not a unifying hypothesis to describe the clinical HF syndrome. In fact, current treatment delays the progression of signs and symptoms but do not stop or cure HF. Any form of heart disease can lead to HF, thus there is not a single causative mechanism and research on this regard is a current active field. A hypothesis considers HF as a progressive model in which several alterations, including adaptation processes, contribute to affect multiple organs, tissues and reflex control mechanisms under diverse conditions and at different timing, adding to the complexity of the syndrome [16].

Due to this complexity, the sequence of events leading to HF, the precise mechanisms involved, and the quantification of the contribution of each individual component remains elusive. Nonetheless, enough information is available to construct a working hypothesis. Fundamentally, a trigger event (clinically “invisible” caused by an unusual stress to the system) causes a loss of myocardium or excessive overload followed by physiological changes, forcing the cardiovascular system to adapt to the “hostile” new environment. In order to sustain an elevated load, first the LV chamber increases in size and, after, the heart dilates. This ensures an increase in EDV to maintain SV

despite a reduced EF, providing a short-term benefit. Indeed, lack of dilation may precede shock and early death [16]. Furthermore, compensatory mechanisms activate the “neurohormonal” systems, including the sympathetic nervous system, and further myocardial remodelling takes place. Ultimately, it becomes obvious that all these physiologic adaptations contribute to the pathologic progression of HF. Nevertheless, specific questions remain to be answered in this apparently coherent but oversimplified hypothesis [16].

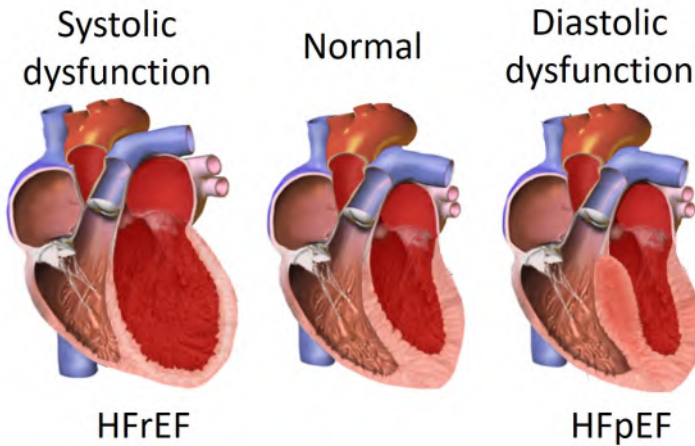


Figure 1.12: Illustration of the anatomical differences between a normal heart and a heart with systolic or diastolic dysfunction. In systolic dysfunction (left), the heart is dilated and cardiac muscle is weakened thus hampering the pump function of the heart and reducing the quantity of ejected blood. In diastolic dysfunction (right), the heart is stiffer (thicker LV wall) impeding proper relaxation and filling. HFrEF: Heart failure with reduced ejection fraction. HFpEF: Heart failure with preserved ejection fraction. Adapted from https://commons.wikimedia.org/wiki/File:Major_categories_of_cardiomyopathy.png. By Npatchett [CC BY-SA 4.0 (<https://creativecommons.org/licenses/by-sa/4.0>)].

HF is a pathophysiological state with variable signs and symptoms, such as shortness of breath (dyspnoea), fatigue and weakness, swelling (oedema) in legs, ankles and feet, and others, in which metabolic tissue demands are not met as a result of a diminished pump function of the heart (see figure 1.12). HF has a poor prognosis and a vast etiologic basis, even if, in most patients, cardiac function and cardiac pump are maintained at rest in early stages by compensatory mechanisms, whereas systemic vascular resistance (SVR) is increased and fails to adapt to variations of metabolic needs [16]. Concretely, systolic dysfunction is characterised by progressive LV dilatative remodelling and the ensuing loss of myocardial contractile strength. Further cardiac remodelling occurs as ventricular dysfunction aggravates,

partially cause by sympathetic activation, deteriorating the emptying capacity of the ventricles, i.e., a reduced EF, with a parallel compensatory increment in diastolic volume. Instead, diastolic dysfunction exhibits an intact emptying capacity but impaired ventricle filling that results in increased filling pressures and, ultimately, in pulmonary oedema (fluid accumulation in the tissue and air spaces of the lungs) [16].

1.3.1.1 *Heart failure classification and stages*

Different classification and staging schemes have been proposed. The New York Heart Association (NYHA) functional classification is the most widely used. It presents four HF stages as table 1.1 shows.

Nonetheless, the NYHA classification is considered imprecise and, therefore, preference is being given to the use of a staging scheme of HF associated with increasing morbidity and mortality, and more closely linked with prevention and therapy. In this scheme (2001 American college of cardiology/American heart association (ACC/AHA) Guidelines) [30], HF is considered a continuum that encompasses four interrelated stages described in table 1.1.

Table 1.1: Heart failure (HF) classification schemes. Adapted from [16].

| Classification Scheme | Class/Stage | Description |
|-------------------------|-------------|---|
| NYHA | I | Patients without symptoms or limitations of physical activity |
| | II | Patients with mild symptoms and slight limitation of physical activity |
| | III | Patients with marked symptoms and pronounced limitation of physical activity |
| | IV | Patients with severe symptoms and serious limitations of physical activity even at rest |
| 2001 ACC/AHA Guidelines | A | Patients with risk factors of HF but without structural heart disease or HF symptoms |
| | B | Patients with structural heart abnormalities but no HF symptoms |
| | C | Patients with structural heart disease and HF symptoms |
| | D | Patients with marked HF symptoms and severe disability |

1.3.1.2 *Mechanisms of heart failure*

To achieve a global understanding of the pathophysiology of HF and its progression, a thorough analysis should be performed, including measurements of mechanical/haemodynamic features, cardiac impaired performance and maladaptive responses.

The basis of the Frank-Starling law is the relation between contractile force (contractility) and sarcomere lengthening. According to this law, if LV volume raises then contractility raises too, together with systolic blood pressure, and hence afterload (see figure 1.7). While EDV is considered a subrogated measure of preload, afterload is defined as the wall tension during

LV ejection [16], [17]. Within a cylinder, the Laplace equation relates wall tension to pressure, radius and wall thickness, as:

$$\text{Wall tension} = \frac{(\text{pressure} * \text{radius})}{2 * \text{wall thickness}} \quad (1.2)$$

This oversimplified equation emphasizes that an increase in wall tension is produced by dilation of the ventricles (i.e., a greater radius) or, at a given radius, an increase in LV pressure. Moreover, an increase in wall thickness caused by hypertrophy balances the increased pressure, reducing the tension on any individual muscle fibre during the phase of compensatory hypertrophy [16].

The dilated heart becomes more sensitive to afterload (and less to pre-load) and, while cardiac efficiency decreases, both wall tension and afterload increase due to the inability of the heart to reduce its radius during contraction. These initially advantageous ventricular dilatation to sustain SV becomes a substantial disadvantage and diminishes further the myocardial performance. Moreover, dilatation leads to functional regurgitation of AV valves, and apoptosis can be induced by stretched myocardial cells thereby contributing to further disease progression. It is worth to mention that additionally to systolic pump function, LV performance depends also on active relaxation, diastolic elastic recoil, passive diastolic properties, and vascular loading conditions [16].

In early stages of HF, CO is normal at rest but is not maintained during stress. In contrast, a more advanced HF stage may show an elevated EDP and CO even at rest with the correspondent augmentation in EDV and ESV, which in turn reduces ventricular elastic recoil during relaxation, and therefore, rapid early filling diminishes. The rise in diastolic pressure also impacts negatively the pulmonary circulation. Clearly, before reaching an advanced HF stage, the body has activated many adaptative mechanisms that have failed progressively to maintain an adequate CO [16].

Although systolic and diastolic dysfunction often coexist and influence each other in HF patients, structural alterations of the ventricles are distinctive (see figure 1.12). In systolic dysfunction, the ventricle is large and dilated (eccentrically hypertrophied) and presents a deteriorated ejection and limited output. This subtype of HF is therefore also called HF with reduced ejection fraction, or abbreviated as HFrEF. In diastolic dysfunction, the ventricle is a small thick-walled and stiffened chamber (concentrically hypertrophied) that is not only unable to distend properly at normal filling pressures but also exhibits limited filling, alterations in relaxation, incoordinate wall motion during isovolumic relaxation, and altered ventricular inflow velocity.

Nonetheless, it is typical that EF is preserved in this patients, leading to the terminology HF with preserved ejection fraction (HFpEF). Additionally, patients have a limitation of exercise tolerance since the SV cannot be augmented at fast HRs. Hence, this condition leads to an increase in ventricular filling pressures and congestive symptoms even if systolic function is (nearly) intact [16], [17].

In contrast to the well-established systolic dysfunction or HFrEF, diastolic dysfunction or HFpEF has been recognized only in past decades as a major and growing epidemiological problem [31]–[33]. Commonly, LV diastolic alterations develop earlier than systolic dysfunction as relaxation is more energy dependent than contraction. Diastolic dysfunction is a multifactorial problem conditioned by age, hypertension, myocardial fibrosis, hypertrophy, ischemia, increased afterload, *inter alia*. Consequently, the contribution of diastolic dysfunction to HF is difficult to establish considering that diastolic and systolic dysfunction symptoms are clinically indistinguishable. In fact, the recognition, evaluation, and treatment of diastolic dysfunction remain a challenge [16], [17].

Nevertheless, detection of patients with diastolic dysfunction is equally essential as they have a prognosis nearly as poor as patients with systolic dysfunction. Even for systolic dysfunction patients, the degree of diastolic dysfunction is a powerful predictor of mortality [17]. Reliable (non-invasive) diagnostic tools and potential therapies for LV diastolic function remain an active field.

1.3.1.3 Heart failure treatment

Prevention should be the primary goal with patients at risk. Hypertension, diabetes, obesity and/or coronary artery disease, particularly in the elderly, must be effectively treated to control the development of HF [17].

Table 1.2: Common medications used to treat heart failure [17].

| Medication | Action | Possible side effects | Examples |
|--|--|--|---|
| Beta-blockers (BB) | ↓ HR ↓ BP Limits/reverses heart damage in HFrEF | Fluid retention, low BP, low pulse, general fatigue, lightheadedness | Carvedilol - metoprolol - bisoprolol |
| Angiotensin-converting enzyme (ACE) inhibitors | Vasodilation ↓ BP ↓ workload on the heart Improve blood flow | Dry cough, low BP, worsening kidney function, electrolyte imbalances | Lisinopril - captopril Enalapril- fosinopril - perindopril |
| Angiotensin II receptor blockers (ARB) | Alternative to ACE inhibitors | Dizziness, changes in kidney function, increased potassium levels | Candesartan - Losartan - Valsartan |
| Hydralazine and nitrates | Vasodilators Improve cardiac function | Dizziness, headache, swelling of the hands, arms, feet, or legs | Hydralazine and isosorbide dinitrate Nitroglycerine |
| Diuretics | Avoid fluid retention Improve signs of pulmonary oedema | Dehydration, electrolyte abnormalities, low BP | Furosemide - bumetanide torsemide - metolazone |
| Aldosterone antagonists | Diuretic effect Improve symptoms in HFrEF | Changes in kidney function, swelling or tenderness in the breasts | Spironolactone - eplerenone |
| Digoxin (digitalis) | ↑ contractility ↓ HR Improve symptoms in HFrEF | Nausea, vomiting, heart rhythm disturbances, kidney dysfunction | Lanoxin |

To reduce both morbidity and mortality, all patients with HFrEF should undergo aggressive treatment of the prime cardiovascular disease, in particular coronary artery disease, valvular heart disease or hypertension. Effective therapies include angiotensin-converting enzyme (ACE) inhibitors or angiotensin II receptor blockers (ARB) and beta-blockers (BB) (see table 1.2). Particularly, ACE inhibitors and BB slow progressive dilation of the heart. Digoxin or diuretics therapies control symptoms but have not been proven to reduce mortality. Nonetheless, improvement of quality of life is crucial and all measures in this regard should be taken [17].

In contrast, an optimal therapy approach for HFpEF is still unknown and few studies have been published on this regard. Following the principles of HFrEF treatment, the underlying cause of HFpEF should be addressed while cardiac loading conditions, HR or cardiac rhythm and efficient depolarisation should be improved. Diuretics and hypertension control could benefit HFpEF patients with pulmonary oedema or dyspnoea. Patients without evidence of increased filling at rest may not benefit from diuretics. Exercise tolerance could be enhanced with ACE inhibitors. LV relaxation therapy slows HR and allows the ventricle to better relax and fill before atrial contraction [17]. In the long term, hypertension control and regression of LV hypertrophy frequently improve HF symptoms. In brief, treatment should be patient specific. ACC/AHA practice guidelines [34]–[36] present a useful foundation to different approaches in the treatment of HF patients.

Nitrate therapies

The major effect of nitrates/nitrites in the cardiovascular system is the relaxation of smooth muscle in veins, larger arterioles and arteries through an endothelial pathway (see figure 1.10), which results in a reduction of BP and afterload due to the shift of central blood volume to the venous system [17]. Two classes of nitrates/nitrites available for treatment, organic and inorganic, mediate their principal effects (see table 1.3) via the NO pathway (see figure 1.10). Nevertheless, there are significant differences between these two classes related to their chemical structure and origin that determine distinctive pharmacokinetic and pharmacodynamic properties [37].

Synthetically produced, organic nitrates are small non-polar hydrocarbon chains attached to a nitrooxy-radical ($-ONO_2$), which imparts its biological effects. Glyceryl trinitrate (GTN) or nitroglycerine (NTG) (see figure 1.13) is the most commonly used medicinal organic nitrate, although other employed organic nitrates include pentaerithrityl tetranitrate, isosorbide dinitrate and isosorbide mononitrate (see table 1.3).

Table 1.3: A comparison of the therapeutic effects of organic and inorganic nitrates/nitrites in humans. Adapted from [37].

| | Organic nitrates/nitrites | Inorganic nitrates/nitrites |
|-------------------------|--|--|
| Endothelial dysfunction | Have a negative impact on endothelial function through the production of reactive oxygen species | Have a positive impact on endothelial function regardless of duration of supplementation acutely |
| Blood pressure | Leads to a fall in systemic BP Rapid in onset (around 15–30 min) Limited by the development of tolerance which ameliorates its BP lowering effects | Leads to a fall in systemic BP Nitrate – slow in onset (around 3 h) Effects more sustained with no evidence of tolerance Dose dependent |
| Pulmonary hypertension | Leads to a reduction in pulmonary arterial pressure when inhaled | Leads to a reduction in pulmonary arterial pressure when inhaled |
| Platelet function | Inhibits platelet aggregation with no evidence of attenuation of this effect with chronic administration | Inhibits platelet aggregation Effects are likely to be mediated by nitrite-NO |
| Other therapeutics | Treatment of acute pulmonary oedema Treatment of angina Treatment of anal fissures | Antimicrobial effects in different parts of the gastrointestinal tract Enhancement of gastric blood flow and mucosal healing Improve exercise capacity |
| Examples and sources | Nitroglycerine, pentaerithryl tetranitrate isosorbide dinitrate, isosorbide mononitrate | Sodium nitroprusside, green leafy vegetables and beetroot |

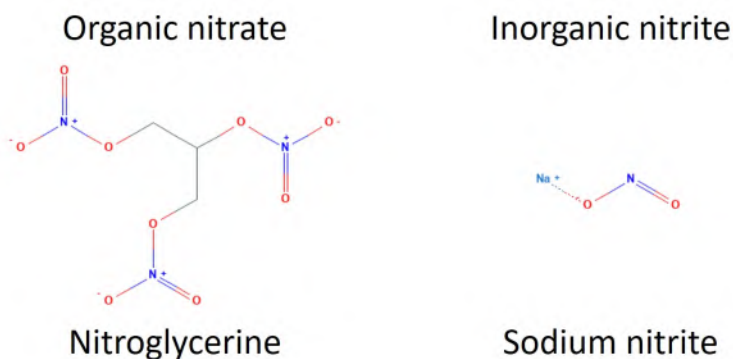


Figure 1.13: Chemical structure of nitroglycerine (organic nitrate) and sodium nitrite (inorganic nitrite). Adapted from National Center for Biotechnology Information. PubChem Database. Nitroglycerin, CID=4510, <https://pubchem.ncbi.nlm.nih.gov/compound/Nitroglycerin> (accessed on Oct. 31, 2019) and National Center for Biotechnology Information. PubChem Database. Sodium nitrite, CID=23668193, <https://pubchem.ncbi.nlm.nih.gov/compound/Sodium-nitrite> (accessed on Feb. 13, 2020).

Inorganic nitrates/nitrites are simpler molecules (salts of nitric acid and nitrous acid respectively, see figure 1.13) produced endogenously and present in the diet with more subtle and prolonged effects dependent on certain conditions [37]. Inorganic nitrates are taken up by plants, especially green leafy vegetables and beetroot, through water and soil, and then ingested by humans, resulting in their reduction to nitrites largely via the entero-salivary circulation (see figure 1.14).

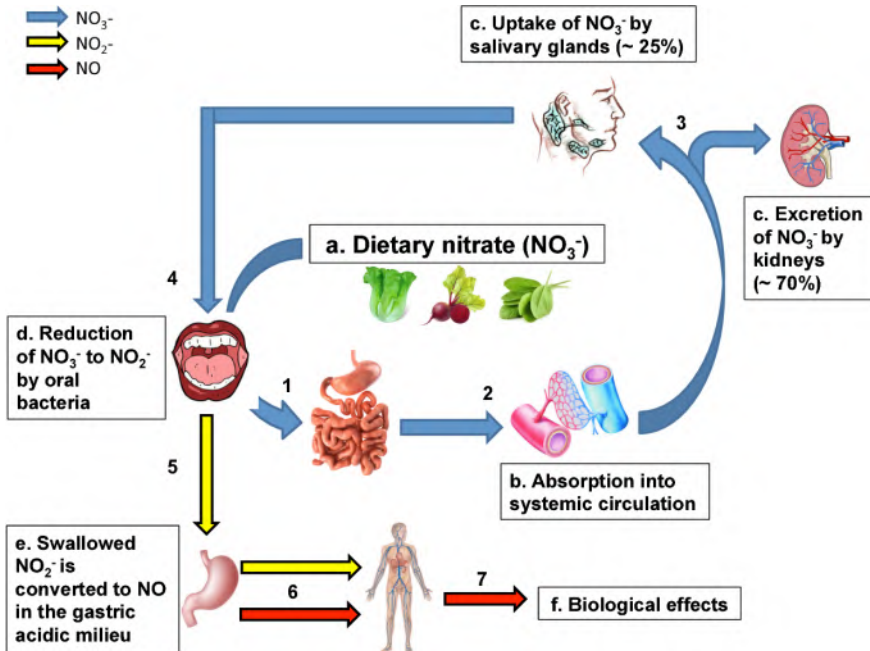


Figure 1.14: The entero-salivary circulation of dietary nitrate. Ingestion of nitrate (NO_3^-) (a) from dietary sources is swallowed and rapidly absorbed across the upper gastrointestinal tract (1) into the systemic circulation (2), where it mixes with endogenous nitrate. Approximately 70% of ingested nitrate is excreted by the kidneys (3) whereas 25% is actively concentrated in the salivary glands (c). Nitrate-rich saliva is secreted into the oral cavity (4) where facultative anaerobic bacteria reduce nitrate to nitrite (NO_2^-) (d) via the action of nitrate reductase enzymes. Nitrite-rich saliva is then swallowed (5) and further metabolized to nitric oxide (NO) nonenzymatically in the acidic stomach (e). NO exerts various biological effects in the body (6-f). Some nitrite escapes gastric acid reduction in the stomach and enters the systemic circulation (6) where it gets reduced to NO in the blood and in other tissues that then exerts biological effects (f). Adapted from [38].

In practice, the use of organic nitrates is prevalent for treatment of cardiovascular diseases to relief symptoms and support BP control. Furthermore, in patients with acute infarction and decreased LV function, organic nitrates limit infarct size and impact positively ventricular remodelling [17]. Nonetheless, beneficial effects of organic nitrates are lost after drug treatment is

discontinued and they show a limited impact in the mortality rate of these patients. Another major limitation of organic nitrates use is tolerance, that is a loss of haemodynamic effects with sustained use. The mechanism of this phenomenon remains unknown, but tolerance can be temporally overcome with escalation of dose [17]. Even though the use of organic nitrates dominates cardiovascular treatment, this may change with the increasing recognition of their limitations, and ongoing discovery of beneficial effects and specific advantages of inorganic nitrate/nitrite [37].

In Chapter 5, we propose a thorough haemodynamic analysis in HFpEF patients comparing the effects of organic and inorganic nitrates/nitrites in cardiovascular function to support the search for a proper treatment.

1.3.2 Atherosclerosis

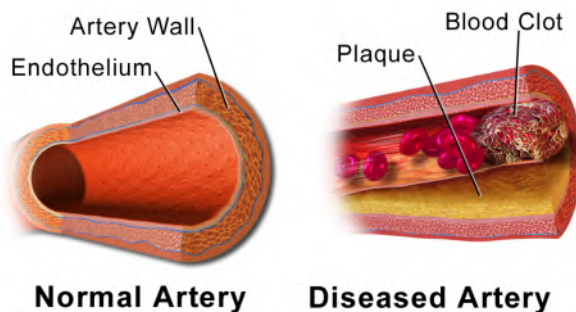


Figure 1.15: Illustration of the anatomical differences between a normal vessel and an atherosclerotic vessel. Adapted from https://commons.wikimedia.org/wiki/File:Blausen_0053_Artery_NormalvsDiseasedVessel.png. By Blausen.com staff (2014). “Medical gallery of Blausen Medical 2014” WikiJournal of Medicine 1 (2). DOI:10.15347/wjm/2014.010. ISSN 2002-4436. [CC BY 3.0 (<https://creativecommons.org/licenses/by/3.0>)].

Atherosclerosis is a major pathological process in large arteries and the most common cause of clinical complications related to arterial wall degeneration. In fact, atherosclerosis is a degenerative disease characterised by the accumulation of cells, matrix fibres, lipids, and tissue debris in the intima (see figure 1.15). Altered biomechanical and haemodynamic conditions trigger adaptive responses in arterial wall thickness, lumen diameter or both to preserve the structural and functional integrity of the arterial tree but

pathological conditions may lead to lumen stenosis, aneurysm formation, or obstructive intimal hyperplasia [20].

Smoking, elevated serum lipid levels, hypertension, obesity, diabetes mellitus, physical inactivity, emotional stress or genetic predisposition are correlated factors associated with atherosclerosis development in certain arterial beds more than in others. Haemodynamics and wall properties, associated with variations in the distribution of shear and tensile stresses, also influence plaque formation. For instance, sites prone to plaque formation are the coronary arteries, carotid bifurcation, infrarenal abdominal aorta, and iliofemoral arteries whilst the thoracic aorta and the common carotid, distal internal carotid, renal, mesenteric, and upper extremity arteries are, in general, spared [20].

1.3.3 Aging

Life expectancy had a tremendous increase in the past century, and never before a society has had as many elderly as nowadays. Considering the high incidence and prevalence of cardiovascular disease among the elderly, the need to understand age-related changes in the cardiovascular system and how they trigger pathological processes becomes obvious. Older patients are more prone to systolic hypertension, HFpEF and to coronary artery disease involving multiple vessels. To lower the elevated morbidity and mortality of cardiovascular diseases among the elderly, effective prevention and treatment must be implemented. However, randomized controlled trials do not specify appropriate treatment adaptation to populations differing from those studied, and these trials rarely enroll elderly patients, despite the greater burden of cardiovascular diseases in this population [18]–[20].

Evidently, more studies should provide evidence-based medicine across age, including specific information on drug efficacy, safety and functional/health status outcomes, especially for patients who account for the greater health care expenditures. Accordingly, a careful consideration of therapeutic benefits across patient age and heterogeneity of aging should guide treatment selection. In summary, a broader perspective, including patient priorities, which are quality of life and functional independence rather than longevity for many older persons, should become pivotal to ensure the best cardiovascular care [18]–[20].

Cardiovascular changes related to aging

Aging is a natural process of adaptation decline that brings several changes in all the body, including the cardiovascular system. Notwithstanding, aging

is a remarkably heterogenous process without a universal definition or an accurate biomarker. In effect, there is not a precise age or progression establishing the onset or development of physiological changes related with aging in all individuals, even though a global pattern exists (see table 1.4).

Table 1.4: Relationship of cardiovascular human aging in health to cardiovascular diseases. Adapted from [16].

| Age-associated changes | Plausible mechanisms | Possible relation to human disease |
|---|---|--|
| Cardiovascular structural remodelling | | |
| ↑ Vascular intimal thickness | ↑ Migration of and ↑ matrix production by vascular smooth muscle cell Possible derivation of intimal cells from other sources | Promotes development of atherosclerosis |
| ↑ Vascular stiffness | Elastin fragmentation ↑ Elastase activity ↑ Collagen production by vascular smooth muscle cell and ↑ cross-linking of collagen Altered growth factor regulation/tissue repair mechanisms | Systolic hypertension LV wall thickening Stroke Decline in cognitive function Atherosclerosis Possible LV hypertrophy |
| ↑ LV wall thickness | ↑ LV myocyte size with altered Ca^{2+} handling ↓ Myocyte number (necrotic and apoptotic death) Altered growth-factor regulation Focal matrix collagen deposition | Retarded early diastolic cardiac filling ↑ Cardiac filling pressure Lower threshold for dyspnoea ↑ Likelihood of HF with relatively normal systolic function Possible LV hypertrophy |
| ↑ Left atrial size | ↑ Left atrial pressure/volume | ↑ Prevalence of atrial fibrillation and other atrial arrhythmias |
| Cardiovascular functional changes | | |
| Altered regulation of vascular tone | ↓ NO production/effects | Vascular stiffening; hypertension Early atherosclerosis |
| Reduced threshold for cell Ca^{2+} overload | Changes in gene expression of proteins that regulate Ca^{2+} handling; increased polyunsaturated fatty acids ratio in cardiac membranes | Lower threshold for atrial and ventricular arrhythmia Increased myocyte death, increased fibrosis Reduced diastolic and systolic function |
| ↓ Cardiovascular reserve | ↑ Vascular load ↓ Intrinsic myocardial contractility Ventricular-vascular load mismatch during stress ↑ Plasma levels of catecholamines ↓ β-adrenergic modulation of HR, myocardial contractility and vascular tone due to postsynaptic signalling deficits | Lower threshold for HF and increased severity of HF |
| Reduced physical activity | | |
| | Learned lifestyle | Exaggerated age changes in some aspects of cardiovascular structure and function, e.g., arterial stiffness Negative impact on atherosclerotic vascular disease, hypertension, and HF |

A hallmark of cardiovascular aging is the weight increase of the heart due to myocyte hypertrophy and connective tissue deposition. Furthermore, increased septal thickness and decreased base-to-apex dimensions result in ventricular size reduction and shape modification. In spite structural changes, greater vascular stiffness and early reflected pulse waves, systolic function remains basically normal at rest, partly due to a beneficial adaptation that enables the continued ejection of blood during late systole. In contrast, the enhanced stiffness impairs compliance and requires greater filling pressure to adapt via the Frank-Starling mechanism producing diastolic dysfunction [18]. This causes a prolonged (impaired) relaxation and slower early diastolic filling. Parallel structural changes, such as mitral or aortic valvular disease,

hypertension, atrial arrhythmias, or senile amyloidosis (accumulation of a protein in the heart causing increased wall thickness), promote additional alterations of haemodynamic conditions aggravating diastolic dysfunction [18].

Alterations in the cardiac conduction system of the aging heart arise from apoptosis and the deposition of collagenous and fatty tissue, concretely at the SAN, and calcification of the AV node and left and right bundle branches. As a result, PR and QT intervals in the ECG frequently show moderate increases together with a longer QRS complex, a lower T wave amplitude and bundle branch blocks. Moreover, episodes of atrial fibrillation become more common among aged individuals. Consistent alterations of autonomic regulation lead to an impaired baroreflex response to physiological stressors and increased central nervous system effects. In consequence, HR and heart rate variability (HRV) are reduced, vasoreactivity is diminished, and cardiac contractile responses are blunted [18].

The aging arterial system shows representative changes in elasticity, distensibility and dilation induced by collagen deposition and a weakened vascular elastin. Particularly, endothelial impairment caused by alterations, such as apoptosis and progressive irregularity in endothelial cell size and shape, is difficult to separate from coexisting hypertension, hypercholesterolemia, and atherosclerosis. The intima develops a more complex content originating a diffuse intimal thickening, which characterises most adult human arteries, even in the absence of atherosclerosis. This process may not parallel lipid accumulation and may occur in individuals without substantial burden of atheroma. Smooth muscle growth and lipid and calcium deposition affect the elastic lamina of the media layer contributing to arterial stiffening and, hence, to a reduction in arterial distensibility and compliance, and the following augmentation of the travel speed of the pulse along an arterial segment, known as pulse wave velocity (PWV). A higher PWV results in a faster propagation speed of waves, hereby leading to faster return of wave reflections boosting further systolic pressure. Moreover, vascular remodelling due to elastance changes and congenital, degenerative, mechanical and haemodynamic factors leads to dilatation and elongation of the aorta and major arteries, setting the stage for dissection or rupture [18]–[20].

Regarding cardiovascular performance, normal aging involves reduction of aerobic capacity due to an impaired O_2 extraction from the circulating blood volume, which in turn is related to a decline in muscle mass and an increase of body fat. To counterbalance aging effects to some extent, successful physical training can enhance exercise tolerance, aortic elasticity, muscle mass, ventricular performance, and even achieve the same peak CO as younger cohorts, albeit by different mechanisms. It is therefore clear that

lifestyle influences the pace of aging and quality of life in later years. Other (risk) factors impacting the aging process include hypertension, hypercholesterolemia, coronary artery disease, diabetes mellitus, smoking and LV hypertrophy [18], [20].

Overall, aging has substantial effects in cardiac structure and function in terms of physiological responses to exertion and clinical responses to disease. Notably, risk factors play a decisive role in pathophysiological progression and can aggravate and accelerate the aging process.

NON-INVASIVE TECHNIQUES FOR CARDIOVASCULAR ASSESSMENT

This chapter builds up on the foundations established in Chapter 1, introducing non-invasive techniques to measure and image the cardiovascular system. In fact, accurate imaging is crucial to evaluate cardiac anatomy, function and metabolism. This chapter focuses on two major cardiovascular imaging modalities that use sound waves (ultrasound) and the magnetic properties of the hydrogen nucleus (magnetic resonance imaging) to characterise the heart and vessels.

The first part of the chapter deals with measuring techniques to obtain arterial pressure waveforms, which are essential to assess arterial stiffness and potential cardiovascular risk factors of a subject. Next, common concepts for imaging techniques are presented, and then imaging modalities are reviewed, discussing basic physical principles, cardiovascular applications and clinical implications. Finally, advantages, limitations and additional considerations regarding each modality are discussed.

This chapter is based, extracted, adapted and/or edited from several bibliographic resources. For writing the first section, regarding the pressure wave measurement, the main sources were the articles: *Expert consensus document on arterial stiffness: methodological issues and clinical applications* [39] of Laurent *et al.*, and *Assessment of arterial pressure wave reflection: methodological considerations* [40] of Swillens and Segers, and the Doctoral dissertation *Development and validation of non-invasive diagnostic tools for the assessment*

of arterial stiffness and wave reflections with application in Sub-Saharan Africa of Kips [41]. The principal sources employed to develop the following sections of the chapter concerning imaging modalities were *Biomedical Signal and Image Processing* book of Najarian and Splinter [42], *Biosignal and medical image processing* book of Semmlow [43], *Hurst's the heart* book of Fuster [16], *Mayo Clinic Cardiology: Concise Textbook* of Murphy [17], *Textbook of cardiovascular medicine* of Topol and Califf [18], *Braunwald's heart disease: a textbook of cardiovascular medicine* of Libby [19], *Vascular surgery* book of Rutherford [20], *Introduction to vascular ultrasonography* book of Zwiebel and Pellerito [22], *Heart failure in children and young adults: from molecular mechanisms to medical and surgical strategies* book of Chang and Towbin [23], *Feigenbaum's Echocardiography* digital edition of Feigenbaum, Armstrong and Ryan [44] and *the heart as a muscle-pump system and the concept of heart failure* article of Weber and Janicki [25].

2.1 NON-INVASIVE ARTERIAL PRESSURE WAVE MEASUREMENT

Arterial pressure waveforms have always been essential for the assessment of the cardiovascular system. The two most commonly used techniques to measure non-invasively the pressure waveform in the vascular periphery are photoplethysmography and applanation tonometry [39].

Based in a technique described by Penaz [45], photoplethysmography uses the changes in light absorption to estimate volume variations of an organ or a structure [39]. Concretely, finger artery size is continuously measured using a finger cuff equipped with a light source and a detector. An external pressure is applied constantly to the artery through an inflatable bladder to counterbalance the internal pressure [46]. Changes in pressure are registered and displayed as pressure waveforms. A disadvantage of the method is that finger pressure waveforms only correspond well with radial pressure waveforms in young, healthy subjects whereas this is not the general case, particularly in pathological states.

Applanation tonometry employs high-fidelity strain micromanometers directly applied on the skin at a constant pressure to record arterial pressure waveforms. This technique relies on the existence of a hard structure against which it is possible to applanate a superficial artery, such as radial, carotid, femoral and brachial locations, even if accurate measurements are difficult to obtain in the brachial artery [39], [41]. Since calibration is a necessary step for tonometric waveforms, different approaches have been proposed. At the brachial artery, calibration is rather easy using systolic and diastolic pressures from sphygmomanometry measurements. At other arterial locations, calibration is more complex. One approach suggests the use of brachial diastolic

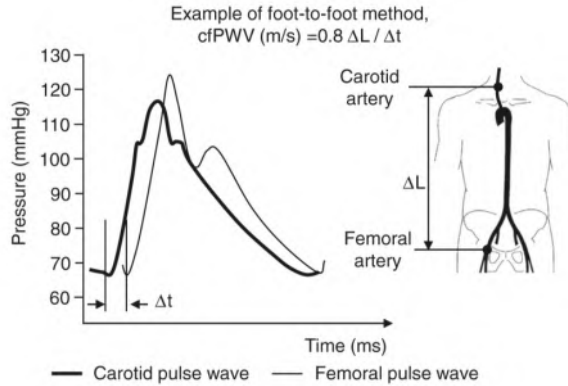


Figure 2.1: Pressure waveforms obtained with applanation tonometry to estimate the carotid-femoral pulse wave velocity. Examples of pressure waveforms of the carotid (thick line) and the femoral (thin line) arteries obtained with applanation tonometry. The foot-to-foot method uses these waveforms for calculating the carotid-femoral pulse wave velocity (cf-PWV) by multiplying the carotid-femoral distance (ΔL) by 0.8 and dividing the result by the time interval (Δt) between the foot of the carotid and the femoral waveform (see Chapters 3 and 6). Adapted from <https://commons.wikimedia.org/wiki/File:Method-of-pulse-wave-analisis.png>. By Omboni S, Posokhov IN [CC BY-SA 4.0 (<https://creativecommons.org/licenses/by-sa/4.0>)].

blood (DBP) and mean arterial (MAP) pressures to calibrate tonometric waveforms at any location [39], [41]. This method is based on the observation that the difference between DBP and MAP remains constant throughout the large arteries [39], [41]. Brachial tonometry is required to calculate MAP from the arithmetic average of a calibrated (brachial) pressure waveform. A simpler approach proposes to estimate MAP as the sum of DBP and 40% of the pulse pressure (PP) [41]. Although the aorta is the most relevant location of the arterial system, aortic pressure waveforms cannot be obtained noninvasively. Thus, transfer functions have been built to synthesised aortic pressure waves from radial pressure curves even if the generalised nature of the method is a limitation, especially in pathophysiological applications. An alternative procedure is to measure the pressure wave at a site closer to the heart, such as the carotid (see figure 2.1) or the subclavian arteries, in spite of a more challenging acquisition [39].

High-fidelity applanation tonometry is also a well-accepted method to estimate pulse wave velocity (PWV) of the carotid-femoral segment (see figure 2.1). In this case, waveforms are recorded sequentially at each site, using a simultaneously recorded electrocardiogram (ECG) signal as time reference

for calculating the transit time of the pressure wave between both locations. Nevertheless, applanation tonometry is a highly user-dependent method so operators must have enough training to perform adequate measurements [39].

2.2 CARDIOVASCULAR IMAGING

2.2.1 Principles of imaging

Unlike other organs, the heart has a fine structure and complex motion that requires imaging modalities with high temporal and spatial resolution. Two major modalities comply with these requirements: ultrasound and magnetic resonance imaging (MRI) [18].

Imaging displays the interaction of energy with matter to discern structure and function. For example, ultrasound shows the differential reflection of acoustic waves from the border of two tissues with distinct acoustic impedances and MRI defines the differential distribution of weak magnetic characteristics within the body. Regardless the differences between both modalities, there are common basic concepts that are relevant to consider [18].

2.2.1.1 *Basic concepts*

Spatial resolution is defined as the smallest separation at which two objects are differentiated. Each imaging modality and each device has a specific spatial resolution, but some generalities can be derived [18]. For instance, spatial resolution for ultrasound is higher in the near field than in the far field and better in the axial direction (along a scanline) than in the lateral direction (across scan lines). Three-dimensional (3D) MRI typically has also greater resolution in the imaged plane than in the axis along which slices of the object are being selected [18]. There is an important difference between physical resolution of the imaging modality, which was described above, resolution display and functional spatial resolution. Resolution display is the spacing of the picture elements (pixels) on the screen and can be greater or lesser than the physical resolution [18]. The functional spatial resolution is the lesser of the physical and screen resolutions. Temporal resolution is described as the shortest time a device needs to generate an image (frames per second). In general, there is a trade-off between temporal and spatial resolution. Velocity resolution refers to the smallest difference in velocity that can be distinguished [18].

Digital acquisition, storage and visualisation is the preferred option for cardiac imaging due to several advantages over analogue techniques, such as a more efficient review of examinations and comparison with previous stored examinations, facilitated access, long-termed archiving without loss of quality, lower costs, etc. To accomplish this goal, a standard format has been implemented together with the improvement of network systems [18].

The digital imaging and communications in medicine (DICOM) image format standard is a set of rules for exchanging images, specifying information about the patient, the purpose and the technique of the examination, and the pixel data themselves. In this format, each imaging modality has specific data elements and storage structures for communication and exchanging information [18]. In practice, echocardiography (ultrasound) has diverse needs, requiring grayscale, colour, and spectral Doppler storage, and images may be stored either uncompressed or with lossless or lossy JPEG compression [18]. Instead, nuclear standard, which includes MRI, encompasses the many complex studies of nuclear cardiology without any compression because the small size of the data [18]. Data reduction in cardiac imaging is fundamental with limited disk storage and network bandwidth. Lossless or lossy digital compression is available in DICOM standard. Lossless algorithms enable the recovery of the original image, but these algorithms have relatively poor compression ratios. Lossy algorithms have higher compression ratios but distort slightly the recovered image. Hence, there is a compromise between quality and storage space [18].

2.2.2 Echocardiographic imaging

Echocardiography is the most used cardiac imaging method to assess structural, functional, or haemodynamic abnormalities of the heart or great vessels [18], [19]. Indeed, the echocardiographic technology is non-invasive, rather inexpensive, portable and harmless to biological tissues, and produces relatively high-resolution images in real time. Furthermore, echocardiographic modalities allow to acquire diverse information, such as anatomical structures from multiple tomographic planes with two-dimensional (2D) imaging and cardiac haemodynamics and blood flow magnitude and direction with Doppler and colour flow imaging [18], [19]. Moreover, flow data provide indirect information on tissue metabolism and functionality. Therefore, echocardiography plays a central role in diagnosis and quantification of the nature and severity of specific cardiovascular pathologies [18], [19].

2.2.2.1 Principles

Ultrasonic waves are acoustic waves with frequencies above the upper audible limit of human hearing ($> 20kHz$). In practice, the most common method to produce medical ultrasound is by mechanical vibrations of a specialised material when an external alternating electric field is applied across it, i.e., the piezoelectric effect. Acoustic waves are generated with devices known as transducers or probes, in which piezoelectric crystals are the core [18]. Placed between two electrodes that apply a voltage, these crystals are induced to expand and contract in a sinusoidal manner. By doing so, appropriate sound waves for diagnostic use are produced. When travelling through matter, a fraction of these waves is reflected or scattered upon finding an impedance mismatched in the boundary of two media while the remaining fraction is transmitted [18]. When acoustic backscatter waves strike the crystal, the piezoelectric effect is opposite, converting the induced vibrations in an electrical signal whose amplitude is proportional to the mechanical pressure [18]. The electric signal is detected by the electrodes attached to the crystal and converted to a digital signal to be further processed for imaging and characterising the medium [18], [19].

Mechanical waves are characterised by: 1) period (T), that is the time between two consecutive repetitions of an identical pattern; 2) frequency (f), the reciprocal of T , defined as number of times a pattern repeats itself per second; and 3) wavelength (λ), which describes the spatial repetition of the pattern sequence [42], [43]. These concepts are related as:

$$\lambda = cT = \frac{c}{f} \quad (2.1)$$

where c is the local speed of sound.

The relationship between speed of sound propagation (c), elastic modulus (K) and local density of a material (ρ) is described as:

$$c = \sqrt{\frac{K}{\rho}} \quad (2.2)$$

This equation shows that the speed of sound is limited by the features of the material, indicating a time delay between the emitted and the detected acoustic waves, known as time of flight (TOF). These time delays provide practical information about physical properties of the tissues under study [42], [43].

In wave propagation, a more general term for the factor limiting the speed of sound is acoustic impedance (Z_A) and depends directly on the density of the material [42], [43]:

$$Z_A = \rho c \quad (2.3)$$

Regarding the interaction of ultrasound waves with matter, the most relevant concepts to consider are attenuation, reflection, refraction and scattering.

Indeed, attenuation is an essential physical phenomenon in medical ultrasound. Body tissue converts acoustic waves into motion as a result of friction, which translates into heat energy. This absorption reduces the intensity of sound waves that are reflected and, ultimately, detected by the transducer. Thus, the process of detection is more difficult in a deep region of interest as the attenuation is higher [42], [43]. The attenuation in the pressure signal, dP , is described as:

$$dP = \alpha P dz \quad (2.4)$$

Where P is the incident pressure; dz is the distance over which the absorption takes place; and α is the attenuation factor of the medium [42], [43]. Solving this equation for P in the case of a plane wave:

$$P(z) = P_o e^{-\alpha z} \quad (2.5)$$

Where P_o is the pressure at $z = 0$. This equation is known as the Beer–Lambert–Bouguer law of attenuation and shows the exponential decrease in amplitude of ultrasound as it passes through homogeneous tissue [42], [43].

Attenuation varies with tissue type (see table 2.1) and is stronger at higher frequencies, particularly at deeper locations, producing a low-pass filtering effect and limiting the frequency that can be used clinically in echocardiography [42], [43].

Attenuation is often defined as the intensity ratio of a measured signal (P_1) to the source signal (P_o) expressed in logarithmic form:

$$dB = 10 \log_{10} \left(\frac{P_1}{P_o} \right) \quad (2.6)$$

Due to the high attenuation coefficient of air, usually a gel with a low attenuation coefficient is used as an interface between the transducer and

Table 2.1: Values of ultrasonic parameters for different biological tissues.
Adapted from [18].

| Tissue | Speed of propagation [m/s] | Attenuation coefficient [cm^{-1}] | Acoustic impedance [$10^4 \text{kg}/\text{m}^2\text{s}$] |
|--------|----------------------------|--|--|
| Blood | 1540 | 0.0198 | 1.6 |
| Bone | 2240 | 3.01 | 3.8-7.4 |
| Fat | 1450 | 0.1 | 1.4 |
| Muscle | 1540 | 0.193 | 1.7 |
| Lung | | | 0.26 |
| Plasma | | 0.0069 | 1.5 |
| Water | 1480 | | |

the skin during ultrasound measurements to avoid air gaps. Additionally, ultrasound is unable to image the lungs, since they contain air, or any structure behind. Bone also has a high attenuation coefficient, making difficult to perform ultrasound measurements of tissues covered by them [42], [43]. Effectively, it is necessary to have a field of vision of the tissue without bones or lungs in the way. For instance, certain windows must be used to image the heart and avoid the lungs [42], [43].

After the transducer emitted acoustic waves, they propagate across the body tissue, finding acoustically different media. At these interfaces, the energy is partially reflected, and the remainder is transmitted into the second tissue, generating secondary waves [42], [43]. By definition, the angle of incidence (θ_i) is equal to the angle of reflection (θ_r) (see figure 2.2). In practice, the angle of incidence should be limited below 3° to avoid reflected waves to miss the transducer [42], [43].

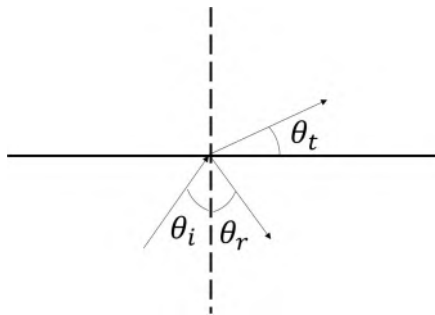


Figure 2.2: Graphical description of the Snell law. At the interface of two different media, the passing through of an incident (i) pressure wave generates a reflected (r) and a transmitted (t) pressure wave-front.

Reflection occurs at a smooth boundary of two media. How much of the incident wave is reflected can be calculated as the ratio of the reflected wave to the incident wave, i.e., the pressure reflection coefficient (r) [42], [43]:

$$r = \frac{P_r}{P_i} = \frac{Z_{A_2} \cos \theta_i - Z_{A_1} \cos \theta_t}{Z_{A_2} \cos \theta_i + Z_{A_1} \cos \theta_t} \quad (2.7)$$

Where θ_i and θ_t are the incident and transmitted angles, respectively; Z_{A_1} and Z_{A_2} are the acoustic impedances of both media; and P_i is the incident pressure and P_r is the reflected pressure. This equation shows that the pressure reflection coefficient is dependent on the acoustic impedance of both media [42], [43].

In turn, the ratio of the transmitted to reflected wave pressures, or the pressure transmission coefficient (t) is defined as:

$$t = \frac{P_t}{P_i} = \frac{2Z_{A_2} \cos \theta_i}{Z_{A_2} \cos \theta_i + Z_{A_1} \cos \theta_t} \quad (2.8)$$

Where transmitted pressure is P_t .

These equations establish that modest variations of acoustic impedance between two media generate noticeable alterations in the intensity of reflected and transmitted signals. In fact, biological tissues have comparable acoustic impedances, allowing most of the sound waves to be transmitted (see table 2.1). Thus, ultrasound can penetrate the body to provide information on deep structures, but it can also “bounce” between interfaces, acting as a source of noise [42], [43].

Another source of noise associated with reflection is induced by the small size of the cells. Reflection at a microscopic scale (structures smaller than the wavelength of sound) undergoes scattering, which is defined as diffuse reflection, meaning the acoustic waves are sent in all directions [42], [43]. Scattering occurs at tissue inhomogeneities that induce the reflected waves to interfere with each other, producing a complex ultrasound pattern known as speckle. Because speckle is relatively constant over time, it is possible to track its motion to detect tissue deformation and strain. In sum, scattering is a form of attenuation and a complex source of noise in ultrasound imaging [42], [43].

Resolution is another relevant parameter of ultrasound imaging. There are two scanning directions, and thus two distinctive resolutions: axial and lateral [18]. Axial resolution is the capacity to distinguish two subsequent layers in the direction of the wave propagation and is a direct function of the emitted signal wavelength, whereas lateral resolution refers to the ability to

discern between two points perpendicular to the wave propagation and is determined by the ultrasound beam width and, hence, by the dimension of the transducer [42], [43].

2.2.2.2 Echocardiography

The transducer sends short pulses of ultrasound to biological tissue, but only a part of the energy is reflected from deep structures to the transducer [18]. The depth (d) of the reflector is calculated with the time delay (Δt) between the emitted and the received signal:

$$d = c \frac{\Delta t}{2} \quad (2.9)$$

Where velocity of sound (c) is assumed to be constant in soft tissue (1540m/s) and the factor of 2 accounts for the time to and from the object.

When a reflected echo strikes the transducer, the piezoelectric crystal produces a minuscule voltage in response to the vibrations from the returning ultrasound. To adjust for the significantly weaker echoes from deep structures, logarithmic compression and time-gain compensation apply greater amplification to echoes returning after longer intervals [18]. Amplitude and phase information is obtained from the amplified signal to localise and display structures [18]. Echoes can be displayed as M-mode, which is a time-distance sweep showing motion of structures along a single scan line (figure 2.3A), B-mode (figure 2.3B) or a surface rendering of a 3D echo.

Intracardiac blood flow velocity measurements are obtained by Doppler echocardiography to derive haemodynamic parameters (see figure 2.4). An ultrasound beam with a known frequency (f_o) is transmitted to the heart or the vessels, and red blood cells reflect the ultrasound waves at a frequency (f_r) that depends on the direction of the cells with respect to the receiver (transducer): toward means a higher frequency, away means a lower frequency [19]. The Doppler shift is detected by the transducer and calculated as [19]:

$$\Delta f = f_r - f_o = 2f_o \frac{v \cdot \cos\theta}{c} \quad (2.10)$$

Where c is the speed of sound in blood (1540m/s), v is the velocity of the moving target and θ is the angle between the ultrasound beam and the direction of the moving target [19].

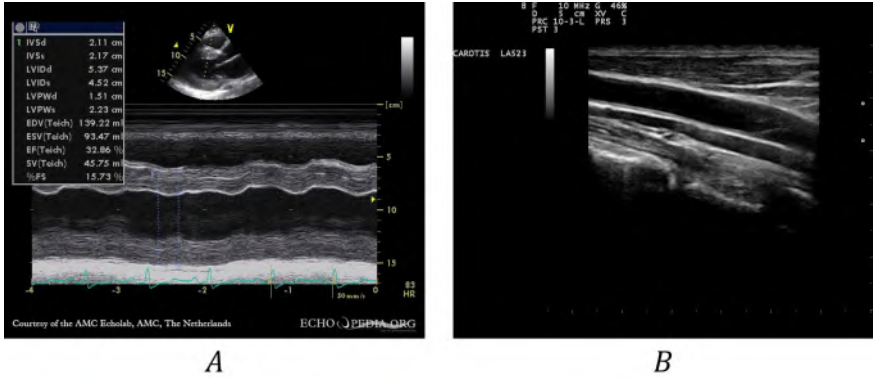


Figure 2.3: Examples of ultrasound images. A) M-mode scan through a left ventricle of a heart with diastolic dysfunction. B) B-mode scan of a carotid artery. A) Adapted from [https://commons.wikimedia.org/wiki/File:HCM,_diastolic_dysfunction_E00544_\(CardioNetworks_ECHOpedia\).jpg](https://commons.wikimedia.org/wiki/File:HCM,_diastolic_dysfunction_E00544_(CardioNetworks_ECHOpedia).jpg). By CardioNetworks: Secretariat [CC BY-SA 3.0 (<https://creativecommons.org/licenses/by-sa/3.0/>)]; B) Adapted from https://commons.wikimedia.org/wiki/File:CCA_Ultrasound_110318140725_1409520.jpg. By © Nevit Dilmen [CC BY-SA 3.0 (<https://creativecommons.org/licenses/by-sa/3.0/>)].

The Doppler shift (Δf) is then translated into a blood flow velocity:

$$v = \frac{\Delta f \cdot c}{2f_0 \cdot \cos\theta} \quad (2.11)$$

The angle θ increases when the ultrasound beam is not parallel with the blood flow direction, resulting in the underestimation of Δf and peak velocity by the factor $\cos\theta$ [19].

Spectral Doppler imaging shows the instantaneous velocity over time, and the time velocity integral (TVI) can be obtained from this curve. The most common spectral Doppler modalities are continuous-wave (CW) Doppler and pulsed-wave (PW) Doppler. A third common modality, Doppler flow mapping (colour Doppler), is a computer-enhanced version of PW Doppler [18].

In CW Doppler, the transducer has two components: an emitter and a receiver, both running continuously. CW Doppler quantifies high-velocity flow (jets and gradients) along the scan line and is not limited by aliasing but does not provide information about the localisation of the source. CW Doppler images show an envelope (the maximal measured velocity) filled with signals [18]. In contrast, in PW Doppler the transducer is composed by a single crystal that transmits brief bursts of ultrasound at a pulse repetition

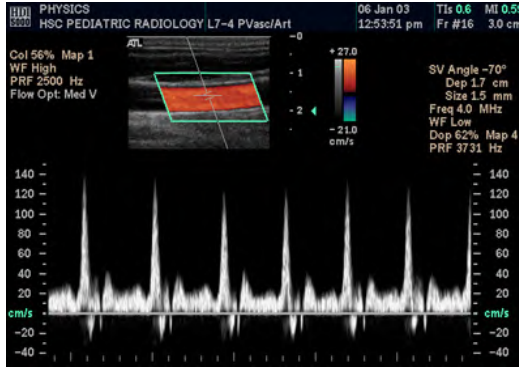


Figure 2.4: Spectral Doppler scan of a common carotid artery. Adapted from <https://commons.wikimedia.org/wiki/File:SpectralDopplerA.jpg>. By Drickey at en.wikipedia [CC BY-SA 2.5 (<https://creativecommons.org/licenses/by-sa/2.5>)].

frequency, yet the receiver activates only after a programmed time delay. PW Doppler allows the measurement of blood velocities at a specific location determined by a sample volume. Graphically, the number of scatters (red blood cells or tissue reflectors) determine the signal intensity (amplitude) whereas the variation in velocity defines the width. The brightest line is the most frequently measured velocity within the sample volume [18]. Aliasing can occur if the Doppler shift frequency is more than one-half the pulse repetition frequency (Nyquist limit), limiting the maximal velocity that can be measured [19]. Lastly, Doppler flow mapping uses PW Doppler information to superimpose colour on 2D imaging to display velocity, direction or turbulence of blood flow, as the upper part of figure 2.4 demonstrates. Thereby, blood flow information is colour coded: red depicts a flow towards the transducer and blue away from it. Practical applications are valvular regurgitation, stenosis, and various shunt lesions. Colour Doppler has also a Nyquist limit and a restriction in frame rate and velocity resolution due to the need to scan multiple lines simultaneously, restriction that can be overcome to some extent by parallel processing [18].

Tissue Doppler imaging (TDI) is a modification of PW Doppler to record the motion of solid tissue (usually from the myocardium) with lower velocities or frequency shifts but larger amplitudes than those of blood flow. For example, TDI can register the motion of the mitral annulus. This is accomplished by the implementation of filters to remove high-velocity/low-intensity signals from blood and to preserve the low-velocity/high-intensity signals from tissue. TDI results are displayed as a spectral Doppler (velocity over time) but can also integrate colour to complement the displayed information. TDI recordings may over or underestimate the active component of the tissue because of translational motion or tethering, respectively [18], [19].

To overcome this limitation, a derived modality is proposed: deformation imaging, strain (ϵ) or strain rate imaging. This modality measures the actual extent of stretching or contraction.

2.2.2.3 *Applications of echocardiography*

Cardiac assessment

2D and M-mode are the most common echocardiographic modes for quantification of heart and chamber dimensions and provide structural and functional information on cardiac disease. These measurements are usually obtained at end diastole and end systole with the transducer on the left parasternal region. Nonetheless, position and plane are dependent on the measurement to be performed. There are three orthogonal planes suggested for cardiac imaging: long-axis (aortic root-apex), short-axis (perpendicular to the long axis), and four-chamber (traversing both ventricles and atria through the mitral and tricuspid valves). Recommended transducer positions for obtaining these planes are parasternal, apical, subcostal, and suprasternal [17] (see figure 2.5).

Doppler echocardiography has been established as a fundamental routine measurement in cardiovascular medicine for haemodynamic assessment, replacing cardiac catheterization. Doppler echocardiography and 2D imaging are not only performed using the same transducer but they delivered complementary information [17], [19]. For instance, 2D imaging operates as visual guidance to identify the region of interest during Doppler echocardiography, and superimposed colour by Doppler echocardiography enhances structural information. For Doppler echocardiography measurements, the same planes as for 2D imaging can be used yet the same transducer position frequently is not favourable for both Doppler echocardiography and anatomical imaging. Additionally, the signal to noise ratio in Doppler echocardiography recordings is higher than for 2D modes [17], [19].

The following section presents a short description of the most important echocardiographic parameters measured in routine clinical practice. Guidelines for cardiovascular assessment have been published by the American Society of Echocardiography (ASE), the European Association of Cardiovascular Imaging (EACVI) [47], [48] and the American College of Cardiology and the American Heart Association (ACC/AHA) [49], [50].

Functional assessment of the cardiac structure

In general, M-mode and B-mode (or 2D imaging) are the appropriate modes to perform structural measurements of the heart. Parameters include chamber dimensions, such as: 1) right atrial (RA) size; 2) left atrial (LA) size and volume; 3) right ventricular (RV) size, wall thickness and RV outflow tract (RVOT); 4) left ventricular (LV) end-diastolic diameter (EDD), end-systolic diameter (ESD), septal wall thickness (SWT), posterior wall thickness (PWT), LV outflow tract (LVOT), mass and volume [17], [19] (see figure 2.5). Moreover, valve areas are also routinely estimated. These parameters are determined through different standardized methods explained in detail in expert guidelines, including general recommendations on the most accurate method according to the location, the echocardiographic mode and view, and complementary measurements.

Ultimately, estimation of echocardiographic parameters provides support to diagnosis. For example, LV enlargement is an important finding, especially in patients with valvular regurgitant lesions, hypertension, cardiomyopathy, and LV remodelling after myocardial infarction. RA size and RV size and wall thickness are particularly important in patients with pulmonary hypertension, pulmonary diseases, and tricuspid or pulmonary valvular lesions. These abnormalities may also reflect the severity of left heart disease [17], [19].

Haemodynamic assessment of cardiac function

Doppler echocardiography measures blood flow velocity parameters. In cardiac assessment, relevant quantities are stroke volume (SV), cardiac output (CO) and volumetric flow. Diastolic filling variables are also measured with Doppler echocardiography and include mitral inflow, pulmonary venous flow velocities, TDI, colour M-mode (CMM) of mitral inflow, and derived pressure parameters such as transvalvular gradients and intracardiac pressures. Haemodynamic assessment allows the detection of abnormalities that impact an adequate cardiac function. These irregularities comprise valvular diseases as valve stenosis (mitral, tricuspid, pulmonary or aortic), valve regurgitation, valve prolapse, anomalies in cardiac elastic properties and filling, among others [17], [19].

Systolic function assessment

Systolic function of the heart can be evaluated with several echocardiographic techniques. At regional level, LV function is assessed using regional wall motion analysis to determine the contractility of 16 LV wall segments: 6 at the

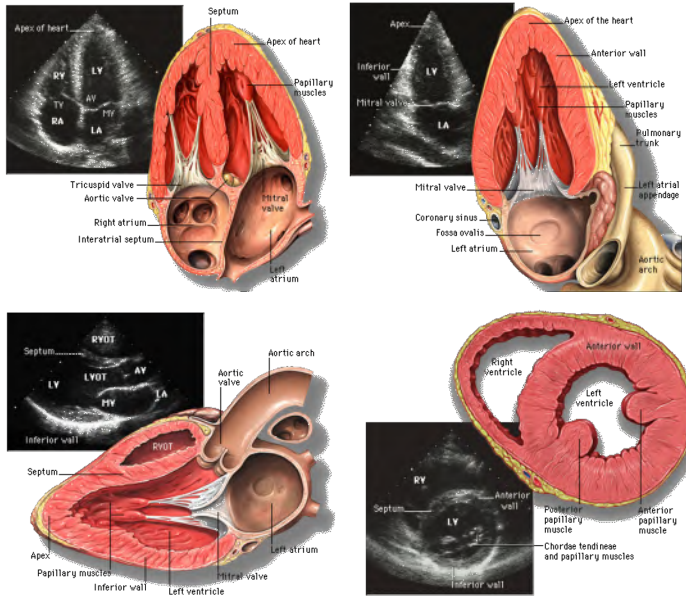


Figure 2.5: Illustration of common transthoracic views in echocardiography and extracted anatomical parameters. Top) Apical 4 (left) and 2 (right) chambers view. Extracted parameters: right atrial (RA) size; left atrial (LA) size; right ventricular (RV) size; Bottom) Left parasternal long axis view (left) and LV short axis view (right). Extracted parameters: RV outflow tract (RVOT); LV outflow tract (LVOT); septal wall thickness (SWT). Adapted from https://commons.wikimedia.org/wiki/File:Apical_4_chamber_view.png, <https://commons.wikimedia.org/wiki/File:Apical2Chamber.png>, <https://commons.wikimedia.org/wiki/File:LeftParasternalLongAxis.gif> and <https://commons.wikimedia.org/wiki/File:LeftVentricleShortAxis.gif>. By Patrick J. Lynch and C. Carl Jaffe [CC BY 2.5 (<https://creativecommons.org/licenses/by/2.5>)].

base, 6 at the mid-ventricle and 4 at the apex. To evaluate LV global systolic function, relevant parameters include SV, CO, cardiac index, LV ejection fraction (EF), strain and systolic tissue velocity of the mitral annulus and myocardium [17].

The general expression to calculate haemodynamic parameters such as flow or SV by Doppler echocardiography is:

$$\text{Flow rate} = \text{CSA} * \text{flow velocity} \quad (2.12)$$

Where CSA is the cross-sectional area of the orifice [19].

In the cardiovascular system, pulsatile flow varies throughout the cardiac cycle and, therefore, individual velocities of the Doppler spectrum are inte-

grated to measure the total volume of flow (see figure 2.6) [19]. This quantity is called the time velocity integral (TVI) and determines SV as:

$$SV = CSA * TVI \tag{2.13}$$

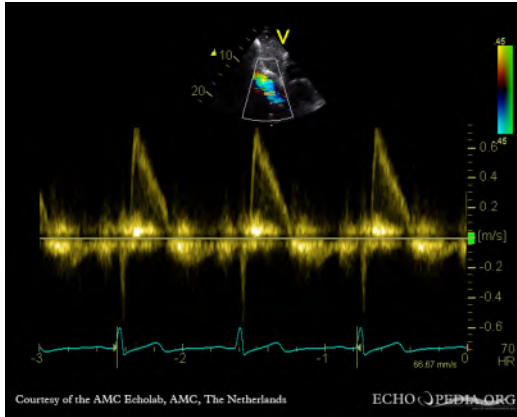


Figure 2.6: Pulsed-wave Doppler of the abdominal aorta flow with reversal flow during diastole. Adapted from [https://commons.wikimedia.org/wiki/File:Endocarditis_of_aortic_valve_E00258_\(CardioNetworks_ECHOpedia\).jpg](https://commons.wikimedia.org/wiki/File:Endocarditis_of_aortic_valve_E00258_(CardioNetworks_ECHOpedia).jpg). By CardioNetworks: Secretariat [CC BY-SA 3.0 (<https://creativecommons.org/licenses/by-sa/3.0>)].

This equation can be applied to calculate flow across any cardiac orifice, even if the most common application is to determine SV at the LVOT. All CSAs are assumed to be circle shaped; thus, circle diameter is also measured. To calculate CO, SV is multiplied by heart rate (HR) and, to estimate cardiac index, CO is divided by body surface area (BSA) [19].

Other method to calculate SV is to determine the difference between LV end-diastolic volume (EDV) and LV end-systolic volume (ESV) if there is no valvular regurgitation. Otherwise, the regurgitant volume needs to be subtracted to obtain SV across the orifice [19].

Systolic velocity of myocardial tissue or mitral annulus

The peak systolic tissue Doppler velocity at the annular level (S'), measured by TDI, reflects overall longitudinal LV contraction, correlates well with LV EF and it has been shown to be a good predictor of clinical outcome in various cardiovascular disorders. Peak systolic annular velocities detect subtle deterioration of myocardial function even with preserved EF, providing objective evidence of myocardial contraction impairment. Moreover, this parameter

reflects a progressive evolution of pathophysiologic states together with the impairment of other measurements of systolic and diastolic function, hence demonstrating that systolic and diastolic function are integrated aspects of myocardial function [19].

Diastolic function assessment

Assessment of (the heterogenous) diastolic function is an integral part of cardiac function examination, comprising active (relaxation), passive (chamber stiffness) and other characteristics of the heart. In fact, the LV filling pattern is the result of the transmitral pressure gradient determined by factors such as elastic recoil (suction), myocardial relaxation and compliance, cardiac rhythm, LA pressure and pericardial compliance [18]. Adequate filling of the ventricles during rest and stress conditions should be guaranteed without an abnormal increase in diastolic pressure or pulmonary venous congestion [18].

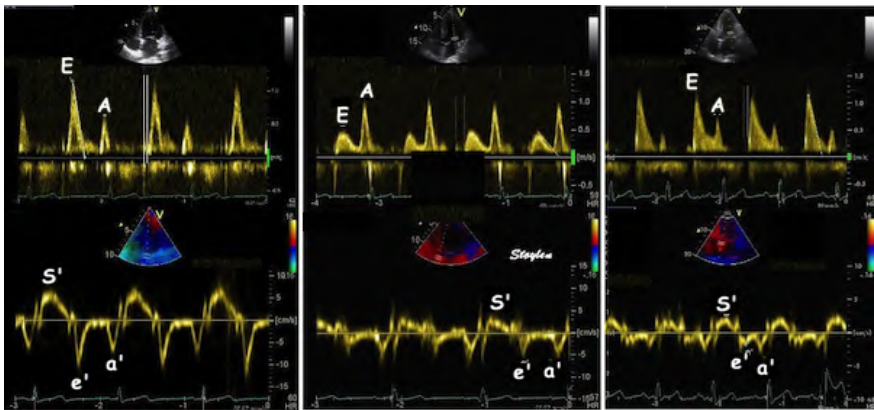


Figure 2.7: Doppler imaging to assess diastolic function. Top) Pulsed-wave Doppler of mitral inflow. Bottom) Tissue Doppler imaging of the mitral annulus. Left images show a healthy subject with normal diastolic function: high peak mitral flow velocity of the early rapid filling wave (E) and longitudinal motion of the mitral annulus during early diastole (e'), and normal E/e' ratio. Middle echocardiographic images of a subject with diastolic dysfunction without increased filling pressure are displayed. These images presented a low E and e' , and normal E/e' ratio. Right images of a subject with diastolic dysfunction and increased filling pressure evinced high E, low e' and high E/e' ratio. Systolic mitral annulus velocity (S') is also reduced in proportion to e' . The A peak is the late diastolic filling wave due to atrial contraction and the a' peak is the longitudinal motion of the mitral annulus during late diastole. Adapted from https://en.wikipedia.org/wiki/File:Diastolic_function.png#file. By Unknow. This work is licensed under the Creative Commons Attribution-ShareAlike 3.0 License.

The standard technique to evaluate diastolic function and estimate filling parameters is non-invasive echocardiography, being M-, B- and Doppler echocardiography the most common used modes, the latter incorporating TDI (see figure 2.7), pulmonary vein Doppler, hepatic vein Doppler, and CMM for determining the propagation velocity of mitral inflow (V_p , see figure 2.8). Significant diastolic parameters are myocardial relaxation, isovolumetric relaxation time (IVRT), mitral inflow, pulmonary venous flow, among other derived measurements [17], [18].

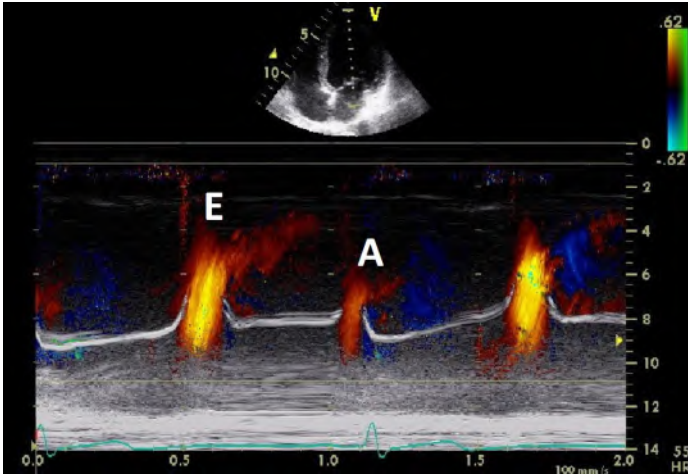


Figure 2.8: Colour Doppler M-mode scan of the mitral inflow. Ventricular filling of a healthy subject showing mitral flow velocity of the early rapid filling wave (E) and flow velocity of the late filling wave caused by atrial contraction (A).

The rate of myocardial relaxation (τ) correlates with the longitudinal motion of the mitral annulus during early diastole (e') and during atrial contraction (a'), which can be obtained by TDI. IVRT (the time between the aortic valve closes and mitral valve opens) depends on τ , aortic end-systolic pressure (ESP) and LA early diastolic pressure, thus a change in these parameters is reflected on IVRT. For instance, IVRT is longer for slowed relaxation and acute ischemia while it is shorter when LA pressure is elevated [18], [19].

Mitral inflow analysis is fundamental for the assessment of diastolic function. Performed measurements to determine the LV filling pattern consist of the peak mitral flow velocity of the early rapid filling wave (E), the peak velocity of the late filling wave caused by atrial contraction (A), the E/A ratio, and the deceleration time (DT), which is the time interval for the peak E velocity to reach zero baseline (see figure 2.7). In general, three abnormal patterns are recognized (see table 2.2): impaired relaxation (grade 1), pseudonormal filling (grade 2), and restrictive filling (grade 3 and 4). Mitral patterns depend

on load conditions so additional assessments are necessary to perform a comprehensive evaluation, especially to distinguish a pseudonormal filling from normal. To confirm the pseudonormal filling pattern, additional data, such as increased maximal LA volume, LV filling changes in response to preload reduction (the Valsalva maneuver), and the mitral annular motion, are necessary to reveal relaxation abnormalities. The ratio of E/e' is also a meaningful parameter since it is directly related to LA pressure and LV end-diastolic pressure (EDP) (see figure 2.7). Indeed, e' is one of the most sensitive parameters for detecting overall myocardial dysfunction [17]–[19].

Moreover, abnormal LV filling patterns and their derived parameters are associated with distinct LV filling pressures although considerations about age, valvular regurgitation, LV EF, and HR need to be done for estimating these pressure patterns. Further studies are necessary to determine the applicability of these methods to all types of cardiac diseases, including prospective studies to compare the prognostic significance of LV systolic and diastolic indices in heart failure (HF) patients (see Chapter 4) [17]–[19].

Additional measurements of diastolic function include V_p into the LV during diastole, which is less preload dependent than the E velocity [18]. V_p is measured as the slope of an apical CMM through the mitral valve during diastole (see figure 2.8). However, the low reproducibility of V_p has hampered its implementation.

Diastolic filling patterns in disease states

Abnormalities of LV filling patterns are associated with changes in LV diastolic properties, filling pressures and prognosis. It is clear then that several parameters determine the grading of diastolic filling patterns (see figure 2.7 and table 2.2). The first sign of diastolic dysfunction in almost all cardiac diseases is impaired relaxation, followed by a compensatory mild decrease in LV compliance and an increment in LA pressure (pseudonormalized filling). In this case, LV suction is diminished and blood is partially forced into the LV in early diastole due to the elevated LA pressure. Progression of the disease leads to a further (and marked) decrease in LV compliance and an increase in LA pressure resulting in rapid ventricular filling in early diastole and minimal filling at atrial contraction. This pattern is termed restrictive and can be reversible with treatment or irreversible, i.e., the end stage of diastolic dysfunction [19]. An example of these filling patterns is shown in figure 2.7. This progression of filling impairment is observed in diverse disorders and in normal aging (see Chapter 1).

Table 2.2: Diastolic dysfunction grading based on diastolic filling patterns.
Adapted from [19].

| Grading | Description | Parameters during rest conditions |
|---|---|--|
| Normal diastolic filling pattern | Normal elastic recoil, myocardial relaxation and filling pressure | $E/A \geq 1.5$; $DT = 160 - 240ms$; $e' \geq 10cm/s$; $E/e' < 8$; $Vp \geq 50cm/s$ |
| Grade 1 (mild dysfunction) | Impaired relaxation with normal filling pressure | $E/A < 1$; Prolonged DT; $e' < 7cm/s$; $E/e' \leq 8$; $Vp < 50cm/s$ |
| Grade 2 (moderate dysfunction) | Pseudonormalized mitral inflow pattern | $E/A = 1 - 1.5$; $DT = 160 - 240ms$; $e' < 7cm/s$; $Vp < 45cm/s$ |
| Grade 3 (severe reversible dysfunction) | Reversible restrictive (high filling pressure) | $E/A > 2$; $DT < 160ms$; $e' < 7cm/s$; |
| Grade 4 (severe irreversible dysfunction) | Irreversible restrictive (high filling pressure) | $E/e' > 15$; |

A: late diastolic velocity; DT: deceleration time; E: early diastolic velocity; e' : early diastolic mitral annular velocity; Vp: propagation velocity .

Vascular assessment

Transthoracic echocardiography is often used to visualise the aortic root and arch, but it has constraints to imaging the whole aorta satisfactorily. Instead, transoesophageal echocardiography (TEE) allows to visualise the entire thoracic aorta in most patients with added advantages over other techniques, such as portability, simultaneous assessment of cardiac function and associated conditions, and no need for contrast agents. Several aortic conditions can be readily evaluated with TEE, for instance aortic aneurysms, rupture, aortic dissection, ulcer, debris, abscess, and coarctation [17].

In elderly patients, atherosclerotic plaques and debris are common findings during routine echocardiographic examinations. Irregularly shaped and mobile aortic plaques are associated with age, smoking, and high systolic blood pressure (SBP), whereas debris is common in patients who suffered an embolic event. In patients with aortic atherosclerosis, plaque can penetrate the internal elastic lamina into the media, producing an ulcer that may result in an intramural hematoma, an aortic dissection, or an aortic rupture [19].

A thorough examination of the carotid region encompasses real-time B-mode imaging, and Doppler analysis of the carotid bifurcation, proximal, medial, and distal internal carotid artery, the proximal external carotid artery,

and the vertebral artery. The incorporation of colour Doppler facilitates the identification of stenosis and shortens the examination time [19]. An additional index of increased risk of major cardiovascular events and cardiovascular mortality is the carotid intima-media thickness (IMT). IMT is measured using B-mode imaging of the carotid artery to identify the “double-line density” of the intima-media complex and the adventitia of the artery. PWV can be also calculated using Doppler imaging. For the estimation of PWV, transit time is calculated from two flow pulses recorded simultaneously or sequentially with ECG gating [39].

Additionally, local arterial stiffness can be determined by echocardiography in superficial arteries, such as the common carotid, common femoral, and brachial arteries. Notably, carotid stiffness is particularly relevant due to the high impact of atherosclerosis at this location [19]. Although common echocardiographic modalities are able to measure changes in diameter and stroke at different locations, precision is limited by the spatial resolution of pixel analysis. Therefore, echo tracking systems were introduced to obtain higher precisions using the radio frequency (RF) signal. These systems allow the non-invasive measurement of local arterial stiffness, local PWV, IMT and arterial distensibility, the later used to estimate the Young’s elastic modulus (see [39] Chapters 3 and 6). However, a high degree of technical expertise and longer times are necessary to perform echo tracking measurements, hence its use is concretely indicated for mechanistic analyses in pathophysiology, pharmacology, and therapeutics, rather than for epidemiological studies [39].

2.2.2.4 *Additional considerations of echocardiographic imaging*

Some more recent echocardiographic modes begin to be available in clinical practice introducing new tools for cardiovascular assessment. Harmonic real-time 3D imaging can deliver a highly accurate and reliable echocardiographic measurement of LV volume and mass [19]. A novel method is vector flow imaging (VFI), which performs a quantitatively estimation of flow velocity at any location into a vessel and displays a more intuitive depiction of the flow movements [51]. Echocardiographic particle image velocimetry (echo-PIV) is a technique for obtaining quantitative velocity maps from contrast ultrasound images [52]. Shear wave elastography is a technique that characterises the mechanical properties of a medium by applying a focused ultrasonic high-energy beam with a conventional ultrasound transducer to analyse the propagation of the internal mechanical perturbation (or shear wave propagation) [53].

Anatomical and functional cardiovascular indexes are extracted from echocardiographic images applying different techniques, such as edge detection, segmentation, among others (see Part II - Novel Cardiovascular

Research). In the frequency domain, imaging analysis may deliver further useful information and improve contrast and resolution. For example, noise has a certain degree of omnipresence with undetermined frequency content even if the high frequency content could be often attributed to noise. Hence, filters can be designed to eliminate this type of high-frequency noise. An interesting approach is the use of wavelet-based filters to reach an optimal trade-off between good signal averaging over homogeneous regions and minimal resolution degradation of image details (see Chapter 7) [42].

Artefacts are a limitation to take into consideration. In echocardiographic images, many artefacts are the result of reflective properties of the tissues. Examples of artefacts are the “comet tail” effect in the image when two reflective surfaces are close to each other and the sound wave bounces between them or the apparent structures that do not exist behind any highly reflective interface that only transmits a small amount of ultrasound [42].

Finally, potential bioeffects of ultrasonic imaging have been addressed, and comprise thermal effects, mechanical and cavitation effects, cellular and subcellular effects, biochemical effects, and the effects of ultrasound on organs and systems. However, no epidemiological data can support any seriously harmful side effect due to ultrasound exposure, especially for imaging purposes as in echocardiography. This is one of the reasons why ultrasound is among the most used diagnostic techniques in hospitals [42].

2.2.3 Cardiovascular magnetic resonance imaging

Cardiovascular magnetic resonance imaging (MRI) is an appropriate technique for the assessment of morphological and physiological anomalies of the heart, pericardium, and great vessels of the thorax. With a considerable growth in the last decades, MRI emerged as a desirable imaging technology due to its speed, reliability, ease of use, harmlessness, reproducibility, high image quality and field of view (FOV). Capitalising these technical advantages, MRI allows near-real-time imaging, tissue tagging-tracking, and four-dimensional (4D) acquisition and display. Concretely, the technique is able to obtain high-detail anatomical images, histologic characterisation, intracardiac or intravascular blood flow, cardiac chamber contraction and filling measurements, parameters of regional myocardial mechanics, and tissue perfusion imaging. Hence, MRI has been established as an essential diagnostic modality in cardiovascular medicine.

2.2.3.1 Basic principles of MRI

Since a complete description of the underlying physics of MRI is complex and requires quantum mechanics, the approach followed in this section to describe the basic principles of MRI uses approximations of classical mechanics.

The principal mechanism of nuclear magnetic resonance is based on the spinning of nuclei with an odd number of nucleons (protons and/or neutrons) in the presence of an external magnetic field. Protons rotate around the axis of the applied magnetic field like spinning tops. The angle and the annular velocity of the rotation (ω) are intrinsic properties of each particle as well as the magnetic field (m) produced by the particle [42], [43]. At a macroscopic level, the interaction between the external and intrinsic magnetic fields is the basis for imaging. Nuclei with these characteristics possess a magnetic dipole and group together to form an ensemble. The sum of all magnetic moments is termed the nuclear magnetization and is zero when there is not an external magnetic field [42], [43]. For imaging, a strong constant magnetic field (H_0 , 0.2 – 4 T) is generated in a selected direction (the z-direction in this description) to produce a nuclear magnetization (M) of the ensemble of nuclei, which is oriented in the direction of the external field, either parallel or in the exact opposite direction (antiparallel) [42], [43]. When particles are submitted to the external magnetic field, they spiral down to align with the forced direction, as represented in figure 2.9. This process is named precession and takes place with a specific frequency to each element defined by:

$$\omega_o = \gamma H \quad (2.14)$$

Where ω_o is the Larmor frequency, H is the magnitude of the magnetic field and γ is the gyromagnetic constant that is primarily determined by the type of nucleus. The hydrogen proton is abundant in tissue, water and many biological molecules, thus this proton is used for clinical imaging and its Larmor frequency and gyromagnetic constant (42.58 MHz/Tesla) play a central role [42], [43].

If these rotating particles (or spins) are exposed to electromagnetic energy at the Larmor frequency, they rotate further and further from the equilibrium position near the z-axis as figure 2.10A shows [42], [43]. Since the Larmor frequency is within the RF range for protons, an RF pulse at the proper frequency in the xy-plane tips the spins away from the z-axis an amount established by:

$$\theta = \gamma H T_p \quad (2.15)$$

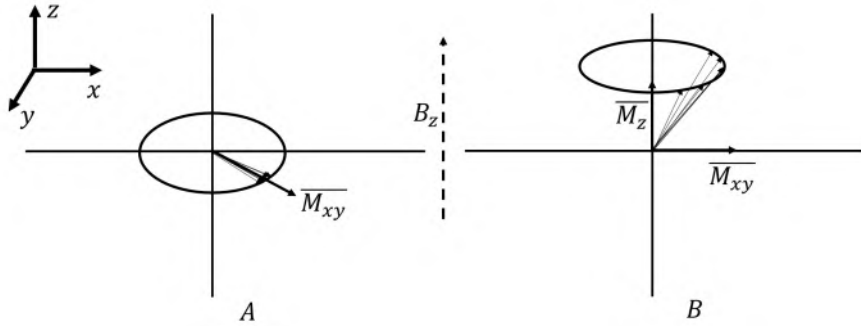


Figure 2.10: Illustration of the application of an RF pulse and the subsequent relaxation. A) After an RF pulse tips the spins 90° , the net magnetic moment approximates a vector rotating in the xy -plane (M_{xy}) and the net vector in the z direction is zero. B) After the RF energy is removed, all spins begin to relax back to their equilibrium position, increasing the z component (M_z), and decreasing the xy -component (M_{xy}). The xy -component also decreases as the spins desynchronize. Adapted from [43].

Considering these relaxation processes, FID signals are defined by the following expression:

$$S(t) = \rho \cos(\omega_0 t) e^{-t/T_2^*} e^{-t/T_1} \quad (2.17)$$

Table 2.3: Magnetic resonance imaging parameters. Adapted from [18].

| Tissue | 1H density (% H^2O) | T_1 [ms] | T_2 [ms] |
|---------------------|------------------------------|---------------|---------------|
| Muscle | 100 | 600 | 40 |
| Liver | 91 | 270 | 50 |
| Renal cortex | 95 | 360 | 70 |
| Renal medulla | 95 | 680 | 140 |
| Spleen | 92 | 480 | 80 |
| Fat | 98 | 180 | 90 |
| White matter | 100 | 390 | 90 |
| Gray matter | 94 | 520 | 100 |
| Blood | 90 | 800 | 180 |
| Cerebrospinal fluid | 96 | 2000 | 300 |
| Water | 100 | 2500 | 2500 |

Equation (2.17) is used to accomplish image contrast. Proton density (ρ) is proportional to the FID signal amplitude but variation within the body is not sufficient to obtain good contrast. Magnetic properties (see table 2.3) such as local relaxation times (T_1 and T_2 or T_2^*) can enhance contrast [42],

[43]. In general, MRI contrast improves with increasing hydrogen density, shortening of T_1 , and lengthening of T_2 . The estimation of relaxation times is done by the manipulation of the RF pulse and local magnetic field gradients. A pulse sequence is defined as a combination of RF and magnetic pulses and delays, and a data acquisition period. A practical pulse sequence eliminates the T_2^* decay by sampling a realigned echo: after the spins start to spread out, an RF pulse with a phase-reversing of 180° is applied so the direction of the spins is reversed, and they come together after a known delay: T_2^* [42], [43]. As a result, this echo approach removes only the M_{xy} decline due to magnetic inhomogeneities but not the variations due to the sample itself produced by the T_2 relaxation, which are of interest. Ultimately, contrast between different tissues relies on excitation and signal readout delay (TE, echo time) and the time between repetitive RF excitations (TR, repeat time). To highlight either T_1 or T_2 differences between tissues, signal reception is delayed for a certain period after the generation of the RF pulse [42], [43]. T_1 and T_2 relaxation times provide the means to identify normal tissue and characterise disease processes. Examples of T_1 and T_2 weighted MRI scans are shown in figure 2.11.

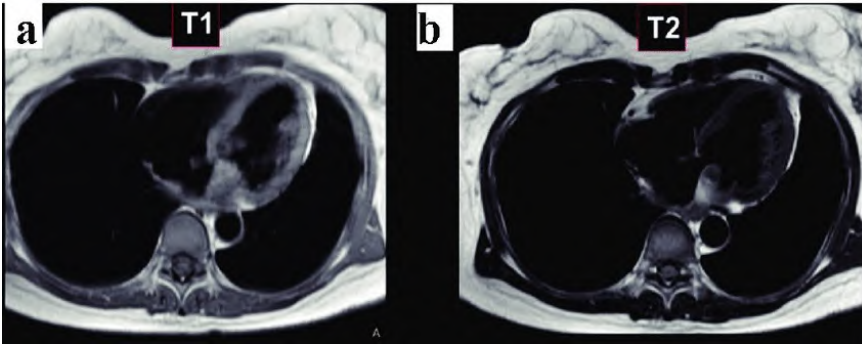


Figure 2.11: Examples of cardiac MRI scans. Heart of a patient with sarcoma in the left atrium. a) T_1 -weighed. b) T_2 -weighed. Adapted from the reference: A Rare Cause of Dyspnea: Undifferentiated Pleomorphic Sarcoma in the Left Atrium - Scientific Figure on ResearchGate. Available from: https://www.researchgate.net/figure/Cardiac-MRI-Both-tumors-are-isointense-in-T1-weighted-black-blood-imaging-a-The_fig4_320679672 [accessed 20 Oct, 2019] via license: Creative Commons Attribution-NonCommercial 4.0 International [54].

Equation (2.14) (Larmor equation) is used to resolve localisation. Localisations can be tagged by resonant frequencies of each position in the sample when the strength of the (locally) applied magnetic field is different. The signal of a specific zone can be determined using an RF pulse with only one frequency component that excites only the spins in one region whose magnetic field correlates with the RF frequency (Larmor frequency). A second

approach is to excite a broader area and modify the magnetic field strength, so each area has a different resonant frequency [42], [43]. Electromagnets (or gradient coils) generate gradient fields in the three dimensions to modify (linearly) the magnetic field strength over a limited area. Specific 2D slices of the studied tissue can be isolated using the gradient field in the remaining direction, e.g., an xy -slice is isolated using the gradient field in the z direction (G_z) [42], [43]. In practice, the applied RF pulse has a range of frequencies (a finite bandwidth) that together with the steepness of the gradient determine the thickness of the slice:

$$\Delta z \propto \gamma G_z Z(\Delta\omega) \quad (2.18)$$

A narrow bandwidth ($\Delta\omega$) and a steep gradient field (G_z) are necessary to obtain a thin slice (Δz).

The general aspect of the image depends on different physical parameters, some related to tissue properties, others to the MRI sequences. An advantage of MRI is the control that the operator has on the generation and use of the data. Size pixel is determined by the number of pixels in the reconstructed image and the actual size of the imaged area, or the FOV [42], [43]. Resolution is limited by the signal-to-noise ratio but can be improved using special receiver coils or averaging, but there is an increase in cost or scan time, respectively. In general, MRI is used to create anatomical images, but it can generate also images of metabolic activities, which is known as functional magnetic resonance imaging (fMRI) [42], [43].

MRI is a phase-sensitive modality in which blood flow velocity and phase changes (linearly proportional to velocity changes) can be encoded and displayed as velocity maps [18], [55]. Signal intensity varies according to the blood flow direction, increasing toward brightness or darkness. Phase-contrast MRI delivers information about instantaneous peak velocity and (spatial) average velocity at time points of the cardiac cycle. Hence, volumetric flow can be estimated by multiplication of (spatial) average velocity with the corresponding vascular CSA. Additionally, time-velocity and volume of flow curves can be derived to determine SV [18]. Furthermore, improvement of MRI devices currently allow the acquisition of 4D phase-contrast cardiac MRI sequences for measurements of velocity vectors in three spatial dimensions, with unrestricted image orientation for estimating pressure gradients *in vivo* [13] (see Chapter 4).

2.2.3.2 Applications of MRI

Cardiac assessment

MRI is the gold standard method to quantify ventricular volumes and mass due to its 3D nature that does not rely on geometric assumptions [19]. Accuracy and reproducibility of MRI measurements of global LV anatomy are well established for basic parameters and considerably superior to that of 2D echocardiography [19]. These parameters comprise LV and RV SVs, aortic flow, LV and RV mass measurements, among others. Furthermore, MRI is useful for the evaluation of regional contractile function performed by visual inspection of cine loops in standard imaging planes. The use of conventional techniques for the quantification of wall motion and thickening can be performed for both the LV and RV, but myocardial tagging, a technique that allows the assessment of myocardial strain and other deformations as a measure of contractility, is preferred [18]. MRI tagging can be applied for full 3D myocardial analysis by collective modelling of the numerous small individual myocardial elements with high spatial and temporal resolution and simplified post processing [18], [19].

Furthermore, MRI techniques are also the gold standard for estimating LV EF and volumes [18]. These measurements and derived parameters are calculated from end-diastolic and end-systolic images of the LV. Improvement of the approach is possible using multilevel-cine MRI, which shows heart and blood motion over different phases of the cardiac cycle. To account for cardiac motion, a small number of phase-encoding steps is used in each breath-hold, resulting in a complete cine examination over a breath-hold period of 10-20 heart beats [18], [19]. In figure 2.12, two frames from distinct cardiac sequences show a 4 chambers view.

Vascular assessment

Arterial wall assessment is essential to study the development of atherosclerosis, which is a systemic process that can commonly result in aneurysms or branch vessel stenosis. MRI enables the acquisition of information related to atherosclerosis formation, which is collected mainly at the aorta or carotid and brachial branches. MRI measures compliance in the ascending aorta and PWV around the aortic arch as both parameters have an age-dependent normal range, are abnormal in early atherosclerosis, and have been shown to be predictive of cardiac events [19]. Moreover, plaque burden, plaque vulnerability, cholesterol pools and overlying fibrous plaque can be evaluated using MRI images. Plaque characterisation has been further achieved by the

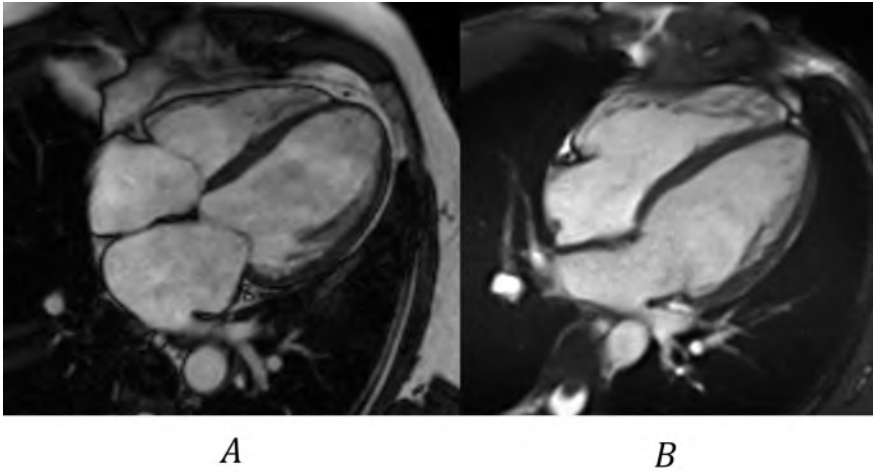


Figure 2.12: Example frames and comparison of cardiac MRI sequences of the 4 chambers view. A) Healthy subject. B) Subject with a chronic infarction, akinetic apex and transmural scar. Additionally, mitral regurgitation is observed. Adapted from https://commons.wikimedia.org/wiki/File:4-CH_cine_normal.gif and https://commons.wikimedia.org/wiki/File:4CH_cine_infarct.gif. By Doregan [CC BY-SA 4.0 (<https://creativecommons.org/licenses/by-sa/4.0>)].

employment of contrast agents, showing inflammation, neo-vasculature, and fibrous plaque. Indeed, magnetic resonance angiography using gadolinium-based contrast agents is fast and routinely used for large and small vessels [18], [19].

2.2.3.3 Additional considerations of MRI

Feature extraction, both geometrical and texture, from MRI images are effective to identify most malignant and benign tumours, and several processing techniques can be applied to analyse MRI images, although results are dependent on resolution. The resolution along the slicing axis (the z-direction in the section introducing the basic principles of MRI) is usually less than the planar resolution so interpolation is performed between two slices to improve overall resolution [42]. Another potential limitation of MRI is noise that could be caused by subject motion, physiological activity, low frequency drift, spontaneous neural and vascular fluctuations, shear and strain noise, thermal noise and artefacts arising from rapid imaging methods [42]. Filtering and adjustment of contrast agents are common strategies to deal with noise but the main method for denoising MRI images is the use of the wavelet transform and coefficients (see Chapter 7).

Although MRI is fundamentally safe, some concerns must be considered. In patients with metallic implants or implanted electronic devices, compatibility could be an issue [42]. Even though most metallic implants are MRI compatible, including prosthetic cardiac valves, vascular stents, and orthopaedic implants, there are still problems with some neurological devices, such as vascular clips used for cerebral aneurysm surgery due to the potential risk of dislodgement from the vessel [42]. Electronic implants like cardiac pacemakers, cardiac defibrillators, and neurologic stimulators represent a contraindication due to the risks of interference with the programming of the device. Haemostatic clips, metallic sternal suture wires, and retained surgical epicardial pacing wires are not known to lead to complications from MRI, aside from local imaging artefacts [42].

Additional safety steps should be considered for patients with different conditions. For example, for critically ill patients that need life-support systems, claustrophobic subjects or allergic reactions to contrast agents, adequate procedures must be implemented to perform safe MRI evaluations [42].

MODELLING AND PROCESSING METHODOLOGIES

Previously, Chapter 1 established fundamental anatomical and physiological concepts of the healthy and pathologic cardiovascular system. Furthermore, evidence of a global epidemic of cardiovascular diseases was discussed, emphasizing the rise in heart failure (HF) cases in an aging population. Subsequently, Chapter 2 introduced non-invasive techniques to assess cardiovascular function, their advantages and pitfalls.

These chapters elucidated the need not only to improve the comprehension of underlying mechanics of an adequate cardiac function and the deviation of pathophysiologic patterns to propose effective treatment but also the urgency to develop better diagnostic tools for identifying subjects at risk. Hence, this chapter expands and revises concepts related to cardiovascular function and its assessment, such as intracardiac fluid dynamics, *in silico* simulations, haemodynamic analysis and signal/image processing algorithms. Furthermore, developed tools for the processing, assessment and analysis of data implemented in the context of this PhD project are introduced in this chapter.

This completes Part I - Fundamentals, providing the basis for the following chapters.

3.1 CARDIAC FUNCTION

The proposed methods to assess cardiac function in Chapter 4 are based on basic knowledge of intracardiac fluid dynamics, including modelling of the left ventricle (LV). Thence, the following section presents a brief review to support and expand some of these concepts

3.1.1 Fluid dynamics of intraventricular flow

Principles of fluid dynamics have been applied to understand and evaluate the pressure-velocity relationship of flow across an orifice in various cardiac situations [56]–[58]. With Doppler echocardiography, these principles allow the calculation of pressure gradients noninvasively. The most basic application of the simplified Bernoulli equation is to calculate transvalvular pressure gradients in a stenotic orifice using Doppler velocity profiles:

$$\Delta P = \frac{\rho v^2}{2} [Pa] \quad (3.1)$$

With the blood density $\rho = 1060 \text{ kg/m}^3$, and velocity v in m/s , this expression can be further simplified:

$$\Delta P = 4v^2 [mmHg] \quad (3.2)$$

However, the simplified Bernoulli equation cannot account for the inertial forces of pressure difference across a non-stenotic orifice or flow within the cardiac chambers. In this case, a more complex mathematical description must be implemented [56], [57].

The Navier-Stokes equations can be expressed as:

$$\begin{aligned} \nabla \cdot v &= 0 \\ -\nabla P + B + \mu \nabla^2 v &= \rho \left[\frac{\partial v}{\partial t} + (v \cdot \nabla)v \right] \end{aligned} \quad (3.3)$$

Where v is the three-component vector of local blood velocity; P is the local pressure; B represents body forces (such as gravity) acting on the fluid; ρ (1060 kg/m^3) and μ ($0.003 - 0.004 \text{ Pa.s}$) are blood density and viscosity, respectively; ∇ is $\frac{\partial}{\partial x} i + \frac{\partial}{\partial y} j + \frac{\partial}{\partial z} k$ (i , j and k are unit vectors). These expressions associate pressure gradients to local and convective accelerations, to

viscosity (or frictional) effects and to global body force terms. Nonetheless, for the calculation of pressure gradients, the viscous term ($\mu \nabla^2 v = 0$) and the gravitational force ($B = 0$) are both negligible in this context, thus the Navier-Stokes equations reduce to:

$$-\nabla P = \rho \left[\frac{\partial v}{\partial t} + (v \cdot \nabla)v \right] \quad (3.4)$$

$$-\frac{\partial P}{\partial x_i} = \rho \frac{\partial v_i}{\partial t} + \rho \left[v_1 \frac{\partial v_i}{\partial x_1} + v_2 \frac{\partial v_i}{\partial x_2} + v_3 \frac{\partial v_i}{\partial x_3} \right] \quad (3.5)$$

Considering flow along a streamline, equation (3.4) becomes the Euler equation:

$$\frac{\partial P}{\partial s} = -\rho \left[\frac{\partial v}{\partial t} + v \frac{\partial v}{\partial s} \right] \quad (3.6)$$

To calculate noninvasively intraventricular pressure differences (IVPDs), equation (3.6) is integrated along an inflow streamline between two selected points (P1 and P2) inside the cardiac chambers:

$$\Delta P[t] = \int_{P_1}^{P_2} \frac{\partial P}{\partial s} ds = \frac{1}{2} \rho (v_{P_1}^2[t] - v_{P_2}^2[t]) + \rho \int_{S_{P_1}}^{S_{P_2}} \frac{\partial v[s, t]}{\partial t} ds \quad (3.7)$$

It becomes clear that the instantaneous pressure difference is the sum of a convective (equation (3.8)) and an inertial (local acceleration, equation (3.9)) component:

$$\Delta P_C[t] = \frac{1}{2} \rho (v_{P_1}^2[t] - v_{P_2}^2[t]) \quad (3.8)$$

$$\Delta P_I[t] = \rho \int_{S_{P_1}}^{S_{P_2}} \frac{\partial v[s, t]}{\partial t} ds \quad (3.9)$$

A more complex analysis of the 3D nature of flow is possible resolving equation (3.4). For the calculation of 3D pressure gradients, three orthogonal contributions are defined, each with a single local acceleration component and three separate convective components (x-, y-, and z-convective terms):

$$-\frac{\partial P}{\partial x} = \rho \frac{\partial v_x}{\partial t} + \rho \left[v_x \frac{\partial v_x}{\partial x} + v_y \frac{\partial v_x}{\partial y} + v_z \frac{\partial v_x}{\partial z} \right] \quad (3.10)$$

$$-\frac{\partial P}{\partial y} = \rho \frac{\partial v_y}{\partial t} + \rho \left[v_x \frac{\partial v_y}{\partial x} + v_y \frac{\partial v_y}{\partial y} + v_z \frac{\partial v_y}{\partial z} \right] \quad (3.11)$$

$$-\frac{\partial P}{\partial z} = \rho \frac{\partial v_z}{\partial t} + \rho \left[v_x \frac{\partial v_z}{\partial x} + v_y \frac{\partial v_z}{\partial y} + v_z \frac{\partial v_z}{\partial z} \right] \quad (3.12)$$

3.1.2 Intraventricular pressure difference estimation

Pressure differences are the force driving blood flow in several segments of the cardiovascular system, including the cardiac chambers. Inside the heart, small IVPDs are associated with an efficient filling of the ventricles and with an efficient ejection of blood during systole. Thus, even if small in magnitude, IVPDs are essential to the proper functioning of the cardiovascular system. Hence, a thorough evaluation of cardiac function should include the estimation of IVPDs.

3.1.2.1 Colour M-Mode based estimation

Colour M-Mode (CMM) echocardiography is conventionally used to assess LV diastolic dysfunction by estimating the propagation velocity of the inflow wave-front (V_p) (see Chapter 2). Additionally, CMM flow velocity data allow to estimate noninvasively the IVPDs using the Euler equation (equation (3.6)).

An automated MATLAB[®] (The Mathworks, Natick, Massachusetts) based algorithm, proposed by Stewart *et al.* [59], was implemented by Vlachos *et al.* [60] to examine CMM echocardiographic images. After selection of the region of interest and the velocity colour scale, a point-by-point velocity reconstruction is performed using de-aliasing and image processing tools. First, the E-wave velocity field is reduced to a series of 27 iso-velocity contours evenly spaced between 45% and 55% of the peak E-wave transmitral velocity. Then, a smoothing spline is fit to the series of iso-velocity contours, and a statistical change-point analysis method is applied to objectively determine the deceleration point.

From the reconstructed velocity field, relative pressures within the region of interest are estimated using the Euler equation (equation (3.6)). Peak diastolic IVPDs from the left atrium (LA) to the LV apex are calculated using equations (3.7) to (3.9). Furthermore, V_p is calculated as two segments determined by the deceleration point since a single straight line is not an accurate approximation for the V_p parameter. These segments are then termed initial and terminal propagation region.

3.1.2.2 MRI based estimation

With the emergence and spread of magnetic resonance imaging (MRI), derived sequences have provided a more complex set of flow data. Thus, two-dimensional (2D) velocity vectors and equations (3.10) and (3.11) are used to estimate pressure gradients in the imaging (xy) plane. Thus, calculation of pressure differences is performed by directly integrating only in-plane pressure gradients over space [58]:

$$\Delta P = \int_{path} \frac{\partial P}{\partial x} dx + \int_{path} \frac{\partial P}{\partial y} dy \quad (3.13)$$

Since the integration constant cannot be obtained from the estimated pressure gradients, the selected path of integration is broken up into linear segments and the total pressure drop, across all the segments, is calculated as a sum using:

$$\Delta P = \sum_i \left[\left(\frac{\partial P}{\partial x} \right)_i \Delta x_i + \left(\frac{\partial P}{\partial y} \right)_i \Delta y_i \right] \quad (3.14)$$

I implemented a MATLAB[®]-based application that employs an interactively user-selected path for IVPD calculations, which is further described in Chapter 4. Furthermore, available MRI data processed by this method allow not only the analysis of diastolic but also of systolic IVPDs. The adaption of the method to calculate 3D flow is also possible if either multi-slice or 3D velocity data is available. Given the increasing accessibility and computational power of MRI devices, a 3D implementation could add value to the approach in the near future.

3.1.3 Computational fluid dynamics model of the left ventricle

Knowledge of the full 3D intracardiac blood flow pattern may enhance current visualisation tools and quantitative assessment of important cardiac parameters, such as volumetric flows (cardiac output, pulmonary blood flow, shunt flow, ...) or pressure gradients in healthy and disease subjects, which might show significantly altered intracardiac blood flow patterns. In the clinical setting, echocardiography measurements are the gold standard approach to assess cardiac function, but several methodological limitations may lead to flawed diagnoses. These limitations include the neglect of the intrinsic 3D character of the haemodynamics by one-dimensional (1D) estimations and aliasing problems. Hence, improved multidimensional flow estimators

are necessary. One appealing approach to validate multidimensional flow estimates is the use of a computational fluid dynamics (CFD) model with a full knowledge of the true haemodynamics. In Chapter 4, as part of the validation method to assess the the proposed methodologies to estimate IVPDs, we made use of a CFD model of a contracting ventricle that was developed by Van Cauwenberge *et al.* [61] and explained in detail in [2], [61], [62].

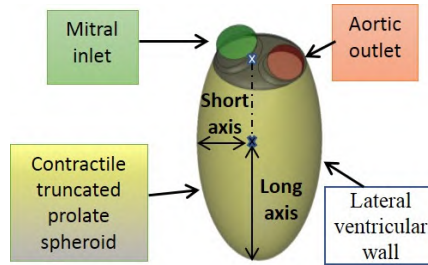


Figure 3.1: Computational fluid dynamics model of the left ventricle. The model is a prolate spheroid with a fixed mitral inlet and aortic outlet, contracting and expanding at a heart rate of $60bpm$ with an ejection fraction of 60%.

To assess the performance of proposed methods to calculate IVPDs, an LV CFD model was built with ANSYS® DesignModeler™ as a prolate spheroid with a fixed mitral inlet and aortic outlet, contracting and expanding at a heart rate (HR) of $60bpm$ with an ejection fraction (EF) of 60% (see Chapter 4). Figure 3.1 shows the main features of the built model. The computational mesh contained 180,000 tetrahedral cells, and the 3D Navier-Stokes equations were solved using a commercial CFD solver (ANSYS® Fluent®). During this CFD simulation, the mesh was adapted mathematically according to a volumetric boundary condition, with the intraventricular blood volume varying between $170ml$ at end-diastole and $69ml$ at end-systole [62].

To account for this volumetric change, each node of the computational mesh needed to be displaced at each time step of the CFD-simulation (see figure 3.2). An Arbitrary Lagrangian-Eulerian mesh motion defined on all interior nodes ensured that the mesh quality was preserved, while avoiding smoothing and remeshing. The systolic and diastolic periods were clearly established by mitral and aortic flows: the mitral inflow presented a specific pattern with two characteristic peaks during diastole (E and A waves), and the aortic outflow showed a unique peak during systole (S wave). The blood was modelled as an incompressible Newtonian fluid with a viscosity of $3.5mPa \cdot s$ and a density of $1060kg/m^3$. Further details are found in [61], [62].

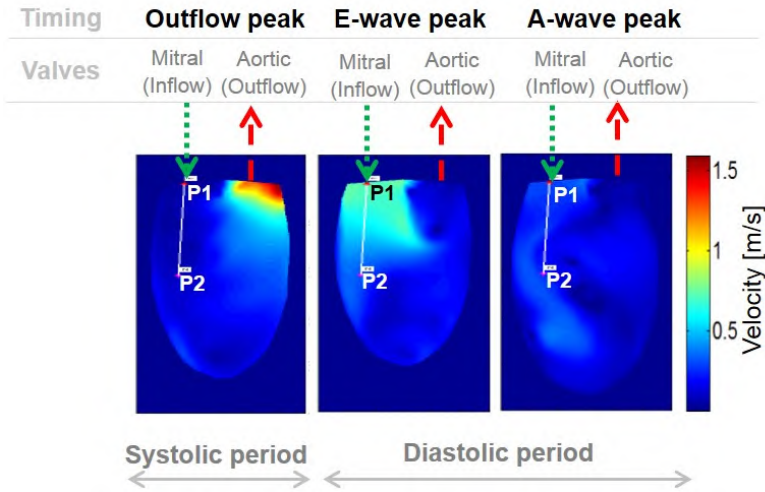


Figure 3.2: Computational fluid dynamics simulation. The model was adapted mathematically according to a volumetric boundary condition, with the intra-ventricular blood volume varying between 170ml at end-diastole (diastolic expansion) and 69ml at end-systole (systolic contraction).

3.2 VASCULAR FUNCTION

Vascular function assessment is a relevant complement to expand and support the development of methods to evaluate overall cardiovascular function. Hence, this section introduces basic definitions on non-invasive estimation of arterial properties and the interaction between the cardiac pump and the peripheral circulation, which are concepts further developed in Chapter 5.

3.2.1 Haemodynamic analysis

A custom-designed software was built in MATLAB® (The Mathworks, Natick, MA) [63], [64] to process off-line central arterial tonometry recordings and Doppler flow velocity files. First, averaging is performed for both signals, which is a more complex process for Doppler flow velocity files. Doppler flow images are processed by selecting the onset and end of systolic ejection for each cardiac cycle with two cursors. Then, contours are automatically traced using the transition in pixel intensity above a user-defined threshold value, and the signal from each cardiac cycle is used to calculate an average blood flow velocity waveform. These operations are summarised in figure 3.3. Next, volumetric flow is calculated by multiplying the previous estimated instantaneous flow velocities and the LV outflow tract cross-sectional area (CSA). Visual time-alignment of pressure and flow curves is effectuated

taking into consideration the concordance of the rapid systolic upstroke of pressure and flow and the pressure dicotic notch and cessation of flow (figure 3.4A). Additionally, time alignment is accomplished by maximizing the zero value of the phase angle of higher-frequency harmonics (7th to 10th) of the input impedance, and the linearity of the early systolic pressure-flow relationship [63], [64].

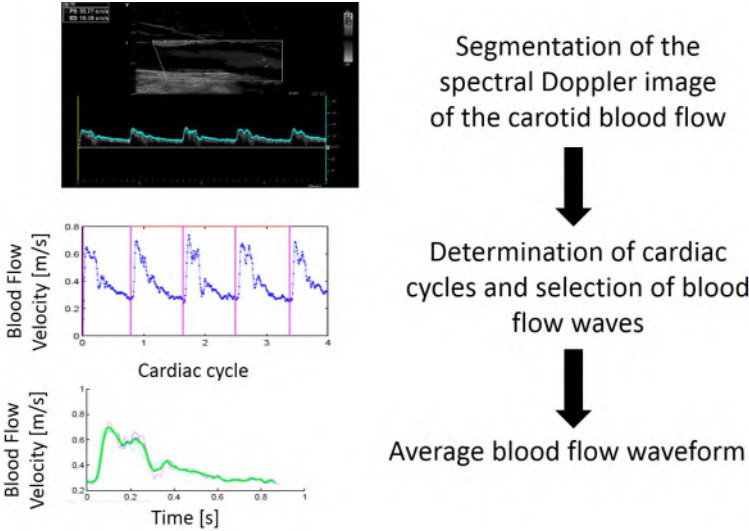


Figure 3.3: Segmentation of spectral Doppler images of blood flow velocity. Doppler flow velocity files are processed by selecting the onset and end of systolic ejection for each cardiac cycle with two cursors. Then, contours are automatically traced using the transition in pixel intensity above a user-defined threshold value. Next, the signal from each cardiac cycle is used to calculate an average blood flow waveform.

Applying the Fourier transform, pressure and flow waveforms are broken down into their harmonic components to perform the analysis in the frequency domain. The ratio of the magnitude (amplitude) of pressure and flow harmonics is known as input impedance (Z_{in}) (figure 3.4B) whereas the average modulus of the 3rd to 10th harmonics of Z_{in} is denominated as the characteristic impedance of the proximal aorta (Z_c) [63]. For calculating Z_c , values 3 times the median value of Z_{in} over that range of harmonics were excluded following [63]. The reflection coefficient (Γ), defined as the amplitude of its first harmonic (heart frequency), is calculated as:

$$\Gamma = \frac{Z_{in} - Z_c}{Z_{in} + Z_c} \quad (3.15)$$

The analysis in the time domain is also performed. The characteristic impedance of the proximal aorta ($Z_c - TD$) is obtained in the time domain

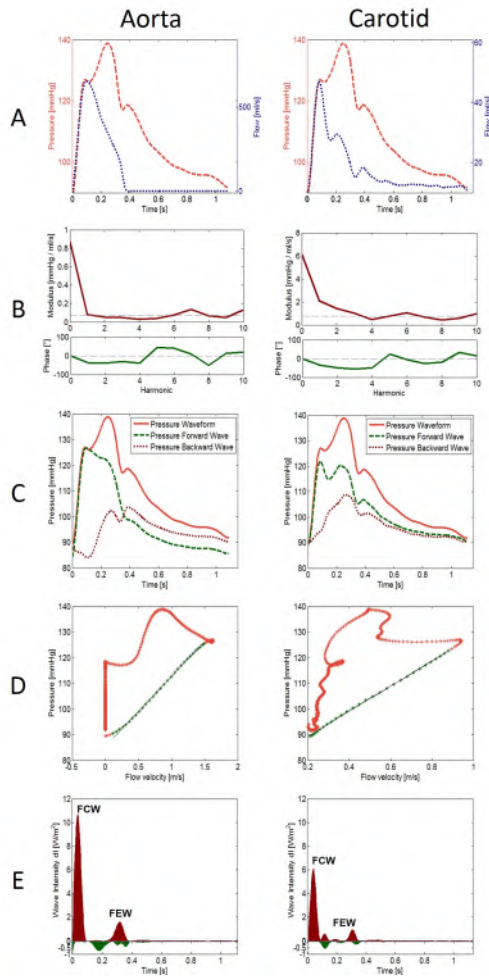


Figure 3.4: Haemodynamic analysis of the aorta and carotid arteries. A custom-designed software was built in MATLAB[®] (The Mathworks, Natick, MA) [63], [64] to process off-line central arterial tonometry recordings and Doppler flow velocity files. A) Visual time-alignment of pressure (dashed red line) and flow (dotted blue line) curves is effectuated taking into consideration the concordance of the rapid systolic upstroke of pressure and flow, and the pressure dicotic notch and cessation of flow. B) Modulus (red line) and phase (green line) of the input impedance (Z_{in}) obtained as the ratio of the magnitude of pressure and flow harmonics. C) Wave separation analysis of the pressure curve. D) Pressure-flow loop calculation with the (linear) early systole portion defined by green markers. E) Wave intensity analysis. FCW corresponds to the forward compression wave and FEW corresponds to the forward expansion wave. The red area is forward wave intensity and the green area is backward wave intensity. Adapted from [4].

since the frequency domain calculation may introduce a bias to lower values of Z_c . $Z_c - TD$ is defined as the ratio of early systolic pulsatile pressure/flow. Systemic vascular resistance (SVR) corresponds to the modulus of Z_{in} at $0Hz$, and total arterial compliance is determined by two methods: pulse pressure (C_{PPM}) [65] and area (C_{area}) method [66].

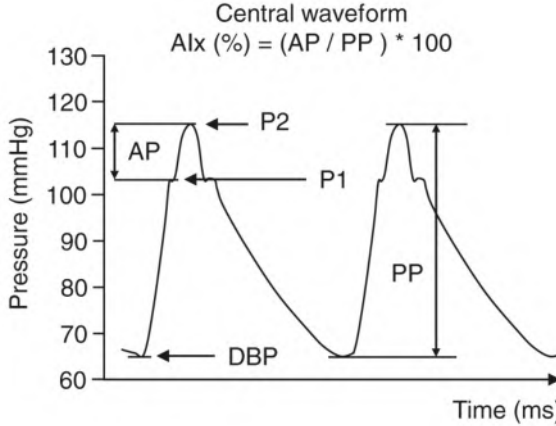


Figure 3.5: Analysis of the central waveform. Central systolic (SBP) and diastolic blood pressure (DBP) and pulse pressure (PP) are derived from a central pressure waveform. The augmentation index (AIx) is computed as the ratio between the augmentation pressure ($AP = P_2 - P_1$) and pulse pressure (PP), expressed as a percentage. Adapted from <https://commons.wikimedia.org/wiki/File:Method-of-pulse-wave-analysys.png>. By Omboni S, Posokhov IN [CC BY-SA 4.0 (<https://creativecommons.org/licenses/by-sa/4.0>)].

Wave separation analysis is computed separating the pressure waveform into forward (P_f) and backward (P_b) traveling components (figure 3.4C), and the ratio of the amplitudes of P_b/P_f is the reflection magnitude. The first (P_1) and the second (P_2) systolic peaks are defined, and derived measurements, such as augmented pressure (AP) and augmentation index (AIx), are determined (figure 3.5):

$$Augmented\ pressure(AP) = (P_2 - P_1) \tag{3.16}$$

$$AIx = \left[\frac{AP}{Pulse\ Pressure} \right] \times 100 \tag{3.17}$$

P_1 and P_2 result from the incident and reflected wave, respectively. Thus, wave reflections increase the AIx.

Wave intensity analysis (WIA) is executed in the time domain and requires pressure and flow to be measured at the exact same location and, preferably, at the same time. The method states that any observed waveform can be built up from a time-dependent succession of wave-fronts [67], which can be interpreted as a disturbance to the flow that causes temporal changes in pressure (dP) and flow velocity (dU) over one sampling interval. These elemental wave-fronts dP and dU propagate with a wave velocity c and can be located in time and space, unlike the sinusoidal waveforms, which only have a phase and frequency [40]. In the intact circulation, traveling wave-fronts represent elemental units of energy transmitted within and between blood vessels and the heart [67]. Infinitesimal wave-fronts dP and dU can be separated in a forward (subscript +) and a backward (subscript -) propagating component:

$$dP_{\pm} = \frac{1}{2}(dP \pm \rho c dU) \quad (3.18)$$

$$dU_{\pm} = \pm \frac{1}{2} \left(dU \pm \frac{dP}{\rho c} \right) \quad (3.19)$$

with ρ the density of blood. The wave speed c can be determined using the water-hammer equation:

$$dP_{\pm} = \pm \rho c dU_{\pm} \quad (3.20)$$

and follows from plotting pressure as a function of velocity (PU-loop, figure 3.4D) for the whole cardiac cycle. After calculation of the infinitesimal wave-fronts dP and dU , wave intensity (dI) can be computed (figure 3.4E) to analyse and represent the nature of waves:

$$dI = dP dU \quad (3.21)$$

For each direction, there are two types of wave-fronts: compression wave-fronts that increase pressure (generated by “blowing”) and expansion wave-fronts that decrease pressure (generated by “sucking”). Any complex wave can be synthesized from a succession of backward and/or forward travelling compression and expansion wave-fronts [67].

In haemodynamic analysis, conversion of velocity (measured in a sample volume) into a volumetric flow assumes a parabolic or flat flow velocity profile. However, the flow velocity profile of the carotid artery is neither, and improvement of the conversion is achieved accounting for the Womersley number for oscillatory flow [68].

3.2.1.1 Carotid flow profile - implementing Womersley theory

Ponzini *et al.* [68] presented a Womersley number-based formula for estimating blood flow, proving its worth over traditional approaches without requiring any different or new acquisition procedures.

The implemented method was based on the flow rate estimated by the Womersley number-based formula:

$$Q_W = k_W V_M \sum_{pi} A_{pi} \quad (3.22)$$

where k_W depends on the Womersley number (W), which is defined as:

$$W = D \sqrt{\frac{f \pi}{2\nu}} \quad (3.23)$$

where D is diameter, f is the frequency giving by the HR and ν is the blood kinematic viscosity ($(2.8 - 3.8) \cdot 10^{-6} m^2/s$). An expression linking the maximum velocity and the flow rate at the peak instant has been proposed [69]:

$$k_W = \begin{cases} g_1, & W \leq 2.7 \\ pg_1 + (1-p)g_2, & 2.7 < W \leq 3.1 \\ g_2, & 3.1 < W \leq 15 \end{cases} \quad (3.24)$$

where

$$\begin{aligned} g_1(W) &= 0.5(1 + a_1 W^{b_1}); \\ g_2(W) &= 0.5b_2 \arctan(a_2 W); \end{aligned} \quad (3.25)$$

with

$$\begin{cases} a_1 = 0.00417 & b_1 = 2.95272 \\ a_2 = 1.00241 & b_2 = 0.94973 \end{cases} \quad (3.26)$$

and

$$p = e^{(W-2.7)^2 / ((W-2.7)^2 - (3.1-2.7)^2)} \quad (3.27)$$

3.2.2 Wave power analysis

Wave power analysis (WPA), a proposed method by Mynard *et al.* [70], links a flow based alternative to wave intensity with a novel time domain analysis of hydraulic power and the concept of wave potential. Furthermore, it provides added value compared with previous methods in that it can be used to study the distribution of wave power at junctions, is relatively insensitive to diameter variations, and is quantitatively linked to transient changes in hydraulic pressure power [70]. Indeed, an advantage of using wave power over wave intensity is that it represents energy (W), a conserved quantity, rather than wave intensity (W/m^2) which is not conserved [70]. These advances enable detailed time domain analysis of cardiovascular processes contributing to hydraulic power and establishing the fundamental links between wave phenomena and hydraulic power. Furthermore, these features of the method support the analysis of transmitted energy into organs, which is particularly relevant for the brain, and may help understanding specific pathophysiological processes, the link between central haemodynamics and brain/cognitive function, or be useful in the analysis of the effects of certain medication, as will be shown in Chapter 5.

Mynard *et al.* [70] described in detail the WPA defining a quantity as “wave power” ($d\pi$) from the 1D equations governing pressure and flow. In figure 3.6, a graphical depiction of WPA is outlined to illustrate its steps and extracted parameters.

As with wave intensity, a linear separation can be performed by assuming constant Z_c , where $Z_c = \rho c/A$, with A the CSA, and $d\pi = d\pi_+ + d\pi_-$, leading to:

$$d\pi_{\pm} = \pm \frac{1}{4Z_c} (dP + Z_c dQ)^2 \quad (3.28)$$

Under these linear flow conditions, $Z_c dQ = \rho c dU$ and wave power and wave intensity are related via $d\pi = AdI$.

In figure 3.6B, wave power curves are characterised by two major positive peaks: a forward compression wave (FCW_{WP}) and a forward expansion wave (FEW_{WP}).

3.2.2.1 Forward and backward components of pressure, flow, and hydraulic power

The forward and backward components of pressure (P_{\pm}) and flow (Q_{\pm}) represent the pressure and flow that would exist if only forward or only backward

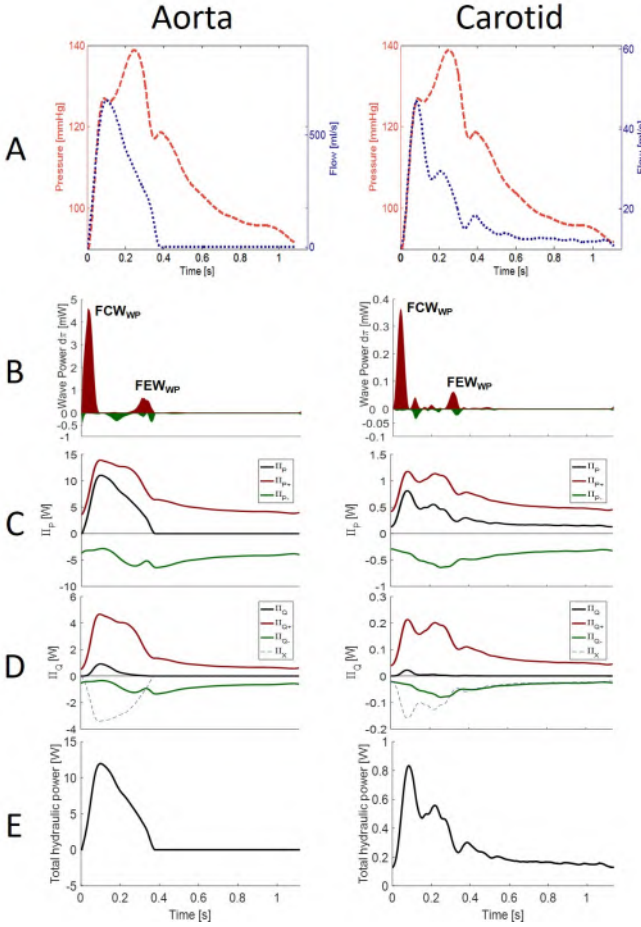


Figure 3.6: Wave power analysis. A) Time-alignment of pressure (dashed red line) and flow (dotted blue line) curves. B) Wave power curves characterised by two major positive peaks: forward compression wave (FCW_{WP}) and forward expansion wave (FEW_{WP}). C) Curves of pressure power (Π_P , black line) and forward (Π_{P+} , red line) and backward (Π_{P-} , green line) components. D) Kinetic power curves (Π_Q , black line) and forward (Π_{Q+} , red line) and backward (Π_{Q-} , green line) components, and a nonlinear interaction component (Π_X , dashed blue line). E) Total hydraulic power (Π).

waves existed [71]. Hydraulic power can be also separated into such components. In most settings, a linear separation could be used [70]:

$$P = P_+ + P_- + P_{ud} \quad (3.29)$$

$$Q = Q_+ + Q_- \quad (3.30)$$

where the constant P_{ud} is undisturbed pressure and represents the equilibrium pressure that is attained when no wave potential or waves exist in the vascular system, typically at a value of $\sim 10\text{mmHg}$ in human adults [71]. The linear separation makes use of the water-hammer equation that relates incremental changes in (P_{\pm}) and (Q_{\pm}) via Zc as follows:

$$dP_{\pm} = \pm Zc dQ_{\pm} \quad (3.31)$$

Combining equations (3.29) to (3.31), and integrating, it can be shown that [70], [71]:

$$P_{\pm} = \frac{1}{2}(P - P_{ud} \pm Zc dQ_{\pm}) \quad (3.32)$$

$$Q_{\pm} = \frac{1}{2} \left[Q \pm \frac{1}{Zc} (P - P_{ud}) \right] \quad (3.33)$$

Ignoring gravitational effects, hydraulic power (Π) at a given location is equal to the sum of pressure (Π_P) and kinetic (Π_Q) components:

$$\Pi = \Pi_P + \Pi_Q = PQ + \frac{\rho Q^3}{2A^2} \quad (3.34)$$

Pressure power represents the potential for hydraulic work per second, while kinetic power represents the rate of energy transfer due to the flowing fluid. Note that the sign of Π simply indicates the direction of power transfer.

From equations (3.29) and (3.30), pressure power can be expressed in terms of P_{\pm} and Q_{\pm} as:

$$\Pi_P = (P_+ + P_- + P_{ud})(Q_+ + Q_-) \quad (3.35)$$

From equations (3.32) and (3.33), an absolute form of the water-hammer equation can be derived:

$$P_{\pm} = \pm Zc Q_{\pm} \quad (3.36)$$

By making use of equation (3.36), equation (3.35) can then be expanded and simplified to yield:

$$\Pi_P = (P_+ + P_{ud})Q_+ + (P_- + P_{ud})Q_- \quad (3.37)$$

Forward and backward components of Π_P can now be defined as:

$$\Pi_{P\pm} = (P_{\pm} + P_{ud})Q_{\pm} = \frac{1}{4} \left[2PQ \pm Zc Q^2 \pm \frac{1}{Zc} (P^2 - P_{ud}^2) \right] \quad (3.38)$$

where the right-hand side is obtained by substituting equations (3.32) and (3.33). Importantly, the pressure power components are additive:

$$\Pi_P = \Pi_{P+} + \Pi_{P-} \quad (3.39)$$

Curves of pressure power (Π_P) and its forward (Π_{P+}) and backward (Π_{P-}) components are shown in figure 3.6C.

Kinetic power may be expressed also in terms of forward and backward flow components:

$$\Pi_Q = \frac{\rho}{2A^2} (Q_+ + Q_-)^3 \quad (3.40)$$

Expanding,

$$\Pi_Q = \frac{\rho}{2A^2} (Q_+^3 + 3Q_-Q_+^2 + 3Q_-^2Q_+ + Q_-^3) \quad (3.41)$$

In the case where $\Pi_{Q\pm}$, the forward and backward components of kinetic power are:

$$\Pi_{Q\pm} = \frac{\rho}{2A^2} Q_{\pm}^3 \quad (3.42)$$

However, the two middle terms in equation (3.41) show that the sum of these components do not equal the net kinetic power. Rather:

$$\Pi_Q = \Pi_{Q+} + \Pi_{Q-} + \Pi_X \quad (3.43)$$

where $\Pi_X = (3Q_-Q_+^2 + 3Q_-^2Q_+) \rho / 2A^2$ describes a nonlinear interaction [70].

All three curves, kinetic power (Π_Q) and its forward (Π_{Q+}) and backward (Π_{Q-}) components, are shown in figure 3.6D.

Total hydraulic power may be written as:

$$\Pi = (\Pi_{P+} + \Pi_{Q+}) + (\Pi_{P-} + \Pi_{Q-}) + \Pi_X \quad (3.44)$$

To remark, the impact of the kinetic power is generally very small compared with pressure power [70]. Total hydraulic power (Π) is presented in figure 3.6E.

3.3 DEDICATED TOOLS FOR THE ASSESSMENT OF ARTERIAL HEALTH (IN NON-ROUTINE CONDITIONS)

In the course of this PhD project, additional dedicated tools for the processing and analysis of data were developed, such as the use of radio frequency (RF) data or supplementary haemodynamic analysis. These are briefly introduced in this section and extended in Chapter 6.

3.3.1 Wall tracking algorithm based on RF ultrasound data

Ultrasound based tracking algorithms serve to measure the vessel diameter, for instance, by a displacement detection system based on autocorrelation. Since autocorrelation methods have lower sampling rate requirements, a modified autocorrelation approach has been proposed by Rabben *et al.* [72] to estimate on complex demodulated RF data both the mean Doppler frequency and the RF centre frequency from an observation window.

The method was implemented by building a custom-written, MATLAB[®]-based application for analysis of vessel distensibility from ultrasound RF M-Mode data [5] (see Chapter 6).

Moreover, in the course of my own PhD work, other PhD students were performing cardiovascular studies in different mouse models. To support their work, a number of dedicated software tools were developed to enable haemodynamic analysis in these animals and to derive arterial properties to feed into computational models.

As it is complicated to measure pressure in longitudinal studies in mice, analyses were based on measurements of diameter distension waveforms and flow velocity in the aorta and carotid arteries. To enable this work, the application was further adapted to obtain the aortic distensibility from data measured using a high-frequency small animal imaging ultrasound system

(Vevo 2100, VisualSonics, Toronto, Canada), reconstructing the complete M-Mode image (see figure 3.7A) from RF data so the user can select a specific zone to process. This zone is plotted as a reference for the user to perform the manual wall segmentation (see figure 3.7B). A complete segmentation process is shown in figure 3.7, including diameter distension curves and the synchronized ECG signal. The method has been used by Trachet *et al.* [15] and De Wilde *et al.* [73].

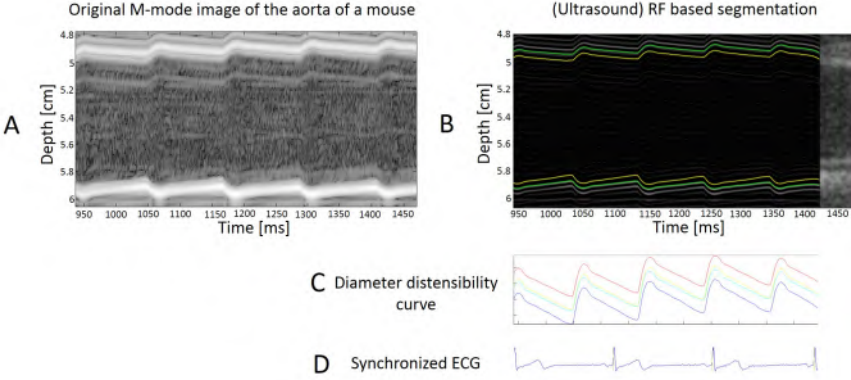


Figure 3.7: Adapted segmentation method for calculating arterial diameter distension curves in mice using an (ultrasound) RF based method. A) Original ultrasound image of the aorta of a mouse. B) Manual segmentation of the aortic lumen. C) Derived diameter distension curves. D) Synchronized ECG signal. Images were acquired with a high-frequency ultrasound device (Vevo 2100, VisualSonics, Toronto, Canada) using a linear array probe (MS 550D, frequency 22 – 55MHz).

3.3.2 Signal alignment using a correlation method

To resolve automatically the time lag between diameter and flow velocity waveforms, a correlation method was adapted [74], defining a correlation factor (R) as:

$$R(s) = \frac{\sigma_{DU}(s)}{\sigma_D \sigma_U(s)} \quad (3.45)$$

Where s is the shift, σ_D and σ_U are the standard deviations of the carotid distension and shifted blood flow velocity signals, respectively, and $\sigma_{DU}(s)$ is the covariance.

The standard deviations were defined as:

$$\sigma_D = \sqrt{\frac{1}{N} \sum_{i=1}^N (D_i - \bar{D})^2} \quad (3.46)$$

$$\sigma_U(s) = \sqrt{\frac{1}{N} \sum_{i=1}^N (U_{i-s} - \bar{U})^2} \quad (3.47)$$

where D_i and U_i represent diameter and blood flow velocity of sample number i , and \bar{D} and \bar{U} mean diameter and blood flow velocity over the N samples between minimum diameter and maximum blood flow velocity.

The covariance, $\sigma_{DU}(s)$, is calculated as:

$$\sigma_{DU}(s) = \frac{1}{N} \sum_{i=1}^N [(D_i - \bar{D})(U_{i-s} - \bar{U})^2] \quad (3.48)$$

The shift corresponding to the highest correlation factor is regarded as the correct delay (see figure 3.8A).

3.3.3 Wave speed determination

Feng *et al.* [75] proposed an approach to determine wave speed based on diameter and flow velocity measurements (rather than on pressure and flow velocity). Wave speed can be expressed as:

$$c^2 = \frac{1}{\rho D_s} \quad (3.49)$$

Where ρ is the density of the fluid and D_s is the distensibility of the wall (figure 3.8B), which is related to the change in pressure (dP) and diameter (dD) through the mathematical expression:

$$D_s = 2 \frac{dD}{DdP} \quad (3.50)$$

Replacing equation (3.50) in equation (3.49):

$$dP = \rho c^2 \frac{2dD}{D} \quad (3.51)$$

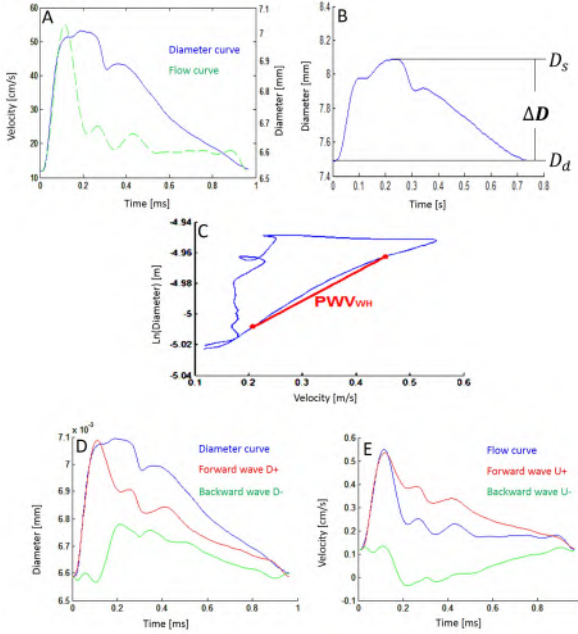


Figure 3.8: Processing and analysis of diameter distension and flow velocity curves. A) Signal alignment using the correlation method. B) Diameter distensibility calculation with D_s = systolic diameter and D_d = diastolic diameter. C) $\ln DU$ loop in which the slope of the loop's linear portion indicates the value of the local pulse wave velocity (PWV_{vwh}). Wave separation of D) diameter distension and E) flow velocity curves. Adapted from [5].

The change in diameter (dD) is the response to traveling waves (backward and forward). Then, changes in velocity (dU) as forward acceleration ($dP > 0$; $dU > 0$) or backward deceleration ($dP > 0$; $dU < 0$) produce an increase in diameter ($dD > 0$) while forward deceleration ($dP < 0$; $dU < 0$) or backward acceleration ($dP < 0$; $dU > 0$) generate a decrease in diameter ($dD < 0$).

Changes in pressure and diameter can be considered as the linear summation of the effects in forward and backward directions. This concept can be expressed as:

$$dP_+ + dP_- = \frac{2\rho c^2}{D}(dD_+ + dD_-) \quad (3.52)$$

The water-hammer equation relates the changes in pressure with the changes in velocity:

$$dP_{\pm} = \pm \rho c dU_{\pm} \quad (3.53)$$

And combining equations (3.52) and (3.53):

$$c = \frac{D (dU_+ + dU_-)}{2 (dD_+ + dD_-)} \quad (3.54)$$

If it is assumed that $\frac{dD}{D} = d \ln D$, then wave speed in terms of velocity (U) and diameter (D) is:

$$c = \pm \frac{1}{2} \frac{dU_{\pm}}{d \ln D_{\pm}} \quad (3.55)$$

The linear relationship described by this equation between U and $\ln D$ for unidirectional waves is evident plotting $\ln D$ against U , as figure 3.8C demonstrates. This plot delivers a $\ln DU$ loop with a linear portion during early systole, which is considered a reflection-less phase. The slope of the linear portion of the loop is equal to $\frac{1}{2}c$.

3.3.4 Wave separation

To perform the separation of waves, Feng *et al.* [75] adapted the water-hammer equation to relate changes of diameter (D) and blood flow velocity (U), and assumed that dU is additive in forward (+) and backward (-) directions, so $dU = dU_+ + dU_-$, then dD and dU in forward (+) and backward (-) directions can be derived as:

$$dD_{\pm} = \frac{1}{2} (dD \pm \frac{D}{2PWV_{WH}} dU) \quad (3.56)$$

$$dU_{\pm} = \frac{1}{2} (dU \pm \frac{2PWV_{WH}}{D} dD) \quad (3.57)$$

D and U waveforms in forward (+) and backward (-) directions can then be obtained by summing the instantaneous changes in D and U in each direction, respectively:

$$D_{\pm} = \sum_{t=0}^T dD_{\pm} + D_{(o)} \quad (3.58)$$

$$U_{\pm} = \sum_{t=0}^T dU_{\pm} + U_{(o)} \quad (3.59)$$

where T is the total cycle time. $D_{(o)}$ and $U_{(o)}$ are the integration constants and can be taken arbitrarily as zero.

In figure 3.8D and E, a wave separation example for diameter distension and flow velocity curves are shown.

3.3.5 Reflection magnitude

Since reflections can modify the total pressure wave due to constructive or destructive interference of the waves, the net-effect of the reflections is important. Making use of the adapted water-hammer equation, the effect could be applicable to diameter distension waves. Once all forward and backward harmonics are calculated, then they can be added to construct one global forward (D_+) and backward (D_-) waveform. It is then straightforward to quantify the magnitude of wave reflections as the ratio of the amplitude of D_- and D_+ [40]:

$$RM = \frac{\max(D_-) - \min(D_-)}{\max(D_+) - \min(D_+)} = \frac{|D_-|}{|D_+|} \quad (3.60)$$

II

Novel Cardiovascular Research

CHAPTERS

| | | |
|----------|--------------------------|------------|
| 4 | Cardiac Function | 89 |
| 5 | Vascular Function | 137 |
| 6 | Dedicated tools | 161 |

CARDIAC FUNCTION

The heart is central to the cardiovascular system and, consequently, its performance, defined as cardiac function, is crucial to maintain proper blood supply to tissues and organs at adequate filling pressures. Competent adaptation mechanisms under different demands, such as exercise, extreme temperatures or even during respiration, should be in place to guarantee a proper cardiac function. However, disease processes or pathological adjustments triggered by an unusual stress to the system can lead to cardiac dysfunction and, ultimately, to heart failure (HF). Several factors influence cardiac function and, thus, a thorough assessment is pivotal to identify subjects at risk, to evaluate treatment selection and to follow-up patient evolution. Particularly, intraventricular pressure gradients (IVPGs) and differences (IVPDs) have raised interest as relevant physics based metrics of cardiac function responsible not only for efficient filling of the ventricles but also for efficient ejection of blood during systole. Thus, even if small in magnitude, IVPDs are essential to the proper functioning of the cardiovascular system and their estimation should be considered in the clinical evaluation of cardiac function.

Non-invasive evaluation of cardiac function is performed, largely, by echocardiography or MRI, which are standard methods in cardiovascular assessment due to their appealing attributes. Therefore, the estimation of IVPDs can be achieved by both imaging techniques, but there is a lack of comparable results to examine and compare the most suitable approach. Since non-invasive *in vivo* measurements miss a ground truth to contrast the estimated IVPDs and invasive measurements are not practical in the

clinical setting, an appealing approach to validate multidimensional flow estimates is the use of computational fluid dynamics (CFD) models with a full knowledge of true haemodynamics. In this chapter, the application of such models supports the implementation of a fitting method to estimate IVPDs noninvasively. Further evaluation of the feasibility of the method in different sample populations is presented to identify differential patterns of cardiac function in subjects without HF and in patients with distinct HF subtypes.

The chapter starts with a review on the non-invasive assessment of IVPGs and IVPDs, and their potential role in characterisation of patients with HF. This section sets the theoretical framework for the entire chapter and it is adapted from a paper published in *Current heart failure reports* and titled "MRI assessment of diastolic and systolic intraventricular pressure gradients in heart failure", vol. 13, no. 1, pp. 37-46, 2016 [13]. The second part of the chapter deals with the assessment of methodologies to calculate IVPDs in computational models and patients, in which an echocardiographic and an MRI approach are evaluated with the use of a CFD model of the left ventricle (LV). This section is based on the paper titled "Assessment of methodologies to calculate intraventricular pressure differences in computational models and patients" and published in *Medical & biological engineering & computing*, vol. 56, no. 3, pp. 469-481, 2018 [2]. These results supported the implementation and feasibility assessment of an MRI based processing algorithm to estimate IVPDs noninvasively in subjects without HF and with heart failure with reduced (HFrEF) or preserved (HFpEF) ejection fraction. Thus, the third section of this chapter is based on a published article in *Open Heart*, vol. 6, no. 2, 2019, that presents the results of this approach under the title "Non-invasive Intraventricular Pressure Differences Estimated with Cardiac MRI in Subjects without Heart Failure and with Heart Failure with Reduced and Preserved Ejection Fraction"[1].

4.1 THEORETICAL BACKGROUND AND RATIONALE OF THE ASSESSMENT OF DIASTOLIC AND SYSTOLIC INTRAVENTRICULAR PRESSURE DIFFERENCES IN HEART FAILURE

4.1.1 Introduction

The increasing incidence and prevalence of HF worldwide [76]–[78] is responsible for a large burden of morbidity and mortality, poor quality of life, and healthcare costs [79]–[81].

Assessment of ventricular function is key to characterise patients with HF. Clinically, two major subtypes of HF are identified based on the LV ejection

fraction (EF): HFrEF and HFpEF [82]–[84]. Although LV systolic dysfunction is thought to be the key pathophysiologic abnormality in HFrEF, diastolic dysfunction is also present in this condition. Similarly, whereas diastolic dysfunction is thought to be a key pathophysiologic abnormality in HFpEF, systolic contractile abnormalities have also been reported in this condition. Particularly, diastolic function of the LV encompasses a complex sequence of interrelated events involving both the active and passive properties of the ventricle as determinants of filling [85]. The pathophysiology of diastolic dysfunction is not fully understood, and the comprehensive characterisation of LV relaxation and filling dynamics and its integration into clinical practice are desirable, particularly in patients with HFpEF [85]–[87].

Non-invasive quantitative analysis of intraventricular flow dynamics can provide important insights into the processes driving LV ejection and filling. Indeed, Doppler echocardiography is the most common approach for the evaluation of diastolic function. Analysis of transmitral flow and annular tissue velocity patterns is the basis of diastolic function assessments in clinical practice. Notwithstanding, several confounding factors (e.g., the rate and extent of ventricular relaxation, suction, atrial and ventricular compliance, mitral valve inertance, and left atrial (LA) pressure) may influence transmitral flow velocity and, consequently, limit its accuracy to characterise LV diastolic dysfunction [88]–[91].

While the analysis of blood flow velocities (in particular, the transmitral flow velocities) is extensively used in the evaluation of LV function [87], [92], [93], much less is known about underlying pressure gradients and differences driving diastolic and systolic intraventricular flow in HFrEF and HFpEF. Derived pressure calculations can be inferred by solving the Euler equation, a simplified version of the Navier-Stokes equations [94], [95], using information regarding the spatiotemporal pattern of LV blood flow velocities, which in turn can be obtained using ultrasound, e.g., colour M-mode (CMM) recordings along a transmitral scanline, or magnetic resonance imaging (MRI). Note that there is a difference in terminology with “gradient” referring to a pressure difference per unit length (e.g., in $mmHg/cm$) while pressure difference is the absolute difference in pressure between two points in space (in $mmHg$) [96].

The computation of IVPDs provides a physical and quantitative indicator of LV diastolic function [94], [96] but can also be applied to systole for interrogating pressure gradients produced by LV ejection. IVPDs calculated from CMM or MRI data have demonstrated good agreement with invasively measured IVPDs in *in vitro* experiments, animal models, and groups of patients undergoing cardiac surgery [94], [95], [97]–[101].

Although the presence of a pressure difference from the base to the apex of the LV was first speculated by Katz *et al.* in the 1930s, it was not until the 1970s that IVPDs were first demonstrated [102]. Since then, multiple animal and human studies have characterised IVPDs/IVPGs in health and disease. Non-invasive methods to estimate IVPGs utilising measures of intraventricular flow velocity have also been developed and applied [57], [103]. This review focuses on the non-invasive assessment of IVPGs and IVPDs, and its potential role in characterisation of patients with HF.

4.1.2 IVPGs/IVPDs: basic concepts

Key to understand the generation of pressure gradients are the principles of fluid mechanics that describe the pressure–velocity relationship of three-dimensional (3D) flow across a cardiac chamber [56]. Such flow is governed by the Navier–Stokes equations for an incompressible fluid [56], [57] with constant density (ρ):

$$\begin{aligned} \nabla \cdot \mathbf{v} &= 0 \\ -\nabla P + B + \mu \nabla^2 \mathbf{v} &= \rho \left[\frac{\partial \mathbf{v}}{\partial t} + (\mathbf{v} \cdot \nabla) \mathbf{v} \right] \end{aligned} \quad (4.1)$$

where ∇ represents: $i \frac{\partial}{\partial x} + j \frac{\partial}{\partial y} + k \frac{\partial}{\partial z}$

where i , j , and k are orthogonal unit vectors, and \mathbf{v} is a three-component vector of local blood velocity, P is the local pressure, B represents body forces (such as gravity) acting on the fluid, and μ is viscosity.

This complex set of coupled differential equations can be simplified on the basis of the following assumptions: (1) the viscous term, $\mu \nabla^2 \mathbf{v}$, is very small compared to the other terms and can be neglected [103]–[105]; and (2) the gravitational force is balanced by hydrostatic buoyancy, and thus $B = 0$ [56], [57] leading to equation (4.2):

$$-\nabla P = \rho \left[\frac{\partial \mathbf{v}}{\partial t} + (\mathbf{v} \cdot \nabla) \mathbf{v} \right] \quad (4.2)$$

In this equation, $\frac{\partial \mathbf{v}}{\partial t}$ represents the inertial component (i.e., the change in velocity through time at a given position), while $(\mathbf{v} \cdot \nabla) \mathbf{v}$ represents the convective component (i.e., the change in velocity through space at a given instant). The minus sign indicates that the blood particle has a positive acceleration when it moves from a region of higher to lower pressure.

Further simplification can be achieved when flow across a restricted orifice is considered. In that case, the amount of blood moving at high velocity is small compared with the volume of the overall column of blood in regions proximal to the stenosis, making the "inertial" component of the equation negligible and the "convective" component almost entirely responsible for the change in velocity (and pressure) that occurs as blood moves from a wide region to a narrow region [95]. The equation obtained after these assumptions is termed the simplified Bernoulli equation. Introduced by Hatle *et al.* [106], this equation provides the ability to calculate transvalvular pressure differences from Doppler measurements of blood velocity [107]:

$$\Delta P = 4v^2 \quad (4.3)$$

The simplified Bernoulli equation is frequently used to estimate pressure differences across restricted orifices to characterise the severity of valvular stenosis [56], [95] and is one of the most commonly used applications of Doppler echocardiography. This simple equation has been validated in *in vitro* settings, for example simulating aortic stenosis [96], [108], and in clinical settings for the assessment of several cardiac diseases, including aortic stenosis [109], mitral stenosis [110], prosthetic valve function [111], [112], obstructive hypertrophic cardiomyopathy, pulmonary hypertension, and intracardiac shunts [107].

Calculating IVPDs from one-dimensional velocity information

As predicted by fluid dynamics principles, and as described in mathematical models of LV filling [104], [105], [113], the simplified Bernoulli equation is applicable to pressure differences across restrictive orifices typical of stenotic and regurgitant lesions, but is not accurate for flow in the absence of a flow-limiting stenosis [105], [114]. When estimating IVPGs/IVPDs noninvasively, this equation has important limitations [115]–[118] because inertial forces are not negligible [108], [119]–[121], as it has been demonstrated in numerical, animal, and clinical models [122]–[124]. Therefore, the assessment of inertial forces is necessary to analyse intraventricular haemodynamics. Keeping the inertial component intact in equation (4.2) and applying it to flow along a streamline (with the distance along the streamline indicated by s), the one-dimensional (1D) Euler equation is obtained:

$$\frac{\partial P}{\partial s} = -\rho \left[\frac{\partial v}{\partial t} + v \frac{\partial v}{\partial s} \right] \quad (4.4)$$

The instantaneous pressure difference between any two points along this streamline $\left(\frac{\partial P}{\partial s}\right)$, is the net result of the change in velocity with time at a given point (inertial component $\rho \frac{\partial v}{\partial t}$), and the change in velocity with space at any given time (convective component, $\rho v \frac{\partial v}{\partial s}$) [57]. Pressure gradients can be directly integrated into pressure differences [95], [98], [101], [107], where the integration path is typically along a presumed streamline from the LV base to apex. Being s the spatial coordinate along the streamline, the unsteady Bernoulli equation is obtained, allowing the non-invasive estimation of the 1D IVPD [56]:

$$\Delta \hat{P}_{IV} [t] = \int_{base}^{apex} \frac{\partial P}{\partial s} ds \quad (4.5)$$

Using this equation, both inertial and convective pressure differences can be calculated from a spatiotemporal velocity map acquired with either ultrasound or magnetic resonance imaging (MRI).

Calculating IVPDs from two-dimensional velocity information

A more complete insight into cardiovascular fluid dynamics can be obtained from the two-dimensional (2D) pressure field, relative to the pressure at some arbitrary point. Unfortunately, a relative pressure field cannot be computed directly by integrating pressure gradients [125] without proper boundary conditions. Two strategies have been employed for this problem type, either a spatial-marching scheme to integrate the pressure gradient directly over the domain of investigation or solving the Poisson equation for the pressure on that domain or a subsection of it [126]. Specifically, a spatial integration method was selected in sections 4.2 and 4.3 to solve the system of equations [58], [127]:

$$IVPD_{2D} = \int_{Path} \frac{\partial P}{\partial x} dx + \int_{Path} \frac{\partial P}{\partial y} dy \quad (4.6)$$

4.1.3 Non-invasive assessment of IVPG/IVPD: ultrasound and MRI

Invasive studies have shown the important pathophysiological information derived from knowledge of the dynamics of ventricular ejection and filling [56], [107]. Simultaneously recorded high-fidelity pressure tracings at different sites within the LV have demonstrated the existence of regional pressure differences in both diastole [128]–[131] and systole (even in the absence of outflow obstruction) [97], [114], [132], [133]. The ability to measure these

pressure differences over time (particularly during diastole) provides unique information and new insights about the complex interaction between LV filling and function [56]. Unfortunately, most research on intracardiac pressure gradients has been limited, due to the need of sophisticated high-fidelity invasive catheterisation procedures that are difficult to perform in a clinical setting [56], [98], [107].

As an alternative, Thomas and Weyman [103] proposed the analysis of CMM echocardiograms. Flow velocity measurements with PW Doppler rely on the principle that the Doppler shift of reflected ultrasound waves, induced by moving blood particles, is proportional to the velocity of those particles. CMM echocardiography provides a spatiotemporal display of velocity along an ultrasound scan (straight) line, which can be used to compute pressure gradients across the line with the 1D Euler equation as described above. This approach assumes that the CMM is measured approximately along a streamline of flow, so that the Euler equation (equation (4.4)) can be applied directly to the data. If the scan line is prescribed from the mitral inflow to the LV apex, diastolic IVPGs can be assessed. Greenberg *et al.* [56], [57] described for the first time the methodology to noninvasively estimate the instantaneous pressure difference across the mitral valve throughout the diastolic filling period, including the contribution of the inertial forces of equation (4.4), in an animal model using CMM echocardiography. This approach was subsequently applied to humans using intraoperative techniques [117], quantifying the relative contribution of convective and inertial forces to the pressure differences across nonrestrictive mitral valves, and validating the non-invasive method to calculate IVPDs using CMM echocardiography, in order to improve the understanding of the complex phenomena underlying LV diastolic filling [98].

A similar approach can be used to compute systolic IVPGs, when the interrogation line is prescribed from the LV apex to the LV outflow during ejection. Bermejo *et al.* [107] presented a detailed description of the processing of standard Doppler CMM echocardiographic images to measure pressure differences during ejection in the absence of outflow obstruction. Intracardiac pressure gradient maps and local pressure differences of LV inflow and ejection closely resembled tracings obtained invasively with pressure probes.

Several studies have further validated this approach in various conditions. Yotti *et al.* [134] compared their non-invasive estimation of IVPG with invasive measurements, reporting high correlation and agreement. Additionally, Rovner *et al.* [99], [135] validated the non-invasive measurement of diastolic IVPG in hypertrophic cardiomyopathy and in HF patients. Therefore, the approach to derive regional pressure differences within the ventricle has

proven to be a viable tool for the assessment of ventricular diastolic and systolic function, which may provide novel insights into the non-invasive characterisation of ventricular function [95].

Important technical details for measuring IVPGs with CMM include adequate gain and aliasing velocity settings, and a proper scan line orientation, which should be aligned to the direction of blood flow and should "pass" through the "core" of the blood flow column. Precise prescription of the interrogation line avoids underestimation of flow velocities (due to imperfect alignment with the direction of blood flow) and allows to capture the most relevant spatiotemporal information of the intraventricular flow field. Interestingly, Greenberg *et al.* [56], [57] demonstrated that a very precise alignment of the scan line is not required: the error in calculating IVPGs was small (mean squared error $< 0.26\text{mmHg}$) even if the scan line was misaligned to up to 20° and even if it was displaced from the centerline to more than halfway to the edge of the mitral valve.

Despite the fact that Doppler ultrasound velocity imaging is the most widely used technique for non-invasive estimation of IVPGs/IVPDs, the method has some important limitations. Moreover, the quality of the original CMM data is dependent on anatomic windows, and the method has sensitivity to motion in a single direction, parallel to the beam path [58]. These issues give rise to potential errors in the estimated pressure differences attributable to insufficient sampling of the blood velocity field [136]–[139]. Whenever spatial or temporal derivatives are applied to discretely sampled data, noise is bound to increase in the process. Although the subsequent spatial integration will smooth out the noise to some degree, it is essential to obtain a complete CMM map before processing [95].

Phase contrast magnetic resonance imaging (PC-MRI) is an alternative technique to assess intraventricular flow velocity [140]–[147] and to calculate pressure gradients and relative pressure differences across vessel or valve stenoses [142], [144], or in more general flow regimes. This technique relies on the fact that when two opposing magnetic gradient pulses are applied to static nuclei aligned in a magnetic field, the effects of the two pulses on their nuclear spin cancel each other out. However, when a particle moves in the time between the pulses, a shift in the phase of the nuclear spins within the moving particle is accumulated, which is proportional to the velocity of movement along the gradient's direction. With PC-MRI, velocity maps along any given anatomical plane can be generated. When the gradient direction is applied exactly perpendicular to the anatomic plane ("through-plane" velocity encoding), flow can be measured along the LV (or blood vessel) cross section. For the assessment of IVPGs, "in-plane" interrogation of a single long axis

LV slice can be used. This technique has been validated using high-fidelity pressure catheters in a pulsatile flow phantom and in a canine model [58].

With in-plane PC-MRI data, a 2D map of flow velocities is obtained by the application of a velocity encoding in one direction: from right to left or from top to bottom of the specific anatomic plane. These two velocity encoding schemes can be applied in the same acquisition, or in separate acquisitions (first from right to left, and then from top to bottom, with subsequent off-line reconstruction of the 2D velocity field).

Finally, the acquisition of 4D PC-MRI images is now possible, allowing for measurements of velocity vectors in three spatial dimensions, with unrestricted image orientation for estimating pressure gradients *in vivo* [100], [127], [141], [147]–[149]. Although this method is less popular than other MRI techniques due to its extended imaging times [150], advances in gradient hardware continues to improve acquisition for 4D MRI data, which may lead to a more widespread use [127].

Among other parameters, PC-MRI sequences require a user-defined velocity encoding sensitivity (VENC), which should be as low as possible to minimize noise during the acquisition, yet higher than peak flow velocity in the region of interest to avoid aliasing. Although the VENC should be tailored to individual measurements, a good starting point for the assessment of IVPGs in the absence of mitral stenosis or significant mitral annular calcification is 130cm/s in most cases. This value must be raised in patients with increased LV inflow velocities, particularly in those with advanced diastolic dysfunction and elevated filling pressures, whom often exhibit peak flow velocities above this threshold.

Some limitations of PC-MRI include phase-offset errors caused by inhomogeneities of the magnetic field environment (short-term eddy currents) [151], which can be recognized as apparent velocities within stationary tissues that tend to increase with distance from the center of the image, being typically stable over all frames of a retrospectively gated cine acquisition [152]. Correction for phase-offset may be performed using PC-MRI data acquired from a stationary phantom [153], or alternatively, using information from stationary tissue located in the imaging plane [154]. Other potential problems of PC-MRI include signal loss due to turbulent flow, or partial volume averaging due to limited spatial resolution. The slice thickness should be optimized to avoid partial volume averaging while preserving a good signal to noise ratio.

We proposed an approach, further developed in sections 4.2 and 4.3, to perform interrogations of intraventricular flow using in-plane PC-MRI of the 3-chamber view ("LVOT" view), in two separate single breath hold

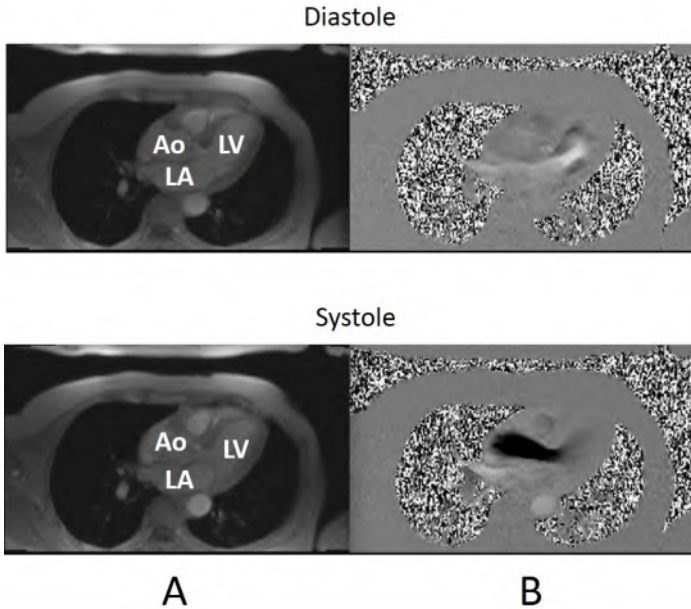


Figure 4.1: In-plane phase contrast MRI interrogations of intraventricular flow velocities in a 3-chamber view of the heart during diastole and systole. For each cardiac stage, panels show A) Magnitude data; B) Phase data. In the magnitude data, cardiac chambers are identified as LV: left ventricle; LA: left atrium; Ao: aorta. Figure adapted from [13].

acquisitions (each with a single-direction velocity encoding, right to left and anterior to posterior). A slice thickness of 5.5mm is used, while maximizing temporal resolution to acquire at least 30 points throughout the cardiac cycle, with a typical VENC of 130cm/s . This acquisition can be easily added to a standard < 1 hour scanning protocol, without compromising the efficiency of the scan. An example of in-plane PC-MRI measurement of intraventricular flow is shown in figure 4.1, whereas the left panels of figure 4.2 show the off-line processing proposed by us [1], [2] of in-plane 2D PC-MRI data to assess IVPDs (between the base and the apex of the LV). Briefly, after the sequence is displayed, two points are placed inside the image: at the mitral annulus (P_1) and at the LV apex (P_2). A total velocity is calculated from both velocity components to project it onto the reference line delimited by P_1 and P_2 , through a complete cardiac cycle, creating a pseudo-ultrasound CMM map (figure 4.2). This velocity information is then used to solve equation (4.4) and obtain the total pressure difference between P_1 and P_2 (see figure 4.2), together with its inertial and convective components.

An analogous approach using CMM echocardiography is also shown in figure 4.2 (right panels). An automated data analysis algorithm, described in

detail elsewhere [59], [60], is used. From original CMM images, the velocity colour scale region and a single beat region of interest (ROI) are selected, and then, the E-wave, A-wave, and the vertical position of the mitral plane are located for orientation of the algorithm. The grayscale values from the CMM image background are removed, thus leaving only the velocity colour scale image to which a dealiasing technique is applied to create a point-by-point velocity reconstruction of the ROI. Finally, the total pressure difference (figure 4.2) and its inertial and convective components are calculated. For further details see sections 4.2 and 4.3.

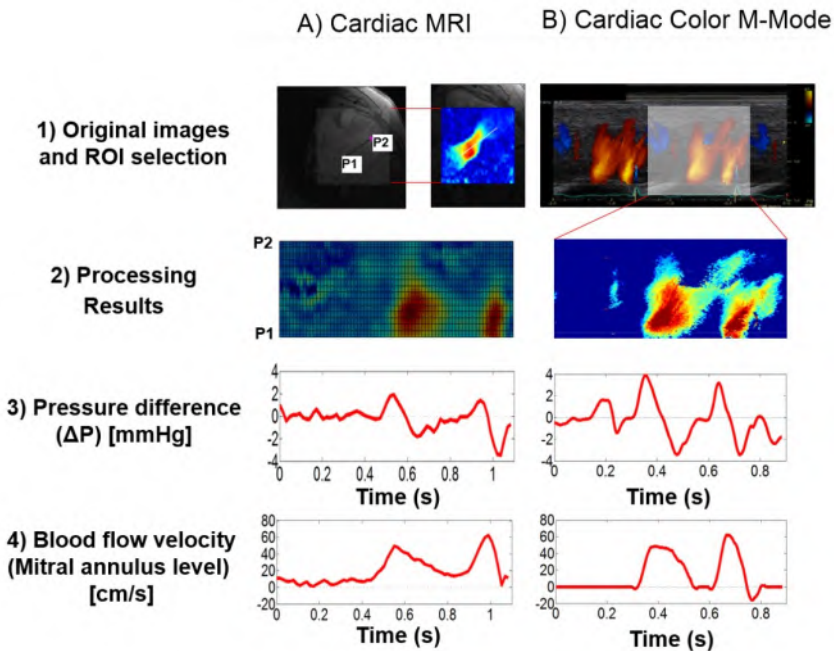


Figure 4.2: Examples of (A) cardiac MRI and (B) colour M-mode (CMM) recordings obtained from a patient with heart failure with preserved ejection fraction (HFpEF). Base-to-apex pressure differences calculated from available velocity information with each modality are shown. Processing of cardiac MRI and echocardiographic CMM data involves the selection of a ROI by the user and the prescription of an anatomic streamline. The spatiotemporal velocity profile along the streamline, represented in colour in (2), is used to compute IVPGs. These data are then used to compute base-to-apex IVPDs (3). Single-point flow velocity curves extracted from the data at the mitral annular level (4) are also shown. Figure adapted from [13].

A related approach for the assessment of diastolic function using intra-ventricular spatiotemporal flow velocity maps (such as those obtained with CMM echocardiography) is the evaluation of LV inflow propagation velocity (V_p). Normal LV intracavitary filling is dominated by an early wave followed

by an atrial-induced filling wave. In the normal ventricle, the early filling wave propagates rapidly toward the apex, which is driven by a pressure gradient between the LV base and the apex. This gradient represents a suction force and has been attributed to LV restoring forces and relaxation [85]. In order to relate intraventricular flow patterns to LV myocardial function in a quantitative manner, the slope method [155], [156] was proposed for measuring mitral to apical flow propagation from a spatiotemporal map of blood flow velocities along a scan line from the mitral annulus to the LV apex [85], [157]. V_p of the inflow jet traveling toward the apex during early diastole is measured as the slope of a linear approximation of an isovelocity contour during early filling [59]. However, limitations of the method have hampered its use, and other approaches have been proposed to expand the assessment of diastolic function [85], [157]. For instance, Stewart *et al.* [59] suggested that a single slope does not accurately represent the V_p for normal subjects or patients with diastolic dysfunction. Instead, they showed that intraventricular early diastolic V_p is characterised by a steep "initial" slope, indicating rapid flow V_p at the base, which abruptly changes to a "terminal", less steep V_p , distal to an inflection point, located along the LV cavity. In general, the assessment of IVPGs represents a more detailed approach to the assessment of intraventricular spatiotemporal velocity profiles.

IVPGs: physiologic determinants and clinical studies

Diastolic IVPGs are related to the complex interaction between LA pressure and suction forces generated by active LV relaxation and recoil [158], [159], whereas ejection-phase IVPGs from the apex to the outflow tract are determined by the interaction between the force generated by LV contraction and the properties of the arterial tree. It should be noted, however, that systolic and diastolic IVPGs are interrelated via the effects of myocardial function and various mechanisms of systolic-diastolic coupling.

The acute effects of changes in cardiac contractility and diastolic function have been studied in multiple animal models. As early as the 1980s, regional pressure differences in the LV, both during diastole and systole, were shown by Falsetti *et al.* [160], using invasive measurements through high fidelity transducers. Pressure differences were amplified with beta-adrenergic agonists and reduced by beta-adrenergic blockers. Courtois *et al.* [130], using invasive measurements in a canine model, found diastolic IVPGs to correlate significantly with EF and demonstrated that coronary occlusion led to a decrease in the peak diastolic base-to-apex LV pressure difference. Steine *et al.* [161] conducted a similar experiment in adult dogs and demonstrated a significant decrease in peak diastolic mitral to apical pressure difference

after coronary microembolization. In their study, this pressure difference correlated with both the time constant of LV isovolumic relaxation (τ) and stroke volume. In addition, an increase in contractility and a decrease in the rate of relaxation induced by isoprenaline infusion were also associated with a decrease in the peak early diastolic LV pressure difference in this model [162]. Firstenberg *et al.* [163] confirmed the association of early diastolic IVPDs with indices of systolic function using both invasive (high-fidelity conductance catheterisation) and non-invasive (CMM echocardiography) measurement techniques and found them to increase with inotropic stimulation. Yotti *et al.* [134] studied the ejection IVPDs from apex to the outflow tract in minipigs using CMM echocardiography and established their correlation with invasively measured indices of systolic function, including peak systolic LV elastance, preload recruitable stroke work, and peak of the first derivative of pressure corrected for the end diastolic volume, during states of varied contractility and induced acute myocardial ischemia.

Although highly informative, most of the previously mentioned studies were conducted in anesthetized, open-chest animal experiments, precluding a precise assessment of the normal human physiology. Firstenberg *et al.* [164] performed an invasive study of IVPDs in humans undergoing coronary surgical revascularization and found that not only peak diastolic gradients increased after revascularization, but this change also correlated with an improvement in the EF and τ , linking these gradients to both systolic and diastolic function.

Myocardial relaxation, LV elastic recoil, and LV filling are dependent on the time-varying systolic load and the deformation of cardiac muscle during contraction [159], [165]. Thus, ejection-phase and diastolic IVPGs are intrinsically linked. A particularly interesting index of systolic–diastolic coupling that can be assessed with the analysis of IVPGs is the late systolic reversal of the ejection-phase apex-to-outflow tract IVPD, which occurs as systolic flow decelerates and the heart relaxes, such that pressure is lower in the apex than in the outflow tract. The magnitude of this reversal jet has been shown to correlate with τ over a variety of lusotropic states in animal studies [166]. Smiseth *et al.* [167] showed in human subjects, using CMM echocardiography, that the apex-to-outflow pressure differences correlated strongly with τ , independent of changes in LV loading conditions. These findings are consistent with those of Yoshida *et al.* [168], who assessed the "inertia force" of late systolic aortic flow among patients with suspected coronary artery disease referred for cardiac catheterisation. In this study, inertia force was computed from the relation between LV pressure and its first derivative ($LVP/dPdT$). Patients with reduced EF had absent late systolic "inertia force." In addition, V_p was lower among patients with reduced EF or those with

preserved EF who had no "inertia force", compared to those with preserved EF who had a measurable "inertia force". The authors suggested that the force generated by late systolic blood inertia unloads the myocardium in late systole, promoting a smaller end-systolic volume and a greater deposition of elastic forces in the myocardium, leading to increased elastic recoil (and diastolic suction) during early diastole. However, the effect of inertial unloading on LV end-systolic volume is likely to be very small. It appears more likely that late systolic unloading may have favourable effects on calcium cycling and on various maladaptive pathways, since a large body of evidence now links increased late systolic load to the development of LV hypertrophy, fibrosis, systolic and diastolic dysfunction, the risk of new-onset HF, and the risk of HF readmission among patients with established HF [165], [169]–[177].

Various studies have assessed IVPGs in experimental models of HF and in humans with established HF. Guerra *et al.* [178] assessed IVPDs in a doxorubicin-induced dilated cardiomyopathy adult rabbit model. Through continuous invasive measurement of IVPDs, they demonstrated that the physiological early diastolic base-to-apex and late diastolic apex-to-base pressure differences, as well as systolic biphasic IVPDs, were abolished in rabbits with HF. Rovner *et al.* [135] studied the relationship between IVPDs and peak oxygen consumption (peak VO_2 , a measure of aerobic capacity) in patients with HFrEF. They found that, compared to normal controls, subjects with HFrEF had a decreased ability to augment their IVPDs during exercise, suggesting a diminished ability to generate ventricular suction. This inability to increase IVPDs correlated well with peak VO_2 . Yotti *et al.* [101] studied the response to stress in cardiomyopathy patients using a different technique. They estimated diastolic IVPDs in patients with dilated cardiomyopathy and healthy controls at baseline and during dobutamine infusions using CMM echocardiography. They found that, while dobutamine increased diastolic IVPDs by 44% in healthy controls, IVPDs showed only a 23% increase in patients with HF, indicating a decreased capacity to recruit a larger suction force with stress. In contrast to the observation in the study by Rovner *et al.* [135], they also found baseline IVPGs to be lower in the HF group. Ohara *et al.* [179], who studied IVPDs in patients undergoing dobutamine-stress echocardiography, reported a similar finding. They demonstrated that subjects with diastolic dysfunction had a decreased ability to augment their IVPDs in response to dobutamine.

As noted by Gillebert and De Buyzere [158], an insufficient adrenergic augmentation of diastolic IVPDs may play a role in exercise intolerance in patients with HFpEF, although further studies are needed to test this hypothesis. It is worth noting that, while IVPD augmentation during exercise and adrenergic stimulation may be informative to characterise subjects with

HFpEF, the inability to demonstrate variations in IVPDs at baseline has generated an interest in other parameters, such as V_s , which is a combination of the V_p parameter and the length of the inflection point where V_p abruptly decelerates [59], [180].

Iwano *et al.* [181] showed that the reduction in IVPDs in patients with HFrEF or HFpEF was driven by a reduced gradient in the apical region, while the basal IVPD was preserved, presumably by an increase in LA pressure. A previous study [10] compared MRI-derived IVPDs among 23 subjects without HF, 13 subjects with HFrEF and 14 subjects with HFpEF. HFpEF was associated with greater amplitude of the reversal of the base-to-apex IVPD during early filling compared to controls and patients with HFrEF. These data may indicate that HFrEF and HFpEF are associated with distinct patterns of IVPD abnormalities during early diastolic filling, supporting fundamental differences in the nature of diastolic dysfunction in these two conditions. These studies, however, are limited by the small sample sizes. Further studies are required to better elucidate the distinction in IVPDs/IVPGs between patients without HF, patients with HFrEF and patients with HFpEF, and the mechanisms behind these differences.

4.1.4 Conclusions

IVPGs provide important insights about ventricular physiology. Overall, methodologies to estimate IVPGs has been underutilised, which may be due to the theoretical complexity of the derivation of IVPGs. A wider availability of automated analysis tools will facilitate the increased use and investigation of IVPGs in HF. Similarly, the continued improvement in MRI pulse sequences and hardware to characterise intraventricular flow fields with great detail using novel techniques (such as 4D flow MRI), may provide additional precision and insights regarding the non-invasive assessment of IVPGs. It remains to be determined whether the assessment of ventricular function by IVPG measurements provides incremental clinically useful information to standard non-invasive assessments. Nevertheless, the assessment of IVPGs represents an informative clinical research tool.

4.2 ASSESSMENT OF METHODOLOGIES TO CALCULATE INTRAVENTRICULAR PRESSURE DIFFERENCES IN COMPUTATIONAL MODELS AND PATIENTS

4.2.1 Introduction

Section 4.1 introduced basic concepts and the rationale for the estimation of IVPGs/IVPDs, including their impact in cardiovascular function, related physiological determinants and fluid dynamic principles, and relevant non-invasive assessment methods. Particularly, MRI and ultrasound based methods were identified as common approaches to estimate IVPGs/IVPDs.

However, it remains unclear how MRI and ultrasound-derived IVPDs compare *in vivo*, as simultaneous assessments are technically impossible and validation studies require the use of invasive procedures, which are difficult in the MRI suite [99]. Furthermore, the impact of including multidimensional velocity information on the computation of IVPDs is undefined. Computational modelling has been used previously to simulate cardiac flow of the heart and the aorta [57], [182]–[186] but has not been used for analysing the accuracy of IVPD determination, which is becoming more relevant in clinical research to complement the understanding, the analysis, and the diagnosis of diastolic dysfunction noninvasively [60], [95], [101], [158].

Therefore, the primary aims of this study are (1) to compare IVPDs deduced from synthetic CMM and 1D and 2D phase contrast MRI data from a CFD model of a relaxing and filling LV, and (2) to assess the feasibility of these methods in a small cohort of patients with HFpEF, who are known to have underlying diastolic dysfunction.

4.2.2 Methods

Previously established, fluid dynamic theory is resumed to describe the IVPD calculations. Thereafter, the CFD model is described together with how the simulated velocity data was processed. Finally, the clinical component of the study is introduced.

Calculating IVPDs from 1D velocity information

From equation (4.5), the non-invasive estimation of the 1D IVPD is obtained as:

$$IVPD_{1D} = \int_{base}^{apex} \frac{\partial P}{\partial s} ds \quad (4.7)$$

$$IVPD_{1D} = \rho \int_{S_{base}}^{S_{apex}} \frac{\partial v}{\partial t} ds + \frac{1}{2} \rho (v^2_{apex} - v^2_{base}) \quad (4.8)$$

Calculating IVPDs from 2D velocity information

To evaluate equation (4.6) for a given path of integration, the selected path is broken up into linear segments, each of which has a vector length defined by $dx \rightarrow \Delta x_i$ and $dy \rightarrow \Delta y_i$, and the total pressure drop, across all segments, is calculated as the sum using [58]:

$$IVPD_{2D} = \sum_i \left[\left(\frac{\partial P}{\partial x} \right)_i \Delta x_i + \left(\frac{\partial P}{\partial y} \right)_i \Delta y_i \right] \quad (4.9)$$

In figure 4.3, a detailed graphical description of the method is presented.

4.2.2.1 Computational fluid dynamics model of the left ventricle

The LV was modeled as a prolate spheroid [62] with a fixed mitral inlet and aortic outlet, contracting and expanding at a heart rate of $60bpm$ with an EF of 60% (figure 4.4, table 4.1). The computational mesh contained 180,000 tetrahedral cells, and the 3D Navier-Stokes equations were solved using ANSYS[®] Fluent[®]. During this CFD simulation, the mesh was adapted mathematically [62] according to a volumetric boundary condition, with the intraventricular blood volume varying between $170ml$ at end-diastole and $69ml$ at end-systole. The systolic and diastolic periods were clearly defined by mitral and aortic flows: the mitral inflow presented a specific pattern with two characteristic peaks during diastole (E- and A-waves), and the aortic outflow showed a unique peak during systole (see figure 4.4). The blood was modeled as an incompressible Newtonian fluid with a viscosity of $3.5mPa \cdot s$ and a density of $1060kg/m^3$.

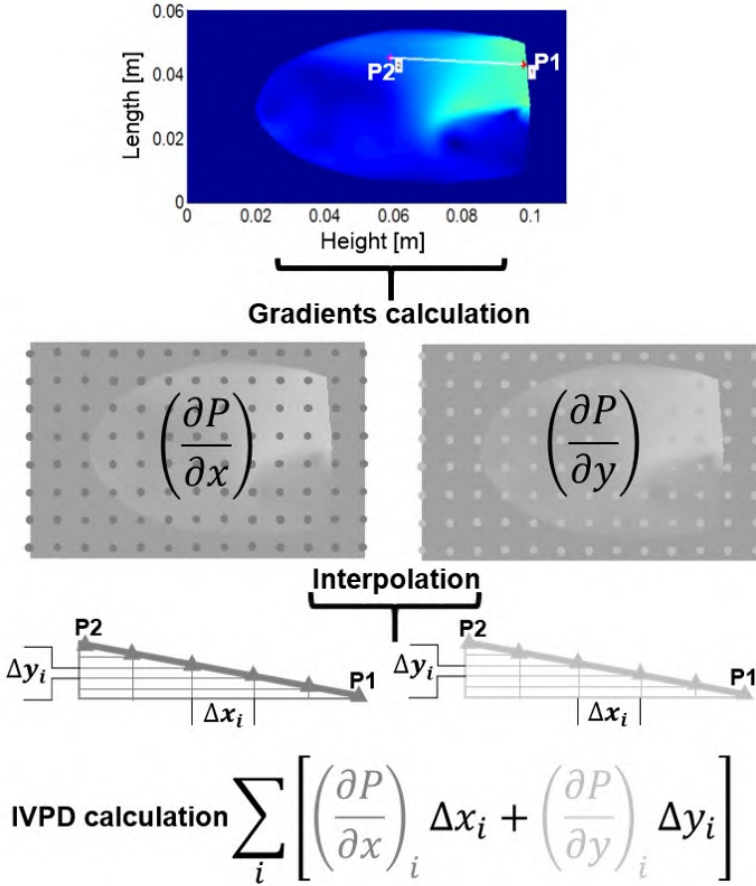


Figure 4.3: Graphical description of the implemented method for calculating IVPDs from 2D data. Top) Reference points (P1–P2) were selected by the user inside the CFD model. The calculation of the pressure gradients was performed for all the points inside each frame. Middle) Through interpolation, values of the line determined by the reference points were obtained, together with Δx and Δy . Bottom) The equation (4.9) is applied to calculate the IVPD curves. Figure adapted from [2].

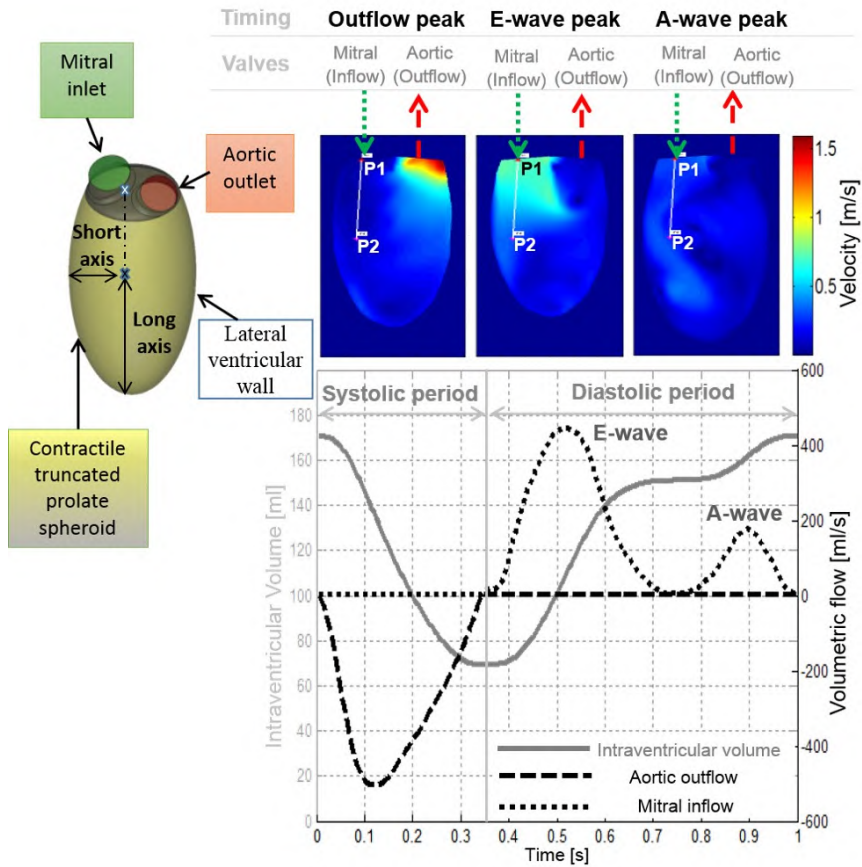


Figure 4.4: CFD model. On the top left of the figure, the structure of the model is shown, indicating its general geometrical parameters and the location of the valves. On the right, the model is shown during systole, early filling (E wave), and late filling (A wave). The bottom panel demonstrates changes in volume (gray solid line), mitral flow velocity (dotted line), and aortic flow velocity (dashed line). Figure adapted from [2].

A dedicated graphical user interface was developed in MATLAB® (The MathWorks, Natick, Massachusetts) for processing the model data. Once the velocity and the pressure information was displayed at frame 1 (i.e., end-diastole, figure 4.5), two points were placed inside the model: P₁ at the LV base and P₂ at a distance of $\sim 4\text{cm}$ near to the LV apex, making sure it was always inside the LV boundary during the complete cycle. The pressure difference between these points was calculated, applying the previously described approaches. The pressure curve $IVPD_{CFD}$ was calculated directly from the CFD model data as the pressure difference between points P₁ and P₂ and used as a reference (figure 4.5). To assess the impact of the virtual scan line definition, IVPDs were calculated using three different placements of P₁ and P₂, with two of them deliberately deviated from the main direction of flow. In figure 4.5, all three configurations are shown: line A represents a well aligned scan line while lines B and C represent a small and an extreme deviation from the main flow direction, respectively.

Table 4.1: CFD model haemodynamic parameters.

| Parameter | Value |
|--|-------|
| Mitral valve short axis [<i>cm</i>] | 1.1 |
| Mitral valve long axis [<i>cm</i>] | 1.7 |
| Mitral valve area [<i>cm</i> ²] | 5.9 |
| Aortic valve diameter [<i>cm</i>] | 2.3 |
| Aortic valve area [<i>cm</i> ²] | 4.2 |
| Signal period [s] | 1 |
| Systolic period [s] | 0.345 |
| Temporal resolution [<i>ms</i>] | 5 |
| HR [bpm] | 60 |
| EF (%) | 60 |
| Maximum volume [<i>ml</i>] | 170.6 |
| Minimum volume [<i>ml</i>] | 69.09 |
| Outflow peak [<i>cm/s</i>] | 120 |
| E-wave inflow peak [<i>cm/s</i>] | 75.31 |
| A-wave inflow peak [<i>cm/s</i>] | 30.07 |

4.2.2.2 IVPD curve characterisation

The diastolic period of the IVPD waveforms, both *in silico* (figure 4.5) and *in vivo* (figure 4.6, bottom), is typically characterised by (i) a large forward positive peak associated with the early filling wave, (ii) a negative peak associated with the deceleration of the early filling, and (iii) a second positive peak associated with the late filling wave due to atrial systole. To facilitate the identification of these three pressure peaks, we defined them as (i) E-wave, (ii)

reversal, and (iii) A-wave peaks, and they were established as the parameters to be extracted and compared for each applied method.

One-dimensional IVPD calculation

The CFD velocity information was projected along a scan line prescribed manually and corresponding with the inflow streamline, between P1 and P2. By this way, the velocity component in the direction of the beam was computed. Thereafter, this information was used as an input to calculate IVPDs using two different approaches:

- $IVPD_{1DMRI}$ determination: equation (4.4) was solved with this velocity information to obtain the pressure difference between P1 and P2 ($IVPD_{1DMRI}$).
- $IVPD_{CMM}$ determination: to mimic the velocity estimate as would be obtained from ultrasound, data were colour-coded and a synthetic pseudo-ultrasound CMM (figure 4.5) image was generated. Using a MATLAB[®] application [59], [60], a pressure difference curve ($IVPD_{CMM}$) was calculated from this pseudo-CMM image. Limits of colour coding for this pseudo-image were chosen to represent the range between maximum and minimum velocities in the CFD field.

Two-dimensional IVPD calculation (pseudo 2D phase-contrast imaging)

To mimic IVPD based on 2D phase-contrast MRI imaging, both the x and y velocity components were used to obtain temporal and spatial gradients in order to calculate the pressure gradient fields. Then, interpolated values along the line delimited by P1 and P2 were used to solve equation (4.9), applying the direct integration method previously described (see figure 4.3).

To study the impact of the lower temporal resolution (as is the case in MRI phase-contrast imaging), data were downsampled to 70 frames for one cardiac cycle, going from a time step of 5 to 14.3ms for the CFD model to compare computed IVPDs with the ground truth.

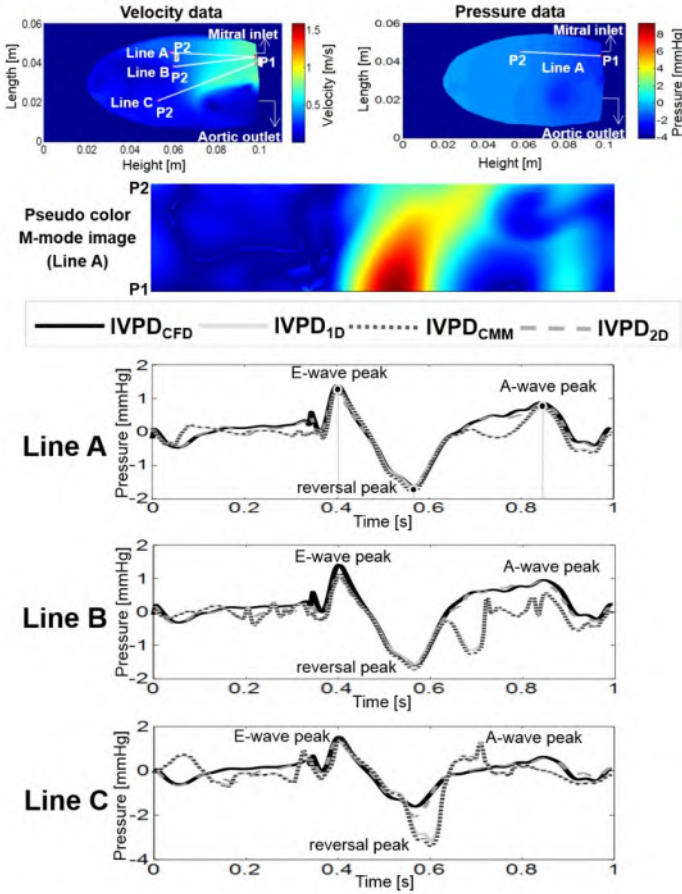


Figure 4.5: General description of the CFD model display and processing interface to illustrate the strategy implemented and the general results. On the top of the figure, the model is displayed in two different plots, showing velocity and pressure data. The figure shows the early mitral inflow or E-wave in frame 108 (0.54s) out of 200. Two points are placed by the user (P1 at the LV base and P2 towards the LV apex) to define a reference line for producing a pseudo-colour M-mode image to show velocity information between those two locations over time. This image becomes the input for the $IVPD_{1D}$ and $IVPD_{CMM}$ calculation using 1D velocity information to determine pressure differences between P1 and P2 during a complete cardiac cycle. At the bottom of the figure, pressure curves derived from the CFD model for different reference point (P1–P2) placements are shown to demonstrate the impact of these alterations on the outcome for all applied methodologies: $IVPD_{CFD}$ (black solid line) curve was extracted directly from the model pressure data and used as reference; $IVPD_{1D}$ (solid light gray line), $IVPD_{CMM}$ (dashed gray line), and $IVPD_{2D}$ (dotted dark gray line). Black circle marks in curves obtained from a properly aligned scan line (line A) are connected through gray vertical lines to the time axis to indicate the timing of extracted parameters presented in table 4.2. Figure adapted from [2].

4.2.2.3 *In vivo application: MRI- and ultrasound-based IVPD calculation and comparison*

Sample population

We studied a clinical sample of patients with HFpEF, recruited at the Corporal Michael J. Crescenz Veterans Affairs (VA) Medical Center.

We included adult patients with HFpEF who met the following criteria: (1) symptomatic HF with current New York Heart Association (NYHA) class II–IV symptoms; (2) LV ejection fraction (LVEF) $> 50\%$; (3) at least one of the following within 1 year prior to consent: hospitalization for decompensated HF, acute treatment for HF with intravenous diuretics or haemofiltration, chronic treatment with a loop diuretic for control of HF symptoms, or chronic diastolic dysfunction evidenced by LA enlargement (LA volume $> 34\text{ml}/\text{m}^2$) or Doppler signs of increased LA pressure as defined by the American Society of Echocardiography [85]; and (4) stable medical therapy. Key exclusion criteria were as follows: (1) clinically significant valve disease (more than mild aortic or mitral stenosis or more than moderate aortic or mitral regurgitation); (2) atrial fibrillation or flutter; (3) significant ischemia seen on stress testing within the past year that was not revascularized; (4) other clinically important causes of dyspnea such as lung disease; (5) hypertrophic, infiltrative, or inflammatory cardiomyopathy; (6) pericardial disease; (7) primary pulmonary arteriopathy; and (8) severe renal dysfunction (estimated glomerular filtration rate $< 30\text{ml}/\text{min}/1.73\text{m}^2$) or liver disease. We included patients who had phase-contrast MRI measurements and CMM measurements within 1 week. Informed consent was obtained from all subjects, and the study was approved by the Corporal Michael J. Crescenz VA Medical Center Institutional Review Board.

Cardiac MRI

We measured intraventricular flow using in-plane phase-contrast MRI from a 1.5T Magnetom Avanto or Espree system (Siemens Medical Solutions). A phase-contrast gradient echo pulse sequence with in-plane velocity encoding was applied using retrospective gating, in a plane corresponding to the three-chamber view ("LV outflow tract view") in which both the mitral inflow and the LV outflow are well visualised. Maximal velocity encoding was usually set at $150\text{cm}/\text{s}$ but adjusted during the examination to avoid aliased velocity measurements. Other typical acquisition parameters included the following: a slice thickness of 5.5mm , a repetition time of 35.15ms , and a flip angle of

10° . View sharing was used, and 70 frames were acquired per cardiac cycle. We performed two consecutive acquisitions, each with in-plane velocity encoding in one direction. Both acquisitions were merged off-line to obtain the in-plane 2D velocity maps.

A MATLAB[®] application was created to open and process phase-contrast MRI data (figure 4.6, left). After the images were loaded and displayed, two points were placed inside the image: one at the mitral annulus (P1) and another one at the LV apex (P2). Two methods were used to calculate the IVPD:

1. A first approach based on the calculation of a total velocity from both velocity components to project it onto the reference line delimited by P1 and P2, through a complete cardiac cycle (figure 4.6, middle left). This velocity information was then used to solve equation (4.4) and obtain the total pressure difference between P1 and P2 ($IVPD_{1DMRI}$; figure 4.6, bottom left, black solid line). A colour-coded image, analogous to an ultrasound CMM, was also produced and displayed in the software interface but was not used directly in the computation of IVPDs.
2. The second method used the 2D velocity information available to perform a direct integration for a linear segment delimited by P1 and P2, calculating the pressure gradients to solve equation (4.9) ($IVPD_{2DMRI}$; figure 4.6, bottom left, gray dashed line).

Doppler echocardiography

Doppler transthoracic echocardiography was performed at rest with the patient in supine position using a Vivid E9 device (GE Healthcare, Horten, Norway), equipped with a cardiac probe. A CMM image was acquired, prescribing a scan line that coincides with the main diastolic intraventricular flow stream as previously described [85].

We used an automated data analysis algorithm, developed in MATLAB[®] and described in detail in previous publications [59], [60], to process the CMM data (figure 4.6, right). From the original CMM images, the velocity colour-scale region and a single beat region of interest (ROI) were selected (figure 4.6, top right), and then the E-wave, A-wave, and the vertical position of the mitral plane were located for orientation of the algorithm. The grayscale values from the CMM image background were removed, thus leaving only the velocity colour-scale image to which a de-aliasing technique was applied

to create a point-by-point velocity reconstruction of the ROI (figure 4.6, middle right). Finally, the IVPD was calculated (figure 4.6, bottom right), allowing the extraction of parameters to be compared with cardiac MRI post-processing results. The following parameters were considered: E-wave, reversal, and A-wave peak pressures.

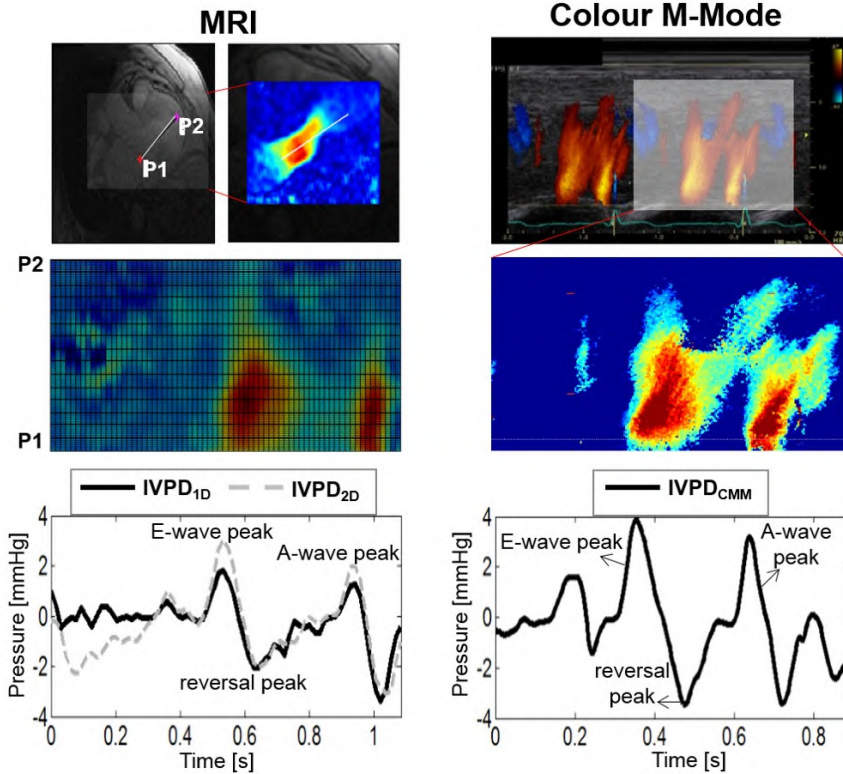


Figure 4.6: Cardiac MRI (left) and CMM (right) based methods to estimate IVPDs. Top) a ROI selection by the user inside an original recording example (from the same patient). Middle) processing results used to calculate and extract all parameters. Bottom) IVPD derived from the application of imaging velocity data to solve equation (4.2); left) solid black line: $IVPD_{1D}$; gray dashed line: $IVPD_{2D}$, right) solid black line: $IVPD_{CMM}$. Figure adapted from [2].

4.2.2.4 Statistical analysis

Continuous variables are described as mean \pm standard deviation. To assess the performance of the methods for determining IVPDs, the root of the mean square error (RMSE) was used as the estimator of the difference

between the IVPD curve obtained directly from the CFD model pressure data ($IVPD_{CFD}$) and IVPD curves calculated from the CFD velocity data with the described approaches ($IVPD_{1DMRI}$, $IVPD_{2DMRI}$, and $IVPD_{CMM}$). For the *in vivo* application, selected parameters (E-wave, reversal, and A-wave pressure peaks) were calculated from cardiac MRI and ultrasound imaging and compared with each other. Scatter plots were constructed, and correlation (Pearson and Spearman) coefficients were computed. Regression analysis and Bland-Altman plots were also used to compare results among the various applied methods. Significance level (α) was set at 0.05.

4.2.3 Results

4.2.3.1 CFD model processing results

The pressure curve from the model ($IVPD_{CFD}$) is shown in figure 4.5 (black line), and selected parameters are summarized in table 4.2. The E-wave peak, coinciding with the absolute maximum IVPD (1.392mmHg), is followed by the reversal of the IVPD, which was the absolute minimum (-1.618mmHg), and the A-wave peak (0.8847mmHg).

The impact of the scan line alignment on the calculated pressure curves is shown in figure 4.5 and table 4.3, using the $IVPD_{CFD}$ curve as a reference. The most accurate results were obtained for scan line A and the $IVPD_{2DMRI}$ method (2D RSME = 0.0798mmHg), while $IVPD_{1DMRI}$ and $IVPD_{CMM}$ delivered inferior results (1D RSME = 0.2550mmHg ; CMM = 0.2633mmHg). A moderate misalignment of the scan line (line B) increased the error for all techniques although $IVPD_{2DMRI}$ demonstrated the best performance (1D RMSE = 0.5016mmHg ; 2D RMSE = 0.1444mmHg , CMM = 0.5215mmHg). The same was true for an extreme misalignment (line C; 1D RMSE = 0.6222mmHg ; 2D RMSE = 0.1782mmHg ; CMM = 0.6853mmHg).

All approaches underestimated the E-wave and the A-wave peak values, whereas reversal peak pressure was overestimated when compared with $IVPD_{CFD}$ peak values (table 4.2). In general, $IVPD_{CMM}$ peaks presented, in almost all cases, the highest values (in magnitude).

To assess the impact of temporal resolution, a scan line with a good correspondence with the inflow streamline was imposed (figure 4.5, line A). There were small effects of reducing the frame rate with slightly lower peak pressures in undersampled data (table 4.2).

4.2.3.2 *In vivo* processing results: calculation of pressure curves from a HFpEF population

In figure 4.7 and figure 4.8, the Bland-Altman and scatter plots contrasting selected parameters (E-wave, reversal, and A-wave peaks) obtained from all three approaches are shown. Figure 4.7 refers to the comparison between MRI-derived methods ($IVPD_{1DMRI}$ vs. $IVPD_{2DMRI}$) while figure 4.8 compares both MRI methods against the CMM approach [$IVPD_{CMM}$ vs. $IVPD_{1DMRI}$ (black circles) and $IVPD_{CMM}$ vs. $IVPD_{2DMRI}$ (gray triangles)].

The lowest and the highest parameter average values were obtained from the $IVPD_{1DMRI}$ (E-wave $1.368 \pm 0.695\text{mmHg}$, reversal $-1.262 \pm 0.812\text{mmHg}$, and A-wave $1.130 \pm 0.475\text{mmHg}$) and the $IVPD_{CMM}$ (E-wave $3.041 \pm 1.197\text{mmHg}$, reversal $-2.541 \pm 1.507\text{mmHg}$, and A-wave $2.287 \pm 0.926\text{mmHg}$) curves, respectively (table 4.4). There was a high correlation between $IVPD_{1DMRI}$ and $IVPD_{2DMRI}$ parameters (figure 4.7; Pearson R for E-wave = 0.88, reversal = 0.94, and A-wave = 0.77). $IVPD_{CMM}$ parameters showed acceptable correlations with 1D MRI data (figure 4.8; Pearson R for E-wave = 0.78 and reversal = 0.79), except for the A-wave peak pressure (Pearson R = 0.17). The correlation between CMM data and 2D data was lower, even if it was similar for all three peaks (figure 4.8; Pearson R for E-wave = 0.55, reversal = 0.68, and A-wave = 0.47).

Table 4.2: Extracted parameters from pressure curves obtained using the CFD model and its downsampled version to assess the impact of reduced temporal resolution. A properly aligned scan line was imposed for this analysis (see line A in figure 4.5).

| Temporal resolution | Parameter | | | | | |
|---------------------|-----------------------------|-------------|-------------------------------|-------------|-----------------------------|-------------|
| | E-wave peak pressure [mmHg] | | Reversal peak pressure [mmHg] | | A-wave peak pressure [mmHg] | |
| | Original | Downsampled | Original | Downsampled | Original | Downsampled |
| $IVPD_{CFD}$ | 1.392 | | -1.618 | | 0.8847 | |
| $IVPD_{1D}$ | 1.236 | 1.204 | -1.626 | -1.675 | 0.7014 | 0.7181 |
| $IVPD_{2D}$ | 1.221 | 1.219 | -1.644 | -1.702 | 0.8304 | 0.8849 |
| $IVPD_{CMM}$ | 1.36 | 1.249 | -1.791 | -1.742 | 0.7729 | 0.7472 |

Table 4.3: Root mean square error (RMSE) quantifying the difference between the reference IVPD directly obtained from the CFD model and the IVPD curves retrieved by applying three methods using three different scan line positions [illustrated in figure 4.5, from the well-aligned line (line A) to the erroneously aligned line (line C)]. Additionally, the range of maximal positive and negative differences (Δ range) is included to complement the analysis.

| RMSE model [mmHg] | Line A | | Line B | | Line C | |
|-------------------|--------|-------------------|--------|-------------------|--------|-------------------|
| | Value | Δ range | Value | Δ range | Value | Δ range |
| $IVPD_{1D}$ | 0.2550 | [-0.6429, 0.4979] | 0.5016 | [-1.7336, 0.2647] | 0.6222 | [-2.2093, 1.2858] |
| $IVPD_{2D}$ | 0.0798 | [-0.2300, 0.3194] | 0.1444 | [-0.3772, 0.2446] | 0.1782 | [-0.6104, 0.2615] |
| $IVPD_{CMM}$ | 0.2633 | [-0.6629, 0.5215] | 0.5215 | [-1.8525, 0.2692] | 0.6853 | [-2.4533, 1.3529] |

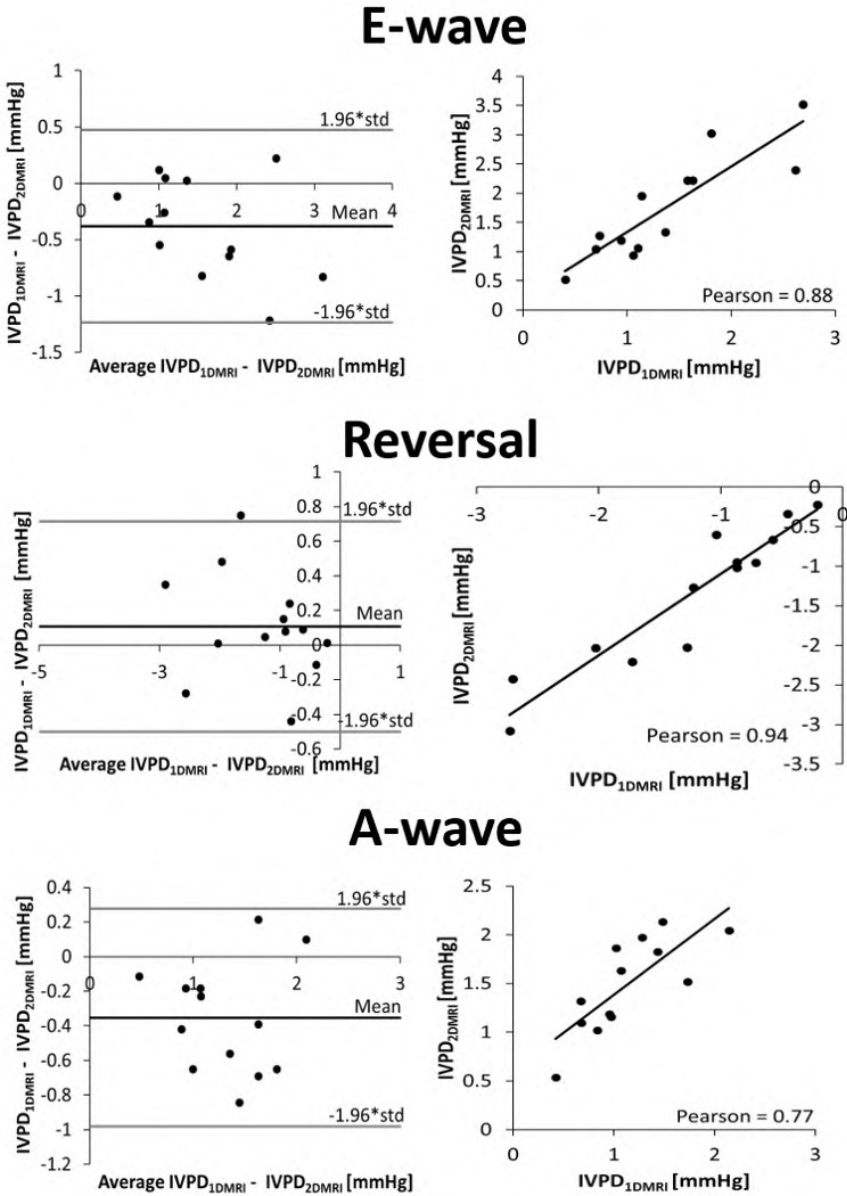


Figure 4.7: Bland-Altman plots and scatter plots comparing the impact of using 1D and 2D MRI-based estimates on the calculation of IVPD parameters. Figure adapted from [2].

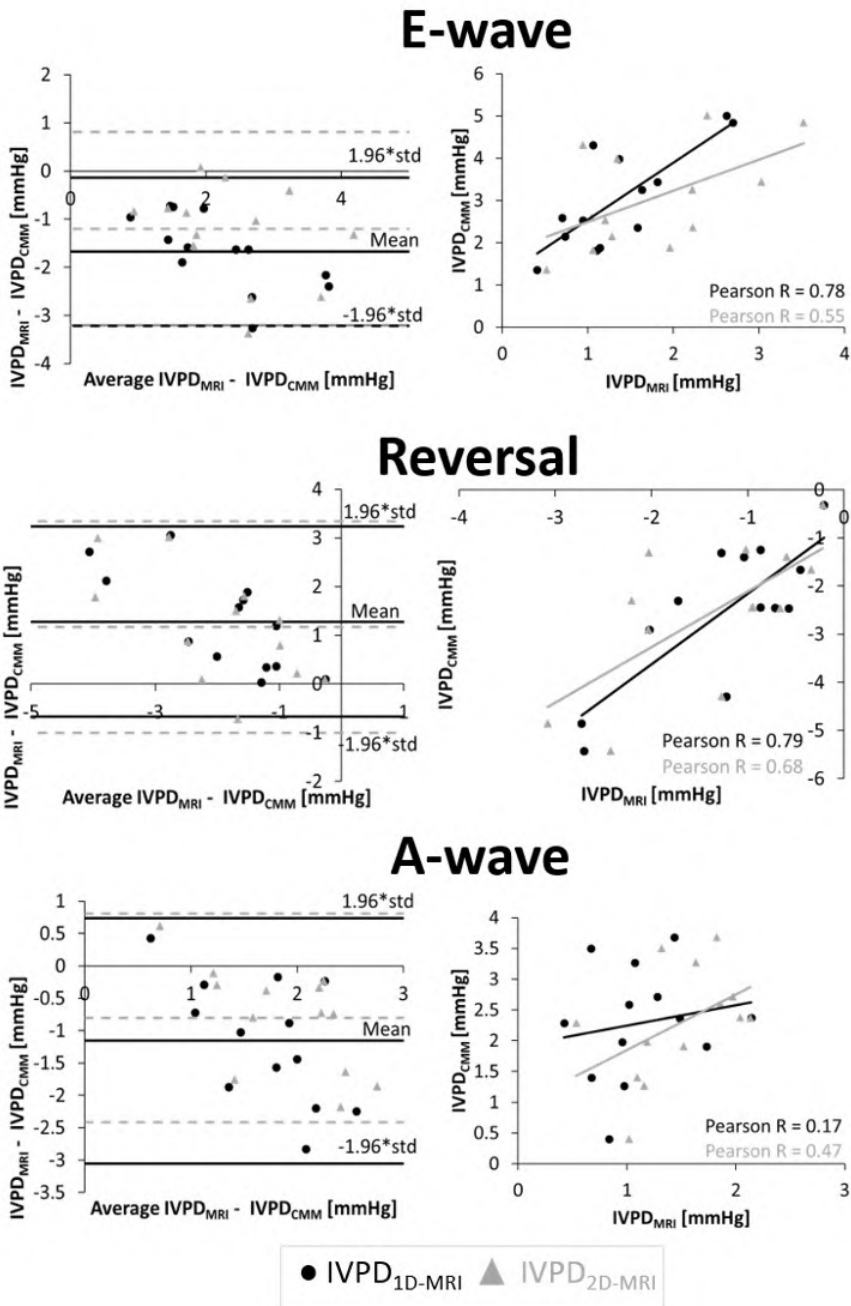


Figure 4.8: Bland-Altman plots and scatter plots comparing the impact of using MRI-based estimates against CMM flow velocity information in the calculation of IVPD parameters [$IVPD_{CMM}$ vs. $IVPD_{1DMRI}$ (black circles), and $IVPD_{CMM}$ vs. $IVPD_{2DMRI}$ (gray triangles)]. Figure adapted from [2].

Table 4.4: Parameters extracted from IVPD curves in a HFpEF patient population.

| | Parameter | | |
|--------------|-----------------------------|-------------------------------|-----------------------------|
| | E-wave peak pressure [mmHg] | Reversal peak pressure [mmHg] | A-wave peak pressure [mmHg] |
| $IVPD_{1D}$ | 1.368 ± 0.695 | -1.262 ± 0.812 | 1.130 ± 0.475 |
| $IVPD_{2D}$ | 1.747 ± 0.890 | -1.369 ± 0.892 | 1.484 ± 0.478 |
| $IVPD_{CMM}$ | 3.041 ± 1.197 | -2.541 ± 1.507 | 2.287 ± 0.926 |

Values are presented as $mean \pm Std(n = 13)$.

4.2.4 Discussion

4.2.4.1 CFD model data

The CFD model data, generated using a 3D LV model and based on the full Navier-Stokes equations, indicate that IVPDs can be fairly well estimated, making use of the Euler equations. As anticipated, the best results were obtained when using the 2D velocity information in the computations (i.e., equation (4.9)), with the estimated pressure gradient fairly predicted throughout the complete cardiac cycle, irrespective of the accurate alignment with the flow (figure 4.5). The 1D methods perform reasonably well for the properly aligned scan line and capture the peak values (E- and A-waves and flow reversal) well.

In clinical practice, most IVPD data have been collected using CMM imaging. The ultrasound-based method has successfully been validated against invasive data [98], [101], and it was shown that scan line misalignments up to 20° result only in small variations in IVPDs ($< 0.26mmHg$) [57]. To emphasize, the presence of vortices, which are formed at the leaflet tips, grows throughout diastole, explaining why results in early diastole tend to be somewhat better than in atrial filling [57].

Additional research on the impact of scan line misalignment indicated that an angle misalignment of $\pm 35^\circ$ (in any spatial direction) was associated with an error of -0.2 to $-0.6mmHg$ (95% confidence limits of agreement), whereas a $\pm 0.5cm$ coaxial displacement from the centerline (representing a 50% uncertainty of the LVOT diameter size) induced an error of 0.3 to $-0.7mmHg$ [134]. However, misalignment errors related to the 1D simplification could be higher in ventricles with geometrical variations such as localized septal hypertrophy [101], [134].

In our CFD model study, we generated synthetic CMM images directly from the CFD data, meaning that we simply colour-coded the velocity component in the scan line direction. As such, data are free of any measuring noise and do not account for any operator-dependent ultrasound settings on the machine. These synthetic images were then further processed using dedicated software developed by Stewart *et al.* [59]. Misalignment deteriorated

the result of the 1D CMM method, although for the tested cases, the estimate of the early filling peak pressure gradient remained acceptable (which was not the case for the flow reversal and A-wave). We speculate that the fact that the 1D method deteriorated most in mid- and late diastole is because of the complexity of the flow field during that phase, with complex multidimensional vortex flow.

The 1D limitation, inherent to the CMM technique, can be overcome when multidimensional flow velocities are available, as is the case for echo PIV [187], [188] and MRI [58]. In the CFD study, we extracted 2D flow velocities in an assumed imaging plane and processed the data in two ways: (i) a 1D approach which is basically an MRI equivalent of a CMM and (ii) direct integration which makes use of the 2D velocity information. The 1D method ($IVPD_{1DMRI}$) yielded virtually identical results as the CMM (due to the way the CMM image was generated). The 2D MRI method ($IVPD_{2DMRI}$) provided the most consistent data, even for the most extreme misalignment case (although it is advisable to define the scan line as much as possible aligned with the flow).

Other important factors affecting the computation of IVPDs are the temporal, spatial, and velocity resolutions of the imaging techniques as they determine the accuracy of the partial derivative terms in the Euler equation [57]. Rojo-Alvarez *et al.* [189] assessed the influence of temporal, spatial, and velocity resolutions of the ultrasound scanner, on cardiovascular parameters derived from velocity images, and found that, for the ideal image model they used, temporal resolution turned out to be the most critical parameter for the accuracy of the results. The impact of temporal resolution on calculated pressure differences derived from MRI has also been addressed to identify minimum requirements to capture components of motion of blood velocities and accelerations in the heart, reducing temporal resolution data sets from higher temporal resolution experiments [58].

In our CFD study, reducing the temporal resolution from 200 to 70Hz had albeit little impact and changed the values of the three most relevant peaks by not more than 8%.

We can thus conclude from the CFD model data that the 2D direct integration method provides the most accurate IVPDs (in the tested settings) but the accuracy of the 1D methods, particularly to estimate the early filling peak pressure difference, is still acceptable for reasonably aligned scan lines.

4.2.4.2 *In vivo* data

The main purpose of the *in vivo* analysis was to (i) demonstrate the feasibility of the MRI-based methods in a HFpEF patient population and (ii) relate the *in vivo* findings to the theoretical CFD results. As illustrated in figure 4.6 for a representative case, derived IVPDs from both modalities showed similar patterns with distinct peaks typical of the diastolic period and associated with the early and late filling waves (E-wave, reversal, and A-wave pressure peaks).

Comparing first the 1D and 2D MRI-based methods (figure 4.7), we found the 1D method to underestimate the magnitude of both the positive wave and negative peaks (though by less than 0.4mmHg on average), with correlation coefficients between 0.7 and 0.9. While differences were smaller for the synthetic CFD model data, these results are in line with the model findings. As these methods are based on the same measured MRI velocities, these data demonstrate the impact of reducing the available velocity information.

The main rationale for calculating $IVPD_{1DMRI}$ from the MRI data was to have a direct equivalent for comparison against $IVPD_{CMM}$ data and to have an intermediate point of comparison for the CMM and MRI-based approaches. As can be observed from figure 4.8, the magnitude of all $IVPD_{CMM}$ peaks is substantially higher than that for $IVPD_{1DMRI}$, with mean differences in the order of 1 to 1.5mmHg . While correlation coefficients are relatively high for the E-wave and the deceleration peaks (close to 0.8), there is virtually no correlation for the A-wave magnitude.

When incorporating the 2D velocity information in the IVPD estimate and comparing $IVPD_{2DMRI}$ with $IVPD_{CMM}$, the correlation deteriorates for the E-wave and flow reversal pressure difference. This is not unexpected, as we are now comparing a 1D technique with a 2D technique. Again, pressure gradients are substantially higher (about 1mmHg on average) when derived from CMM images. Several factors may contribute to this difference. First, it is impossible to have identical integration paths (points P1 and P2) in ultrasound and MRI. In MRI, the integration path is based on a 2D image that is processed off-line; with ultrasound, the integration path is defined by the operator aligning the ultrasound beam from the apex to the base. Also, the integration path is not necessarily the same due to the difference in the access window for example, being longer with ultrasound in our study (MRI = $5.10 \pm 1.02\text{cm}$, CMM = $7.57 \pm 0.62\text{cm}$). This would lead to larger instantaneous pressure differences. Second, there are intrinsic differences in the physical principles underlying the velocity estimation by the MRI and ultrasound imaging techniques. Third, different software is used to process the data. Fourth, images are not acquired simultaneously (within a time frame of a week) and with the patient in (slightly) different positions.

It is clear from the above that straightforward and direct comparison of the different methods is extremely hard in an *in vivo* setting, which was the main rationale for setting up the CFD model simulations. Taken together, our data indicate that (i) IVPDs based on 2D velocity information (as acquired by MRI) are more accurate than IVPDs derived from 1D methods and (ii) the correlation between IVPDs estimated from CMM and MRI-based methods is relatively poor.

In this study, we mainly focused on technical aspects related to the computation of IVPDs from flow velocity data acquired from colour Doppler ultrasound or 2D phase-contrast MRI and demonstrated (via the computer model study) that the accuracy of the calculation is significantly enhanced when accounting for the multidirectionality of the flow velocity vectors. This is particularly true for the pressure difference in mid- to late diastole, when diastolic vortex formation generates complex intraventricular flow patterns in an enlarged cavity. From a clinical perspective, most diagnostic information is probably to be gained from the peaks related to the early filling wave, where the ability of the ventricle to forcefully relax, “suck in” the blood, and generate large IVPDs links to the active relaxation properties of the myocardium. Nonetheless, larger studies would be needed to make stronger statements on the clinical utility of pressure-related parameters that can be derived from velocity data. Such studies should ideally be based on 2D (or 3D) MRI flow velocity data to allow assessing the added value of analysing pressure differences in mid- to late diastole.

4.2.5 Limitations of the study

Our study has some intrinsic limitations. First, the CFD model is idealized in terms of anatomy and physiology and we did not study the performance of the methods over a wide range of LV sizes and EFs. Nonetheless, the model is representative for the patients studied, i.e., patients with preserved systolic function and EF (> 50%). We did run simulations in a model with an EF of 49%, with virtually identical conclusions regarding the comparison of the different methods (data not shown). Second, MRI and CMM images were obtained in different moments, in some cases within a week, and therefore, baseline conditions were certainly different, making a direct comparison of the results difficult.

4.2.6 Conclusions

In conclusion, our modelling data indicate that methods incorporating 2D velocity information, as can be acquired via phase-contrast MRI, provide more accurate estimates of IVPDs. At the same time, this study also pinpoints difficulties in validating these new measures against CMM-based data, the presumed gold standard method. More research is warranted, and *in vivo* validation of MRI-based methods is ideally based on invasive recordings of IVPDs.

4.3 NONINVASIVE INTRAVENTRICULAR PRESSURE DIFFERENCES
ESTIMATED WITH CARDIAC MRI IN SUBJECTS WITHOUT HEART
FAILURE AND WITH HEART FAILURE WITH REDUCED AND PRESERVED
EJECTION FRACTION

4.3.1 Introduction

Section 4.1 described two major HF subtypes, HFrEF and HFpEF, whose differences may impact clinical outcomes. Thus, characterisation of these subtypes is relevant to have a better understanding of the nature of physiologic abnormalities in HF patients, both for diastolic and systolic function.

Although echocardiography is the standard method for assessing diastolic function, it has intrinsic limitations. In contrast, cardiac MRI can measure 2D or 3D velocity vectors in a plane or volume, with more accurate and reproducible measurements [190]. Moreover, MRI is increasingly utilised for the evaluation of cardiac function [58], [101], [191] and represents an alternative to better assess the intraventricular flow and, through it, linked by mathematical expressions, the IVPDs, as results in section 4.2 suggest.

Therefore, the aim of this study is to demonstrate the feasibility of an MRI-based method to characterise IVPDs throughout diastole and systole.

4.3.2 Methods

We prospectively enrolled a sample of patients at the Corporal Michael J. Crescenz VA Medical Center. The protocol was approved by the Philadelphia VA Medical Center Institutional Review Board, and all subjects provided written informed consent.

HFrEF was defined as a symptomatic HF in the presence of a LVEF < 50%. HFpEF was defined as the presence of all of the following: 1) NYHA class II-IV symptoms consistent with HF; 2) LVEF > 50%; 3) mitral inflow early diastolic (E-wave) to annular tissue velocity (e') ratio > 14, [84] or at least 2 of the following: (a) an average mitral E/ e' ratio > 8; (b) treatment with a loop diuretic for control of HF symptoms; (c) LA volume index > $34\text{mL}/\text{m}^2$ of body surface area (BSA); (d) NT-pro B-type natriuretic peptide level > $200\text{pg}/\text{mL}$; (e) LV mass index > $149\text{g}/\text{m}^2$ in men and $122\text{g}/\text{m}^2$ in women (measured by cardiac MRI) [92]. No-HF subjects had an LVEF > 50%, no significant valvular disease, and no symptoms and signs consistent with HF [93].

Key exclusion criteria were: 1) claustrophobia; 2) presence of metallic objects or implanted medical devices in body; 3) more than mild aortic stenosis;

4) atrial fibrillation; 5) conditions that would make the study measurements less accurate or unreliable (i.e., arrhythmia affecting cardiac gating, inability to perform an adequate breath hold for cardiac MRI acquisitions); 6) known infiltrative or hypertrophic cardiomyopathy, or extracardiac amyloidosis or sarcoidosis [93].

4.3.2.1 Doppler echocardiography

Doppler transthoracic echocardiography was performed at rest with the patient in supine position using a Vivid E9 device (GE Healthcare, Horten, Norway), equipped with a cardiac probe.

4.3.2.2 2D Phase Contrast imaging acquisition and processing

Intraventricular flow velocities were measured with phase-contrast MRI, using a 1.5T MRI scanner (Avanto system, Siemens Healthcare, Erlangen, Germany). A phase contrast gradient echo pulse sequence with in-plane velocity encoding was applied using retrospective gating in a plane corresponding to the 3-chamber view (“LV outflow tract view”) in which both the mitral inflow and the LV outflow are well visualised. We performed two consecutive breath-held acquisitions, each with in-plane velocity encoding in 1 direction. Both acquisitions were merged off-line to obtain the in-plane 2D-velocity maps. Images were obtained with the following imaging parameters: TE = 2.7ms, TR = 4.8ms, temporal resolution = 39.8ms, bandwidth = 450Hz/pixel, field-of-view = 360x360mm², matrix = 152 – 192x256, spatial resolution = 1.88x1.88mm², slice thickness = 6mm, flip angle = 20°. Maximal velocity encoding was usually set at 130cm/s but adjusted during the examination to avoid aliased velocity measurements.

4.3.2.3 Image processing and computation of IVPDs

A MATLAB[®] (MathWorks, Natick, MA) custom-designed graphic user interface was programmed to process all phase-contrast MRI sequences. The pressure difference between two points in a plane (the scanning plane) can be calculated from the 2D planar velocity information as [58]:

$$IVPD = \sum_i \left[\left(\frac{\partial P}{\partial x} \right)_i \Delta x_i + \left(\frac{\partial P}{\partial y} \right)_i \Delta y_i \right] \quad (4.10)$$

with pressure derivatives linked through the Euler equation to the 2D-velocity information:

$$\frac{\partial P}{\partial x, y} = -\rho \left[\frac{\partial v_{x,y}}{\partial t} + v_x \frac{\partial v_{x,y}}{\partial x} + v_y \frac{\partial v_{x,y}}{\partial y} \right] \quad (4.11)$$

with v the 2D-component vector (v_x, v_y) of local blood velocity and ρ , blood density (1060 kg/m^3).

For the assessment of diastolic IVPDs, 2-4 reference points were placed inside the LV along the inflow direction at the mitral annulus (Point 1, P1) and the LV apex (Point 2, P2) (figure 4.9A and figure 4.9B). For the assessment of systolic IVPDs, 2-4 reference points were placed along the outflow direction, from the LV apex (P1) to the aortic annulus (P2) (figure 4.9E and figure 4.9F). To note, points were: 1) placed using the frame with the best anatomical view of the structures, and 2) stationary through the whole cardiac cycle. A pseudo-CMM image was calculated projecting velocity components within the path delimited by the reference points and displayed for processing visual guidance (figure 4.9C and figure 4.9G).

Available velocity components were used to calculate pressure gradient fields and differences. Then, interpolated values along the line delimited by P1 and P2 were used to solve equation (4.10), applying a direct integration method [58] to obtain the IVPD curves (figure 4.9D and figure 4.9H).

4.3.2.4 Statistical analysis

Descriptive data are presented as mean \pm standard deviation (SD) or mean (95% Confidence Interval, CI) for continuous variables or counts (%) for categorical variables. Differences between groups were determined by one-way ANOVA and adjusted for potential confounders (ANCOVA). Physiologic indices were expressed as absolute values as well as absolute differences between measurements (with 95% CIs). A P-value < 0.05 was considered statistically significant. We presented a model with unadjusted data, and three adjusted models: Model 1) adjusted for clinical data (age, sex, African American ethnicity, BMI, Coronary Artery Disease, eGFR and beta-blocker, ACE-Inhibitor/ARB, loop diuretic, and spironolactone use); Model 2) Model 1 additionally adjusted for echo parameters (mitral E-wave velocity, E-wave deceleration time, mitral annular e' septal); Model 3): Model 2 additionally adjusted for MRI data (LV mass index and EDVI). Statistical analyses were performed using MATLAB® statistics and machine learning toolbox

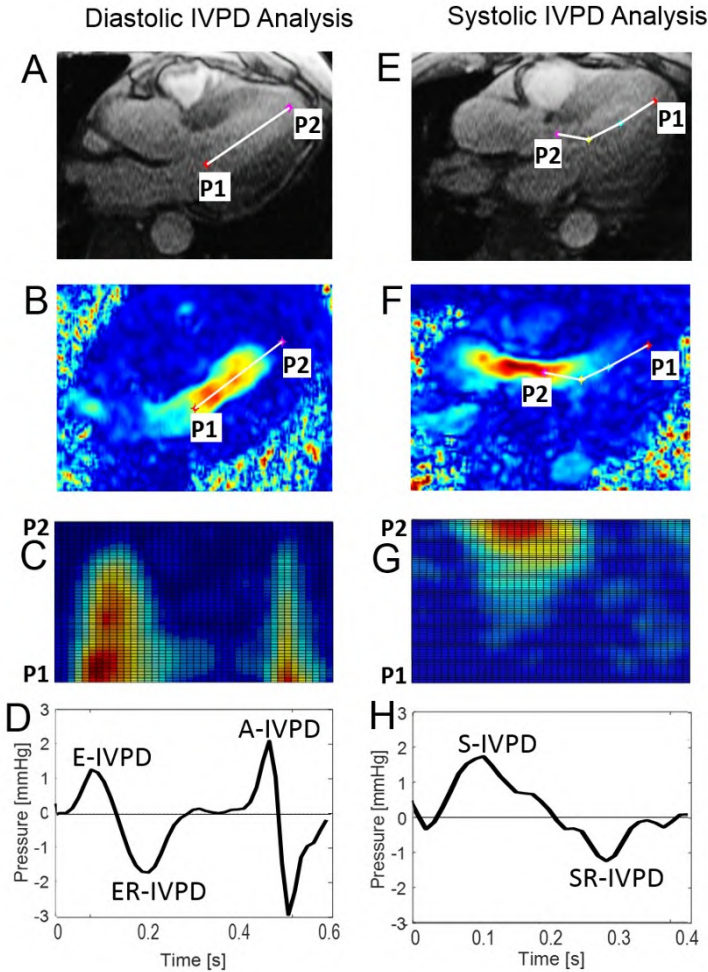


Figure 4.9: Graphical description of the phase-contrast MRI sequence processing to assess diastolic function (left column) and systolic function (right column). A) and E) Original magnitude images and B) and F) calculated velocity vectors images, showing the reference points selection, located at: Left) the mitral annulus (P1) and LV apex (P2); and Right) LV apex (P1) and aortic annulus (P2). C) and G) the pseudo CMM image, calculated from the 2D velocity vectors, was used as quality reference of the IVPD curves. Calculated IVPD curves (solid black line): D) during diastole, showing the (i) E-wave (E-IVPD), (ii) reversal E-wave (ER-IVPD) and (iii) A-wave (A-IVPD) pressure peaks, and H) during systole, showing the (i) S-wave (S-IVPD) and (ii) reversal S-wave (SR-IVPD) pressure peaks. C-D and G-H are aligned in time, respectively. Important to remark, the colour scale in B, C, F and G is a visual guidance for the user during the processing, and the linear (2 points) or the curvilinear (4 points) approximations could be selected by the user for diastolic and/or systolic analysis. Figure adapted from [1].

(MATLAB[®] 2016b, the Mathworks; Natwick, MA) and SPSS for Mac v22 (SPSS Inc., Chicago, IL).

4.3.2.5 *Reproducibility and repeatability assessment*

To test the method's reproducibility (measurements performed by two different operators at least one year apart) and repeatability (measurements performed by the same operator at least one week apart), 10 cases (included in the study) were assessed, calculating the Pearson r-value squared (r^2), the sum of squared error (SSE) and the reproducibility coefficient (RPC).

4.3.2.6 *Echocardiographic/MRI correlation assessment*

To evaluate the potential added value of the proposed technique, correlation coefficients were calculated between selected MRI parameters and established Doppler-echocardiographic indices of diastolic function.

4.3.3 **Results**

General characteristics of the study population are shown in table 4.5. The mean age of participants with HFrEF, HFpEF and without HF was 65.9, 62.9 and 61.8 years, respectively. The HFrEF group demonstrated a high prevalence of hypertension, diabetes, coronary artery disease and pronounced LA enlargement. Consistent with the HFpEF phenotype, subjects in this group were obese and had a high prevalence of hypertension and diabetes. Most subjects with HFrEF and HFpEF were receiving beta blockers, ACE inhibitors or ARBs, and loop diuretics. The study sample was composed predominantly of males, with a high proportion of African-Americans, particularly in the HFrEF group.

In all three groups (No-HF, HFrEF and HFpEF), subjects exhibited, in general, consistent IVPD patterns described previously using CMM echocardiography [98], [101], [134], [162] or cardiac MRI [58], [148], [192] (figure 4.9D and figure 4.9H). The diastolic period of the calculated IVPD waveforms was typically characterised by (i) a large early diastolic forward positive difference (E-IVPD) during ventricular relaxation, associated with early diastolic rapid filling; (ii) an early diastolic negative peak associated with the deceleration of the early filling (ER-IVPD); (iii) a second, late diastolic, positive peak (A-IVPD) associated with atrial contraction (see figure 4.9D). The systolic

Table 4.5: General characteristics of study subjects.

| Variable | No-HF (n = 159) | HFrEF (n = 47) | HFpEF (n = 32) | P-value |
|--|--------------------|--------------------|-------------------|------------|
| Age [years] | 61.8 ± 11.5 | 65.9 ± 10.7 | 62.9 ± 8.6 | 0.09 |
| Male | 145(91) | 46(98) | 28(88) | 0.18 |
| Race | | | | |
| African-American | 72(45) | 31(66) | 16(50) | 0.04† |
| Caucasian | 74(47) | 15(32) | 15(47) | 0.20 |
| BMI [kg/m^2] | 29.5(25.7, 33.1) | 27.9(24.2, 32.9) | 35(29.3, 41.7) | 0.0007§‡ |
| Heart rate [bpm] | 68.9 ± 13 | 69 ± 11.9 | 67.4 ± 11.9 | 0.84 |
| Ejection duration [ms] | 319 ± 30 | 311 ± 47 | 325 ± 33 | 0.27 |
| Current smoker | 43(28) | 15(33) | 8(25) | 0.73 |
| Hypertension | 118(75) | 41(89) | 29(91) | 0.03 |
| Diabetes | 64(41) | 27(59) | 18(56) | 0.04† |
| Coronary artery disease | 47(30) | 24(51) | 11(34) | 0.03† |
| Drug therapy | | | | |
| Beta blocker | 74(47) | 43(91) | 24(75) | < 0.0001†§ |
| ACE-inhibitor/ARB | 80(51) | 37(79) | 26(81) | < 0.0001†§ |
| Calcium-channel blocker | 41(26) | 12(26) | 13(41) | 0.23 |
| Spironolactone | 3(2) | 6(13) | 4(13) | 0.002†§ |
| Statin | 103(65) | 36(77) | 21(66) | 0.33 |
| Aspirin | 84(53) | 37(79) | 19(59) | 0.007† |
| Thiazide | 34(22) | 11(23) | 5(16) | 0.74 |
| Loop diuretics | 2(1) | 35(74) | 23(72) | < 0.0001†§ |
| eGFR ($mL/min/1.73m^2$)* | 86(65, 99.8) | 74(56.5, 92.3) | 84(63, 99) | 0.056† |
| Left ventricular ejection fraction [%] | 59.6(52.2, 65.6) | 36.6(23.7, 42.5) | 61.4(58, 70.3) | < 0.0001†‡ |
| LA Volume Index [mL/m^2] | 30.7(23.8, 39.5) | 46.1(35.7, 65.3) | 36.6(26.4, 49.9) | < 0.0001† |
| LV EDVi [mL/m^2] | 69.9(58.4, 82.4) | 102.7(85.8, 141.4) | 69.1(56.7, 79.5) | < 0.0001†‡ |
| LV mass index BSA [g/m^2] | 64.5(56.9, 76.5) | 88.6(77.9, 107.1) | 72(59.3, 83.2) | < 0.0001†‡ |
| Mitral E-wave velocity [cm/s] | 69.5(58.1, 85.5) | 74.3(54.7, 93.6) | 69.6(60.5, 92.7) | 0.54 |
| Mitral E-wave deceleration time [ms] | 210(170, 240) | 180(140, 220) | 220(170, 270) | 0.06 |
| Mitral A-wave velocity [cm/s] | 74.6 ± 21.7 | 62.3 ± 22.3 | 74.7 ± 19.6 | 0.008† |
| Mitral annular e', septal [cm/s] | 7.58(5.9, 9.65) | 5.61(4.12, 7.9) | 6.77(5.24, 8.19) | 0.0007† |

Values are mean ± SD or mean(95%CI), or counts(percentages). *eGFR was calculated using the

Modification of Diet in Renal Disease (MDRD) Study equation. † $P < 0.05$ for No-HF vs. HFrEF. ‡ $P < 0.05$ for HFrEF vs. HFpEF. § $P < 0.05$ for No-HF vs. HFpEF. eGFR = estimated glomerular filtration rate; ACE = Angiotensin convertase enzyme; ARB = Angiotensin receptor blocker.

period was characterised by a typical biphasic configuration with (i) a large forward positive peak (S-IVPD) associated with ventricular systole (rapid ejection) followed by (ii) a negative peak (SR-IVPD) associated with flow deceleration (slow ejection phase) (see figure 4.9H). Selected IVPD parameters are shown and compared in table 4.6, and figure 4.10 and figure 4.11.

4.3.3.1 Diastolic IVPDs

Unadjusted comparisons demonstrated no significant differences in E-IVPD (No-HF = 0.76; HFrEF = 0.83; HFpEF = 0.83mmHg; $P = 0.63$) and A-IVPD (No-HF = 0.93; HFrEF = 0.72; HFpEF = 0.92mmHg; $P = 0.07$) between the groups (table 4.6 and figure 4.10). In contrast, ER-IVPD was significantly different between the groups (ANOVA $P = 0.01$), consistent

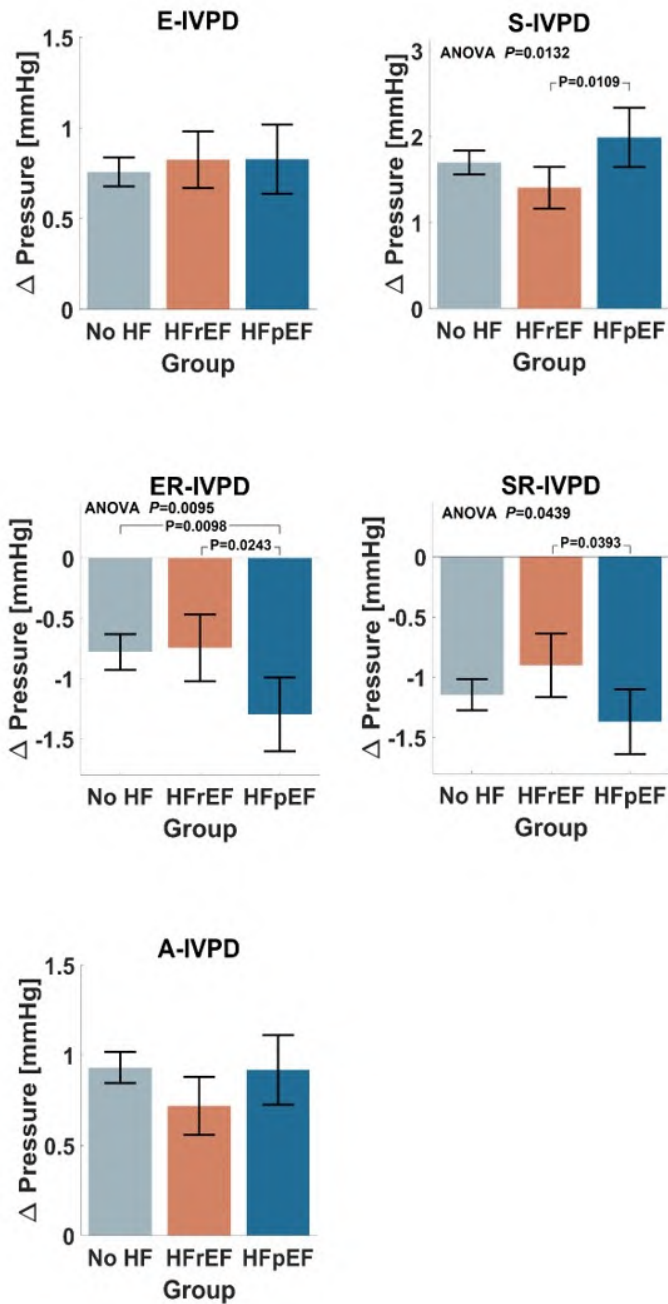


Figure 4.10: Comparison of IVPDs between groups for the unadjusted model. Computed parameters from diastole (left) and systole (right) are shown. Error bars represent 95% Confidence Intervals. Figure adapted from [1].

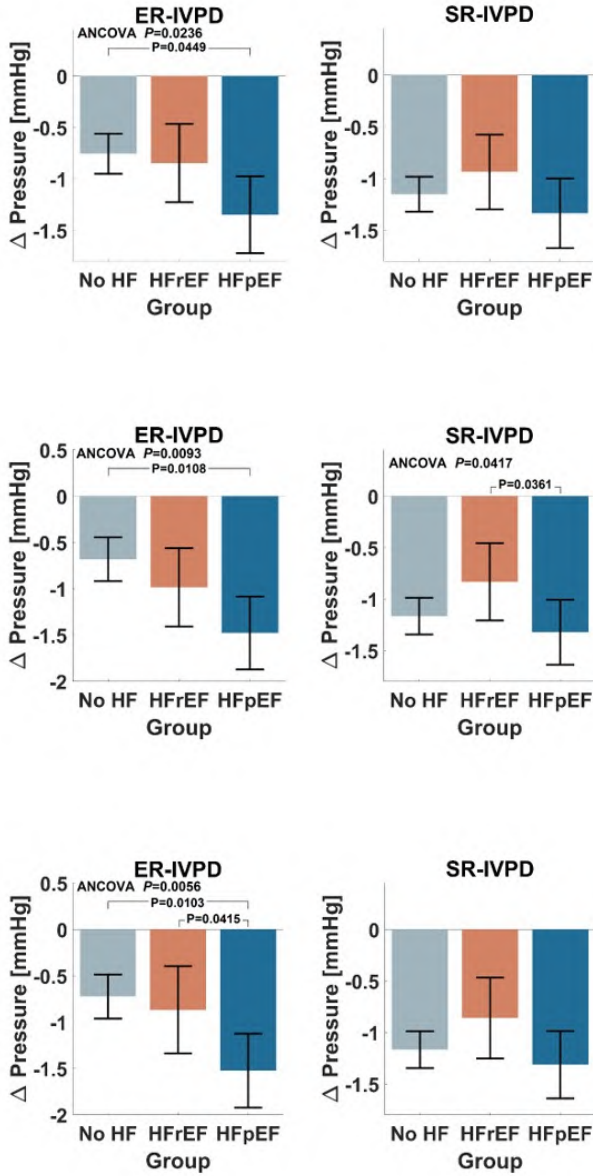


Figure 4.11: Selected IVPD parameters (ER and SR – wave pressure peaks) with statistically significant differences between groups for adjusted models: Top) Adjusted Model 1. Middle) Adjusted Model 2. Bottom) Adjusted Model 3. Computed parameters from diastole (left) and systole (right) are shown. Error bars represent 95% Confidence Intervals. Figure adapted from [1].

with a more pronounced reversal of the early diastolic IVPD in HFpEF (-1.30mmHg) compared to the No-HF group (-0.78mmHg) and the HFrEF group (-0.75mmHg). After adjustment for age, sex, African American ethnicity, BMI, coronary artery disease, eGFR and medication use (adjusted model 1), these differences in ER-IVPDs persisted (No-HF = -0.76 ; HFrEF = -0.85 ; HFpEF = -1.35mmHg ; $P = 0.02$). Similarly, these differences were present after further adjustment for Doppler-echocardiographic parameters (adjusted model 2: No-HF = -0.68 ; HFrEF = -0.99 ; HFpEF = -1.48mmHg ; $P = 0.009$) and LV structure (adjusted model 3: No-HF = -0.72 ; HFrEF = -0.87 ; HFpEF = -1.52mmHg ; $P = 0.006$) (see figure 4.11).

4.3.3.2 *Systolic IVPDs*

In unadjusted analyses (table 4.6 and figure 4.10), there were significant differences between groups in S-IVPD (No-HF = 1.7 ; HFrEF = 1.41 ; HFpEF = 1.99mmHg ; $P = 0.01$) and SR-IVPD (No-HF = -1.15 ; HFrEF = -0.90 ; HFpEF = -1.37mmHg ; $P = 0.04$), with more pronounced IVPDs in the HFpEF group compared to the HFrEF group. Between-group differences in SR-IVPD were also present after adjustment for general clinical characteristics and Doppler-echocardiographic parameters (adjusted model 2; table 4.6 and figure 4.11), but no significant differences in systolic IVPDs were found between the groups after further adjustment for LV structure (adjusted model 3; table 4.6 and figure 4.11).

4.3.3.3 *Reproducibility and repeatability assessment*

Higher reproducibility was demonstrated for diastolic E-IVPD and ER-IVPD parameters ($r^2 \geq 0.70$; $\text{SSE} \leq 0.58$; $\text{RPC} \leq 0.55$) in comparison with A-IVPD ($r^2 = 0.56$; $\text{SSE} = 0.98$; $\text{RPC} = 0.65$) and systolic parameters (S-IVPD: $r^2 = 0.04$; $\text{SSE} = 5.3$; $\text{RPC} = 1.6$; SR-IVPD: $r^2 = 0.47$; $\text{SSE} = 1.3$; $\text{RPC} = 0.76$). This trend was maintained for the repeatability assessment, albeit altogether higher indexes were found in this case (diastolic parameters: $r^2 \geq 0.92$; $\text{SSE} \leq 0.21$; $\text{RPC} \leq 0.32$; systolic parameters: $r^2 \geq 0.71$; $\text{SSE} \leq 1.6$; $\text{RPC} \leq 0.87$).

4.3.3.4 *Echocardiographic/MRI correlation assessment*

There were only weak correlations between standard Doppler-echocardiographic parameters and IVPD parameters ($R < 0.20$ for

Table 4.6: Comparisons of diastolic and systolic intraventricular pressure difference parameters between the groups.

| Variable | No-HF (n = 159) | HFrEF (n = 47) | HFpEF (n = 32) | P-value |
|-------------------------|---------------------|---------------------|---------------------|----------|
| Unadjusted Model | | | | |
| E-IVPD [<i>mmHg</i>] | 0.76(0.68, 0.84) | 0.83(0.67, 0.98) | 0.83(0.64, 1.02) | 0.63 |
| ER-IVPD [<i>mmHg</i>] | -0.78(-0.93, -0.63) | -0.75(-1.02, -0.47) | -1.30(-1.60, -0.99) | 0.01\$‡ |
| A-IVPD [<i>mmHg</i>] | 0.93(0.85, 1.02) | 0.72(0.56, 0.88) | 0.92(0.73, 1.11) | 0.07 |
| S-IVPD [<i>mmHg</i>] | 1.7(1.56, 1.84) | 1.41(1.16, 1.65) | 1.99(1.65, 2.34) | 0.01‡ |
| SR-IVPD [<i>mmHg</i>] | -1.15(-1.28, -1.02) | -0.90(-1.17, -0.64) | -1.37(-1.64, -1.10) | 0.04‡ |
| Adjusted Model 1 | | | | |
| E-IVPD [<i>mmHg</i>] | 0.75(0.65, 0.85) | 0.86(0.64, 1.08) | 0.85(0.61, 1.08) | 0.70 |
| ER-IVPD [<i>mmHg</i>] | -0.76(-0.95, -0.56) | -0.85(-1.23, -0.47) | -1.35(-1.72, -0.97) | 0.02§ |
| A-IVPD [<i>mmHg</i>] | 0.94(0.83, 1.05) | 0.71(0.49, 0.92) | 0.94(0.70, 1.17) | 0.15 |
| S-IVPD [<i>mmHg</i>] | 1.7(1.52, 1.89) | 1.49(1.14, 1.84) | 1.89(1.47, 2.3) | 0.16 |
| SR-IVPD [<i>mmHg</i>] | -1.15(-1.32, -0.98) | -0.94(-1.30, -0.58) | -1.34(-1.67, -1) | 0.14 |
| Adjusted Model 2 | | | | |
| E-IVPD [<i>mmHg</i>] | 0.84(0.71, 0.97) | 0.93(0.67, 1.19) | 0.79(0.54, 1.04) | 0.62 |
| ER-IVPD [<i>mmHg</i>] | -0.68(-0.92, -0.45) | -0.99(-1.41, -0.56) | -1.48(-1.87, -1.08) | 0.009§ |
| A-IVPD [<i>mmHg</i>] | 0.97(0.84, 1.11) | 0.75(0.50, 1.00) | 0.97(0.72, 1.22) | 0.27 |
| S-IVPD [<i>mmHg</i>] | 1.72(1.49, 1.96) | 1.46(1.03, 1.89) | 1.86(1.39, 2.33) | 0.25 |
| SR-IVPD [<i>mmHg</i>] | -1.17(-1.34, -0.99) | -0.83(-1.21, -0.46) | -1.32(-1.64, -1.01) | 0.04‡ |
| Adjusted Model 3 | | | | |
| E-IVPD [<i>mmHg</i>] | 0.85(0.72, 0.99) | 0.91(0.63, 1.20) | 0.79(0.54, 1.05) | 0.76 |
| ER-IVPD [<i>mmHg</i>] | -0.72(-0.96, -0.49) | -0.87(-1.34, -0.40) | -1.52(-1.92, -1.13) | 0.006\$‡ |
| A-IVPD [<i>mmHg</i>] | 0.98(0.85, 1.12) | 0.73(0.46, 1.00) | 0.99(0.73, 1.24) | 0.24 |
| S-IVPD [<i>mmHg</i>] | 1.74(1.5, 1.98) | 1.47(1.01, 1.92) | 1.86(1.37, 2.34) | 0.34 |
| SR-IVPD [<i>mmHg</i>] | -1.17(-1.35, -0.99) | -0.86(-1.25, -0.47) | -1.31(-1.64, -0.99) | 0.11 |

Data are presented as mean (95%CI). † P < 0.05 for No-HF vs. HFrEF. ‡ P < 0.05 for HFrEF vs. HFpEF. § P < 0.05 for No-HF vs. HFpEF.

Unadjusted Model; Adjusted Model 1: adjusted for clinical data (age, sex, African American ethnicity, BMI, Coronary Artery Disease, eGFR and Beta Blocker, ACE-Inhibitor, ARB, loop diuretic, and spironolactone use); Adjusted Model 2: Model 1 additionally adjusted for echo parameters (Mitral E-wave velocity, E-wave deceleration time, Mitral annular e' septal); Adjusted Model 3: Model 2 additionally adjusted for MRI data (LV mass index and EDVI).

all, except for the correlation between ER-IVPD and peak A-wave velocity ($R = -0.30$). Correlation coefficients between standard Doppler-echocardiographic indices of diastolic function and IVPD parameters are presented in figure 4.12.

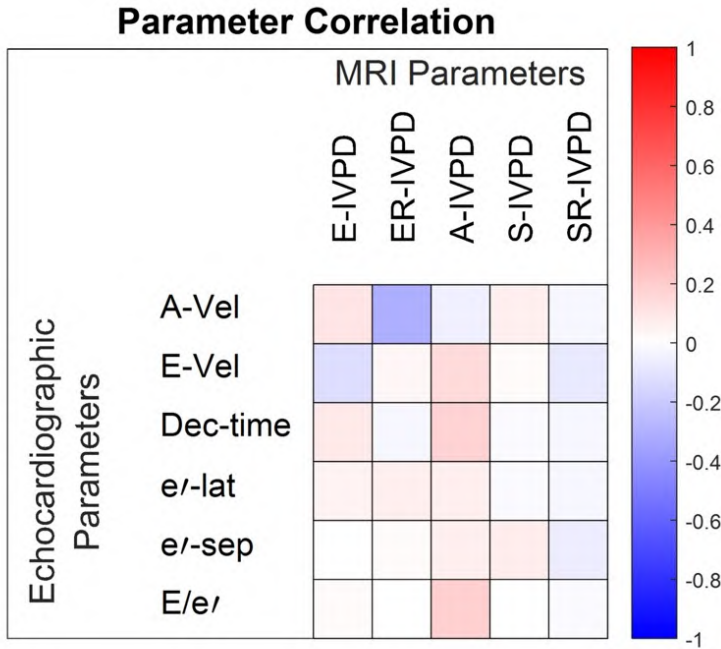


Figure 4.12: Correlation coefficients between echocardiographic and MRI-based IVPDs parameters, showing the correlation between IVPD (MRI-based) parameters: E-wave pressure peak (E-IVPD), E-wave reversal pressure peak (ER-IVPD), A-wave pressure peak (A-IVPD), S-wave pressure peak (S-IVPD) and S-wave reversal pressure peak (SR-IVPD); and echocardiographic parameters: peak E and A-wave velocities by Doppler (E and A-Vel), deceleration time (Dec-time), e' velocity (lateral (e' -lat) and septal (e' -sep)) and E/e' . Figure adapted from [1].

4.3.4 Discussion

We compared diastolic and systolic IVPDs between subjects with HFrEF, HFpEF or No-HF. We found physiologically expected patterns of IVPD in all 3 groups, with significant differences in diastolic IVPDs. Specifically, subjects with HFpEF exhibited more pronounced reversal peak of early diastolic IVPDs, which was independent of clinical parameters, echocardiographic parameters of LV filling, and LV structure assessed by MRI. Subjects with HFrEF demonstrated a non-significant trend of increasing E-IVPD and

decreasing A-, S- and SR-IVPD. Our findings suggest distinct patterns of diastolic and systolic IVPDs and differences in the nature of both diastolic and systolic dysfunction between HF subtypes. IVPD parameters demonstrated only weak correlations with standard Doppler-echocardiographic parameters.

Previous studies have shown that, despite being small in magnitude, IVPDs have a significant role in efficient filling and emptying of the LV and could be used to characterise cardiac performance [57], [193]. However, the assessment and interpretation of IVPGs and IVPDs in clinical practice remains complicated by its dependency on a large number of factors and interactions [84], [194]. Furthermore, flow occurs in multiple and rapidly changing directions, forming complex vortex patterns [84], [193]. The complexity of intraventricular flow and technical limitations of ultrasound imaging, the standard method in cardiovascular assessment, make it difficult to relate intraventricular flow patterns and derived IVPDs to LV myocardial function in a quantitative manner [84], [193], [194].

The increasing availability of cardiovascular MRI has made it an advantageous alternative from a technical point of view due to its high image quality, reproducibility, repeatability, plane of view flexibility, sufficient spatial and temporal resolution and reduced operator dependency. Furthermore, MRI-based IVPD calculations allow for a more flexible definition and alignment of the operator's "scan line", which could be relevant when the blood flow exhibits a curved trajectory [134]. Additionally, 2D-velocity information from phase contrast MRI improves the accuracy of IVPDs even if the temporal resolution, a critical parameter to calculate IVPDs [189], is lower in comparison with ultrasound. In fact, Thompson *et al.* [58] reported that a minimum temporal resolution of 44ms may avoid significant underestimation of the local acceleration contribution to the total intracardiac pressure differences. Previously, making use of computational fluid dynamics simulations, we assessed the impact of temporal resolution in IVPD calculations, showing that the temporal resolution of phase contrast MRI is, at least in theory, sufficient to resolve IVPDs. Furthermore, we also showed that IVPDs estimated by a 1D method as colour-Doppler ultrasound are larger in magnitude than when the 2D velocity information was used, but the estimates based on 2D velocity information are more accurate, especially in extreme scan line misalignments [2], which could be particularly sensible after mid- and late diastole due to formation of vortices [57], [162]. We speculate that this explains, at least partly, some of the difference between values reported here and in other studies [56], [98], [101], [134].

There were no significant differences in E- and A-IVPD between the groups. This may be a consequence of early filling pseudonormalization due

to greater filling pressures. Additionally, in HFpEF patients, pronounced diastolic abnormalities can often be elicited only during physiologic perturbations, such as exercise or dobutamine infusions [135], [158], [179], as subjects with HFpEF exhaust their reserve to preserve the diastolic suction force at rest, limiting their ability for adaptation to stress [135], [179]. Nonetheless, our results demonstrate that HFpEF is associated with a greater magnitude of the ER-IVPD. Although, the slope of mitral inflow deceleration temporally coincides with ER-IVPD, it is interesting to note that we did not find significant differences in the deceleration time between the groups, and that ER-IVPD was not strongly related to the deceleration time. Therefore, our data suggests that ER-IVPD may be a more sensitive marker of diastolic function in HFpEF.

We also examined systolic IVPDs. A typical biphasic IVPD pattern was observed in systole, with a positive peak immediately followed by a negative one. HFrfEF individuals exhibited lower values, whereas the HFpEF group presented an overall higher total magnitude of S-IVPD and SR-IVPD, suggesting differences in systolic flow dynamics between groups. These differences could be related to the unsteady nature of ejective flow, abnormalities in chamber geometry, and/or the sequence of regional contraction [193].

Our reproducibility and repeatability assessments suggest a general adequate inter and intra-operator variability for early diastolic IVPD parameters. Reproducibility and repeatability were lower for A-IVPD, probably due to a more complex flow after mid- and late diastole [57], [162]. Systolic parameters evidenced a need to refine the standardisation of the method, particularly for S-IVPD. The overall correlation between IVPD parameters and echocardiographic indexes was weak or non-existent. In fact, previous publications have pointed out a weak correlation between Doppler echocardiographic estimates of LV filling pressure with invasive filling pressure measurements and the necessity to include further analysis of non-invasive measures [195], [196]. In contrast, echocardiographic [101], [134] and MRI [58] based IVPD parameters have shown good agreement against invasive intraventricular measurements, adding potentially relevant information for cardiovascular assessments.

The reported data should be interpreted considering the strengths and limitations of the study. Strengths of this study are the inclusion of patients with HFrfEF and HFpEF, and the assessment of IVPDs with phase-contrast MRI, which overcomes a number of assumptions made with CMM echocardiography and allows for a more consistent interrogation of intraventricular flow. Our study also has limitations. We did not perform invasive catheter-based measures of distensibility which would have been unfeasible in the absence of a clinical indication for LV catheterisation. From a technical

point of view, the MRI acquisition requires relative long breath-holds (~ 20s) and has limited temporal and through plane spatial resolution, while the processing could be affected by the image alignment and assumptions made about the nature of flow from the 3 chambers view. Upon computation of the IVPDs, viscous forces are neglected and it is assumed that inflow and outflow is laminar [56], [134], [135]. On average, our HFpEF subjects did not have marked LA enlargement, suggesting the presence of mild HFpEF. This may have led to underestimations of true underlying differences. Our population was a clinical sample referred for a cardiac MRI study, which may not fully represent population-based trends. Moreover, complementary myocardial mechanic studies could be included to improve the analysis [197].

4.3.5 Conclusions

In conclusion, we demonstrated the feasibility to assess IVPDs throughout the cardiac cycle using phase-contrast MRI and compared IVPDs between subjects without HF and subjects with HFrEF and HFpEF. Our findings suggest distinct patterns of diastolic IVPDs in HFpEF, implying differences in the nature of diastolic dysfunction between the HF subtypes. Further research is warranted to exploit MRI analysis thoroughly to assess the significance of these novel indices regarding risk stratification and response to therapy.

VASCULAR FUNCTION

As cardiac function (see Chapter 4), vascular function is a key factor for the appropriate operation of the cardiovascular system and, therefore, vascular assessment is becoming a fundamental step in clinical practice. Several mechanisms, including metabolic, neural, myogenic and humoral/endothelial, regulate vascular function and peripheral blood flow, concerning complex interactions determined partly by environmental conditions. The endothelium, for example, influences vascular tone by releasing vasoactive molecules, such as nitric oxide (NO). Concretely, NO acts on smooth muscle cells producing a dilatation of blood vessels and, thus, increasing blood supply and reducing blood pressure (BP). In fact, the major effect of the use of NO therapeutics (nitrate [NO_3^-] or nitrite [NO_2^-]) in the cardiovascular system is the relaxation of smooth muscle in veins, larger arterioles and arteries through an endothelial pathway, termed the nitrate–nitrite–NO pathway. Thus, it has been hypothesized that the use of nitrates has a positive effect in the treatment of cardiovascular dysfunction, even if there is still a gap between research and epidemiological evidence, particularly related to the use of nitrates for the treatment of patients with heart failure with preserved ejection fraction (HFpEF). As it was stated in Chapter 1, although the morbidity and mortality rates are comparable in patients with heart failure and reduced ejection fraction (HFrEF) and in patients with HFpEF, the recognition, evaluation, and treatment of the later remains a challenge.

This chapter entails a research study on non-invasive assessment of arterial properties, the interaction between the cardiac pump and the peripheral

circulation and the impact on them by the employment of organic and inorganic nitrates in a HFpEF sample population. The first section introduces the evaluation of vascular function through classical haemodynamic assessment in time and frequency (Fourier transform) domains, including the analysis of pressure-flow waveforms, wave separation and wave intensity. This study was published in the *European journal of heart failure* under the title "Effects of organic and inorganic nitrate on aortic and carotid haemodynamics in heart failure with preserved ejection fraction", vol. 19, no. 11, pp. 1507-1515, 2017 [4]. The second section of the chapter describes the implementation of a novel analysis proposed by Mynard *et al.* [70] to evaluate wave power transmission into the cerebrovascular circulation, a research based on the article titled "Effect of organic and inorganic nitrates on cerebrovascular pulsatile power transmission in patients with heart failure and preserved ejection fraction" published in *Physiological measurement*, vol. 39, no. 4, pp. 044001, 2018 [3].

5.1 EFFECTS OF ORGANIC AND INORGANIC NITRATE ON AORTIC AND CAROTID HAEMODYNAMICS IN HEART FAILURE WITH PRESERVED EJECTION FRACTION

5.1.1 Introduction

Heart failure (HF) affects around 2% of the western population and is the most common cause of hospitalisation in adults >65 years of age. Approximately half of patients with HF have a preserved left ventricular (LV) ejection fraction (HFpEF) [33]. Multiple effective pharmacological therapies that result in substantial clinical benefit in HF with reduced ejection fraction are available. In contrast, there are currently no proven effective pharmacological therapies to improve outcomes in HFpEF.

Pulsatile arterial load exerts important effects on LV function and remodelling. In particular, wave reflections originating at the periphery and conducted back to the heart, have been shown to cause LV diastolic dysfunction, hypertrophy and fibrosis in experimental models, a concept supported by an increasing body of human studies [165], [172]–[175], [177]. Acute administration of organic nitrates has been shown to reduce wave reflections arriving at the central aorta in hypertensive or healthy subjects in some, but not all studies [198]–[204]. The effects of organic nitrates on pulsatile arterial haemodynamics have not been well characterised in HFpEF. In recent trials in patients with HFpEF [205]–[207], organic nitrates have not only been poorly tolerated but have also been linked to important side effects such as hypotension and headaches, suggesting adverse effects on the cerebrovascular territory.

In contrast to the unfavourable effects of organic nitrates in HFpEF, recent randomized controlled trials have demonstrated that inorganic nitrate, administered as a single dose [208] or after one week of sustained administration [209], improves exercise capacity in patients with HFpEF. Inorganic nitrate undergoes a two-step reduction to NO via the nitrate–nitrite–NO pathway [210], [211]. The conversion of nitrite to NO occurs in conditions of hypoxia and acidosis, but a recent report indicates that it also occurs via paradoxical normoxic activation in conduit arteries [212], indicating potential effects on pulsatile arterial haemodynamic function and arterial wave reflections. Furthermore, in contrast to the frequent occurrence of headache with organic nitrate, the administration of inorganic nitrate has not been associated with headaches or other side effects in two recent trials in this population [208], [209].

We aimed to assess the effect of organic and inorganic nitrate in HFpEF on (i) wave reflections arriving at the central aorta, and (ii) carotid arterial haemodynamics (i.e. to characterise cerebrovascular effects).

5.1.2 Methods

We performed two sub-studies. In the first sub-study (sub-study 1), we assessed aortic and carotid haemodynamics at baseline and after the administration of 0.4mg of sublingual nitroglycerin (NTG). In the second sub-study (sub-study 2), we analysed aortic and carotid pressure–flow data from our previous randomized controlled trial of inorganic nitrate administration in HFpEF [208]. Protocols were approved by the University of Pennsylvania and Philadelphia VA Medical Center Institutional Review Boards, as appropriate. All subjects provided written informed consent.

5.1.2.1 Study population

For sub-study 1, we included subjects with HFpEF who met the following criteria: (i) symptomatic HF with a LV ejection fraction > 50%; (ii) at least one of the following within one year prior to consent: hospitalisation for decompensated HF, acute treatment for HF with intravenous diuretics or haemofiltration, chronic treatment with a loop diuretic for control of HF symptoms, or chronic diastolic dysfunction evidenced by left atrial (LA) enlargement (LA volume index > 34mL/m²), or Doppler signs of increased left atrial pressure, as defined by the European Society of Cardiovascular Imaging/American Society of Echocardiography [84]; (iii) stable medical therapy.

Key exclusion criteria were: (i) clinically significant valve disease (more than mild aortic/mitral stenosis or more than moderate aortic/mitral regurgitation); (ii) atrial fibrillation/flutter; (iii) current nitrate therapy; (iv) significant ischaemia on stress testing within the past year that was not revascularized; (v) other clinically important causes of dyspnoea; (vi) hypertrophic, infiltrative, or inflammatory cardiomyopathy; (vii) pericardial disease; (viii) primary pulmonary arteriopathy; (ix) BP < 110/40mmHg or > 180/100mmHg; (x) resting heart rate (HR) > 100bpm; (xi) LV ejection fraction < 50% in the past; (xii) adverse reactions to organic nitrates or phosphodiesterase inhibitor use; (xiii) severe renal dysfunction (glomerular filtration rate < 30mL/min/1.73m²), or liver disease. In sub-study 2, we utilized very similar inclusion/exclusion criteria, as previously described [208].

5.1.2.2 Study protocol

Sub-study 1

Twenty-six subjects participated in this sub-study. After > 10 minutes of rest in the supine position, BP was taken in the right arm with a validated oscillometric device (Omron HEM-705CP, Omron Corporation, Kyoto, Japan). Carotid pressure (figure 5.1) was recorded via applanation tonometry, using a SphygmoCor-CPV System (AtCor Medical, Itasca, IL, USA) equipped with a high-fidelity Millar tonometer (Millar Instruments, Houston, TX, USA). Aortic pressure waveforms are only obtainable through invasive measurements, which is not applicable in clinical practice. Therefore, derived measurements should be used instead and, previously, it has been demonstrated that carotid pressure waveforms represent reasonable surrogates of the aortic pressure waveform [213], [214].

Pulsed-wave Doppler measurements of flow velocities in the LV outflow tract (figure 5.1) were performed using a GE-e9 ultrasound machine (GE Healthcare, Fairfield, CT, USA), with the Doppler sample immediately proximal to the aortic valve leaflets within the centerline of the LV outflow tract. We computed LV outflow tract cross-sectional area from its radius (r) measured in the parasternal long-axis view ($area = \pi r^2$). Carotid diameters and blood velocities were also acquired, using a vascular linear probe. Carotid flow was computed as flow velocity multiplied by lumen cross-sectional area ($area = \pi r^2$). After baseline measurements were obtained, a single dose (0.4mg) of NTG was administered sublingually, and measurements were repeated starting 2 minutes after administration. Comparisons were made between the measurements obtained pre- vs. post-NTG administration.

Sub-study 2

Seventeen subjects participated in a randomized, double-blind, cross-over study of a single dose of inorganic nitrate given as concentrated nitrate-rich beetroot (BR) juice (NO_3^- , BEET-IT Sport, James White Drinks Ltd, Ipswich, UK) containing $12.9\text{mmolL} \text{NO}_3^-$ in 140mL , vs. an otherwise identical nitrate-depleted placebo (PB) juice (James White Drinks, Ltd, Ipswich, UK). The interventions were separated by a wash-out period of at least 5 days. We measured aortic and carotid haemodynamics using identical methods as in sub-study 1, $\sim 2.5\text{h}$ after juice ingestion. Comparisons were made between measurements obtained after administration of BR vs. PB juice. One subject was excluded from these analyses due to lack of carotid flow data during one of the study visits.

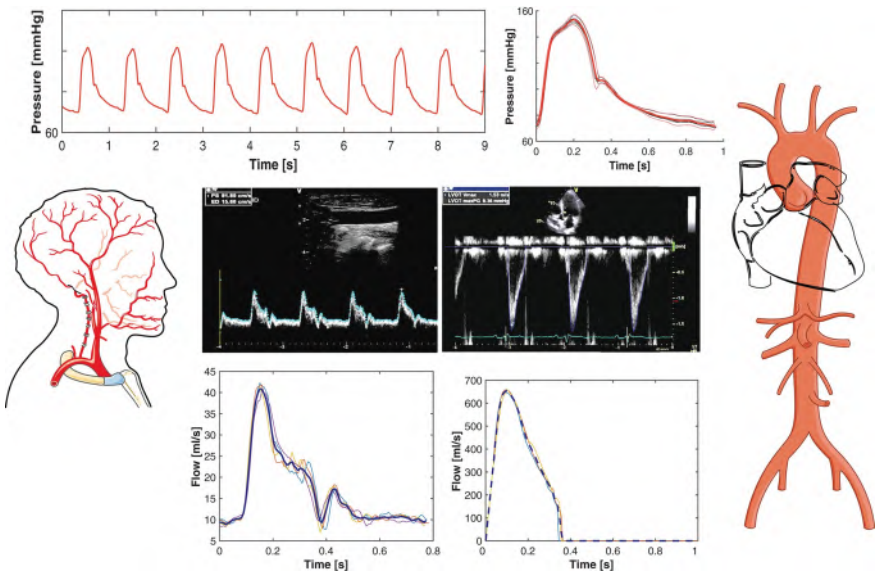


Figure 5.1: Example of pressure–flow analyses. Tonometric pressure data are shown at the top (left), along with the signal-averaged pressure waveform (top right, red). Doppler flow interrogations were performed, as shown at the middle position for the carotid (left) and LV outflow (right) locations. Tracing and signal averaging of flow waveforms (bottom blue curves) was subsequently performed. The carotid pressure waveform is used for both carotid pressure–flow analyses and aortic pressure–flow analyses, since the carotid pressure is a good surrogate of the aortic pressure waveform [213], [214]. Figure adapted from [4].

5.1.3 Pressure–flow analyses

A custom-designed software was built in MATLAB® (The Mathworks, Natick, MA, USA) [63], [64] to process off-line central arterial tonometry recordings and Doppler flow velocity files. A representative example of pressure–flow data processing is shown in figure 5.1 and figure 5.2. Signal averaging was performed first, followed by the time alignment of both signals as previously described [63], [215]. Time alignment of pressure and blood flow curves was performed to maximize: (i) the rapid systolic upstroke of pressure and flow; (ii) concordance of the pressure dicrotic notch and cessation of flow in the LV outflow tract, or the flow dicrotic notch in the carotid; (iii) linearity of the early systolic pressure–flow relationship.

We computed aortic input impedance (figure 5.2), which characterises the ratio of pulsatile pressure over flow in each harmonic of HR. In this analysis, the fundamental frequency, or 1st harmonic, is the HR, and higher harmonics are multiples of that frequency. Proximal aortic characteristic impedance (Z_c) was computed in the frequency domain. Each pressure and flow harmonic was separated into forward and backward components using wave separation analysis [216], [217]. We assessed the reflection coefficient in the first three harmonics. These are the relevant harmonics for assessing wave reflections because: (i) they contain the vast majority of the pulsatile energy in pressure and flow signals; (ii) at higher frequencies, reflections cancel out at random, and the input impedance spectrum hovers around aortic root characteristic impedance, mimicking a reflection-free system.

As the reflection coefficient is derived from the ratio of two sine waves, it is a complex number with an amplitude and phase-angle, which can correspond to different degrees of destructive or constructive interference between forward and backward waves. Therefore, the net effect of reflections was expressed as the real part of the reflection coefficient, which becomes increasingly positive as pressure from wave reflections increases (constructive interference), and negative when destructive interference leads to a net decrease in pressure by wave reflections at a given harmonic [218].

We also reconstructed the forward and backward pressure waves in the time domain. The sum of forward and backward pressure harmonics yields the forward and backward waves, respectively (figure 5.2). The time of onset of the reflected wave was defined as the time at which the reflected wave starts adding to mean pressure. We computed the Buckberg index (also known as the sub-endocardial viability ratio), as the ratio of diastolic/systolic pressure–time integrals (i.e. areas under the pressure curve). This index provides an assessment of the effect of pulsatile haemodynamics on myocardial oxygen demand (systolic load) vs. supply (perfusion pressure) [215].

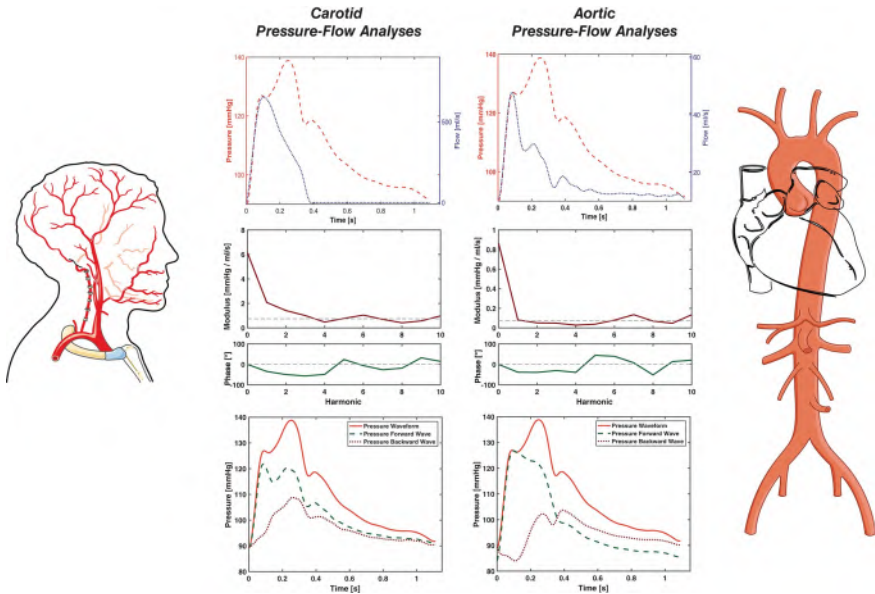


Figure 5.2: Carotid (left panels) and aortic (right panels) pressure–flow pairs are processed via mathematical analyses in the frequency domain. Top) Time alignment result of pressure waveform (red dashed lines) and blood flow velocity (blue dotted line) curves. Middle) The input impedance spectrum, which consists of modulus (red) and phase (green) is obtained. Characteristic impedance (Z_c , dashed line in modulus plot) is computed based on the average modulus of higher harmonics of the input impedance modulus. Z_c is a local vascular property of the aortic root or carotid artery, which governs the local pressure–flow relation in the absence of wave reflections. Once Z_c is known, the modulus and phase of the reflection coefficient in the frequency domain (at each harmonic) can be computed (not shown), along with the net contribution of reflections to pressure at each harmonic (i.e. the real part of the reflection coefficient). Reflection coefficients in the frequency domain are derived purely from the input impedance spectrum and thus depend purely on arterial load. The first three harmonics contain the vast majority of the pulsatile energy and are the relevant harmonics. Bottom) We also performed wave separation in the time domain. This approach yields forward (green dashed line) and backward (red dotted line) waves reconstructed in the time domain. At the aorta, forward and backward wave amplitude and morphology in the time domain are not purely dependent on arterial load, but depend also on re-reflections in the heart and the LV contraction pattern. Figure adapted from [4].

We also performed analyses of carotid pressure–flow relations. Haemodynamic analysis commonly assumes a parabolic or flat flow velocity profile to convert velocity measured in a sample volume into a volumetric flow. However, this simplification may be inadequate for the carotid artery, as the flow velocity profile is neither of both. We therefore implemented a conversion accounting for the Womersley number (a well-established dimensionless fluid-dynamics parameter for oscillatory flow), as previously described by Ponzini *et al.*[68].

In our laboratory, repeated measurements of all indices from aortic and carotid pressure–flow analyses yielded coefficients of variation of 17% or less.

5.1.3.1 *Statistical analysis*

Descriptive data are presented as mean \pm standard deviation (SD) for continuous variables, or counts (%) for categorical variables. Comparisons between pre- and post-NTG values for sub-study 1, and between values corresponding to BR vs. PB juice administration for sub-study 2, were performed using paired Student's t-test. Physiologic indices were expressed as absolute values at each time point, as well as absolute differences between measurements (with 95% confidence intervals). Positive differences represent an increase in the values associated with organic/inorganic nitrate administration, whereas negative differences represent a decrease in such values. A two-tailed P value of < 0.05 was considered statistically significant. Statistical analyses were performed using SPSS v-15 for Mac-OS and SPSS v-21 for Windows (SPSS Inc., Chicago, IL, USA).

5.1.4 **Results**

General characteristics of the study populations for sub-studies 1 and 2 are shown in table 5.1. The characteristics of study subjects in both sub-studies were very similar. In both sub-studies, subjects were obese, with a high prevalence of hypertension and diabetes, as well as LA enlargement and a high mitral E/e' ratio. Both study samples were composed predominantly of males, with a high proportion of African-Americans. All subjects in both sub-studies had New York Heart Association class II–III symptoms.

Table 5.1: General characteristics of study subjects.

| Variable | NTG study (sub-study 1) (n=26) | Beetroot study (sub-study 2) (n=16) | P-value |
|--|-----------------------------------|--|---------|
| Age, years [median (IQR)] | 60(56 – 65) | 65(62.5 – 70.5) | 0.10 |
| Male sex | 20(76.9) | 14(87.5) | 0.68 |
| Race | | | |
| African-American | 16 (61.5) | 14 (87.5) | |
| Caucasian | 9 (34.6) | 2 (12.5) | |
| BMI [kg/m^2] | 36.5(6.5) | 34.4(3.5) | 0.24 |
| Obesity (BMI $>30kg/m^2$) | 22(84.6) | 15(93.8) | 0.63 |
| Current smoker | 4(15.4) | 1(6.3) | 0.63 |
| Hypertension | 24(92.3) | 16(100) | 0.52 |
| Diabetes | 17(65.4) | 11(68.8) | 0.82 |
| Coronary artery disease | 8(30.8) | 3(18.8) | 0.49 |
| Chronic kidney disease (eGFR $<60mL/min/1.73m^2$) | 9(34.6) | 5(31.3) | 0.82 |
| Drug therapy | | | |
| Beta-blocker | 14(53.9) | 10(62.5) | 0.58 |
| ACE-inhibitor/ARB | 18(69.2) | 10(62.5) | 0.65 |
| Calcium-channel blocker | 14(53.9) | 7(43.8) | 0.53 |
| Mineralocorticoid receptor antagonist | 0(0) | 1(6.3) | 0.38 |
| Statin | 15(57.7) | 9(56.3) | 0.93 |
| Aspirin | 17(65.4) | 14(87.5) | 0.16 |
| Thiazide | 14(53.9) | 4(25.0) | 0.07 |
| Loop diuretic | 13(50.0) | 6(37.5) | 0.43 |
| Laboratory data | | | |
| eGFR* [$mL/min/1.73m^2$] [median (IQR)] | 74.1(53.5 – 95.4) | 65.5(52.4 – 89.5) | 0.95 |
| Echocardiography | | | |
| LV ejection fraction [%] [median (IQR)] | 57.4(55.0 – 65.5) | 62.4(57.5 – 69.8) | 0.30 |
| Left atrial volume index [mL/m^2] | 30.3(10.9) | 35.7(10.9) | 0.13 |
| Mitral E-wave velocity [cm/s] | 81.8(24.9) | 71.7(16.4) | 0.16 |
| Mitral A-wave velocity [cm/s] | 79.2(24.6) | 73.3(24.2) | 0.45 |
| Mitral septal tissue Doppler velocity [cm/s] | 6.6(2.2) | 6.5(1.7) | 0.88 |
| Mitral E/e' ratio [median (IQR)] | 12.8(11.0 – 14.4) | 11.4(9.2 – 13.3) | 0.17 |
| TAPSE [cm] [median (IQR)] | 2.3(2.1 – 2.6) | 2.6(2.1 – 2.8) | 0.44 |
| TAPSE $<1.6cm$ | 0(0) | 0(0) | |
| Tricuspid regurgitant jet peak gradient† [$mmHg$] | 31.8(3.7) | 27.9(8.9) | 0.054 |
| LV end-diastolic diameter [cm] | 4.8(0.6) | 4.5(0.6) | 0.12 |
| LV mass [g] [median (IQR)] | 243.7(214.1 – 318.3) | 236.6(183.2 – 275.2) | 0.62 |
| LV mass indexed to height [$g/m^{1.7}$] [median (IQR)] | 96.9(71.7 – 114.1) | 91.6(70.7 – 102.8) | 0.39 |
| LV mass indexed to BSA [g/m^2] | 109(23.5) | 106.3(37.6) | 0.77 |
| Relative wall thickness [cm] [median (IQR)] | 0.52(0.47 – 0.58) | 0.59(0.54 – 0.66) | 0.041 |
| NT-proBNP [pg/mL] [median (IQR)] | 250.5(90.5 – 510.6) | 148.0(61.7 – 272.5) | 0.16 |
| Ejection duration [ms] | 318(28) | 330(35) | 0.22 |

Values are expressed as mean \pm standard deviation, or number (%), unless otherwise specified.

ACE: angiotensin-converting enzyme; ARB: angiotensin receptor blocker; BMI: body mass index; BSA: body surface area; eGFR: estimated glomerular filtration rate; IQR: interquartile range; LV: left ventricular; NT-proBNP: N-terminal pro-brain natriuretic peptide; TAPSE: tricuspid annular plane systolic excursion.

*eGFR was calculated using the modification of diet in renal disease (MDRD) study equation.

†Could be assessed reliably from the tricuspid regurgitation envelope in only nine subjects in sub-study 1 and in seven subjects in sub-study 2.

Table 5.2: Aortic and carotid pulsatile haemodynamics before (pre) and after (post) administration of sublingual nitroglycerin (NTG).

| Variable | Pre-NTG | Post-NTG | P-value |
|---|--------------|-------------|----------|
| Central systolic blood pressure [mmHg] | 133.6(27.6) | 120.5(29.8) | 0.011 |
| Central pulse pressure [mmHg] | 59.5(23.6) | 50(19.4) | 0.06 |
| Central mean arterial pressure [mmHg] | 96.8(17) | 90.5(20.4) | 0.019 |
| Central diastolic blood pressure [mmHg] | 74(15.4) | 70.5(15.3) | 0.18 |
| Aortic pressure–flow relations | | | |
| Aortic characteristic impedance [$dynes \cdot s/cm^5$] | 172(69) | 174(119) | 0.93 |
| Reflection coefficient, 1st harmonic | 0.093(26) | 0.002(26) | 0.017 |
| Reflection coefficient, 2nd harmonic | -0.071(26) | -0.117(26) | 0.16 |
| Reflection coefficient, 3rd harmonic | -0.012(26) | 0.058(26) | 0.054 |
| Forward wave amplitude [mmHg]* | 52.6(20.2) | 47.6(16.6) | 0.26 |
| Backward wave amplitude [mmHg]* | 19.1(9.1) | 16.9(7.5) | 0.21 |
| Backward/forward wave amplitude* | 0.36(0.07) | 0.35(0.08) | 0.33 |
| Time to reflected wave onset [ms] | 78(30) | 89(44) | 0.22 |
| Buckberg index [%] | 130(33) | 129(33) | 0.81 |
| Carotid pressure–flow relations | | | |
| Carotid characteristic impedance [$dynes \cdot s/cm^5$] | 3440(2757) | 1923(1277) | 0.002 |
| Carotid cross-sectional area [cm^2] | 0.38(0.09) | 0.43(0.1) | < 0.0001 |
| Carotid bed vascular resistance [$dynes \cdot s/cm^5$] | 19580(13402) | 13078(8974) | 0.001 |

*Computed in the time domain.

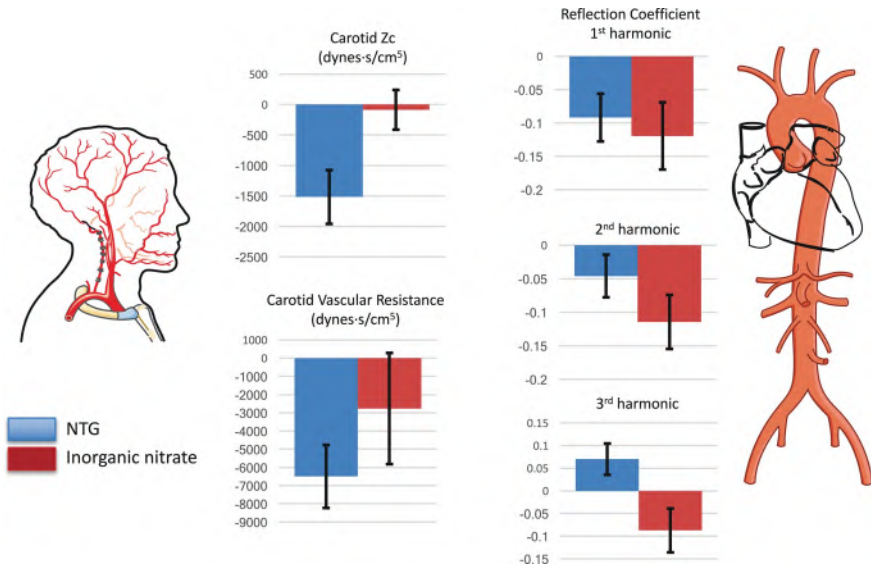


Figure 5.3: Changes in key pulsatile haemodynamic indices in the aorta (right) and the carotid artery (left), in sub-study 1 (sublingual nitroglycerin (NTG), solid blue bars) and sub-study 2 (inorganic nitrate, solid red bars). Mean changes±standard errors are shown. Figure adapted from [4].

Sub-study 1: effects of sublingual nitroglycerin on aortic and carotid haemodynamics

Key haemodynamic parameters measured before and after the administration of NTG are shown in table 5.2 and figure 5.3. NTG reduced central systolic and mean pressure. NTG did not have any significant effect on the amplitude of forward or backward waves, the ratio of backward/forward wave amplitudes, or the time to reflected wave onset. NTG tended to delay the peak of the reflected wave, but did not improve the Buckberg index. NTG did not significantly reduce aortic root characteristic impedance.

The effect of NTG on the real part of the reflection coefficient in the first three harmonics is shown in table 5.2 and figure 5.3. NTG reduced the reflection coefficient of the 1st harmonic, but did not reduce it in the 2nd harmonic and actually tended to increase the reflection coefficient of the 3rd harmonic.

Despite these inconsistent effects on systemic wave reflections, NTG markedly reduced carotid artery Z_c , increased carotid cross-sectional area and reduced carotid bed vascular resistance.

Sub-study 2: effects of inorganic nitrate on aortic and carotid haemodynamics

Key comparisons of haemodynamic parameters obtained after administration of BR vs. PB juice are shown in table 5.3 and figure 5.3. Inorganic nitrate did not significantly reduce central systolic or mean pressure. Similar to NTG, inorganic nitrate did not have any significant effect on the amplitude of forward or backward waves or the ratio of backward/forwards wave amplitudes, and did not reduce aortic root characteristic impedance. However, it significantly delayed the systolic onset of the reflected wave, moved its peak well into diastole, and tended to improve the Buckberg index.

Both table 5.3 and figure 5.3 show the effect of inorganic nitrate on the real part of the reflection coefficient in harmonics 1–3. Inorganic nitrate significantly reduced the reflection coefficient of the 1st and 2nd harmonics, and tended to reduce the reflection coefficient of the 3rd harmonic. In contrast to NTG, inorganic nitrate did not reduce carotid artery Z_c , carotid cross-sectional area, or carotid bed vascular resistance.

Table 5.3: Aortic and carotid pulsatile haemodynamics after administration of 12.9mmol of inorganic nitrate (BR) vs. placebo juice (PB).

| Variable | PB | BR | P-value |
|---|--------------|--------------|---------|
| Central systolic blood pressure [mmHg] | 130(20.8) | 126.6(24.2) | 0.50 |
| Central pulse pressure [mmHg] | 55.3(16.7) | 51(18) | 0.34 |
| Central diastolic blood pressure [mmHg] | 74.7(12.6) | 75.6(9.8) | 0.70 |
| Central mean arterial pressure [mmHg] | 97.6(14.8) | 96.4(15.2) | 0.70 |
| Aortic pressure–flow relations | | | |
| Aortic characteristic impedance, [$dynes \cdot s/cm^5$] | 163(74) | 185(64) | 0.20 |
| Reflection coefficient, 1st harmonic | 0.119(0.15) | -0.001(0.21) | 0.032 |
| Reflection coefficient, 2nd harmonic | -0.03(0.13) | -0.144(0.15) | 0.012 |
| Reflection coefficient, 3rd harmonic | 0.046(0.16) | -0.042(0.16) | 0.091 |
| Forward wave amplitude [mmHg]* | 47.2(13.8) | 47.1(14.1) | 0.98 |
| Backward wave amplitude [mmHg]* | 16.8(6) | 18.8(7.9) | 0.30 |
| Backward/forward wave amplitude* | 0.35(0.05) | 0.39(0.08) | 0.08 |
| Time to reflected wave onset [ms] | 64(30) | 93(30) | 0.016 |
| Buckberg index [%] | 128(29) | 141(25) | 0.053 |
| Carotid pressure–flow relations | | | |
| Carotid characteristic impedance [$dynes \cdot s/cm^5$] | 3013(1867) | 2928(1279) | 0.80 |
| Carotid cross-sectional area [cm^2] | 0.37(0.08) | 0.40(0.12) | 0.15 |
| Carotid bed vascular resistance [$dynes \cdot s/cm^5$] | 19391(13557) | 16624(6800) | 0.38 |

*Computed in the time domain.

5.1.5 Discussion

We assessed the effects of organic and inorganic nitrate on aortic and carotid pulsatile haemodynamics in HFpEF. We demonstrated that organic nitrate substantially reduced BP, but reduced arterial wave reflections inconsistently across the first three harmonics of the pressure–flow relation (in which most of the pulsatile energy is contained). NTG did not significantly improve the Buckberg index and produced profound vasodilatation in the carotid territory, with a reduction in cerebrovascular resistance and carotid characteristic impedance. In contrast, inorganic nitrate produced consistent reductions in wave reflections across the first three harmonics, with a delay in the reflected wave and a trend for improvement in the Buckberg index, without significant cerebrovascular dilatation. These haemodynamic differences likely underlie the differential clinical effects of organic vs. inorganic nitrate observed in recent clinical trials.

While both organic and inorganic nitrate/nitrite ultimately act by increasing NO bioavailability, biochemical differences exist between the two classes of drugs that lead to important differences in their action. Inorganic nitrate is reduced to nitrite and NO via the nitrate–nitrite–NO pathway [210], [211], which involves the reduction of nitrate to nitrite upon ingestion and when nitrate is subsequently excreted by the salivary glands (enterosalivary circulation) [219]. Subsequent reduction of nitrite to NO occurs via: (i) a hypoxia/acidosis-dependent mechanism (which enhances reductions in mi-

crovascular resistance during exercise) [208], and (ii) a ‘paradoxic’ normoxia-dependent mechanism operating in muscular conduit arteries [212], which explains the effect on arterial wave reflections [208], [212]. There also appears to be non-enzymatic nitrite reduction to NO in the acid gastric medium [220]. In contrast, organic nitrates require activation in the cytochrome-P450 system, leading to tonic NO release [37]. Alternative activation via mitochondrial aldehyde dehydrogenase for NTG and other organic nitrates also occurs [37].

Headache is a common side effect of organic nitrates, and can limit compliance with these medications. Hypotension can be seen, and may result in syncope [205], [210]. In contrast, inorganic nitrate has been well tolerated in HFpEF, with no limiting side effects, as reported in two recent trials [208], [209]. No significant hypotension and, in particular, no vasoactive symptoms (such as headache) were reported. These side effect differences are consistent with the haemodynamic effects observed in our study. The profound carotid bed vasodilatation seen in response to NTG, but not inorganic nitrate, is likely due to differences in the activation of these compounds. The high mitochondrial content of neurons may facilitate the activation of NTG by mitochondrial aldehyde dehydrogenase in the brain, thus reducing microvascular resistance in the cerebrovascular bed. In contrast, inorganic nitrite (produced via reduction in inorganic nitrate) is reduced to NO in the microvasculature, but this conversion occurs preferentially in conditions of hypoxia/acidosis [210], [211]. Such conditions are not present in the brain, a highly aerobic organ which demonstrates relatively preserved microvascular oxygenation [221] due to its low resistance and high arterial flow. Therefore, conditions of hypoxia and acidosis are not present in the cerebral microvasculature, explaining the lack of significant effects of inorganic nitrate in our study.

Wave reflections originate at sites of impedance mismatch throughout the arterial tree and return to the heart during ejection, increasing pulsatile load and affecting the LV loading sequence (early vs. late systolic load) [217], [222]. Wave reflections and late systolic load have been shown to cause diastolic dysfunction and myocardial remodelling in animal models [173], [175]. Human studies demonstrated a relationship between increased wave reflections/late systolic load and worse longitudinal LV function [165], LV hypertrophy [174], and a higher risk of incident new-onset HF [177] and readmission after an episode of established acute decompensated HF [172].

In our study, both NTG and inorganic nitrate reduced wave reflections. However, inorganic nitrate produced numerically greater and more consistent reductions in the real part of the reflection coefficient across the first three harmonics, which contain most of the pulsatile energy. In contrast,

NTG reduced the real component of the reflection coefficient only in the 1st harmonic, without an effect in the 2nd harmonic, and an increase in the 3rd harmonic. The real part of the reflection coefficient characterises the net effect of wave reflections on the pressure–flow relation in the aorta at a given harmonic [218]. Inorganic nitrate, but not NTG, delayed the reflected wave and tended to improve the Buckberg index (which characterises the effect of pulsatile haemodynamics on LV systolic load vs. diastolic perfusion pressure). The reduction in wave reflections with inorganic nitrate occurred without reductions in systemic vascular resistance or BP. This clearly indicates that the effects of inorganic nitrate on microvascular resistance/BP and those on wave reflections are not necessarily linked. Reductions in wave reflections can thus be achieved in the absence of significant hypotension. Although these haemodynamic effects are unexpected from the well-known hypoxia-mediated reduction of nitrite in the microvasculature, they are consistent with the recently described paradoxical normoxia-dependent activation of inorganic nitrite in the wall of muscular conduit arteries [212], because muscular arteries are known to modify the magnitude and phase of wave reflections returning to the proximal aorta [217].

The effects of inorganic nitrate on pulsatile load from wave reflections demonstrated in our study, along with the absence of cerebrovascular effects and side effects, is helpful not only to interpret its demonstrated short-term clinical effects (i.e., improvements in exercise tolerance and the absence of side effects such as headache), but may also have implications for its long-term clinical effects. By virtue of reducing wave reflections, which are deleterious for the LV, inorganic nitrate may exert long-term "disease-modifying" effects in HFpEF, potentially reducing LV diastolic dysfunction and remodelling. We are currently assessing the efficacy of sustained administration of inorganic nitrate (oral potassium nitrate) in a randomized cross-over phase IIb trial funded by the National Heart, Lung and Blood Institute (KNO₃CK OUT HFPEF trial; [clinicaltrials.gov NCT02840799](https://clinicaltrials.gov/ct2/show/study/NCT02840799)). A single-dose study with inorganic nitrite yielded promising results in HFpEF [223], and a larger study with inhaled sodium nitrite (INDIE HFPEF; [clinicaltrials.gov NCT02742129](https://clinicaltrials.gov/ct2/show/study/NCT02742129)) is ongoing.

An interesting observation is the absence of significant effects of either NTG or inorganic nitrate on the ratio of amplitudes of backward/forward waves, which is a commonly used index of wave reflections. It should be noted that this ratio does not account for the time-resolved shape of the waveforms (which can be different despite identical amplitudes). Similarly, this ratio does not account for the time at which the reflected wave exerts its effects on central pressure (late systole vs. diastole). Furthermore, the amplitudes of both forward and backward waves are not purely a function

of arterial properties, but are heavily dependent on ventricular contraction dynamics. In addition, the ratio of backward/forward waves is confounded by rectified reflections (i.e., re-reflections in the heart), which substantially contribute to forward wave amplitude [224]. Despite the lack of change in reflection magnitude, detailed analyses in the time domain demonstrated favourable changes (delay in the onset of the reflected wave after ejection, and a trend towards improvement in the Buckberg index) with inorganic nitrate, but not with NTG.

Our study should be interpreted in the context of its strengths and limitations. Strengths include the careful assessment of pulsatile carotid and aortic haemodynamics using state-of-the-art non-invasive pressure–flow analyses, rather than pressure-only approaches. Input impedance assessments distinctly characterise arterial properties distal to the point of measurement, whereas pressure-only approaches (such as assessments of augmentation index) can be confounded by changes in ventricular contraction or preload. Additional strengths of our study include the use of identical methods to measure haemodynamics after organic and inorganic nitrate administration, facilitating the interpretation of differential haemodynamic effects.

Our study also has limitations. Our study populations were relatively small; however, the paired nature of the analyses reduced measurement variability and enhanced detection of drug effects in each sub-study. Owing to the characteristics of the patient population at the VA Medical Center, where most subjects were enrolled, our study populations were composed primarily of men. Our population was predominantly African-American. Larger studies will be required to assess whether the haemodynamic effects of inorganic nitrate differ by ethnicity. Enrollment in the ongoing KNO₃CK OUT HFpEF trial is stratified based on gender and ethnicity; this study is also assessing detailed haemodynamic phenotypes and will clarify this issue. The exclusion of patients with atrial fibrillation reduces generalizability of the findings to the important subject of patients who have atrial fibrillation in the setting of HFpEF. We performed two separate sub-studies with different designs. We tested the effects of NTG compared to the values before drug administration, whereas the effects of inorganic nitrate were tested in a cross-over blinded design. This was an acute administration study, and the chronic effects of these drugs on the carotid and peripheral circulations could be different. The patient population had relatively mild HFpEF as evidenced by the relatively low use of loop diuretics; therefore, these results may not apply to patients who have more severe or advanced HFpEF.

5.1.6 Conclusions

We compared the effects of organic and inorganic nitrates on aortic and carotid pulsatile haemodynamics in patients with HFpEF. We demonstrated that organic nitrate administration reduced arterial wave reflections less consistently than observed with inorganic nitrate. Organic nitrate also produced profound vasodilatation in the carotid territory, with a reduction in cerebrovascular resistance and carotid characteristic impedance, whereas inorganic nitrate did not produce significant cerebrovascular dilatation. These important haemodynamic differences are likely related to the differential clinical effects of these agents documented in recent clinical trials.

5.2 EFFECT OF ORGANIC AND INORGANIC NITRATES ON CEREBROVASCULAR PULSATILE POWER TRANSMISSION IN PATIENTS WITH HEART FAILURE AND PRESERVED EJECTION FRACTION

5.2.1 Introduction

In section 5.1 [4], we found that the acute administration of organic nitrates has a profound effect on carotid haemodynamics, with a marked reduction in carotid bed vascular resistance and dilation of the carotid artery, which may account for the high incidence of headaches and dizziness, respectively. The effects of vasoactive drugs on cerebrovascular haemodynamics, however, may be relevant beyond acute side effects such as headache. Accumulating evidence links increased penetration of pulsatile energy (power) to the brain, with the development and/or progression of cognitive dysfunction and dementia [225], [226], which are common comorbidities in the HFpEF population. The brain is a high-flow, low-resistance organ, in which the microvasculature is more directly exposed to the pulsatility that occurs in central arteries.

Although organic nitrates reduce central pulse pressure in HFpEF [4], the marked associated cerebrovascular vasodilatory effect, with reduction of carotid characteristic impedance and carotid bed vascular resistance, may actually facilitate pulsatile power penetration into the brain microvasculature, potentially undermining the beneficial effects of these drugs on central pulse pressure. The effects of organic nitrates on power penetration to the brain have not been previously assessed, nor have these effects been compared with the effects of inorganic nitrates.

The aim of this study is therefore to quantify and characterise the patterns of hydraulic power carried by waves traveling through the proximal aorta and the carotid artery, and the effects of organic and inorganic nitrates on these parameters among patients with HFpEF.

5.2.2 Methods

The present work is based on previous studies of organic [4] and inorganic nitrates [208] in HFpEF, here referred to as sub-studies 1 and 2 and described in detail in section 5.1 together with the implemented haemodynamic and statistical analyses. Protocols were approved by the University of Pennsylvania and Philadelphia Veterans Affairs (VA) Medical Center Institutional Review Boards, as appropriate. All subjects provided written informed consent be-

fore enrollment. Inclusion and exclusion criteria are described in detail in section 5.1 [4] and elsewhere [208].

5.2.2.1 Wave power analysis

Recently, Mynard *et al.* [70] introduced the concept of wave power as a means to analyse the energy carried by the incident and reflected pressure and flow waves. This technique finds its origin in wave intensity analysis but has the major advantage of allowing for a quantitative analysis of how the energy transmitted by the heart into the aorta is distributed over the arterial tree.

Figure 5.4 shows a graphical depiction of wave power analysis. In Chapter 3 a more detailed description of the method is developed. After digitally resampling signals to 500Hz for a more accurate time-alignment of pressure and flow, wave power ($d\pi$) was defined as the product of the instantaneous changes in pressure and flow ($dP * dQ$). Wave power can be separated into the power carried by forward-traveling ($d\pi_+$) and backward-traveling ($d\pi_-$) waves:

$$d\pi_{\pm} = \pm \frac{1}{4Z_c} (dP \pm Z_c dQ)^2 \quad (5.1)$$

where Z_c is the characteristic impedance (calculated in the frequency domain), and total power ($d\pi$) equals the sum of power carried by forward ($d\pi_+$) and backward ($d\pi_-$) waves.

Wave power is a function of time and demonstrates two major positive peaks: a forward compression wave (FCW), generated by the contraction of the LV in early systole, and a forward expansion wave (FEW), generated as the rate of myocardial shortening is reduced in late systole [70], [227]. We report the area under the curve (AUC) of FCW (red area) and FEW (blue area) at the aorta and the carotid arteries, while the green area is the backward wave (figure 5.4B).

We also computed total hydraulic power, which is related to the rate of energy production and expenditure in the cardiovascular system, as previously described [70]. We calculated the AUC in total hydraulic power as the total energy transmitted from the heart to the aorta and to the carotid artery. We also computed the peak values of the total hydraulic power curve at both locations (figure 5.4C).

We computed the power penetration from the aorta into the carotid vascular circulation as an index based on total hydraulic power parameters (peak power or energy as the AUC) as follows:

$$\%P_{penetration} = \frac{CarotidPower_{parameter}}{AorticPower_{parameter}} * 100 \quad (5.2)$$

5.2.3 Results

General characteristic parameters obtained from both sub-study populations are shown in table 5.1 and described in section 5.1. While general haemodynamic results are summarized in tables 5.2 and 5.3, table 5.4 contains additional haemodynamic parameters for each sub-study.

Sub-study 1: effects of organic nitrate

Parameters obtained from wave and hydraulic power analysis before and after NTG intake are summarized in table 5.4. Aortic and carotid FCW and FEW were not significantly different after NTG administration. There was a reduction in the total aortic hydraulic power energy (1.53J/beat to 1.35J/beat, change: 11.8% decrease, $P = 0.01$) and a trend towards a decrease in peak hydraulic power (7.26W to 6.59W; change: 9.2% decrease, $P = 0.06$). In contrast, there was a significant increase in peak carotid hydraulic power (0.39W to 0.54W; change: +38.5% increase, $P = 0.008$) after NTG administration. In figure 5.5A, the post-NTG change in total hydraulic power parameters is clear. The observed increase in carotid hydraulic power despite a reduced aortic hydraulic power implies an increase in the percentage of power transmission from the aorta into the carotid (peak total hydraulic power penetration: 5.68% vs. 8.62%; $P = 0.001$; total hydraulic energy penetration: 8.69% vs. 11.63%; $P = 0.01$, figure 5.6A).

Sub-study 2: effects of inorganic nitrate

Table 5.4 displays the calculated wave and hydraulic power parameters for sub-study 2. No significant changes were found for aortic or carotid values between PB and BR intake. Figure 5.5B shows the percent difference in total hydraulic power parameters at the aorta and the carotid arteries in the BR

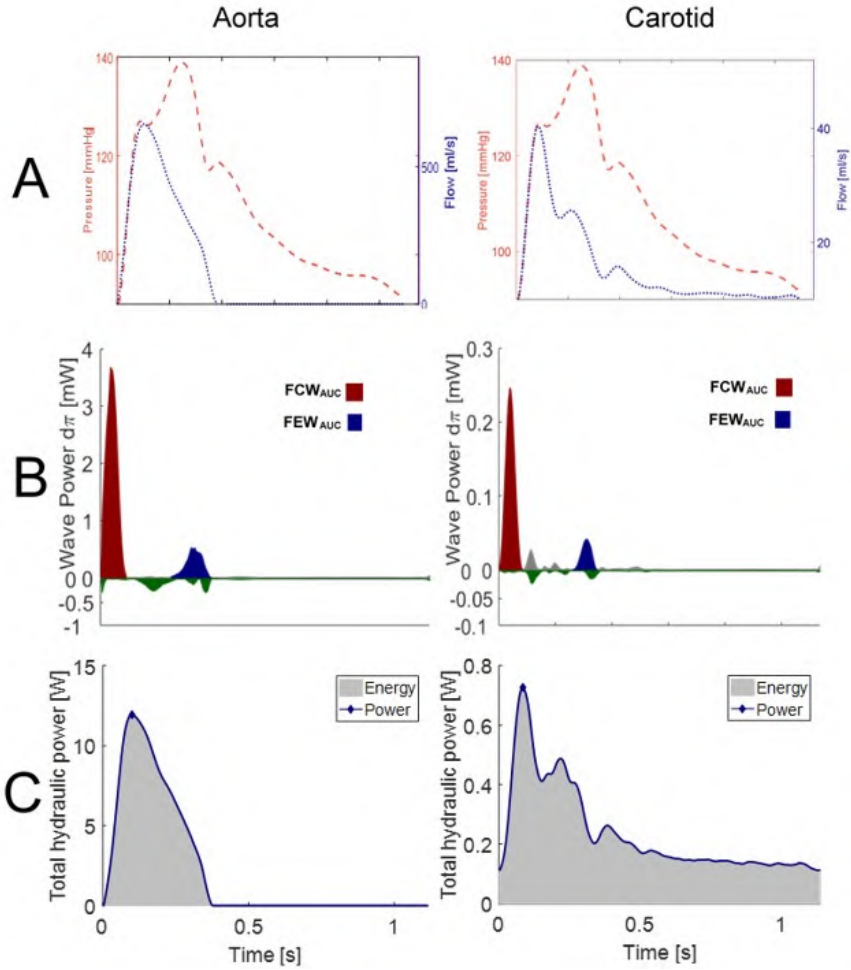


Figure 5.4: Graphical depiction of wave and hydraulic power analysis to illustrate steps and parameters extracted, including A) tonometry (red dashed line) and ultrasound (blue dotted line) signals alignment; B) wave power analysis ($d\pi$); and C) total hydraulic power analysis and selected parameters: AUC (Energy, gray area) and peak values (Power, blue diamond). At left and right panels, aortic and carotid signals and curves are shown, respectively. Displayed signals are pre-NTG. AUC: area under the curve; FCW: forward compression wave (red area); FEW: forward expansion wave (blue area); green represents the backward wave. Figure adapted from [3].

intervention compared to the PB intervention. Lastly, figure 5.6B displays a comparison of the percent changes in power penetration parameters between these 2 conditions, demonstrating non-significant differences between these haemodynamic parameters after PB vs. BR intake.

Table 5.4: Aortic and carotid haemodynamics and power analysis before (Pre-) and after (Post-) administration of sublingual nitroglycerin (NTG) (sub-study 1) and after nitrate-depleted (PB) and nitrate-rich beet root juice administration (sub-study 2).

| Variable | Sub-study 1 (organic nitrate) | | | Sub-study 2 (inorganic nitrate) | | |
|---|-------------------------------|----------------|---------|---------------------------------|-----------------|---------|
| | Pre-NTG | Post-NTG | P-value | PB | BR | P-value |
| Haemodynamics | | | | | | |
| Cardiac output [$l \text{ min}^{-1}$] | 5.64(1.40) | 5.81(1.23) | 0.32 | 5.40(1.42) | 4.89(1.15) | 0.04 |
| Stroke volume [ml] | 90.41(21.91) | 89.07(21.64) | 0.65 | 83.58(16.02) | 78.71(15.05) | 0.07 |
| Heart rate [bpm] | 63.23(10.82) | 66.58(11.06) | 0.004 | 65.19(12.78) | 62.28(10.39) | 0.09 |
| Peak aortic blood flow [$cm^3 \text{ s}^{-1}$] | 408.61(100.90) | 410.03(103.16) | 0.93 | 371.71(64.88) | 350.39(65.71) | 0.20 |
| Mean aortic blood flow [$cm^3 \text{ s}^{-1}$] | 94.01(23.31) | 96.86(20.42) | 0.32 | 90.10(23.59) | 81.45(19.12) | 0.04 |
| Peak carotid blood flow [$cm^3 \text{ s}^{-1}$] | 23.92(15.35) | 34.31(21.51) | 0.001 | 21.25(11.62) | 22.19(13.51) | 0.74 |
| Mean carotid blood flow [$cm^3 \text{ s}^{-1}$] | 9.80(6.73) | 13.08(8.38) | 0.008 | 9.35(5.24) | 10.03(6.91) | 0.60 |
| Aortic wave power analysis | | | | | | |
| FCW_{AUC} [mJ] | 0.129(0.053) | 0.117(0.050) | 0.26 | 0.107(0.046) | 0.093(0.043) | 0.31 |
| FEW_{AUC} [mJ] | 0.041(0.031) | 0.032(0.023) | 0.17 | 0.036(0.017) | 0.033(0.015) | 0.53 |
| Aortic hydraulic power analysis | | | | | | |
| Power [mW] | 7256(2549) | 6591(2204) | 0.06 | 6666(2165) | 5845(1846) | 0.20 |
| Energy [mJ] | 1531(511) | 1351(428) | 0.01 | 1429(447) | 1275(418) | 0.18 |
| Carotid wave power analysis | | | | | | |
| FCW_{AUC} [mJ] | 0.007(0.006) | 0.010(0.011) | 0.12 | 0.0056(0.0040) | 0.0049(0.0027) | 0.40 |
| FEW_{AUC} [mJ] | 0.0014(0.0014) | 0.0018(0.0020) | 0.25 | 0.0014(0.0009) | 0.0011(0.00045) | 0.13 |
| Carotid hydraulic power analysis | | | | | | |
| Power [mW] | 387(240) | 536(383) | 0.008 | 356(207) | 351(195) | 0.91 |
| Energy [mJ] | 127(78) | 150(84) | 0.12 | 126(76) | 129(68) | 0.90 |

PB: placebo; BR: nitrate-rich beetroot juice; AUC: area under the curve; FCW: forward compression wave; FEW: forward expansion wave.

5.2.4 Discussion

In this study, we quantified the effect of organic and inorganic nitrates on pulsatile power penetration to the brain in patients with HFpEF. Administration of NTG, an organic nitrate, led to a significant reduction of aortic hydraulic power, an increase in power penetration to the carotid artery (due to cerebrovascular vasodilation), and an absolute increase in carotid hydraulic power. In contrast, inorganic nitrate administration did not induce significant changes in aortic and carotid wave power or percentage of power penetration. Our findings have important implications for our understanding of the cerebrovascular haemodynamic effects of organic and inorganic nitrates in this population, which in turn may have implications for the adverse effect profile of these drugs and cerebro-microvascular health.

In contrast to inorganic nitrate [210], organic nitrates result in undesirable side effects, such as pulsatile headache, flushing, hypotension or even syncope [4], [201]. In particular, recent trials of organic nitrates in HFpEF

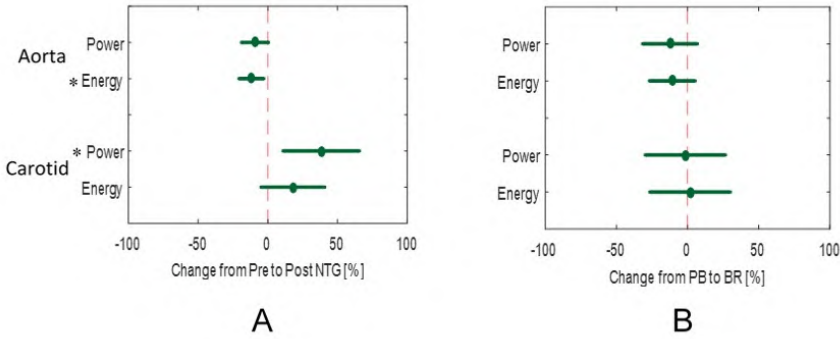


Figure 5.5: Forest plots describing the change in percentage of selected parameters. A) After the administration of sublingual NTG; B) Between nitrate-depleted (PB) and nitrate-rich (BR) beet root juice intake.

* Indicates a statistically significant change ($P < 0.05$). Figure adapted from [3].

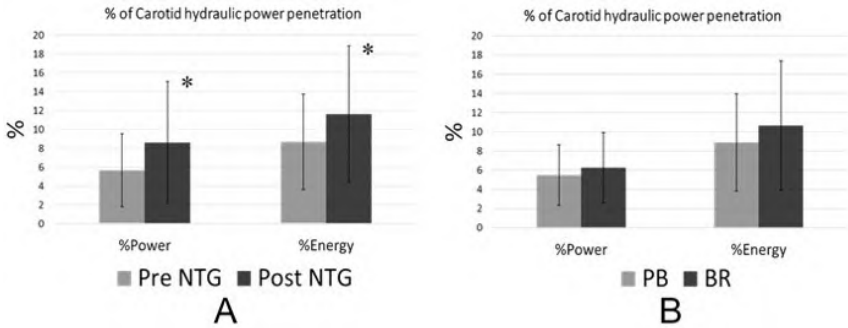


Figure 5.6: Percentage of carotid total hydraulic power penetration. A) After the administration of sublingual NTG; B) Between nitrate-depleted (PB) and nitrate-rich (BR) beet root juice intake.

* Indicates a statistically significant change against (A) pre-NTG or (B) PB. Figure adapted from [3].

have demonstrated poor tolerability, with a high incidence of side effects [205], [207] and frequent discontinuation of long-term use [206]. The important incidence of headaches is possibly related to the increase on pulsatile power penetration to the cerebrovascular territory demonstrated in our study. However, the importance of this haemodynamic effect may extend beyond its role in headaches. Increased penetration of pulsatile power to the brain is progressively recognized as an important factor in the development of cognitive dysfunction and dementia [225], [226], which are common comorbidities in the HFpEF population [228], [229]. Due to its high blood flow needs, the brain vasculature is a low-resistance bed, in which the microvasculature is more directly exposed to the pulsatility that occurs in conduit

vessels. Therefore, the pulsatile power transmission from the aorta to the conduit branches that feed the cerebrovascular territory is a key determinant of pulsatile haemodynamics in the cerebrovascular microcirculation. We demonstrate, for the first time, that despite the reduction in BP induced by NTG in HFpEF, the marked associated cerebrovascular vasodilatory effect actually leads to increased (rather than decreased) hydraulic power transmission into the carotid territory. In contrast, we demonstrate that inorganic nitrates do not increase pulsatile power penetration to the brain.

Nitrates/nitrites-related adverse events can limit compliance with these medications and have an undesired impact on various outcomes (such as outpatient physical activity) in HFpEF. Detailed assessments of their haemodynamic effects can contribute to elucidate the mechanisms of these side effects. Given that the incidence of headaches has been reported to be greater with organic vs. inorganic nitrates, our study focused on the differential effects of these agents on brain haemodynamics. However, we acknowledge that the relationship between our haemodynamic findings and the incidence of adverse events should be further investigated in future studies.

Additionally to the strengths and limitations discussed in section 5.1, a particular strength of the research discussed in this section is the implementation of an ad hoc method to assess pulsatile power in the aorta and carotid arteries, as recently proposed by Mynard *et al.* [70]. This method quantifies the distribution of wave power at junctions, is relatively insensitive to diameter variations, and is quantitatively linked to transient changes in hydraulic pressure power, a concept related to the rate of energy production and expenditure in the cardiovascular system.

We note that the haemodynamic effects reported herein for inorganic nitrate likely do not apply to short-acting inorganic nitrite preparations. Inhaled sodium nitrite, which is currently being studied in HFpEF, demonstrates markedly different pharmacokinetic properties compared to orally administered inorganic nitrate [230]. The half-life of inhaled sodium nitrite is only ~ 35 minutes [231] (in contrast to several hours for inorganic nitrate) [232] and intermittent inhaled administration is associated with pronounced circulating level fluctuations, which may cause hypotensive episodes in elderly patients with HFpEF. To our knowledge, no studies have assessed the cerebrovascular haemodynamic effects of sodium nitrite in HFpEF. Ongoing trials (the KNO₃CK OUT HFpEF trial with orally administered potassium nitrate and the INDIE HFpEF trial with inhaled sodium nitrite [230]) will help clarify the side effect profiles and haemodynamic differences between inorganic nitrite and nitrate in this patient population.

5.2.5 Conclusions

In conclusion, to the extent of our knowledge, this study is the first to assess the effects of organic and inorganic nitrates on aortic and carotid wave and hydraulic power and energy in patients with HFpEF. Our study demonstrates that organic nitrates increase power penetration from the aorta into the carotid, which leads to a significant increase in carotid pulsatile hydraulic power, despite a reduction in aortic power. In contrast, inorganic nitrate administration did not induce significant changes in aortic and carotid wave and hydraulic power or percentage of power penetration. These haemodynamic effects likely have implications for the pulsatile haemodynamic stress of the microvasculature of the brain. In the short term, these haemodynamic differences may contribute to the differential incidence of side effects (such as headaches) with organic vs. inorganic nitrate therapy. In the long term, they may have implications for cognitive decline. However, the causal link between carotid pulsatile haemodynamics and cognitive decline, particularly in the setting of vasodilator therapy, requires further study.

EXPLORATION AND DEVELOPMENT OF DEDICATED TOOLS FOR THE ASSESSMENT OF ARTERIAL HEALTH (IN NON-ROUTINE CONDITIONS)

Previously, Chapter 4 and Chapter 5 addressed novel research based on cardiac and vascular function assessment. In this chapter, further dedicated tools to study the cardiovascular system are explored. Dissimilar topics, such as autonomic regulation, protocol standardization or space exploration find a common ground in cardiovascular research, and can impact and expand current knowledge.

With this perspective, the chapter starts presenting a study concerning the influence of the autonomic nervous system (ANS) in adjustments of the cardiovascular function under stress conditions. Indeed, the regulatory influence of the ANS (see Chapter 1) is paramount for the proper functioning of the cardiovascular system, and the understanding of these interactions can elucidate unclear adaptation and pathological mechanisms. Then, the second section introduces a web application to support the standardization of vascular stiffness parameters and to promote their widespread use in common clinical practice. Finally, the third section is an exploratory feasibility study of a continuous physiological and medical monitoring system, based on tonometry and ultrasound measurements, with potential applications in space science.

6.1 CAROTID HAEMODYNAMICS DURING SYMPATHETIC NERVOUS SYSTEM STIMULATION VIA HANDGRIP AND COLD PRESSOR TESTING IN YOUNG HEALTHY SUBJECTS: A FEASIBILITY STUDY

This section is based on a study published in *Artery Research* under the title “*Carotid haemodynamics during sympathetic nervous system stimulation via handgrip and cold pressor testing in young healthy subjects: A feasibility study*”, vol. 8, no. 4, pp. 178-188, 2014 [5].

6.1.1 Introduction

Common functional measurements to assess the cardiovascular system (cardiac systolic and diastolic function or arterial stiffness, for example) are typically performed during resting conditions. However, in real life, humans are active and there is an intrinsic variability in the cardiovascular status that must be considered when interpreting the results of these type of tests. This variability is related to the ANS, which regulates the visceral functions of the body and helps to control arterial blood pressure (BP), sweating, body temperature, and many other activities. One of the most striking characteristics of the ANS is the rapidity and intensity with which it can change visceral functions [233]. Thus, the nervous system, acting through the autonomic nerve fibres, can exert rapid and effective control of many, if not most, of the internal functions of the body. The signals are transmitted to the body through two major subdivisions termed sympathetic and parasympathetic system [233]. Therefore, assessment of the ANS can provide additional information of the cardiovascular control and general state of a subject’s health. This assessment can be done through the use of sympathetic nervous stressors, such as the hand grip test (HGT) or the cold pressor test (CPT).

Physical activity, for example isometric exercise as in the HGT, produces intensity-dependent increases in arterial BP that are mediated by central signals arising from higher brain centres (i.e., central command) and by peripheral feedback from skeletal muscle (i.e., exercise pressor reflex or EPR) with further modulation provided by the arterial baroreflex [234] (see figure 6.1A). The arterial baroreflex is a critical cardiovascular reflex that provides a continuous buffering of acute fluctuations of arterial BP controlling two of the major variables that determine it: cardiac output (CO) and systemic vascular resistance (SVR) [235]. HGT produces simultaneous increases in BP and heart rate (HR), which are not (totally) blunted by the arterial baroreflex. This led to the speculation that baroreflexes are altered in some fashion to allow this deviation from normal baroreflex physiology to occur [236]. The current understanding of the mechanisms for baroreflex resetting during exercise is

that the feed forward mechanism of central command is probably the primary regulator of baroreflex resetting, while the negative feedback mechanism of the EPR is more of a modulator of resetting [237] (see figure 6.1C).

CPTs are often performed in the clinical evaluation of autonomic disorders to ensure the integrity of central vasomotor processes and their efferent pathways. The test elicits remarkable increases in arterial pressure and muscle sympathetic nerve activity (MSNA) with no significant changes in HR [238]. In most healthy human subjects, cold nociceptors in the skin conduct afferent signals that serve to regulate MSNA [238]. Thus, CPT is performed to assess sympathetic neural control of the peripheral and coronary circulations in humans [239] (see figure 6.1B). Besides, CPT is suggested to be a method that mimics the effects of chronic pain conditions effectively because of its unpleasantness with excellent reliability and validity. Hence, fast and efficient evaluations of pain treatments are made possible in healthy participants, making this technique a useful and less expensive prerequisite to clinical studies [240].

Both described stressors have distinct neural paths and receptors [238] (see figure 6.1) and, consequently, a differential response to each stimulus should be measurable selecting an adequate anatomical target and appropriate parameters. We hypothesize that the functional assessment of carotid arterial properties and haemodynamics would be a good candidate for such investigation due to its relation with the baroreflex.

The aim of this study was therefore to assess the feasibility of non-invasively monitoring carotid haemodynamics in response to sympathetic nervous system stressors. Ultrasound was used to assess blood flow velocity and carotid diameter distension waveforms throughout the protocol, with subsequent derivation of functional parameters related to the tonus of the carotid artery (stiffness - local carotid pulse wave velocity) and the downstream vascular bed (reflection magnitude).

6.1.2 Methods

6.1.2.1 Subjects

Measurements were performed on twelve young (presumably) healthy volunteers (six males, six females). Subjects were instructed to refrain from eating and ingesting beverages containing caffeine and alcohol for at least 2h before testing. Volunteers were studied in supine position in a quiet, lightly dimmed room (temperature 25 – 28°C).

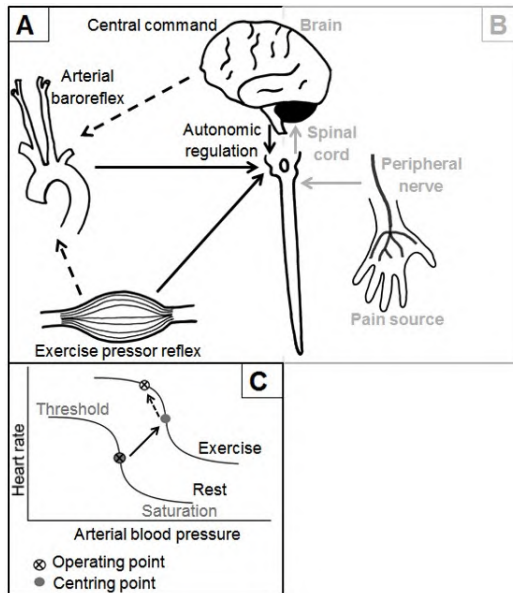


Figure 6.1: Distinct neural paths of stressors. A) Isometric exercise produces intensity-dependent increases in arterial BP that are mediated by central signals arising from higher brain centres (i.e., central command) and by peripheral feedback from skeletal muscle (i.e., exercise pressor reflex or EPR) with further modulation provided by the arterial baroreflex [234]. Classically, the central command is defined as a feed forward mechanism involving parallel activation of motor and cardiovascular centres [241]. In the EPR or the “muscle metaboreflex”, neural signals arising from stimulation of chemosensitive receptors in the contracting muscles would activate reflexively the cardiovascular control areas in the medulla [242]. The arterial baroreflex is a critical cardiovascular reflex that provides a continuous buffering of acute fluctuations of arterial BP controlling the two variables that determine it: CO and SVR [235]. B) Cold pressor test: in most healthy human subjects, cutaneous application of ice water (i.e., CPT) increases arterial BP, HR, and SVR. Cold nociceptors in the skin conduct afferent signals by unmyelinated C-fibres, and the pathway may involve vasomotor centres that serve to regulate MSNA. Thus, CPT is performed to assess sympathetic neural control of the peripheral and coronary circulations in humans [239]. C) Baroreflex stimulus-response curve during rest and exercise (resetting). The centring point is the point at which there is an equal depressor and pressor response to a given change in BP. The operating point is the prestimulus BP. The threshold is the point where no further increases in HR are elicited by further reductions in BP. Saturation is the point where no further decreases in HR are elicited by further increases in BP. The relocation of the operating point (away from the centring point and closer to the threshold of the stimulus-response curve) with increasing exercise intensity modifies the baroreflex in a more optimal condition to counter hypertensive stimuli [241]. Figure adapted from [5].

6.1.2.2 *Protocol instrumentation and setup*

Measurements included continuous haemodynamic recordings using a finger cuff with an optical plethysmograph (Nexfin, BMEYE B.V., Amsterdam, The Netherlands) that provided systolic blood pressure (SBP), diastolic blood pressure (DBP), the BP waveform and HR. Ultrasound measurements of the carotid artery were done at discrete moments during the protocol (Vivid7, GE-Vingmed Ultrasound AS, Horten, Norway) and consisted of: 1) diameter distension measurements using a “wall tracking” application [72] and 2) pulsed-wave (PW) Doppler measurements.

Figure 6.2 shows the general setup during the protocol. Analogue outputs of the Nexfin monitor were connected to an external acquisition device (SC-2345, National instruments, Austin, Texas, United States), which sent the signals to a PC. During measurements, a holder was used to fix the ultrasound probe on the carotid artery (volunteer’s dominant hand side). In figure 6.2A, the setup for the HGT is shown. The hand grip device (Precision dynamometer G200, Biometrics Ltd, Newport, United Kingdom) was connected to the external PC to provide a visual feedback to the volunteer during the test. In figure 6.2B, the CPT setup is shown. During the test, the subject immersed the dominant hand in cold water for about 3 min.

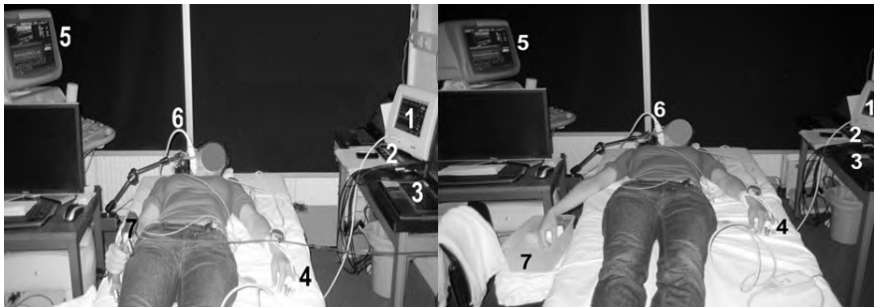


Figure 6.2: General protocol setup. (1) Nexfin monitor (Nexfin, BMEYE B.V., Amsterdam, The Netherlands), (2) National instruments acquisition device (SC-2345, National instruments, Austin (Texas), United States), (3) External PC, (4) Finger cuff, (5) Ultrasound device (Vivid7, GE-Vingmed Ultrasound AS, Horten, Norway), (6) Ultrasound probe. Left) HGT: (7) Hand grip device (Precision dynamometer G200, Biometrics Ltd, Newport, United Kingdom). Right) CPT: (7) Cold water. Figure adapted from [5].

6.1.2.3 *Protocol implementation*

Before the start of the protocol, basic anthropometric measurements were performed while a general explanation of the procedures was given to each

Table 6.1: Overview of the implemented protocol.

| Step | Action | | |
|--------------------|--|----------------|----------|
| MVC | Determination of Maximal Voluntary Contraction | | |
| Rest | 20 min (minimum) | | |
| HGT _{30%} | Baseline | 30% MVC (120s) | Recovery |
| Rest | 10 min (minimum) | | |
| HGT _{40%} | Baseline | 40% MVC (90s) | Recovery |
| Rest | 10 min (minimum) | | |
| CPT | Baseline | CPT (180s) | Recovery |

HGT_{30%}: hand grip test performed at 30% of the MVC; HGT_{40%}: hand grip test performed at 40% of the MVC; CPT: cold pressor test.

volunteer. Then, the subject was asked to lay down and to perform three brief maximal voluntary contractions (MVCs) with her/his dominant hand using the hand grip device. The highest value obtained was selected as the reference value and defined as the MVC. Following, to achieve a haemodynamic steady state in each volunteer, there was an initial resting period of at least 20 minutes in supine position.

Hand grip test (isometric exercise)

The first test performed was an HGT at 30% of the MVC (HGT_{30%}) followed by a resting period. Taking into account the time limitations and values used in literature [238], [243]–[245], it was decided that a resting time period of 10 minutes in between tests was adequate. Next, a second HGT was carried out at 40% of the MVC (HGT_{40%}).

For both tests, ultrasound measurements were obtained at baseline, during the test and upon recovery. The time span of the test period was 2 minutes for HGT_{30%} and 90s for HGT_{40%}, during which time subjects were provided with visual feedback of their contraction force production. In all cases, ultrasound measurements were performed only after one minute of the onset of test and recovery periods.

Cold pressor test

With a resting period in between HGT_{40%} and CPT of at least 10 minutes, and after baseline measurements were performed, the subjects immersed their dominant hand into a cold water bath (0–5°C) up to the wrist for a period of ~ 3 minutes. Two ultrasound measurements were performed, one during the first half of the test (between the onset and 90s) and the second during the final part of the test (between 90s and the end). This second measurement was eventually used to perform the analysis of results. This

test was performed as fast as possible to avoid discomfort of the volunteers, therefore the timing differed accordingly for each subject. When the test period was over, the last ultrasound measurement was obtained after at least 1 minute recovery.

A general summary of the protocol is presented in table 6.1.

6.1.2.4 Signal processing

All post processing was done off-line, meaning that all signals were saved, stored and labelled for later use. Continuous haemodynamic signals (SBP/DBP/HR/BP wave) were sampled at 200Hz and saved as ASCII files. These signals were divided into three established periods (baseline, test and recovery). The test period was split as well in two parts, being expected that the reaction to the stressors should be more prominent during the second part (see figure 6.3), and therefore this was used for further analysis. Finally, a mean value (and standard deviation) of each period was calculated and used for post processing.

Mean arterial pressure (MAP) was calculated from DBP and SBP values using the equation [246]:

$$MAP = 0.4 * (SBP - DBP) + DBP [mmHg] \quad (6.1)$$

An RF-based wall-tracking application [72] developed in MATLAB[®] was used to obtain a diameter distension waveform (see figure 6.4, top left) from which carotid distension ($\Delta D/D$) was calculated as:

$$\frac{\Delta D}{D} = \frac{D_s - D_d}{D_d} \quad (6.2)$$

where D is the outer diameter (measured between the media-adventitia transition of far and near wall) of the carotid artery during systole (D_s) or diastole (D_d). Results represent the mean value and standard deviation of at least 3 cardiac cycles (see figure 6.4. Middle left: carotid diameter distension curve - solid line).

The envelope of the blood flow velocity waveform was automatically traced from PW Doppler mode measurements and divided in individual cardiac cycles, providing information about the flow velocity changes in the carotid artery. At least three cycles were obtained from each image for deriving mean and peak blood flow velocities (see figure 6.4. Top right: example segmentation of a PW Doppler mode image. Middle left: carotid blood flow velocity curve - dashed line).

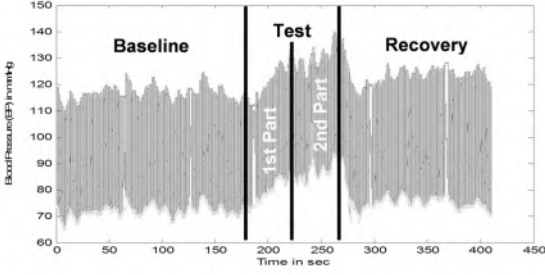


Figure 6.3: Haemodynamic signal obtained with the Nexfin monitor (finger cuff) during HGT_{40%}. Derived parameters from the signal were obtained: SBP (average from the top signal envelop), DBP (average from the bottom signal envelop) and BP wave. Haemodynamic parameters were calculated by the division of the signal in three periods (baseline, test and recovery) to obtain a final value as the mean of each period. Using timing data, the test period was divided in two parts. The second part was used to calculate derived parameters and to perform comparisons against baseline data. Figure adapted from [5].

6.1.2.5 Carotid pulse wave velocity and reflection magnitude

As carotid diameter distension and blood flow velocity curves are not acquired simultaneously, they had to be aligned in time to perform further processing. We implemented a correlation method [74] to automatically align the signals (see figure 6.4, middle-left).

As described by Feng *et al.* [75], the local pulse wave velocity (PWV_{WH}) can be derived from the blood flow velocity curve (U) and the natural logarithm of the diameter distension curve ($\text{Ln}D$) via the well-established water hammer equation (equation (6.3)). Plotting $\text{Ln}D$ against U ($\text{Ln}DU$ loop in figure 6.4, middle-right), a linear portion is expected during the early part of systole, when it is most probable that reflected waves do not exist [75]. Two points were selected (manually) from this linear portion of the $\text{Ln}DU$ loop to determine the slope of the segment, and therefore, the local PWV_{WH} :

$$PWV_{WH} = \pm \frac{1}{2} \frac{dU_{\pm}}{d\text{Ln}D_{\pm}} \left[\frac{m}{s} \right] \quad (6.3)$$

Adapting the water hammer equation to relate changes of diameter (D) and blood flow velocity (U), forward (D_+ , U_+) and backward (D_- , U_-) waveforms can be obtained (see figure 6.4, bottom) from which the magnitude of

wave reflections can be derived as the ratio of the amplitude of D_+ and D_- [40]:

$$RM = \frac{\max(D_-) - \min(D_-)}{\max(D_+) - \min(D_+)} = \frac{|D_-|}{|D_+|} \quad (6.4)$$

6.1.2.6 Statistical analysis

Wilcoxon signed rank tests were applied to compare baseline against test and recovery mean values. A statistical significant difference was accepted at a p-value ≤ 0.05 . Data are presented as mean \pm standard deviation.

6.1.3 Results

Measurements were technically feasible in all 12 subjects throughout the complete protocol. However, for 2 subjects, ultrasound data during HGT_{30%} was missing due to storage problems (unrelated to feasibility) while data from one volunteer was missing for HGT_{40%} due to post processing difficulties (see table 6.2). The general features of the sample population were: mean age, height and weight of 26 ± 2 years, $173 \pm 11\text{cm}$ and $72 \pm 13\text{kg}$, respectively.

Hand grip test: haemodynamic parameters

There was a consistent increase of BP (SBP, DBP, MAP and PP) during both HGT's in comparison to baseline values, as well as an increase in HR (63.38 ± 6.62 to $69.29 \pm 8.76\text{bpm}$ for HGT_{30%}; 61.72 ± 6.43 to $74.80 \pm 12.98\text{bpm}$ for HGT_{40%}). MAP did not fully return to baseline levels over the recovery period, but HR did. Furthermore, blood flow velocity showed a high variability during the tests and no clear trends were observed (see figure 6.5 and table 6.2).

Hand grip test: carotid (local) parameters

The change in carotid diameter during HGT_{30%} was not statistically significant from baseline, in contrast to the diameter during HGT_{40%}, which was significantly increased. In addition, carotid distension ($\Delta D/D$) showed a remarkable decrease during both HGTs. During the recovery period, carotid diameter and distension returned to baseline levels.

As figure 6.6 and table 6.2 evince, local PWV_{WH} and RM demonstrated a general high variability, which increased during the testing periods. No clear trends were detectable for these parameters throughout the protocol.

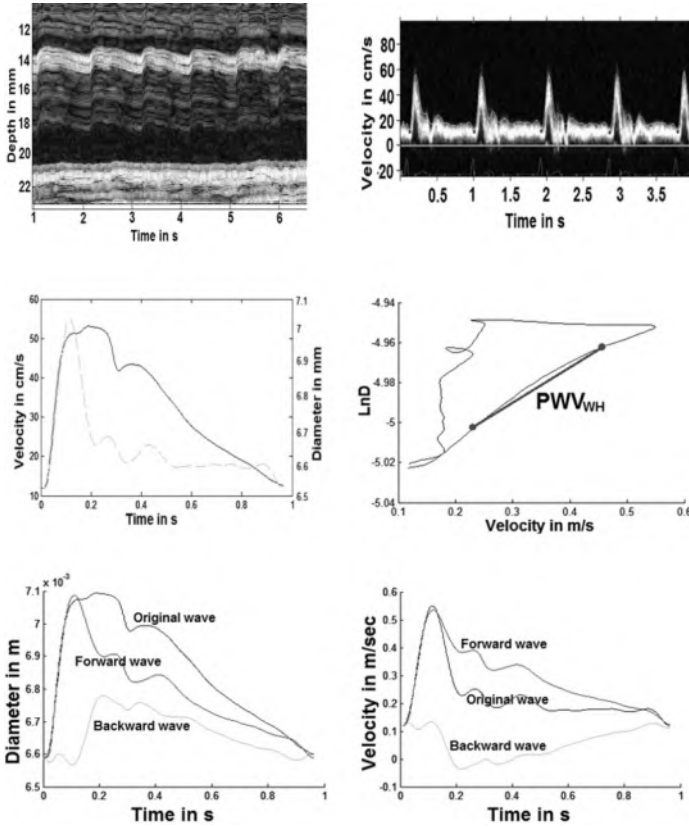


Figure 6.4: General segmentation and post processing methodologies applied to protocol signals. Top left) Manual wall tracked segmentation results of carotid distensibility using ultrasound images of the carotid artery (dominant hand side) during CPT. Top right) PW-mode ultrasound signal of carotid blood flow velocity and segmentation results: signal envelop was used as velocity curve. The velocity curve was divided in cardiac cycles to obtain an average curve (of at least 3 cardiac cycles) for post processing: each cycle was defined between two consecutive minimal blood flow velocity points before the steep rise in velocity during systole. Mean blood flow velocity was obtained as the average of the values of a velocity curve, while the peak blood flow velocity was the maximal value of the velocity curve. Middle left) Time alignment result of the carotid blood flow velocity (dashed line) and diameter distension (solid line) curves using the correlation method [74]. Middle right) LnDU-loop built plotting the natural logarithm of the carotid artery diameter distension curve against the blood flow velocity curve. According to the used methodology [75], the slope of the loop's linear portion indicates the value of the local pulse wave velocity (PWV_{WH}). Bottom) Wave separation [75] results of carotid artery: left) diameter distension and right) blood flow velocity curves, indicating the original wave and the derived forward and backward waves. Figure adapted from [5].

Cold pressor test: haemodynamic parameters

The highly significant increase in BP during CPT is comparable with the one obtained during both HGTs while the increase in HR was more modest for CPT. MAP did not fully return to baseline values upon recovery, but HR did. Again, velocity parameters were highly variable, and none of the observed differences were statistically significant. All results are shown in figure 6.5 and table 6.2.

Cold pressor test: carotid (local) parameters

During CPT, carotid diameter increased while distension decreased, and all parameters returned to baseline values upon recovery. PWV_{WH} and RM exhibited less variability than during HGT. PWV_{WH} increased significantly and did not return to baseline values during recovery while RM presented a borderline significant increase ($p = 0.054$) during the test period (see figure 6.6 and table 6.2).

6.1.4 Discussion

Compatible with previous results [234], [238], [241], [247], [248], HGT leads to an increase in both BP (around 10mmHg for MAP) and HR ($+6 - 13\text{beats/minute}$). Functionally, this allows the baroreflex to operate at the prevailing BP evoked by the exercise [237] (see figure 6.1C). As illustrated in figure 6.5, the CPT led to a similar increase in BP ($+11\text{mmHg}$), but this increase was not accompanied by a similar increase in HR, as precedent results on CPT have shown [238], [239], [249], [250]. This is consistent with the notion, outlined in the introduction, that physical exercise (in this case isometric exercise) somewhat “blunts” the baroreflex, suppressing the reduction in HR that one would anticipate in case of active pressure control. Moreover, prior experimentation has verified that the arterial baroreflex is reset from rest to exercise in direct relation to the work intensity [40]. This plausibly explains the difference in HR during $\text{HGT}_{30\%}$ (lower exercise intensity, lower HR) and $\text{HGT}_{40\%}$ (higher exercise intensity, higher HR). Additionally, baroreflex resetting has been observed at the onset of isometric exercise [251], [252]. Baroreflex resetting also occurs during CPT although only about 120s after the onset of the cold stimulus [253]. This is consistent with our data, demonstrating that the HR was still under baroreflex control when measurements were performed (see figure 6.5 and table 6.2).

Similarly to BP trends during all tests, carotid diameter showed an increase, even if it was less prominent. Due to a higher distending pressure, an

Table 6.2: General results of selected parameters during the implemented protocol (n = 12).

| Parameter | Test | Baseline | Test period | Recovery |
|------------------------------------|--------------------|----------------|-----------------------------|-----------------------------|
| MAP [<i>mmHg</i>] | HGT _{30%} | 91.00 ± 11.86 | 100.70 ± 13.33 ^b | 94.00 ± 12.22 ^a |
| | HGT _{40%} | 89.83 ± 6.85 | 101.03 ± 9.05 ^b | 92.49 ± 7.63 ^a |
| | CPT | 91.03 ± 6.97 | 102.24 ± 8.59 ^b | 93.96 ± 7.89 ^a |
| SBP [<i>mmHg</i>] | HGT _{30%} | 119.49 ± 16.13 | 131.31 ± 19.71 ^b | 125.01 ± 17.32 ^a |
| | HGT _{40%} | 118.85 ± 8.12 | 131.13 ± 11.86 ^b | 123.59 ± 9.65 ^a |
| | CPT | 119.85 ± 9.23 | 133.53 ± 11.66 ^b | 124.08 ± 9.80 ^a |
| DBP [<i>mmHg</i>] | HGT _{30%} | 72.01 ± 9.47 | 80.30 ± 9.58 ^b | 73.32 ± 9.28 |
| | HGT _{40%} | 70.48 ± 6.64 | 80.97 ± 7.72 ^b | 71.75 ± 6.74 |
| | CPT | 71.81 ± 6.07 | 81.38 ± 7.21 ^b | 73.88 ± 6.94 ^a |
| PP [<i>mmHg</i>] | HGT _{30%} | 47.48 ± 8.44 | 51.00 ± 11.67 ^a | 51.69 ± 9.68 ^b |
| | HGT _{40%} | 48.38 ± 4.95 | 50.16 ± 6.50 ^a | 51.84 ± 5.13 ^b |
| | CPT | 48.04 ± 5.62 | 52.14 ± 7.05 ^a | 50.21 ± 4.59 ^a |
| HR [<i>bpm</i>] | HGT _{30%} | 63.38 ± 6.62 | 69.29 ± 8.76 ^a | 62.82 ± 6.47 |
| | HGT _{40%} | 61.72 ± 6.43 | 74.80 ± 12.98 ^b | 61.10 ± 5.84 |
| | CPT | 59.13 ± 5.56 | 64.25 ± 8.61 ^a | 59.54 ± 6.38 |
| D _s [<i>mm</i>] | HGT _{30%} | 7.45 ± 0.59 | 7.61 ± 0.71 ^c | 7.43 ± 0.60 |
| | HGT _{40%} | 7.52 ± 0.57 | 7.68 ± 0.65 ^a | 7.45 ± 0.56 |
| | CPT | 7.52 ± 0.57 | 7.71 ± 0.64 ^a | 7.46 ± 0.59 |
| ΔD/D | HGT _{30%} | 0.09 ± 0.02 | 0.07 ± 0.02 ^{b,c} | 0.09 ± 0.02 |
| | HGT _{40%} | 0.09 ± 0.02 | 0.07 ± 0.02 ^b | 0.09 ± 0.02 |
| | CPT | 0.10 ± 0.02 | 0.08 ± 0.02 ^a | 0.10 ± 0.02 |
| L PWV _{WH} [<i>m/s</i>] | HGT _{30%} | 4.07 ± 1.56 | 4.23 ± 3.08 ^c | 3.39 ± 1.51 |
| | HGT _{40%} | 3.67 ± 1.91 | 4.39 ± 2.73 ^d | 3.44 ± 1.70 |
| | CPT | 3.17 ± 1.12 | 3.99 ± 1.06 ^{a,d} | 4.19 ± 1.64 ^a |
| RM | HGT _{30%} | 0.42 ± 0.08 | 0.43 ± 0.08 ^c | 0.39 ± 0.04 |
| | HGT _{40%} | 0.42 ± 0.06 | 0.42 ± 0.09 ^d | 0.39 ± 0.04 |
| | CPT | 0.42 ± 0.06 | 0.46 ± 0.06 ^d | 0.45 ± 0.06 |
| M BFV [<i>cm/s</i>] | HGT _{30%} | 23.71 ± 5.56 | 22.19 ± 7.04 | 22.79 ± 3.95 |
| | HGT _{40%} | 21.31 ± 4.13 | 24.18 ± 6.93 ^a | 21.89 ± 5.28 |
| | CPT | 22.02 ± 5.38 | 23.88 ± 6.15 | 24.11 ± 6.27 |
| P BFV [<i>cm/s</i>] | HGT _{30%} | 61.56 ± 12.43 | 49.80 ± 12.75 ^a | 59.08 ± 12.03 |
| | HGT _{40%} | 57.06 ± 11.41 | 53.75 ± 13.32 | 58.27 ± 15.48 |
| | CPT | 57.64 ± 14.60 | 57.37 ± 14.98 | 66.83 ± 19.83 ^a |

Values are shown as mean ± standard deviation. MAP: mean arterial pressure, SBP: systolic blood pressure, DBP: diastolic blood pressure, PP: pulse pressure, HR: heart rate, D_s: systolic diameter, ΔD/D: carotid distension, L-PWV_{WH}: local pulse wave velocity, RM: reflection magnitude, M BFV: mean blood flow velocity, P BFV: peak blood flow velocity.

^a $p < 0.05$.

^b $p < 0.001$.

^c Data based on a sample of 10 volunteers (n = 10).

^d Data based on a sample of 11 volunteers (n = 11).

increase in diameter of this elastic artery is slightly blunted by the increase in muscular tone which may explain why the increase in diameter was smaller than the increase in BP. There was a remarkable decrease in carotid distension during all tests although trends were different. This can be explained by the increase in muscular tone, operating BP, functional stiffness, and the (inverse) influence of HR [247]. Previous studies showed similar outcomes during HGT [254] and CPT [249]. During recovery, BP did not return to baseline values, while HR, diameter and distension did (see figures 6.5 and 6.6 and table 6.2).

In figure 6.5, additional parameters extracted from ultrasound images, such as mean blood flow velocity and peak blood flow velocity, can be observed. However, these results were affected by high variability, precluding any further attempts to extract useful information from them.

Results for local PWV_{WH} are presented in figure 6.6 and high variability is clearly a major issue. The same method was used previously to assess PWV_{WH} during resting conditions (\sim baseline) in 40 consecutive samples from the Asklepios study [255]. They found a PWV_{WH} of $6.00 \pm 1.93 m/s$ [256] while the baseline value we obtained was of $3.64 \pm 1.53 m/s$ (mean value of the three baseline periods). As can be expected for a younger population, our local PWV_{WH} value was lower. In another study, a homogeneous population of 22 healthy male volunteers was recruited from the military academy (mean age 21.7 ± 1.4 years, range 19-24 years) to calculate the local PWV_{WH} during baseline ($4.28 \pm 1.00 m/s$) and CPT ($5.58 \pm 1.68 m/s$) [249]. Although the absolute values in their study are somewhat higher both at baseline and during CPT than the values we calculated, the relative increase of 30% is close to the increase of 26% obtained by us. The differences in absolute value may be due to a difference in methodology: they used pressure curves instead of diameter distension curves for calculating the local PWV_{WH} .

Finally, the RM was calculated. As values rely on local PWV_{WH} for their calculation, also these data showed a high variability (figure 6.6). The data suggest a (borderline) higher RM value during CPT ($p = 0.054$) possibly as a consequence of an increase in down stream resistance [257]. Note, however, that the methodology used to calculate the local PWV_{WH} and the RM might be prone to error. In a recent study, it was demonstrated that although reflection-free periods will emerge as straight sections in single point loop methods as the LnDU-loop method, the opposite is not necessarily true: a straight section in the loop does not necessarily mean that wave reflections are absent during that part of the cardiac cycle [258], corrupting the pulse wave velocity estimations in general [256].

To the best of our knowledge, few previous studies presented an analysis of the baroreflex based on both HGT and CPT stressors and none included

ultrasound measurements. This setup delivered interesting insights not only related to the physiological phenomena but on practical issues in order to improve the acquisition and subsequent analysis. Obviously, the proposed protocol can be easily extended, including a dynamic exercise test and/or head down measurements, using an alternative methodology for calculating the local pulse wave velocity, or improving the acquisition to synchronize the haemodynamic parameters with the ultrasound imaging for assessing the baroreflex sensitivity and for investigating baroreflex resetting during CPT. Moreover, an interesting addition to the setup would be a neck suction device to expand the comprehension over the reset phenomena during different stress stimuli.

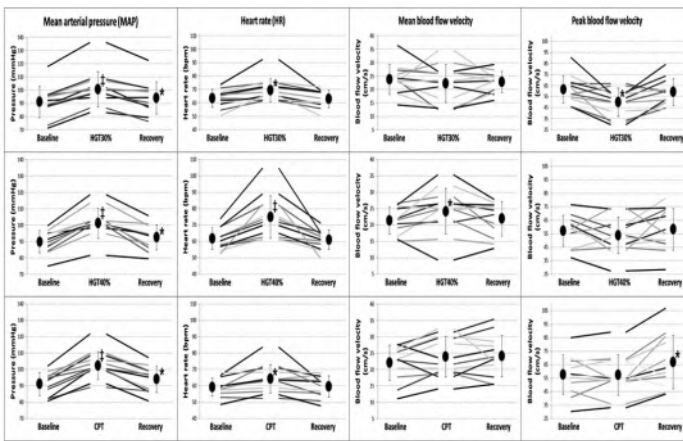


Figure 6.5: Haemodynamic parameter results. Black circles represent mean values during a period (indicated below) of each test. A difference from baseline is denoted as significant * ($p < 0.05$) or highly significant ‡ ($p < 0.001$). Figure adapted from [5].

6.1.5 Limitations

The sample size was enough to conduct a feasibility study but a larger sample is necessary to draw any meaningful physiological conclusion. Additionally, it was assumed that all volunteers were healthy subjects at the moment of the protocol and a previous screening was not performed.

The study tests were not randomized. Therefore, even if baseline values were, in general, obtained between tests, it cannot be excluded that repetitive application of the stressors may influence the individual response.

During the protocol, respiratory changes were not tracked and ultrasound signals were not acquired continuously neither simultaneously, introducing

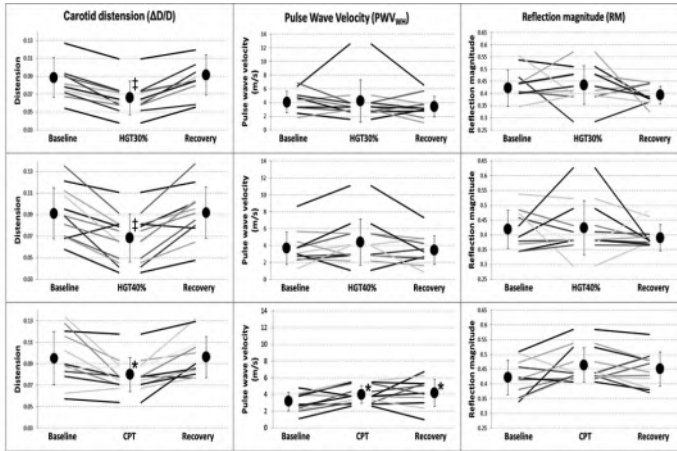


Figure 6.6: Carotid local parameters results. Black circles represent mean values during a period (indicated below) of each test. A difference from baseline is denoted as significant * ($p < 0.05$) or highly significant ‡ ($p < 0.001$). Figure adapted from [5].

potential inaccuracies to calculate local PWV_{WH} and RM. Ultrasound images could be affected by movement artefacts due to the effort of the volunteers during the tests. This problem was mitigated by the use of a holder but not completely eliminated, causing problems especially for Doppler measurements (velocity parameters).

6.1.6 Conclusions

It is feasible to monitor non-invasively the carotid haemodynamic response to a sympathetic nervous system stimulus using carotid ultrasound, although the variability, especially on the flow-related parameters, is high. Further analysis showed supporting evidence of specific physiological response of the autonomous cardiovascular system to regulate adequately each stress stimulus, suggesting the possibility of assessment of the several subsystems involved.

6.2 AN EASY WEB INTERFACE FOR THE ASSESSMENT OF CAROTID-FEMORAL PULSE WAVE VELOCITY AND LOCAL ARTERIAL STIFFNESS RELATIVE TO THE REFERENCE VALUES DATABASES

This research was adapted for submission and accepted as an oral presentation at the *25th European Meeting on Hypertension and Cardiovascular Protection*, Milan, Italy. The abstract, titled "A simple calculator for the assessment of measurements of carotid-femoral pulse wave velocity and local arterial stiffness relative to the reference values database", was published in the *Journal of hypertension*, vol. 33, e-Supplement 1, pp. e60, 2015 [6].

Further improvements of the application were submitted and accepted as an oral presentation at the *Artery 15* conference (Krakow, Poland) under the title "An easy and intuitive web interface for the assessment of measurements of carotid-femoral pulse wave velocity and local arterial stiffness relative to the reference values database". The abstract was published in *ARTERY RESEARCH*, vol. 12, pp. 43, 2015 [7].

6.2.1 Introduction

Arterial stiffness is a crucial parameter for the assessment of cardiovascular risk, and carotid to femoral pulse wave velocity (cf-PWV) has become the gold standard measure of arterial stiffness and a routine parameter in clinical assessment of patients because it is relatively easy to calculate, its reliability and, most importantly, because of the large evidence demonstrating its association with incident cardiovascular disease, independently of traditional risk factors in various populations.

Nevertheless, a wider implementation of arterial stiffness assessment has been hampered by the lack of established reference values on a large population and the absence of standardisation of the methodology for PWV evaluation. For instance, several methods are applied for determining the aortic path length distance, introducing under or overestimations that could reach the 25-30% of the real travelled aortic path length determined by MRI, as table 6.3 indicates. Thus, reference values of cf-PWV and local carotid and femoral arterial stiffness, derived from the distensibility coefficient (DC), have been established [259]–[261], and standardisation of the method has been proposed by experts [262]. Therefore, the aim of this project was to create an application that allows easy assessment - for different methodological approaches - of a given measured value of arterial stiffness, providing the percentile reference associated with that specific value.

Table 6.3: Comparison of methodologies to calculate the reference distance (n = 98). Adapted from [263].

| Tape measured distance | Tape - MRI [Mean (SD)] | Tape/MRI [%] | cf-PWV cut-off value [m/s] |
|------------------------|------------------------|--------------|----------------------------|
| (CA-FA) - (SSN-CA) | 2.32 (3.8) | +4% | 9.98 |
| (CA-FA) - (SN-CA) | -2.35 (3.8) | -5% | 9.12 |
| (SSN-FA) - (SSN-CA) | -5.11 (3.5) | -10% | 8.64 |
| (CA-FA) | 12.99 (4.2) | +25% | 12.00 |
| (SN-FA) - (SN-CA) | -14.77 (3.9) | -29% | 6.82 |
| (CA-FA) x 0.8 | 0.26 (3.8) | +0.4% | 9.64 |
| Body height/4+7.28 | -0.5 (3.9) | -1% | 9.50 |
| Body height x 0.29 | -0.9 (4.0) | -1.8% | 9.43 |

Distance measured in centimetres. The reference distance is the real travelled aortic path length determined by MRI: (AA-FA)-(AA-CA) = 50.7 (4.2). Tape measured distance refers to the distances determined by tape measure directly on the body surface. SD: standard deviation; cf-PWV: carotid-femoral pulse wave velocity; AA: ascending aorta; CA: carotid artery; FA: femoral artery; SN: sternal notch; SSN: suprasternal notch.

6.2.2 Methods

Reference values of cf-PWV (11,092 individuals; age range: 15-97 years, 49.8% men) and local carotid (22,708 individuals; age range 15-99 years; 54% men) and femoral (5,069 individuals; age range: 15-87 years; 49.5% men) arterial stiffness were obtained [259]–[261]. Individuals without cardiovascular diseases and established cardiovascular risk factors constituted a healthy sub-population and were used to determine equations for percentiles of cf-PWV and sex-specific percentiles of carotid and femoral DC across age [260], [261]. The final derived equations of mean and standard deviation (SD) were:

- For cf-PWV [259]:

$$Mean_{PWV} \left(\frac{m}{s} \right) = 4.6 - (0.1 * Age) + (1.8^{-3} * Age^2) + (6.0^{-4} * Age * MAP) + (2.8^{-2} * MAP) \quad (6.5)$$

$$SD_{PWV} \left(\frac{m}{s} \right) = -0.50 + (Age * 0.02) + (MAP * 5.10^{-3}) \quad (6.6)$$

- For local carotid artery stiffness [260]:
In men:

$$Mean_{carotid} (10^{-3} kPa^{-1}) = -12.85 + 70.85 * \left(\frac{Age}{10} \right)^{-0.5} \quad (6.7)$$

$$SD_{carotid}(10^{-3}kPa^{-1}) = 2.51 + 15.43 * \left(\frac{Age}{10}\right)^{-1} \quad (6.8)$$

In women:

$$\begin{aligned} Mean_{carotid}(10^{-3}kPa^{-1}) &= 4.958 + 1.399 * \left(\frac{Age}{10}\right)^{-2} + \\ &218.2 * \left(\frac{Age}{10}\right)^{-2} * \ln\left(\frac{Age}{10}\right) \end{aligned} \quad (6.9)$$

$$SD_{carotid}(10^{-3}kPa^{-1}) = -3.664 + 21.55 * \left(\frac{Age}{10}\right)^{-0.5} \quad (6.10)$$

- For local femoral artery stiffness [261]:

In men:

$$\begin{aligned} Mean_{femoral}(10^{-3}kPa^{-1}) &= 5.604 + 0.779 * \left(\frac{Age}{10}\right)^2 \\ &- 0.411 * \left(\frac{Age}{10}\right)^2 * \ln\left(\frac{Age}{10}\right) \end{aligned} \quad (6.11)$$

$$SD_{femoral}(10^{-3}kPa^{-1}) = 2.829 + 3.677 * \left(\frac{Age}{10}\right)^{-1} \quad (6.12)$$

In women:

$$\begin{aligned} Mean_{femoral}(10^{-3}kPa^{-1}) &= 9.438 + 0.163 * \left(\frac{Age}{10}\right)^3 - \\ &0.092 * \left(\frac{Age}{10}\right)^3 * \ln\left(\frac{Age}{10}\right) \end{aligned} \quad (6.13)$$

$$SD_{femoral}(10^{-3}kPa^{-1}) = 5.984 - 0.005 * \left(\frac{Age}{10}\right)^3 \quad (6.14)$$

To calculate the arterial stiffness percentile of a patient, the real stiffness value has to be compared with the expected normal stiffness value. While the expected mean and SD values are calculated using equations (6.5) to (6.14), the Z_{score} is derived as:

$$Z_{score} = \frac{Parameter - ExpectedValue_{mean}}{ExpectedValue_{SD}} \quad (6.15)$$

Finally, the Z_{score} is converted into a percentile using the standard normal distribution.

Using these equations, an application was created to provide the percentile reference value from routine parameters obtained in clinical practice. Additionally, standardisation of cf-PWV measurements is also available in accordance to the expert consensus document, which supports the use of 80% of the direct carotid-femoral distance [262] (see table 6.3).

Figure 6.7: Web interface for the assessment of arterial stiffness parameters. There is an upper menu for selecting the parameter to be determined (or standardised) among: a. Carotid; b. Femoral; c. cf-PWV, or d. cf-PWV (conv.). In the figure, the option for Carotid DC is selected and displayed. DC: distensibility coefficient; cf-PWV: carotid-femoral pulse wave velocity; conv.: conversion means that standardisation of PWV measurements is performed to the 80% of the direct carotid-femoral distance method [262].

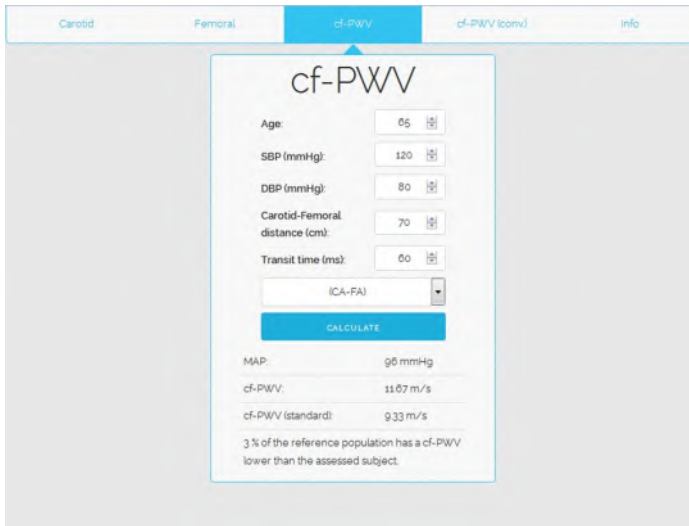
The screenshot shows a web application interface for calculating the Carotid Distensibility Coefficient (DC). At the top, there is a navigation menu with options: Carotid (selected), Femoral, cf-PWV, cf-PWV (conv.), and info. The main content area is titled 'Carotid DC' and contains several input fields: Age (60), Diameter (mm) (6), Distension (mm) (0.4), SBP (mmHg) (120), and DBP (mmHg) (80). Below these are three dropdown menus: the first is set to '1 cm', the second to 'ART.LAB', and the third to 'Female'. A blue 'CALCULATE' button is positioned below the dropdowns. Underneath the button, the calculated results are shown: 'DC: 25.83 10e-3/kPa', 'PWV-local: 6.04 m/s', and a note stating '97 % of the reference population has a carotid DC lower than the assessed subject.'

Figure 6.8: Calculation of carotid distensibility coefficient. Data of a 60 years old woman with a carotid artery diameter and distension of 6mm and 0.4mm , respectively, a SBP/DBP of $120/80\text{mmHg}$, and whose measurements has been done with an ART.LAB device at 1cm proximal to the carotid bifurcation. Results show a local arterial stiffness (DC) of $25.83 \cdot 10^{-3}/\text{kPa}$, a local PWV of 6.04m/s and an arterial stiffness percentile of 97, meaning that 97% of the healthy reference population has a lower carotid DC.

6.2.3 Results

The tool can be found at: <http://users.ugent.be/~flondono/> and consists in an upper menu where the user selects the parameter to be determined (or standardised). Then, a panel is displayed according to the selected option: a. Carotid; b. Femoral; c. cf-PWV, or d. cf-PWV (conv.). Subsequently, the user provides a number of inputs which are used to calculate the selected parameter, the percentile and, when relevant, additional information. Figure 6.7 shows the interface of the web application.

For the calculation of carotid or femoral DC, the interface requires the age (in years), diameter and distension (in mm), and SBP and DBP (in mmHg). When this information is provided, three drop-down menus allow to select: 1) the anatomical location of the diameter/distension measurement: 0 to 1, 1, 1 to 2, or 2cm proximal to the flow divider of the arterial bifurcation; 2) the echo-tracking system used: ART.LAB, Wall Track system, Vivid-7 or Carotid Studio; 3) the sex of the subject. After all parameters are correctly introduced, the application calculates and presents the arterial stiffness value expressed as distensibility coefficient (DC), the local PWV and the patient's stiffness percentile. To calculate the percentile, the arterial stiffness value is



Carotid Femoral **cf-PWV** cf-PWV (conv) Info

cf-PWV

Age:

SBP (mmHg):

DBP (mmHg):

Carotid-Femoral distance (cm):

Transit time (ms):

CALCULATE

MAP: 96 mmHg

cf-PWV: 11.67 m/s

cf-PWV (standard): 9.33 m/s

3% of the reference population has a cf-PWV lower than the assessed subject.

Figure 6.9: Calculation of carotid-femoral pulse wave velocity. The used information is of a 65 years old individual with a SBP/DBP of 120/80mmHg, an arterial path length of 70cm obtained with the full CA-FA distance method and a transit time of 60ms. Calculations show a MAP of 96mmHg, a cf-PWV of 11.67m/s, a cf-PWV (standard) of 9.33m/s and a percentile 3, indicating that 3% of the healthy reference population has a lower cf-PWV. CA: carotid artery; FA: femoral artery.

rescaled to the standards of the "reference values database": the ART.LAB as the device and 1cm proximal to the flow divider as the location. An example of carotid artery stiffness calculation is shown in figure 6.8, introducing the data of a 60 years old woman with a carotid artery diameter and distension of 6mm and 0.4mm, respectively, a SBP/DBP of 120/80mmHg, and whose measurements has been done with an ART.LAB device at 1cm proximal to the carotid bifurcation. The application plots the calculated parameters below the described menu, which in this case indicates that for this subject the local arterial stiffness (DC) is $25.83 \cdot 10^{-3} / kPa$, the local PWV is 6.04m/s and her arterial stiffness percentile is 97. This percentile indicates that 97% of the healthy reference population has a lower carotid DC. Local femoral artery stiffness is similarly obtained.

Analogously for the calculation of the PWV, interface fields must be filled with age (in years), SBP and DBP (in mmHg), the measured arterial path length (in cm) and the transit time (in ms). Again, there is an additional drop-down menu to select the distance method used to measure the arterial path length. The options include the standard distance method being 80% of the full carotid-femoral (CA-FA) distance, the full CA-FA distance, subtracted distance methods using the sternal (SN) or the suprasternal (SSN) notch, and distances based on body height (see table 6.3). Employing these data, the

The screenshot shows a web application interface with a navigation bar at the top containing 'Carotid', 'Femoral', 'cf-PWV', 'cf-PWV (conv.)', and 'Info'. The 'cf-PWV (conv.)' tab is active. The main content area contains a form with the following fields and values:

- Age: 40
- SBP (mmHg): 120
- DBP (mmHg): 80
- cf-PWV (m/s): 9
- Distance method: (CA-FA) - (SSN-CA)

A blue 'CALCULATE' button is located below the form. Below the button, the results are displayed:

- MAP: 96 mmHg
- cf-PWV (standard): 8.64 m/s
- Percentile: 57

A note at the bottom of the results section states: '57% of the reference population has a cf-PWV lower than the assessed subject.'

Figure 6.10: Standardisation of carotid-femoral pulse wave velocity measurements. Data of a 40 years old person with a SBP/DBP of $120/80\text{mmHg}$ and a cf-PWV of 9m/s obtained with the subtracted (CA-FA)-(SSN-CA) distance method. The results are a MAP of 96mmHg , a standard cf-PWV of 8.64m/s and a percentile of 57, indicating that 57% of the healthy reference population has a cf-PWV lower than this subject. Standardisation means that PWV measurements are rescaled to the same metric of the approach performed to the 80% of the direct carotid-femoral distance method [262]. CA: carotid artery; FA: femoral artery; SSN: suprasternal notch.

application calculates and displays the MAP, the measured PWV depending on the distance method used, the standard PWV and the percentile. An example of such calculation is shown in figure 6.9, introducing the information of a 65 years old individual with a SBP/DBP of $120/80\text{mmHg}$, an arterial path length of 70cm obtained with the full CA-FA distance method (see table 6.3) and a transit time of 60ms . The interface delivers a MAP of 96mmHg , a cf-PWV of 11.67m/s , a cf-PWV (standard) of 9.33m/s and the percentile 3. This percentile indicates that 3% of the healthy reference population has a lower cf-PWV.

The last example concerns the standardisation of a cf-PWV measurement, rescaling it to the same metric of the proposed standard method [262]. The required information for this calculation is the age (in years), SBP and DBP (in mmHg), the cf-PWV value and the selection of the distance method used to determine the arterial path length from a drop-down menu. Then, the application shows the MAP, the standardised cf-PWV value and the percentile. A practical example of this function is presented in figure 6.10 using the data of a 40 years old person with a SBP/DBP of $120/80\text{mmHg}$ and

a cf-PWV of $9m/s$ obtained with the subtracted (CA-FA)-(SSN-CA) distance method (see table 6.3). The results are a MAP of $96mmHg$, a standard cf-PWV of $8.64m/s$ and a percentile of 57, indicating that 57% of the healthy reference population has a cf-PWV lower than this subject.

6.2.4 Conclusions

An easy and intuitive interface was created to assess a given measurement of arterial stiffness relative to known reference values. Further work includes the promotion and improvement of the application so that arterial stiffness becomes a routine parameter to assess the cardiovascular state of a subject, enhanced by the standardisation of the methodologies and the use of reference values.

6.3 APPLANATION TONOMETRY AND ULTRASOUND IMAGING FOR CONTINUOUS PHYSIOLOGICAL AND MEDICAL MONITORING TO SUPPORT ESA SPACE RESEARCH

Results regarding the short arm human centrifuge (SAHC) were adapted for submission and accepted as an oral presentation at the *25th European Meeting on Hypertension and Cardiovascular Protection*, Milan, Italy. The abstract, titled "*Continuous monitoring of hemodynamics in the short arm human centrifuge: a feasibility study*", was published in the *Journal of hypertension*, vol. 33, e-Supplement 1, pp. e104-e105, 2015 [8].

6.3.1 Introduction

Space exploration is a challenging field not only in terms of aeronautic engineering but in many different domains, including medicine and biomedical engineering. One of the most evident needs is to better understand vascular adaptation mechanisms due to microgravity and define cardiovascular risks for long duration flights. Additionally, it is crucial to find an adequate method to assess and validate the efficiency of countermeasures against microgravity effects. Currently, non-invasive haemodynamic recordings at the finger are obtained to perform cardiovascular assessment for astronauts due to its ease of use. However, the value of these measurements is under debate due to the distance of the measurement locations to the heart. Thus, a system denominated continuous physiological and medical monitoring (CPMM) is proposed to improve the non-invasive analysis of the cardiovascular state in subjects submitted to microgravity conditions on ground and in space. The term "continuous" implies repeated measurements to be able to document changes, and not long-term permanent/continuous measurements. The CPMM system consisted in a combination of pressure and flow measurements using tonometry and ultrasound, respectively.

The aim of the study was to assess the feasibility of measurements of the system and its characteristics, such as ease of use, robustness, and user dependability. Furthermore, the study explored the obtainment of useful and reliable parameters to evaluate the cardiovascular state of a subject under different stress conditions, including physiological changes induced by artificial gravity in the SAHC (Verhaert, Kruijbeke, Belgium) with the goal of detecting and preventing potential disorders induced by weightlessness. The project was developed under a European Space Agency (ESA) contract (and with its support) by the Belgian company Verhaert in consortium with the Institute for Space Medicine and Physiology (MEDES, Toulouse, France) and Ghent University.

6.3.2 Methods

6.3.2.1 Sample population

CPMM clinical assessments were performed on 14 healthy volunteers (7 men and 7 women). The candidates were recruited via the MEDES internal file of volunteers and complied with the main basic selection criteria: i.e., age 20 – 40 years, non-smokers, no overweight nor excessive thinness with body mass index (BMI, weight $kg / (\text{height})^2 m^2$) between 20 and 25, active (normally fit) and free from any orthopaedic, musculoskeletal and cardiovascular disorders (see table 6.4). The medical selection was carried out at MEDES Space Clinic.

Table 6.4: General characteristics of study subjects for the CPMM protocol implementation.

| Parameter | Age [y] | Weight [kg] | Height [cm] | BMI [kg/m ²] | SBP [mmHg] | DBP [mmHg] | HR [bpm] |
|-------------|---------|-------------|-------------|--------------------------|------------|------------|----------|
| <i>Min</i> | 20 | 51.8 | 161 | 20.0 | 95 | 48 | 37 |
| <i>Max</i> | 40 | 84.4 | 191 | 24.7 | 132 | 91 | 87 |
| <i>Mean</i> | 28.6 | 66.5 | 174.1 | 21.8 | 112.1 | 64.6 | 62.4 |
| <i>SD</i> | 6.14 | 9.19 | 8.32 | 1.42 | 11.97 | 11.04 | 13.89 |

SD: standard deviation; BMI: body mass index; SBP: systolic blood pressure; DBP: diastolic blood pressure; HR: heart rate.

6.3.2.2 CPMM protocol

The performed protocol, summarized in figure 6.11, consisted in five parts, changing the posture or activity of the subject: 1) lying down (baseline); 2) in tilt position; 3) submitted to a lower body negative pressure (LBNP); 4) walking; and 5) cycling. Each evaluation session was performed by an operator under medical supervision by a MEDES physician assisted by a technician. BP measurements (SBP, DBP and HR) were obtained every 5 minutes by a Dinamap© Pro (GE Medical Systems) device.

6.3.2.3 Tonometry measurements

The tonometry acquisition system allows for an easy placement of the tonometer and reduces motion artefacts. Specifically, the arterial pressure is transferred by direct contact of a silicone rubber surface with the skin, and a very sensitive pressure sensor is utilised to measure the pressure wave. Tonometry post processing includes averaging of the signal and posterior wave shape analysis (see figure 6.12).

6. DEDICATED TOOLS

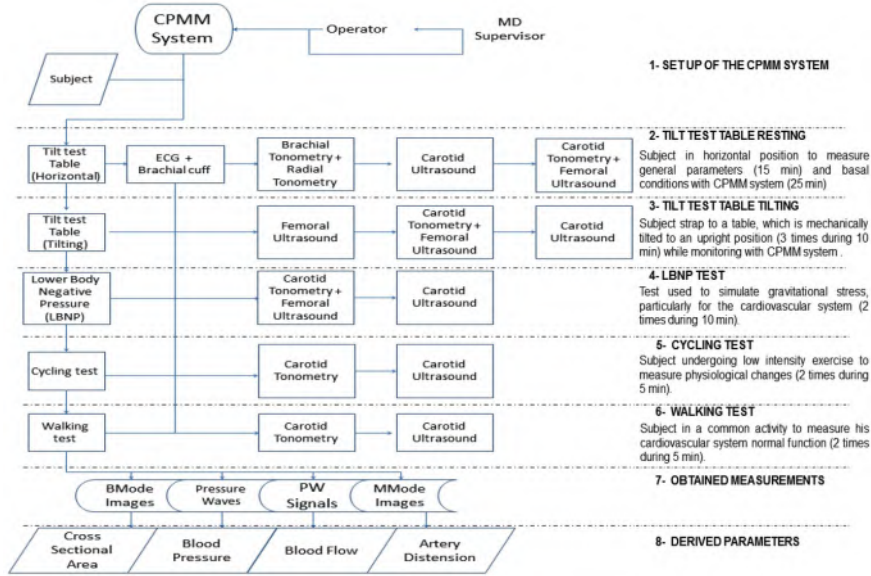


Figure 6.11: CPMM scientific evaluation campaign flow chart. CPMM: continuous physiological and medical monitoring.

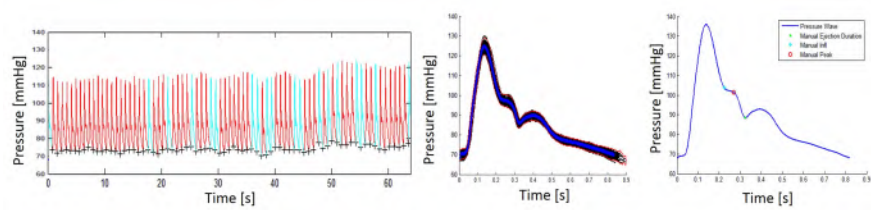


Figure 6.12: Example of a tonometry signal obtained from the carotid artery during the test campaign of the CPMM system. Left) Tonometry signal showing several pressure waves during a ~1-minute period. Middle) Averaged tonometry signal. Right) Wave shape analysis of the pressure wave (blue line), showing the (manually selected) inflection point (cyan) and the ejection duration point (green).

6.3.2.4 *Ultrasound measurements*

The ultrasound system corresponds to an acquisition unit (Telemed, Lithuania) and a biplane transducer (Mepy, Belgium/France). The system is compact, and the innovative linear array probe can physically be split in two, with the probe being equipped with connectors for setting both halves of the probe in a linear or T-junction configuration, as shown in figure 6.13.

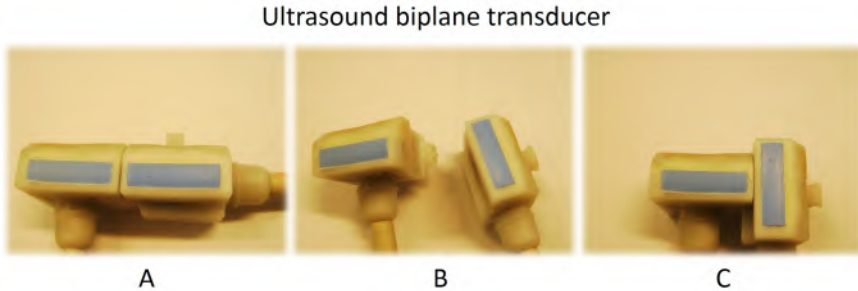


Figure 6.13: Ultrasound linear array probe. The biplanar probe of the ultrasound system has an innovative design that allows different configurations: A) linear configuration of the probe; B) splitting of the probe in two separated segments; C) T-junction configuration of the probe.

6.3.2.5 *Ultrasound image processing*

The segmentation implemented for post-processing of ultrasound images was based on the algorithm proposed by Faita *et al.* [264]. The semi-automatic algorithm was developed in MATLAB® [265] and consists of 4 steps: filtering, heuristic search, outlier removal and parameter estimation. To initiate the processing of B-mode arterial images, the user must click on a pixel representing the inside of the arterial lumen. All steps are performed for the upper and lower portions of the image (in reference to the selected point) independently.

First, the filtering operates with a sobel kernel, then with an edge detector and, finally, with various morphological operators to pre-process the image and to deliver a mask. This pre-processing step is performed to identify the pixels belonging to the intima-media complex and the adventitia of the artery. Next, the heuristic search finds a predetermined pattern for each column. The algorithm searches for three values in comparison with a given threshold: higher - lower - higher (in this order). Only the columns that comply with this pattern are considered for further processing. The remaining points are used as inputs for a cubic spline interpolation. Points located too far from

this spline are identified as outliers and removed. Finally, the segmentation delivers two lines indicating the intima-media layer of the analysed artery at the upper and the lower portions of the image.

From this segmentation, different parameters are calculated, such as the diameter, which is obtained using the polyline distance method [266]. Adaptations of this segmentation algorithm were implemented to obtain arterial cross-sectional areas from B-mode images, and to process M-mode ultrasound images to determine diameter distension curves and PW Doppler images to define the envelop of blood flow curves and derived parameters. Examples of segmented ultrasound images using the implemented algorithm are shown in figure 6.14.

6.3.2.6 SAHC measurements

All measurements were performed at MEDES facilities in 4 young (presumably) healthy volunteers (3 males). In two (male) volunteers, the protocol was divided in three periods: acceleration, steady rotation velocity and deceleration, obtaining carotid PW-Mode ultrasound images during each period. For one (female) volunteer, carotid PW-Mode ultrasound images and brachial and radial tonometry signals were acquired at baseline and during the steady rotation period. For one (male) volunteer, carotid and femoral PW-Mode ultrasound images and brachial, radial and carotid tonometry signals were acquired at baseline and during an initial and a following faster rotation velocity. Next day, follow-up measurements of this volunteer were obtained. The SAHC and the setup of the CPMM system are shown in figure 6.15A.

6.3.3 Results

A complete data set was recorded in all 14 volunteers. Results were analysed to evaluate the feasibility and practical application of the CPMM system. The last two parts of the protocol, cycling and walking, involved the movement of the volunteer, introducing artefacts to the signals. In contrast to tonometry, ultrasound delivered better results and proved to be a more robust technique in extreme conditions.

6.3.3.1 Sphygmomanometer measurements

Four parameters were obtained (SBP, DBP, MAP and HR), and pulse pressure (PP) was calculated with the formula:

$$PP = SBP - DBP \tag{6.16}$$

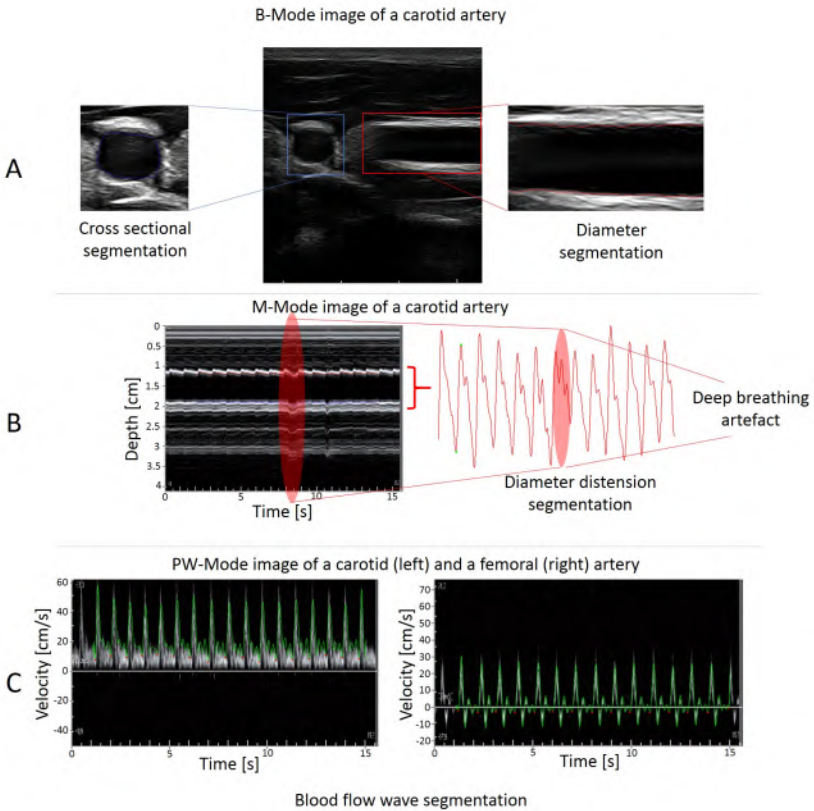


Figure 6.14: Ultrasound imaging examples obtained during the test campaign of the CPMM system. A) B-mode image of the carotid artery and segmentation of the cross-sectional area (left, blue line) and the diameter (right, red line). B) M-Mode image of the carotid artery and segmentation results of the diameter distension. The red shaded regions highlight the deep breath artefact of the signals. C) Spectral PW Doppler images of the carotid (left) and the femoral (right) arteries, showing the segmentation results of the envelop flow curve (green line) and the start/end of each cardiac cycle (red points). CPMM: continuous physiological and medical monitoring.

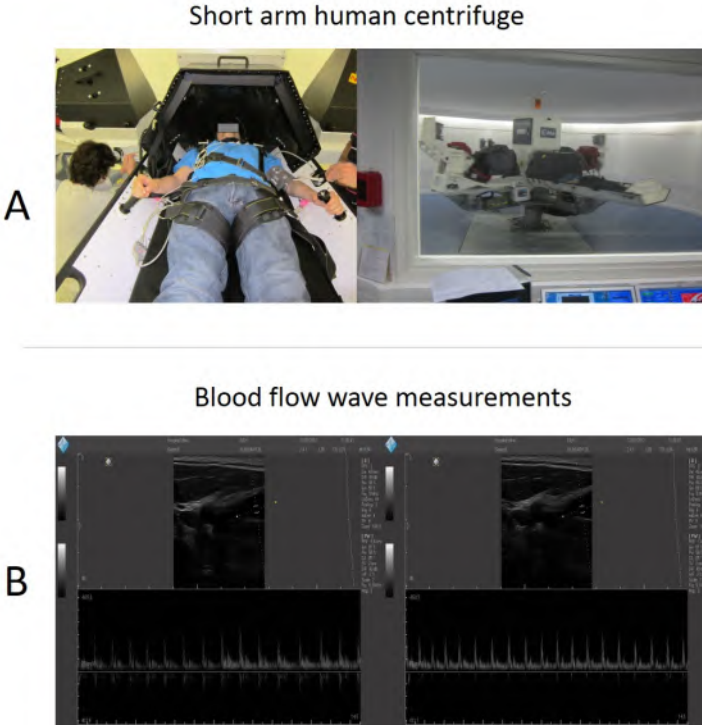


Figure 6.15: CPMM test campaign in the short arm human centrifuge. A) Photos of the short arm centrifuge including preparation of the volunteer. B) Spectral PW Doppler images of the carotid artery during acceleration (left) and deceleration (right) phases of the protocol. CPMM: continuous physiological and medical monitoring.

Values for the sample population are shown in table 6.4.

6.3.3.2 Tonometry measurements

Tonometry signals were processed to calculate parameters such as pressure estimations, augmentation index (Aix), ejection duration (the duration of the left ventricular systolic ejection or systolic time interval in *ms*), among others. A tonometry signal example is shown in figure 6.12. Tonometry signals are calibrated using sphygmomanometer information as:

$$MAP = DBP + 40\%PP \quad (6.17)$$

With MAP, DBP and tonometry signals, SBP and PP values were calculated.

6.3.3.3 *Ultrasound measurements*

In figure 6.14A, a B-Mode image of the carotid artery is displayed. At the left, there is a zoomed region of the original image to show the segmentation results of the cross-sectional carotid area (blue line) and, at the right, there is a longitudinal zoom to show the segmentation of the carotid diameter (red lines). The image is divided in two parts due to the ultrasound probe configuration (T-shape), which allows to achieve a longitudinal and a transversal view of the artery simultaneously, improving time acquisition, especially for B-Mode images. Femoral images were also obtained and processed analogously but quality was, in general, lower than for carotid results. Figure 6.7B shows an example of an M-Mode image of a carotid artery and the correspondent (derived) distension curve. Interestingly, this image exhibits an artefact produced by deep breathing, easily recognizable to avoid its selection when calculating a distension curve. For M-mode images, quality of carotid segmentation results was also higher in contrast to femoral results. PW-Mode ultrasound images of carotid (left) and femoral (right) arteries are displayed in figure 6.14C. The envelop of blood flow curves was obtained (green line) whereas red points indicated the start and/or the end of one cardiac cycle. All (complete) cycles were included to calculate the blood flow mean and peak velocities.

6.3.3.4 *SAHC measurements*

PW-Mode ultrasound images of the carotid artery were obtained in all 4 volunteers during different steps of the protocol. Femoral ultrasound imaging revealed greater difficulties related mainly to the placement of the probe after baseline, even if in one case results were feasible. Tonometry was, in general, more challenging due to the intrinsic sensitivity of the method. Overall, radial arterial tonometry provided the best results, while brachial arterial results were acceptable only in one occasion. Carotid tonometry was measured only for one subject with suitable results for processing. Figure 6.15B displays PW-Mode images obtained during the acceleration (left) and deceleration (right) phases of the protocol.

6.3.4 **Conclusions**

The CPMM system provided interesting and promising results for future applications, and remarkable qualities as it is inexpensive, practical and flexible. Acquisition and processing improvements are still necessary to deliver optimal results. Concrete strategies for enhancing the fixation system

are primary to reduce the variability of the data and improve acquisition. Finally, the use of the CPMM system in the SAHC was assessed successfully. Tonometry measurements were feasible under a spin velocity limit, while PW-Mode ultrasound images were more robust and stable. However, a larger sample population must be included to support general conclusions. Nevertheless, suitable signals and locations were identified for future research.

III

Closure Thoughts

CHAPTERS

7 **Conclusions**

195

CONCLUSIONS

Throughout the history of cardiovascular research, successive milestones have been achieved to prevent, diagnose and treat cardiovascular diseases (CVDs). From the comprehension of the electrical signalling of the heart for implementing electrocardiography (ECG) and the development of cardiovascular surgery to the appearance of cardiovascular implantable devices and heart transplant procedures, the fast evolution of cardiovascular medicine has contributed to change the role of health care in society [267]. Furthermore, cardiac imaging, cardiovascular drugs, preventive cardiology and, more recently, the concept of arterial health have also transformed diverse aspects of health care beyond the clinical setting. Nowadays, genetics and molecular biology, along with a period of technological development, are remodelling cardiovascular medicine, partly due to concepts that already revolutionized information technologies but only until now are emerging in health care [268] with promising results to empower patients and stimulate them to change lifestyle, and improve diagnosis and treatment. In consequence, interdisciplinary research is becoming a paradigm in medicine. The contribution of this PhD is to be sought within this context, aiming to improve technical methodologies in cardiovascular research with an interdisciplinary perspective on two areas that still face several challenges: heart failure with preserved ejection fraction (diastolic dysfunction), which has not an effective treatment yet, and arterial health assessment, which lacks of a widespread application in medical practice.

Hence, Part II - Novel Cardiovascular Research presents the development of non-invasive methodologies for the assessment of cardiovascular func-

tion. The three specific goals established for this PhD project were developed and structured in distinct but associated chapters. In addition to the novel strategies and findings described through this dissertation, the proposed research raised several questions to be answered yet, and we consider this PhD project as a positive starting point for further cardiovascular investigation. For instance, validation remains a fundamental requirement for all proposed studies to corroborate in more general conditions, i.e., larger and heterogeneous populations, the discussed results and, thus, to support the conclusions. Nevertheless, precise questions generated by each study should be also considered.

Chapter 4 was dedicated to the assessment of cardiac function and the accomplishment of goal 1, i.e., to develop and to validate a non-invasive processing tool for the estimation of intraventricular pressure differences (IVPDs) in order to characterise patients without heart failure (HF), and with HF and reduced (HFrEF) or preserved (HFpEF) ejection fraction, on the basis of previous work [56]–[58], [98], [101], [127], [134]. In this chapter, we proposed novel technical tools, including an MRI-based algorithm, to estimate noninvasively IVPDs during diastole and systole, and a computational fluid dynamics (CFD) model to assess and to validate the performance of the proposed algorithms to estimate IVPDs. Concisely, we found that even if intraventricular pressure gradients (IVPGs) and IVPDs provide interesting insights about cardiac function, the application of non-invasive methodologies to estimate these parameters is limited. The progress of cardiac imaging modalities and the development of advanced methods merging CFD and flow velocity measurements could promote the use of IVPDs in the clinical setting as a result of greater availability, more robust validation approaches and accurate results. Effectively, we demonstrated the feasibility to assess IVPDs throughout the cardiac cycle using phase-contrast MRI to identify distinct patterns in patients without HF and subjects with HFrEF and HFpEF. Nonetheless, the proposed research on IVPD estimation raises practical questions on how a more accurate left ventricle (LV) model over a wide range of sizes and ejection fractions (EFs) would impact the assessment of the proposed approaches or how invasive catheter-based measures would compare with non-invasive calculations. Additionally, the impact of technical issues about the MRI-based method should be evaluated, including the limited temporal and through plane spatial resolution, image alignment and assumptions made about viscous forces and the nature of flow from the 3 chambers view.

The focus of Chapter 5 was the evaluation of vascular function to support the realization of goal 2, which is to evaluate the differential effects of organic and inorganic nitrates in the vascular function of HFpEF patients,

building on previously formulated haemodynamic analysis [40], [63]–[71]. We established that organic nitrate administration reduced arterial wave reflections less consistently than observed with inorganic nitrate and produced profound vasodilatation in the carotid territory, with a reduction in cerebrovascular resistance and carotid characteristic impedance. Additionally, our study also evidenced that organic nitrates increase power penetration from the aorta into the carotid, which led to a significant increase in carotid pulsatile hydraulic power, despite a reduction in aortic power. In contrast, inorganic nitrate did not produce significant cerebrovascular dilatation nor induce significant changes in aortic and carotid wave and hydraulic power or percentage of power penetration. These haemodynamic differences may underlie the distinct effects on exercise capacity, adverse events, such as the differential incidence of headaches, and pulsatile haemodynamic stress of the brain microvasculature in HFpEF patients. Further questions to be considered are the influence of the design of both studies, the chronic effects of these drugs on the carotid and peripheral circulations and the potential association between carotid pulsatile haemodynamics and cognitive decline.

Finally, goal 3: to propose and to develop additional strategies for improving cardiovascular medicine in different applications, was addressed in Chapter 6. In brief, we proved the feasibility to monitor noninvasively the carotid haemodynamic response to a sympathetic nervous system stimulus using ultrasound measurements. Also, we developed an easy and intuitive interface to assess a given measurement of arterial stiffness relative to known reference values. Additionally, we proposed a system to evaluate vascular function, based on tonometry and ultrasound measurements. The system proved to be inexpensive, practical and flexible, and was assessed successfully in the short arm human centrifuge (SAHC), although tonometry measurements were feasible under a spin velocity limit, while PW-Mode ultrasound images were more robust and stable. Notably, these proposed strategies should be improved and further promoted to achieve a higher impact.

Beyond the specific (novel) interrogations generated by the research presented in this dissertation, it is also stimulating to consider emerging methodologies in the cardiovascular field for addressing the posed challenges. Hence, potential future work is discussed hereafter, proposing the integration of different approaches to enhance and optimize cardiovascular research.

PROSPECTIVE AND PERSPECTIVE

Part II proposed novel cardiovascular research based on traditional and state-of-the-art analysis for the assessment of cardiovascular function. Currently,

the prevalent digitalization of medical data offers an appealing opportunity towards the automatization of critical and time-consuming procedures, such as segmentation and parameter calculation from medical signals and images. Therefore, this section outlines technologies that can potentially facilitate and, at best, improve cardiovascular research.

The wavelet transform is a relevant time–frequency analysis and coding tool that exceeds other applications based on traditional Fourier methods for processing biomedical signals in specific tasks, such as denoising/filtering, compression, and extraction of scale-based features. Wavelet-based approaches are employed to a wide variety of signals, such as electromyography (EMG), electroencephalography (EEG), clinical sounds, respiratory patterns, blood pressure trends and DNA sequences, even if ECG processing implementations are the most common [269]–[271]. Therefore, ECG processing through wavelet approaches could complement classical haemodynamic analyses, such as the ones described in Chapter 5, and assessment studies on the autonomic nervous control of the cardiovascular function, as the one proposed in Chapter 6, section 6.1. Moreover, most protocols include already ECG recordings that could be processed off-line and further analysed without adding costs or time to acquisition protocols. Data compression, image enhancement and reconstruction are also important wavelet applications to improve analysis [272]–[275], which could boost a wider spread of cardiac MRI protocols and reinforce the use of related parameters, such the ones proposed in Chapter 4. Furthermore, De Melis *et al.* [276] proposed a wavelet method to analyse the blood pressure waveform, providing and displaying specific features related to wave reflection and aortic valve closure, which can be an interesting addition to traditional haemodynamic assessment (see Chapter 5) using the same measurements. In fact, pattern extraction tools are becoming more important as inputs of machine learning algorithms for automatic classification problems, which is currently a field of great interest and development. Khatami *et al.* [277], for instance, combine the denoising properties of the wavelet transform to pre-process medical images with deep belief networks to classify them.

The adoption of machine learning is ubiquitous in information technology and is reaching rapidly and strongly for medical practice. Several reasons have driven this change towards the application of these techniques in research and clinical care, among which are the digitalization of health care, the advances in high-performance computing, the availability of big data and the increasing accessibility of machine learning algorithms capable of performing complex tasks. Thus, machine learning has been integrated with more traditional approaches and standard protocols to address unsolved issues and to optimize relevant processes, such as risk stratification, diagnosis,

treatment and follow-up of patients. For instance, cardiovascular risk prediction is based on regression models and assumes that each risk factor is related in a linear fashion to CVD outcomes [278]. Although useful and robust, these statistical methods oversimplify complex relationships, including non-linear interactions, and they are limited to use a small number of predictors that operate in the same way on everyone, and uniformly throughout their range [279]. In contrast, machine learning methods are conceived for solving particular challenges that are not well addressed by typical regression approaches [279].

Furthermore, machine learning has the potential to transform medicine by better exploiting big data for algorithm development [278]. Currently, computer analysis and high-level interpretation of cardiac imaging are becoming feasible, boosting machine learning capacity to provide a powerful platform for integration of clinical and imaging data and for optimization of diagnosis and prognosis [268]. Indeed, machine learning methods could impact the prediction, prevention and proactive management of CVDs by, for example, uncovering hidden structures in cardiology data to support the identification of subtypes in chronic (multifactorial) complex diseases, such as HF [268], potentially leading to novel therapeutic discoveries and personalised cardiovascular care [280], [281]. It is thus clear that machine learning promises to transform medical research with more sophisticated and reproducible conclusions drawn from comparisons against training databases. Moreover, machine learning may represent a cost-effective risk stratification and diagnostic tool and, ultimately, it may lead to the optimization of day-to-day clinical workflow [268].

In practice, several studies showed the solid performance of machine learning algorithms at predicting CVD cases and excluding non-cases correctly [278]. Machine learning algorithms have proved to differentiate successfully complex patterns of cardiac structural and functional abnormalities in different cardiac pathologies [282], to classify properly LV wall motion based on spatiotemporal profiles from cardiac cine MRI [283] or even to segment the LV in cardiac MRI [284]. In fact, large numbers of machine learning applications are becoming common topics for submissions to medical journals [285]. Thereby, the incorporation of machine learning algorithms into studies proposed in Part II - Novel Cardiovascular Research corresponds to the current evolution of medical research. Concretely, the proposed methods described in Chapter 4 could benefit greatly with machine learning approaches, from MRI reconstruction to IVPDs analysis, improving timing and supporting diagnosis. For instance, a supervised machine learning algorithm for classification of HF subtypes using IVPD extracted parameters and/or other variables may facilitate risk stratification, diagnosis, treatment and follow-up of patients. This proposal could be extended to echocardiographic data

used in Chapters 5 and 6 to enhance the proposed haemodynamic analysis. Moreover, unsupervised machine learning could be applied experimentally to datasets presented in Part II to discover hidden patterns for improving the analysis without additional time consuming and bias (manual) segmentation processes.

Machine learning is an essential step towards a functional automatization of processes, together with the construction of large databases containing relevant and diverse cardiovascular signals and images to train efficient algorithms. The next step is to overcome the shortcomings of machine learning through the implementation of deep learning methods, which develop more complex strategies to improve the performance in specific applications [286]. With this perspective, deep learning arises as a further milestone in the road to improve cardiovascular medicine.

A pending task to implement successfully deep learning in cardiovascular medicine is the creation of extensive databases for training and testing. Concretely, the analysis of cardiac function is essential in clinical cardiology for patient management, disease diagnosis, risk assessment, and therapy decision. Due to remarkable characteristics, cardiac MRI has become the standard method to assess cardiac function (Chapter 2). However, in daily practice this type of analysis is still a semi-automatic task because of the lack of accuracy of fully automatic cardiac segmentation methods, leading to time consuming tasks prone to intra- and inter-observer variability. Only recently, few datasets have been proposed to gauge performances of state-of-the-art cardiac MRI segmentation methods [287]–[290] for supporting interpretation and diagnosis of many cardiomyopathies, but there is still a gap to be filled.

It has been demonstrated that deep learning methods can successfully classify patient data and get highly accurate segmentation results in cardiac MRI. In particular, convolutional neural networks (CNN) [291], [292] evidenced accurate correlation scores on clinical metrics and low bias and standard deviation on commonly used physiological measures, even if additional limitations should be also improved [291]. Furthermore, a fully automatic segmentation of the LV in cardiac MRI can be achieved as well using a combined deep-learning and deformable-model approach [293]. Other effective applications of deep learning algorithms include automated cardiac MRI volume analysis [294] and MRI reconstruction [295]. Beyond the specific aim of these implementations, practical lessons can be further extracted regarding the development of deep learning methods. For instance, the previously stated necessity of huge amount of data to train algorithms could be tackled by using artificial data enlargement, pre-training and careful design, so deep learning methods can be successfully employed for medical image

segmentation [293]. Many of these studies could become a starting point for developing methods to process the data employed in Part II and support further analysis. Regarding waveform analysis and/or feature extraction, using a CNN could lead to more accurate calculations of established parameters, extraction of novel measurements or automated classification of cases with the advantage of using a full set of available features.

Although several challenges remain for the successful implementation of machine and deep learning [279], [285], [296], [297], these methods will surely change medical practice [298], [299].

PERSONAL PERSPECTIVE

This PhD project evinces the current prominence and need of progress in cardiovascular research and medicine at different levels to face successfully the global CVD epidemic in an increasingly aging population. Nonetheless, in order to deal with this challenge effectively, the implementation of interdisciplinary research and interdisciplinary health care is vital. The dramatic progress in medical technologies, the new challenges posed by economic and social costs in medicine, the necessity to rely on meaningful statistical analysis, the importance of bioethical principles on patient care, the arrival of new approaches for data management and, naturally, the central role of medicine, they all demonstrate that the future of the medicine resides in the constructive collaboration of interdisciplinary groups to successfully delivering quality care for patients.

The manifest focus of this dissertation on (cardiovascular) interdisciplinary research raises a fundamental question: which is the role of biomedical engineering in this transforming health care scenario? Reasonably, there are many potential responses from several viewpoints, thereby the following (partial) answer is essentially based on the experience gained during this PhD project. Most of the research conducted was possible as the result of joint efforts of professionals with various academic backgrounds and expertise fields. For instance, studies on arterial stiffness were supported by collaborative work of research groups of the medicine and engineering faculties of Ghent University (see Part II), the HF investigation, described in Chapters 4 and 5, was performed in association with the arterial haemodynamics and cardiovascular core lab of the University of Pennsylvania (Philadelphia, USA), and the development of an integrative system of applanation tonometry and ultrasound imaging for continuous physiological and medical monitoring to support space research (see Chapter 6) was feasible through a consortium with the company Verhaert (Kruibeke, Belgium), the Institute for Space

Medicine and Physiology (MEDES, Toulouse, France) and the European Space Agency (ESA). This collaborative work was not only fruitful but also an enriching professional and personal experience in which there were also challenges to overcome, such as finding a productive way of communication with other professionals. Nevertheless, those challenges became great opportunities to improve ideas and to achieve more complex objectives. And it is in this context that the role of the biomedical engineering becomes apparent as a crucial bridge between medicine and engineering to strengthen interdisciplinary research, to generate fundamental understanding of different fields and to catalyse the research process.

Remarkably, the key conclusion of this PhD project is the decisive responsibility of biomedical engineering, and of health care in general, to produce a substantial social impact from an interdisciplinary and scientific perspective. The investment of resources must be reflected in the improvement of the quality of life of patients, family and society overall. It is critical that the academia approaches society to generate long-term (effective) solutions for real and relevant problems, to justify its work and efforts.

BIBLIOGRAPHY

- [1] F. Londono-Hoyos, P. Segers, Z. Hashmath, G. Oldland, M. R. Koppula, K. Javaid, R. Miller, R. Bhuvva, I. Vasim, A. Tariq, W. Witschey, S. Akers and J. A. Chirinos, 'Non-invasive intraventricular pressure differences estimated with cardiac mri in subjects without heart failure and with heart failure with reduced and preserved ejection fraction', *Open Heart*, vol. 6, no. 2, 2019.
- [2] F. J. Londono-Hoyos, A. Swillens, J. Van Cauwenberge, B. Meyers, M. R. Koppula, P. Vlachos, J. A. Chirinos and P. Segers, 'Assessment of methodologies to calculate intraventricular pressure differences in computational models and patients', *Medical & biological engineering & computing*, vol. 56, no. 3, pp. 469–481, 2018.
- [3] F. Londono-Hoyos, P. Zamani, M. Beraun, I. Vasim, P. Segers and J. A. Chirinos, 'Effect of organic and inorganic nitrates on cerebrovascular pulsatile power transmission in patients with heart failure and preserved ejection fraction', *Physiological measurement*, vol. 39, no. 4, p. 044 001, 2018.
- [4] J. A. Chirinos, F. Londono-Hoyos, P. Zamani, M. Beraun, P. Haines, I. Vasim, S. Varakantam, T. S. Phan, T. P. Cappola, K. B. Margulies *et al.*, 'Effects of organic and inorganic nitrate on aortic and carotid haemodynamics in heart failure with preserved ejection fraction', *European journal of heart failure*, vol. 19, no. 11, pp. 1507–1515, 2017.
- [5] F. Londono, T. S. Klopmeijer, D. Georgakopoulos, E. G. Lovett, L. Van Bortel and P. Segers, 'Carotid haemodynamics during sympathetic nervous system stimulation via handgrip and cold pressor testing in young healthy subjects: A feasibility study', *Artery Research*, vol. 8, no. 4, pp. 178–188, 2014.
- [6] F. Londono, J. Bossuyt, L. Engelen, C. Stehouwer, I. Ferreira, S. Laurent, P. Boutouyrie, P. Segers and L. Van Bortel, '4d. 01: A simple calculator for the assessment of measurements of carotid-femoral pulse wave velocity and local arterial stiffness relative to the reference values database', *Journal of hypertension*, vol. 33, e60, 2015.

- [7] F. J. Londono Hoyos, J. Bossuyt, P. Segers and L. Van Bortel, 'An easy and intuitive web interface for the assessment of measurements of carotid-femoral pulse wave velocity and local arterial stiffness relative to the reference values database', in *Artery 15, Artery research*, vol. 12, 2015, pp. 43–43.
- [8] F. Londono, B. Uytterhaegen, R. Kassel, R. VanRaemdonck, A. Beck, B. Comet, A. Runge and P. Segers, '8a. 03: Continuous monitoring of hemodynamics in the short arm human centrifuge a feasibility study', *Journal of hypertension*, vol. 33, e104–e105, 2015.
- [9] F. J. Londono Hoyos, B. Meyers, P. Vlachos, J. Chirinos and P. Segers, 'Effect of organic nitrates on intraventricular pressure gradients in heart failure patients with preserved ejection fraction', in *Artery 14*, vol. 8, 2014, pp. 147–147.
- [10] F. J. Londoño, P. Segers, P. Shiva kumar, P. Konda, P. Zamani, R. Bhuva, A. Dunde, V. Ferrari and J. A. Chirinos, 'MRI assessment of diastolic and systolic intraventricular pressure gradients in heart failure', *Circulation*, vol. 130, no. suppl_2, A20360–A20360, 2014.
- [11] F. J. Londono Hoyos, P. Shiva-Kumar, S. Peddireddy, J. Chirinos and P. Segers, 'Sublingual nitroglycerin in patients with heart failure and preserved ejection fraction: Impact on central and regional carotid and radial input impedance and hemodynamics', in *Artery 14*, vol. 8, 2014, pp. 147–147.
- [12] F. J. Londono Hoyos, A. Swillens, B. Trachet and P. Segers, 'Wall tracking for the assessment of aortic distensibility during a follow up of 49 days in angiotensin ii-infused apoe-/-mice', in *ARTERY 12*, Elsevier, vol. 6, 2012, pp. 181–181.
- [13] S. Jain, F. J. Londono, P. Segers, T. C. Gillebert, M. De Buyzere and J. A. Chirinos, 'MRI assessment of diastolic and systolic intraventricular pressure gradients in heart failure', *Current heart failure reports*, vol. 13, no. 1, pp. 37–46, 2016.
- [14] T. S. Phan, F. Londono, J. A. Chirinos and J. K. Li, 'Augmentation index is blind to early-systolic effects of arterial wave reflections', *Journal of the American Society of Hypertension*, vol. 10, no. 4, e34, 2016.
- [15] B. Trachet, R. A. Fraga-Silva, F. J. Londono, A. Swillens, N. Stergiopoulos and P. Segers, 'Performance comparison of ultrasound-based methods to assess aortic diameter and stiffness in normal and aneurysmal mice', *PloS one*, vol. 10, no. 5, e0129007, 2015.
- [16] V. Fuster, 'Hurst's the heart'. McGraw-Hill, Medical Pub. Division, 2004.

-
- [17] J. G. Murphy, 'Mayo Clinic Cardiology: Concise Textbook'. CRC Press, 2006.
- [18] E. J. Topol and R. M. Califf, 'Textbook of cardiovascular medicine'. Lippincott Williams & Wilkins, 2007.
- [19] P. Libby, 'Braunwald's heart disease : a textbook of cardiovascular medicine'. Philadelphia: Saunders/Elsevier, 2008.
- [20] R. Rutherford, 'Vascular surgery'. Philadelphia: Saunders, 2005.
- [21] M. Moscucci, 'Grossman & Baim's cardiac catheterization, angiography, and intervention'. Lippincott Williams & Wilkins, 2013.
- [22] W. J. Zwiebel and J. S. Pellerito, 'Introduction to vascular ultrasonography'. Elsevier Saunders Philadelphia, PA, USA: 2005.
- [23] A. C. Chang and J. A. Towbin, 'Heart failure in children and young adults: from molecular mechanisms to medical and surgical strategies'. WB Saunders Company, 2006.
- [24] G. Martínez, 'Cirugía vascular'. Medellín, Colombia: Editorial Universidad de Antioquia, 2013.
- [25] K. T. Weber and J. S. Janicki, 'The heart as a muscle-pump system and the concept of heart failure', *American heart journal*, vol. 98, no. 3, pp. 371–384, 1979.
- [26] N. Westerhof, J.-W. Lankhaar and B. E. Westerhof, 'The arterial windkessel', *Medical & biological engineering & computing*, vol. 47, no. 2, pp. 131–141, 2009.
- [27] D. Unic-Stojanovic, 'Optimal perioperative fluid management: What is the strategy?', *Serbian Journal of Anesthesia and Intensive Therapy*, vol. 38, pp. 75–81, 2016.
- [28] K. Walley, 'Left ventricular function: Time-varying elastance and left ventricular aortic coupling', *Critical Care*, vol. 20, 2016.
- [29] R. Barst, 'A review of pulmonary arterial hypertension: Role of ambrisentan', *Vascular health and risk management*, vol. 3, pp. 11–22, 2007.

- [30] S. A. Hunt, D. W. Baker, M. H. Chin, M. P. Cinquegrani, A. M. Feldman, G. S. Francis, T. G. Ganiats, S. Goldstein, G. Gregoratos, M. L. Jessup *et al.*, 'Acc/aha guidelines for the evaluation and management of chronic heart failure in the adult: Executive summary: A report of the american college of cardiology/american heart association task force on practice guidelines (committee to revise the 1995 guidelines for the evaluation and management of heart failure) developed in collaboration with the international society for heart and lung transplantation endorsed by the heart failure society of america', *Journal of the American College of Cardiology*, vol. 38, no. 7, pp. 2101–2113, 2001.
- [31] B. A. Borlaug and W. J. Paulus, 'Heart failure with preserved ejection fraction: Pathophysiology, diagnosis, and treatment', *European heart journal*, vol. 32, no. 6, pp. 670–679, 2010.
- [32] C. S. Lam, E. Donal, E. Kraigher-Krainer and R. S. Vasan, 'Epidemiology and clinical course of heart failure with preserved ejection fraction', *Eur J Heart Fail*, vol. 13, no. 1, pp. 18–28, 2011.
- [33] J. E. Udelson, 'Heart failure with preserved ejection fraction', *Circulation*, vol. 124, no. 21, e540–3, 2011.
- [34] C. W. Yancy, M. Jessup, B. Bozkurt, J. Butler, D. E. Casey, M. H. Drazner, G. C. Fonarow, S. A. Geraci, T. Horwich, J. L. Januzzi *et al.*, '2013 accf/aha guideline for the management of heart failure: A report of the american college of cardiology foundation/american heart association task force on practice guidelines', *Journal of the American College of Cardiology*, vol. 62, no. 16, e147–e239, 2013.
- [35] C. W. Yancy, M. Jessup, B. Bozkurt, J. Butler, D. E. Casey, M. M. Colvin, M. H. Drazner, G. Filippatos, G. C. Fonarow, M. M. Givertz *et al.*, '2016 acc/aha/hfsa focused update on new pharmacological therapy for heart failure: An update of the 2013 accf/aha guideline for the management of heart failure: A report of the american college of cardiology/american heart association task force on clinical practice guidelines and the heart failure society of america', *Journal of the American College of Cardiology*, vol. 68, no. 13, pp. 1476–1488, 2016.
- [36] C. W. Yancy, M. Jessup, B. Bozkurt, J. Butler, D. E. Casey, M. M. Colvin, M. H. Drazner, G. S. Filippatos, G. C. Fonarow, M. M. Givertz *et al.*, '2017 acc/aha/hfsa focused update of the 2013 accf/aha guideline for the management of heart failure: A report of the american college of cardiology/american heart association task force on clinical practice guidelines and the heart failure society of america', *Journal of the American College of Cardiology*, vol. 70, no. 6, pp. 776–803, 2017.

-
- [37] S. A. Omar, E. Artime and A. J. Webb, 'A comparison of organic and inorganic nitrates/nitrites', *Nitric Oxide*, vol. 26, no. 4, pp. 229–240, 2012.
- [38] C. Monaco, 'The effects of dietary nitrate supplementation on contractile function and mitochondrial bioenergetics in the heart', PhD thesis, 2016.
- [39] S. Laurent, J. Cockcroft, L. Van Bortel, P. Boutouyrie, C. Giannattasio, D. Hayoz, B. Pannier, C. Vlachopoulos, I. Wilkinson and H. Struijker-Boudier, 'Expert consensus document on arterial stiffness: Methodological issues and clinical applications', *European heart journal*, vol. 27, no. 21, pp. 2588–2605, 2006.
- [40] A. Swillens and P. Segers, 'Assessment of arterial pressure wave reflection: Methodological considerations.' *Artery Research*, vol. 2, no. 4, pp. 122–131, 2008.
- [41] J. Kips, 'Development and validation of non-invasive diagnostic tools for the assessment of arterial stiffness and wave reflections with application in sub-saharan africa', eng, PhD thesis, Ghent University, 2011, pp. XXXIV, 229.
- [42] K. Najarian and R. Splinter, 'Biomedical signal and image processing'. CRC press, 2005.
- [43] J. L. Semmlow, 'Biosignal and medical image processing'. CRC press, 2008.
- [44] H. Feigenbaum, W. Armstrong and T. Ryan, 'Feigenbaum's echocardiography. 6', *Philadelphia: Lippincott Williams & Wilkins*, 2005.
- [45] J. Penaz, 'Photoelectric measurement of blood pressure, volume and flow in the finger'in: Digest of the 10th international conference on medical and biological engineering', *Dresden*, vol. 104, 1973.
- [46] R. D. Boehmer, 'Continuous, real-time, noninvasive monitor of blood pressure: Peñaz methodology applied to the finger', *Journal of clinical monitoring*, vol. 3, no. 4, pp. 282–287, 1987.
- [47] S. F. Nagueh, O. A. Smiseth, C. P. Appleton, B. F. Byrd, H. Dokainish, T. Edvardsen, F. A. Flachskampf, T. C. Gillebert, A. L. Klein, P. Lancellotti *et al.*, 'Recommendations for the evaluation of left ventricular diastolic function by echocardiography: An update from the american society of echocardiography and the european association of cardiovascular imaging', *European Journal of Echocardiography*, vol. 17, no. 12, pp. 1321–1360, 2016.

- [48] T. H. Marwick, T. C. Gillebert, G. Aurigemma, J. Chirinos, G. Derumeaux, M. Galderisi, J. Gottdiener, B. Haluska, E. Ofili, P. Segers *et al.*, 'Recommendations on the use of echocardiography in adult hypertension: A report from the european association of cardiovascular imaging (eacvi) and the american society of echocardiography (ase)', *European Heart Journal-Cardiovascular Imaging*, vol. 16, no. 6, pp. 577–605, 2015.
- [49] M. D. Cheitlin, J. S. Alpert, W. F. Armstrong, G. P. Aurigemma, G. A. Beller, F. Z. Bierman, T. W. Davidson, J. L. Davis, P. S. Douglas, L. D. Gillam *et al.*, 'Acc/aha guidelines for the clinical application of echocardiography: A report of the american college of cardiology/american heart association task force on practice guidelines (committee on clinical application of echocardiography) developed in collaboration with the american society of echocardiography', *Circulation*, vol. 95, no. 6, pp. 1686–1744, 1997.
- [50] M. D. Cheitlin, W. F. Armstrong, G. P. Aurigemma, G. A. Beller, F. Z. Bierman, J. L. Davis, P. S. Douglas, D. P. Faxon, L. D. Gillam, T. R. Kimball *et al.*, 'Acc/aha/ase 2003 guideline update for the clinical application of echocardiography: Summary article: A report of the american college of cardiology/american heart association task force on practice guidelines (acc/aha/ase committee to update the 1997 guidelines for the clinical application of echocardiography)', *Journal of the American College of Cardiology*, vol. 42, no. 5, pp. 954–970, 2003.
- [51] A. Goddi, M. Fanizza, C. Bortolotto, M. V. Raciti, I. Fiorina, X. He, Y. Du and F. Calliada, 'Vector flow imaging techniques: An innovative ultrasonographic technique for the study of blood flow', *Journal of Clinical Ultrasound*, vol. 45, no. 9, pp. 582–588, 2017.
- [52] K. Sampath, T. T. Harfi, R. T. George and J. Katz, 'Optimized time-resolved echo particle image velocimetry–particle tracking velocimetry measurements elucidate blood flow in patients with left ventricular thrombus', *Journal of biomechanical engineering*, vol. 140, no. 4, p. 041 010, 2018.
- [53] A. Caenen, 'A biomechanical analysis of shear wave elastography in pediatric heart models', PhD thesis, Ghent University, 2018.
- [54] M. Munin, M. Goerner, I. Raggio, J. Wisner, A. Tettamanzi, J. Godia, M. Penalosa and J. Guetta, 'A rare cause of dyspnea: Undifferentiated pleomorphic sarcoma in the left atrium', *Cardiology Research*, vol. 8, pp. 241–245, 2017.

-
- [55] K. S. Nayak, J.-F. Nielsen, M. A. Bernstein, M. Markl, P. D. Gatehouse, R. M. Botnar, D. Saloner, C. Lorenz, H. Wen, B. S. Hu *et al.*, 'Cardiovascular magnetic resonance phase contrast imaging', *Journal of Cardiovascular Magnetic Resonance*, vol. 17, no. 1, p. 71, 2015.
- [56] N. L. Greenberg, P. M. Vandervoort and J. D. Thomas, 'Instantaneous diastolic transmitral pressure differences from color doppler m mode echocardiography', *American Journal of Physiology-Heart and Circulatory Physiology*, vol. 271, no. 4, H1267–H1276, 1996.
- [57] N. L. Greenberg, P. M. Vandervoort, M. S. Firstenberg, M. J. Garcia and J. D. Thomas, 'Estimation of diastolic intraventricular pressure gradients by doppler m-mode echocardiography', *American Journal of Physiology-Heart and Circulatory Physiology*, vol. 280, no. 6, H2507–H2515, 2001.
- [58] R. B. Thompson and E. R. McVeigh, 'Fast measurement of intracardiac pressure differences with 2d breath-hold phase-contrast mri', *Magnetic resonance in medicine*, vol. 49, no. 6, pp. 1056–66, 2003.
- [59] K. C. Stewart, R. Kumar, J. J. Charonko, T. Ohara, P. P. Vlachos and W. C. Little, 'Evaluation of lv diastolic function from color m-mode echocardiography', *JACC. Cardiovascular imaging*, vol. 4, no. 1, pp. 37–46, 2011.
- [60] P. P. Vlachos, C. L. Niebel, S. Chakraborty, M. Pu and W. C. Little, 'Calculating intraventricular pressure difference using a multi-beat spatiotemporal reconstruction of color m-mode echocardiography', *Annals of Biomedical Engineering*, vol. 42, no. 12, pp. 2466–2479, 2014.
- [61] J. Van Cauwenberge, L. Lovstakken, S. Fadnes, A. Rodriguez-Morales, J. Vierendeels, P. Segers and A. Swillens, 'Assessing the performance of ultrafast vector flow imaging in the neonatal heart via multiphysics modeling and in vitro experiments', *IEEE transactions on ultrasonics, ferroelectrics, and frequency control*, vol. 63, no. 11, pp. 1772–1785, 2016.
- [62] S. Annerel, J. Degroote, T. Claessens, P. Segers, P. Verdonck and J. Vierendeels, 'The upstream boundary condition influences the leaflet opening dynamics in the numerical fsi simulation of an aortic bmvh', *International Journal for Numerical Methods in Biomedical Engineering*, vol. 28, no. 6-7, pp. 745–760, 2012.
- [63] P. Segers, E. R. Rietzschel, M. L. De Buyzere, S. J. Vermeersch, D. De Bacquer, L. M. Van Bortel, G. De Backer, T. C. Gillebert, P. R. Verdonck and i. Asklepios, 'Noninvasive (input) impedance, pulse wave velocity, and wave reflection in healthy middle-aged men and women', *Hypertension*, vol. 49, no. 6, pp. 1248–55, 2007.

- [64] J. A. Chirinos, P. Segers, A. K. Gupta, A. Swillens, E. R. Rietzschel, M. L. De Buyzere, J. N. Kirkpatrick, T. C. Gillebert, Y. Wang, M. G. Keane, R. Townsend, V. A. Ferrari, S. E. Wiegers and M. St John Sutton, 'Time-varying myocardial stress and systolic pressure-stress relationship: Role in myocardial-arterial coupling in hypertension', *Circulation*, vol. 119, no. 21, pp. 2798–807, 2009.
- [65] N. Stergiopoulos, P. Segers and N. Westerhof, 'Use of pulse pressure method for estimating total arterial compliance in vivo', *American Journal of Physiology-Heart and Circulatory Physiology*, vol. 276, no. 2, H424–H428, 1999.
- [66] Z. Liu, K. P. Brin and F. Yin, 'Estimation of total arterial compliance: An improved method and evaluation of current methods', *American Journal of Physiology-Heart and Circulatory Physiology*, vol. 251, no. 3, H588–H600, 1986.
- [67] R. A. Bleasdale, K. H. Parker and C. J. Jones, 'Chasing the wave. unfashionable but important new concepts in arterial wave travel', *American Journal of Physiology-Heart and Circulatory Physiology*, vol. 284, no. 6, H1879–H1885, 2003.
- [68] R. Ponzini, C. Vergara, G. Rizzo, A. Veneziani, A. Roghi, A. Vanzulli, O. Parodi and A. Redaelli, 'Womersley number-based estimates of blood flow rate in doppler analysis: In vivo validation by means of phase-contrast mri', *IEEE transactions on bio-medical engineering*, vol. 57, no. 7, pp. 1807–15, 2010.
- [69] R. Ponzini, C. Vergara, A. Redaelli and A. Veneziani, 'Reliable cfd-based estimation of flow rate in haemodynamics measures', *Ultrasound in medicine & biology*, vol. 32, no. 10, pp. 1545–55, 2006.
- [70] J. P. Mynard and J. J. Smolich, 'Novel wave power analysis linking pressure-flow waves, wave potential, and the forward and backward components of hydraulic power', *Am J Physiol Heart Circ Physiol*, vol. 310, no. 8, H1026–38, 2016.
- [71] —, 'Wave potential and the one-dimensional windkessel as a wave-based paradigm of diastolic arterial hemodynamics', *Am J Physiol Heart Circ Physiol*, vol. 307, no. 3, H307–18, 2014.
- [72] S. I. Rabben, S. Baerum, V. Sorhus and H. Torp, 'Ultrasound-based vessel wall tracking: An auto-correlation technique with rf center frequency estimation', *Ultrasound in medicine & biology*, vol. 28, no. 4, pp. 507–17, 2002.

-
- [73] D. De Wilde, B. Trachet, G. De Meyer and P. Segers, 'The influence of anesthesia and fluid–structure interaction on simulated shear stress patterns in the carotid bifurcation of mice', *Journal of biomechanics*, vol. 49, no. 13, pp. 2741–2747, 2016.
- [74] M. J. Swalen and A. W. Khir, 'Resolving the time lag between pressure and flow for the determination of local wave speed in elastic tubes and arteries', *Journal of biomechanics*, vol. 42, no. 10, pp. 1574–7, 2009.
- [75] J. Feng and A. W. Khir, 'Determination of wave speed and wave separation in the arteries using diameter and velocity', *Journal of biomechanics*, vol. 43, no. 3, pp. 455–62, 2010.
- [76] D. Mozaffarian, E. J. Benjamin, A. S. Go, D. K. Arnett, M. J. Blaha, M. Cushman, S. de Ferranti, J. P. Despres, H. J. Fullerton, V. J. Howard, M. D. Huffman, S. E. Judd, B. M. Kissela, D. T. Lackland, J. H. Lichtman, L. D. Lisabeth, S. M. Liu, R. H. Mackey, D. B. Matchar, D. K. McGuire, E. R. Mohler, C. S. Moy, P. Muntner, M. E. Mussolino, K. Nasir, R. W. Neumar, G. Nichol, L. Palaniappan, D. K. Pandey, M. J. Reeves, C. J. Rodriguez, P. D. Sorlie, J. Stein, A. Towfighi, T. N. Turan, S. S. Virani, J. Z. Willey, D. Woo, R. W. Yeh, M. B. Turner, A. H. A. S. Comm and S. S. Subcomm, 'Heart disease and stroke statistics-2015 update a report from the american heart association', *Circulation*, vol. 131, no. 4, E29–E322, 2015.
- [77] A. L. Bui, T. B. Horwich and G. C. Fonarow, 'Epidemiology and risk profile of heart failure', *Nature Reviews Cardiology*, vol. 8, no. 1, pp. 30–41, 2011.
- [78] J. McMurray, S. Adamopoulos, S. Anker, A. Auricchio, M. Bohm, K. Dickstein, V. Falk, G. Filippatos, C. Fonseca, M. Gomez-Sanchez *et al.*, 'Developed in collaboration with the heart failure association (hfa) of the esc', *Eur Heart J*, vol. 33, no. 14, pp. 1787–847, 2012.
- [79] S. Stewart, A. Jenkins, S. Buchan, A. McGuire, S. Capewell and J. J. V. McMurray, 'The current cost of heart failure to the national health service in the uk', *European Journal of Heart Failure*, vol. 4, no. 3, pp. 361–371, 2002.
- [80] S. Stewart, K. MacIntyre, S. Capewell and J. J. V. McMurray, 'Heart failure and the aging population: An increasing burden in the 21st century?', *Heart*, vol. 89, no. 1, pp. 49–53, 2003.
- [81] S. M. Dunlay and V. L. Roger, 'Understanding the epidemic of heart failure: Past, present, and future', *Current heart failure reports*, vol. 11, no. 4, pp. 404–15, 2014.

- [82] S. F. Nagueh, O. A. Smiseth, C. P. Appleton, B. F. Byrd III, H. Dokainish, T. Edvardsen, F. A. Flachskampf, T. C. Gillebert, A. L. Klein, P. Lancellotti *et al.*, 'Recommendations for the evaluation of left ventricular diastolic function by echocardiography: An update from the american society of echocardiography and the european association of cardiovascular imaging', *Journal of the American Society of Echocardiography*, vol. 29, no. 4, pp. 277–314, 2016.
- [83] M. Cameli, S. Mondillo, M. Solari, F. M. Righini, V. Andrei, C. Contaldi, E. D. Marco, M. D. Mauro, R. Esposito, S. Gallina, R. Montisci, A. Rossi, M. Galderisi, S. Nistri, E. Agricola and D. Mele, 'Echocardiographic assessment of left ventricular systolic function: From ejection fraction to torsion', *Heart Failure Reviews*, vol. 21, no. 1, pp. 77–94, 2016.
- [84] S. F. Nagueh, C. P. Appleton, T. C. Gillebert, P. N. Marino, J. K. Oh, O. A. Smiseth, A. D. Waggoner, F. A. Flachskampf, P. A. Pellikka and A. Evangelisa, 'Recommendations for the evaluation of left ventricular diastolic function by echocardiography', *European journal of echocardiography : the journal of the Working Group on Echocardiography of the European Society of Cardiology*, vol. 10, no. 2, pp. 165–93, 2009.
- [85] S. F. Nagueh, C. P. Appleton, T. C. Gillebert, P. N. Marino, J. K. Oh, O. A. Smiseth, A. D. Waggoner, F. A. Flachskampf, P. A. Pellikka and A. Evangelista, 'Recommendations for the evaluation of left ventricular diastolic function by echocardiography', *J Am Soc Echocardiogr*, vol. 22, no. 2, pp. 107–33, 2009.
- [86] P. Alter, A. R. Kocuzulla, C. Nell, J. H. Figiel, C. F. Vogelmeier and M. B. Rominger, 'Wall stress determines systolic and diastolic function-characteristics of heart failure', *International Journal of Cardiology*, vol. 202, pp. 685–693, 2016.
- [87] J. K. Oh, S. J. Park and S. F. Nagueh, 'Established and novel clinical applications of diastolic function assessment by echocardiography', *Circulation. Cardiovascular imaging*, vol. 4, no. 4, pp. 444–55, 2011.
- [88] M. J. Boogers, J. M. van Werkhoven, J. D. Schuijff, V. Delgado, H. M. El-Naggar, E. Boersma, G. Nucifora, R. J. van der Geest, B. P. Paelinck, L. J. Kroft, J. H. C. Reiber, A. de Roos, J. J. Bax and H. J. Lamb, 'Feasibility of diastolic function assessment with cardiac ct feasibility study in comparison with tissue doppler imaging', *Jacc-Cardiovascular Imaging*, vol. 4, no. 3, pp. 246–256, 2011.

-
- [89] J. J. Hartiala, G. H. Mostbeck, E. Foster, N. Fujita, M. C. Dulce, A. F. Chazouilleres and C. B. Higgins, 'Velocity-encoded cine mri in the evaluation of left-ventricular diastolic function - measurement of mitral-valve and pulmonary vein flow velocities and flow volume across the mitral-valve', *American Heart Journal*, vol. 125, no. 4, pp. 1054–1066, 1993.
- [90] S. R. Ommen, R. A. Nishimura, C. P. Appleton, F. A. Miller, J. K. Oh, M. M. Redfield and A. J. Tajik, 'Clinical utility of doppler echocardiography and tissue doppler imaging in the estimation of left ventricular filling pressures: A comparative simultaneous doppler-catheterization study', *Circulation*, vol. 102, no. 15, pp. 1788–94, 2000.
- [91] N. H. Prakken, A. J. Teske, M. J. Cramer, A. Mosterd, A. C. Bosker, W. P. Mali, P. A. Doevendans and B. K. Velthuis, 'Head-to-head comparison between echocardiography and cardiac mri in the evaluation of the athlete's heart', *British journal of sports medicine*, vol. 46, no. 5, pp. 348–54, 2012.
- [92] W. J. Paulus, C. Tschöpe, J. E. Sanderson, C. Rusconi, F. A. Flachskampf, F. E. Rademakers, P. Marino, O. A. Smiseth, G. D. Keulenaer, A. F. Leite-Moreira, A. Borbély, I. Édes, M. L. Handoko, S. Heymans, N. Pezzali, B. Pieske, K. Dickstein, A. G. Fraser and D. L. Brutsaert, 'How to diagnose diastolic heart failure: A consensus statement on the diagnosis of heart failure with normal left ventricular ejection fraction by the heart failure and echocardiography associations of the european society of cardiology.' *European Heart Journal*, vol. 28, no. 20, pp. 2539–2550, 2007.
- [93] J. A. Chirinos, S. R. Akers, L. Trieu, H. Ischiropoulos, P. Doulias, A. Tariq, I. Vasim, M. R. Koppula, A. A. Syed, H. Soto-Calderon, R. R. Townsend, T. P. Cappola, K. B. Margulies and P. Zamani, 'Heart failure, left ventricular remodeling, and circulating nitric oxide metabolites', *Journal of the American Heart Association*, vol. 5, no. 10, 2016.
- [94] H. Tsujino, E. Shiki, M. Hirama and K. Iinuma, 'Quantitative measurement of volume flow rate (cardiac output) by the multibeam doppler method', *Journal of the American Society of Echocardiography : official publication of the American Society of Echocardiography*, vol. 8, no. 5 Pt 1, pp. 621–30, 1995.
- [95] J. D. Thomas and Z. B. Popovic, 'Intraventricular pressure differences - a new window into cardiac function', *Circulation*, vol. 112, no. 12, pp. 1684–1686, 2005.
- [96] B. J. Bellhouse, 'Fluid mechanics of a model mitral valve and left ventricle', *Cardiovascular research*, vol. 6, no. 2, pp. 199–210, 1972.

- [97] A. Pasipoularides, J. P. Murgo, J. J. Bird and W. E. Craig, 'Fluid dynamics of aortic stenosis: Mechanisms for the presence of subvalvular pressure gradients', *The American journal of physiology*, vol. 246, no. 4 Pt 2, H542-50, 1984.
- [98] M. S. Firstenberg, P. M. Vandervoort, N. L. Greenberg, N. G. Smedira, P. M. McCarthy, M. J. Garcia and J. D. Thomas, 'Noninvasive estimation of transmitral pressure drop across the normal mitral valve in humans: Importance of convective and inertial forces during left ventricular filling', *Journal of the American College of Cardiology*, vol. 36, no. 6, pp. 1942-1949, 2000.
- [99] A. Rovner, R. Smith, N. L. Greenberg, E. M. Tuzcu, N. Smedira, H. M. Lever, J. D. Thomas and M. J. Garcia, 'Improvement in diastolic intraventricular pressure gradients in patients with hocom after ethanol septal reduction', *American journal of physiology. Heart and circulatory physiology*, vol. 285, no. 6, H2492-9, 2003.
- [100] J. P. Tasu, O. Jolivet and J. Bittoun, 'From flow to pressure: Estimation of pressure gradient and derivative by mr acceleration mapping', *Magma (New York, N.Y.)*, vol. 11, no. 1-2, pp. 55-7, 2000.
- [101] R. Yotti, J. Bermejo, J. C. Antoranz, M. M. Desco, C. Cortina, J. L. Rojo-Alvarez, C. Allue, L. Martin, M. Moreno, J. A. Serrano, R. Munoz and M. A. Garcia-Fernandez, 'A noninvasive method for assessing impaired diastolic suction in patients with dilated cardiomyopathy', *Circulation*, vol. 112, no. 19, pp. 2921-2929, 2005.
- [102] D. Ling, J. S. Rankin, 2. Edwards C. H., P. A. McHale and R. W. Anderson, 'Regional diastolic mechanics of the left ventricle in the conscious dog', *The American journal of physiology*, vol. 236, no. 2, H323-30, 1979.
- [103] J. D. Thomas and A. E. Weyman, 'Numerical modeling of ventricular filling', *Annals of biomedical engineering*, vol. 20, no. 1, pp. 19-39, 1992.
- [104] J. D. Thomas, J. B. Newell, C. Y. P. Choong and A. E. Weyman, 'Physical and physiological determinants of transmitral velocity - numerical-analysis', *American Journal of Physiology*, vol. 260, no. 5, H1718-H1730, 1991.
- [105] E. L. Yellin, S. Nikolic and R. W. M. Frater, 'Left-ventricular filling dynamics and diastolic function', *Progress in Cardiovascular Diseases*, vol. 32, no. 4, pp. 247-271, 1990.
- [106] L. Hatle, B. A. Angelsen and A. Tromsdal, 'Non-invasive assessment of aortic stenosis by doppler ultrasound', *British heart journal*, vol. 43, no. 3, pp. 284-92, 1980.

-
- [107] J. Bermejo, J. C. Antoranz, R. Yotti, M. Moreno and M. A. Garcia-Fernandez, 'Spatio-temporal mapping of intracardiac pressure gradients. a solution to euler's equation from digital postprocessing of color doppler m-mode echocardiograms', *Ultrasound in Medicine and Biology*, vol. 27, no. 5, pp. 621-630, 2001.
- [108] C. Clark, 'Relation between pressure difference across aortic-valve and left-ventricular outflow', *Cardiovascular Research*, vol. 12, no. 5, pp. 276-287, 1978.
- [109] P. J. Currie, D. J. Hagler, J. B. Seward, G. S. Reeder, D. A. Fyfe, A. A. Bove and A. J. Tajik, 'Instantaneous pressure-gradient - a simultaneous doppler and dual catheter correlative study', *Journal of the American College of Cardiology*, vol. 7, no. 4, pp. 800-806, 1986.
- [110] R. A. Nishimura, C. S. Rihal, A. J. Tajik and D. R. Holmes, 'Accurate measurement of the transmitral gradient in patients with mitral-stenosis - a simultaneous catheterization and doppler-echocardiographic study', *Journal of the American College of Cardiology*, vol. 24, no. 1, pp. 152-158, 1994.
- [111] G. T. Wilkins, L. D. Gillam, G. L. Kritzer, R. A. Levine, I. F. Palacios and A. E. Weyman, 'Validation of continuous-wave doppler echocardiographic measurements of mitral and tricuspid prosthetic valve gradients - a simultaneous doppler-catheter study', *Circulation*, vol. 74, no. 4, pp. 786-795, 1986.
- [112] A. P. Yoganathan, W. H. Corcoran and E. C. Harrison, 'Pressure drops across prosthetic aortic heart-valves under steady and pulsatile flow - invitro measurements', *Journal of Biomechanics*, vol. 12, no. 2, pp. 153-164, 1979.
- [113] Y. Sun, B. J. Sjoberg, P. Ask, D. Loyd and B. Wranne, 'Mathematical-model that characterizes transmitral and pulmonary venous flow velocity patterns', *American Journal of Physiology-Heart and Circulatory Physiology*, vol. 268, no. 1, H476-H489, 1995.
- [114] A. Pasipoularides, 'Clinical-assessment of ventricular ejection dynamics with and without outflow obstruction', *Journal of the American College of Cardiology*, vol. 15, no. 4, pp. 859-882, 1990.
- [115] S. F. C. Stewart, E. P. Nast, F. A. Arabia, T. L. Talbot, M. Proschan and R. E. Clark, 'Errors in pressure-gradient measurement by continuous wave doppler ultrasound - type, size and age effects in bioprosthetic aortic valves', *Journal of the American College of Cardiology*, vol. 18, no. 3, pp. 769-779, 1991.

- [116] P. S. Teirstein, P. G. Yock and R. L. Popp, 'The accuracy of doppler ultrasound measurement of pressure-gradients across irregular, dual, and tunnel-like obstructions to blood-flow', *Circulation*, vol. 72, no. 3, pp. 577–584, 1985.
- [117] P. M. Vandervoort, N. L. Greenberg, M. Pu, K. A. Powell, D. M. Cosgrove and J. D. Thomas, 'Pressure recovery in bileaflet heart-valve prostheses - localized high velocities and gradients in central and side orifices with implications for doppler-catheter gradient relation in aortic and mitral position', *Circulation*, vol. 92, no. 12, pp. 3464–3472, 1995.
- [118] S. D. Vasko, S. J. Goldberg, J. A. Requarth and H. D. Allen, 'Factors affecting accuracy of invitro valvar pressure-gradient estimates by doppler ultrasound', *American Journal of Cardiology*, vol. 54, no. 7, pp. 893–896, 1984.
- [119] C. Clark, 'The fluid mechanics of aortic stenosis–i. theory and steady flow experiments', *Journal of biomechanics*, vol. 9, no. 8, pp. 521–8, 1976.
- [120] —, 'The fluid mechanics of aortic stenosis - ii. unsteady flow experiments', *Journal of biomechanics*, vol. 9, no. 9, pp. 567–73, 1976.
- [121] J. D. Thomas and A. E. Weyman, 'Fluid dynamics model of mitral valve flow: Description with in vitro validation', *Journal of the American College of Cardiology*, vol. 13, no. 1, pp. 221–33, 1989.
- [122] K. Isaz, 'A theoretical model for the noninvasive assessment of the transmitral pressure-flow relation', *Journal of biomechanics*, vol. 25, no. 6, pp. 581–90, 1992.
- [123] R. A. Nishimura, M. D. Abel, L. K. Hatle, J. Holmes D. R., P. R. Housmans, E. L. Ritman and A. J. Tajik, 'Significance of doppler indices of diastolic filling of the left ventricle: Comparison with invasive hemodynamics in a canine model', *American heart journal*, vol. 118, no. 6, pp. 1248–58, 1989.
- [124] D. David, R. M. Lang, A. Neumann, P. Sareli, R. Marcus, K. T. Spencer and K. M. Borow, 'Comparison of doppler indexes of left ventricular diastolic function with simultaneous high fidelity left atrial and ventricular pressures in idiopathic dilated cardiomyopathy', *The American journal of cardiology*, vol. 64, no. 18, pp. 1173–9, 1989.
- [125] T. Ebbers and G. Farneback, 'Improving computation of cardiovascular relative pressure fields from velocity mri', *Journal of Magnetic Resonance Imaging*, vol. 30, no. 1, pp. 54–61, 2009.

-
- [126] B. W. van Oudheusden, 'Piv-based pressure measurement', *Measurement Science and Technology*, vol. 24, no. 3, 2013.
- [127] J. M. Tyszka, D. H. Laidlaw, J. W. Asa and J. M. Silverman, 'Three-dimensional, time-resolved (4d) relative pressure mapping using magnetic resonance imaging', *Journal of magnetic resonance imaging : JMRI*, vol. 12, no. 2, pp. 321–9, 2000.
- [128] M. Courtois, J. Kovacs S. J. and P. A. Ludbrook, 'Transmitral pressure-flow velocity relation. importance of regional pressure gradients in the left ventricle during diastole', *Circulation*, vol. 78, no. 3, pp. 661–71, 1988.
- [129] M. Courtois, B. Barzilai, F. Gutierrez and P. A. Ludbrook, 'Characterization of regional diastolic pressure gradients in the right ventricle', *Circulation*, vol. 82, no. 4, pp. 1413–23, 1990.
- [130] M. Courtois, S. J. Kovacs and P. A. Ludbrook, 'Physiological early diastolic intraventricular pressure gradient is lost during acute myocardial ischemia', *Circulation*, vol. 81, no. 5, pp. 1688–96, 1990.
- [131] M. Courtois, Z. Vered, B. Barzilai, N. A. Ricciotti, J. E. Perez and P. A. Ludbrook, 'The transmitral pressure-flow velocity relation. effect of abrupt preload reduction', *Circulation*, vol. 78, no. 6, pp. 1459–68, 1988.
- [132] J. J. Bird, J. P. Murgo and A. Pasipoularides, 'Fluid dynamics of aortic stenosis: Subvalvular gradients without subvalvular obstruction', *Circulation*, vol. 66, no. 4, pp. 835–40, 1982.
- [133] A. Pasipoularides, J. P. Murgo, J. W. Miller and W. E. Craig, 'Nonobstructive left ventricular ejection pressure gradients in man', *Circulation research*, vol. 61, no. 2, pp. 220–7, 1987.
- [134] R. Yotti, J. Bermejo, M. M. Desco, J. C. Antoranz, J. L. Rojo-Alvarez, C. Cortina, C. Allue, H. Rodriguez-Abella, M. Moreno and M. A. Garcia-Fernandez, 'Doppler-derived ejection intraventricular pressure gradients provide a reliable assessment of left ventricular systolic chamber function', *Circulation*, vol. 112, no. 12, pp. 1771–1779, 2005.
- [135] A. Rovner, N. L. Greenberg, J. D. Thomas and M. J. Garcia, 'Relationship of diastolic intraventricular pressure gradients and aerobic capacity in patients with diastolic heart failure', *American journal of physiology. Heart and circulatory physiology*, vol. 289, no. 5, H2081–8, 2005.
- [136] K. Isaz, 'Expanding the frontiers of doppler echocardiography for the noninvasive assessment of diastolic hemodynamics', *Journal of the American College of Cardiology*, vol. 36, no. 6, pp. 1950–2, 2000.

- [137] B. O. Haugen, S. Berg, K. M. Brecke, H. Torp, S. A. Slordahl, T. Skaerpe and S. O. Samstad, 'Blood flow velocity profiles in the aortic annulus: A 3-dimensional freehand color flow doppler imaging study', *Journal of the American Society of Echocardiography : official publication of the American Society of Echocardiography*, vol. 15, no. 4, pp. 328–33, 2002.
- [138] N. Thomas, P. Taylor and S. Padayachee, 'The impact of theoretical errors on velocity estimation and accuracy of duplex grading of carotid stenosis', *Ultrasound in medicine & biology*, vol. 28, no. 2, pp. 191–6, 2002.
- [139] G. Weber, A. L. Strauss, H. Rieger, A. Scheffler and J. Eisenhoffer, 'Validation of doppler measurement of pressure gradients across peripheral model arterial stenosis', *Journal of vascular surgery*, vol. 16, no. 1, pp. 10–6, 1992.
- [140] S. N. Urchuk and D. B. Plewes, 'Mr measurement of time-dependent blood pressure variations', *Journal of magnetic resonance imaging : JMRI*, vol. 5, no. 6, pp. 621–7, 1995.
- [141] G. Z. Yang, P. J. Kilner, N. B. Wood, S. R. Underwood and D. N. Firmin, 'Computation of flow pressure fields from magnetic resonance velocity mapping', *Magnetic resonance in medicine*, vol. 36, no. 4, pp. 520–6, 1996.
- [142] L. Sondergaard, P. Hildebrandt, K. Lindvig, C. Thomsen, F. Stahlberg, E. Kassis and O. Henriksen, 'Valve area and cardiac output in aortic stenosis: Quantification by magnetic resonance velocity mapping', *American heart journal*, vol. 126, no. 5, pp. 1156–64, 1993.
- [143] L. Sondergaard, F. Stahlberg, C. Thomsen, A. Stensgaard, K. Lindvig and O. Henriksen, 'Accuracy and precision of mr velocity mapping in measurement of stenotic cross-sectional area, flow rate, and pressure gradient', *Journal of magnetic resonance imaging : JMRI*, vol. 3, no. 2, pp. 433–7, 1993.
- [144] L. Sondergaard, C. Thomsen, F. Stahlberg, E. Gyomoese, K. Lindvig, P. Hildebrandt and O. Henriksen, 'Mitral and aortic valvular flow: Quantification with mr phase mapping', *Journal of magnetic resonance imaging : JMRI*, vol. 2, no. 3, pp. 295–302, 1992.
- [145] S. N. Urchuk and D. B. Plewes, 'A velocity correlation method for measuring vascular compliance using mr imaging', *Journal of magnetic resonance imaging : JMRI*, vol. 5, no. 6, pp. 628–34, 1995.
- [146] D. B. Plewes, S. N. Urchuk, S. Kim and I. Soutar, 'An mr compatible flow simulator for intravascular pressure simulation', *Medical physics*, vol. 22, no. 7, pp. 1111–5, 1995.

-
- [147] S. N. Urchuk and D. B. Plewes, 'Mr measurements of pulsatile pressure gradients', *Journal of magnetic resonance imaging : JMRI*, vol. 4, no. 6, pp. 829–36, 1994.
- [148] T. Ebbers, L. Wigstrom, A. F. Bolger, J. Engvall and M. Karlsson, 'Estimation of relative cardiovascular pressures using time-resolved three-dimensional phase contrast mri', *Magnetic resonance in medicine*, vol. 45, no. 5, pp. 872–9, 2001.
- [149] J. P. Tasu, E. Mousseaux, A. Delouche, C. Oddou, O. Jolivet and J. Bittoun, 'Estimation of pressure gradients in pulsatile flow from magnetic resonance acceleration measurements', *Magnetic resonance in medicine*, vol. 44, no. 1, pp. 66–72, 2000.
- [150] L. Wigstrom, L. Sjoqvist and B. Wranne, 'Temporally resolved 3d phase-contrast imaging', *Magnetic resonance in medicine*, vol. 36, no. 5, pp. 800–3, 1996.
- [151] P. D. Gatehouse, J. Keegan, L. A. Crowe, S. Masood, R. H. Mohiaddin, K. F. Kreitner and D. N. Firmin, 'Applications of phase-contrast flow and velocity imaging in cardiovascular mri', *European radiology*, vol. 15, no. 10, pp. 2172–84, 2005.
- [152] P. D. Gatehouse, M. P. Rolf, M. J. Graves, M. B. Hofman, J. Totman, B. Werner, R. A. Quest, Y. Liu, J. von Spiczak, M. Dieringer, D. N. Firmin, A. van Rossum, M. Lombardi, J. Schwitter, J. Schulz-Menger and P. J. Kilner, 'Flow measurement by cardiovascular magnetic resonance: A multi-centre multi-vendor study of background phase offset errors that can compromise the accuracy of derived regurgitant or shunt flow measurements', *Journal of cardiovascular magnetic resonance : official journal of the Society for Cardiovascular Magnetic Resonance*, vol. 12, p. 5, 2010.
- [153] A. Chernobelsky, O. Shubayev, C. R. Comeau and S. D. Wolff, 'Baseline correction of phase contrast images improves quantification of blood flow in the great vessels', *Journal of cardiovascular magnetic resonance : official journal of the Society for Cardiovascular Magnetic Resonance*, vol. 9, no. 4, pp. 681–5, 2007.
- [154] E. Heiberg, J. Sjogren, M. Ugander, M. Carlsson, H. Engblom and H. Arheden, 'Design and validation of segment–freely available software for cardiovascular image analysis', *BMC medical imaging*, vol. 10, p. 1, 2010.
- [155] P. Brun, C. Tribouilloy, A. M. Duval, L. Iserin, A. Meguira, G. Pelle and J. L. Dubois-Rande, 'Left ventricular flow propagation during early filling is related to wall relaxation: A color m-mode doppler analysis', *Journal of the American College of Cardiology*, vol. 20, no. 2, pp. 420–32, 1992.

- [156] M. J. Garcia, M. A. Ares, C. Asher, L. Rodriguez, P. Vandervoort and J. D. Thomas, 'An index of early left ventricular filling that combined with pulsed doppler peak e velocity may estimate capillary wedge pressure', *Journal of the American College of Cardiology*, vol. 29, no. 2, pp. 448–54, 1997.
- [157] J. D. Thomas and Z. B. Popovic, 'Assessment of left ventricular function by cardiac ultrasound', *Journal of the American College of Cardiology*, vol. 48, no. 10, pp. 2012–25, 2006.
- [158] T. C. Gillebert and M. L. De Buyzere, 'Hfpef, diastolic suction, and exercise', *Jacc-Cardiovascular Imaging*, vol. 5, no. 9, pp. 871–873, 2012.
- [159] A. Opdahl, E. W. Remme, T. Helle-Valle, E. Lyseggen, T. Vartdal, E. Pettersen, T. Edvardsen and O. A. Smiseth, 'Determinants of left ventricular early-diastolic lengthening velocity: Independent contributions from left ventricular relaxation, restoring forces, and lengthening load', *Circulation*, vol. 119, no. 19, pp. 2578–86, 2009.
- [160] H. L. Falsetti, M. S. Verani, C. J. Chen and J. A. Cramer, 'Regional pressure differences in the left ventricle', *Catheterization and cardiovascular diagnosis*, vol. 6, no. 2, pp. 123–34, 1980.
- [161] K. Steine, M. Stugaard and O. A. Smiseth, 'Mechanisms of retarded apical filling in acute ischemic left ventricular failure', *Circulation*, vol. 99, no. 15, pp. 2048–54, 1999.
- [162] K. Steine, M. Stugaard and O. Smiseth, 'Mechanisms of diastolic intraventricular regional pressure differences and flow in the inflow and outflow tracts', *Journal of the American College of Cardiology*, vol. 40, no. 5, pp. 983–90, 2002.
- [163] M. S. Firstenberg, N. L. Greenberg, M. J. Garcia and J. D. Thomas, 'Relationship between ventricular contractility and early diastolic intraventricular pressure gradients: A diastolic link to systolic function', *Journal of the American Society of Echocardiography*, vol. 21, no. 5, pp. 501–506, 2008.
- [164] M. S. Firstenberg, N. G. Smedira, N. L. Greenberg, D. L. Prior, P. M. McCarthy, M. J. Garcia and J. D. Thomas, 'Relationship between early diastolic intraventricular pressure gradients, an index of elastic recoil, and improvements in systolic and diastolic function', *Circulation*, vol. 104, no. 12, pp. I330–I335, 2001.
- [165] J. A. Chirinos, P. Segers, E. R. Rietzschel, M. L. De Buyzere, M. W. Raja, T. Claessens, D. De Bacquer, M. St John Sutton, T. C. Gillebert and I. Asklepios, 'Early and late systolic wall stress differentially relate to myocardial contraction and relaxation in middle-aged adults: The asklepios study', *Hypertension*, vol. 61, no. 2, pp. 296–303, 2013.

-
- [166] R. Yotti, J. Bermejo, Y. Benito, J. C. Antoranz, M. M. Desco, D. Rodriguez-Perez, C. Cortina, T. Mombiola, A. Barrio, J. Elizaga and F. Fernandez-Aviles, 'Noninvasive estimation of the rate of relaxation by the analysis of intraventricular pressure gradients', *Circulation-Cardiovascular Imaging*, vol. 4, no. 2, pp. 94–104, 2011.
- [167] O. A. Smiseth, K. Steine, G. Sandbaek, M. Stugaard and T. O. Gjolberg, 'Mechanics of intraventricular filling: Study of lv early diastolic pressure gradients and flow velocities', *American Journal of Physiology-Heart and Circulatory Physiology*, vol. 275, no. 3, H1062–H1069, 1998.
- [168] T. Yoshida, N. Ohte, H. Narita, S. Sakata, K. Wakami, K. Asada, H. Miyabe, T. Saeki and G. Kimura, 'Lack of inertia force of late systolic aortic flow is a cause of left ventricular isolated diastolic dysfunction in patients with coronary artery disease', *Journal of the American College of Cardiology*, vol. 48, no. 5, pp. 983–991, 2006.
- [169] P. Zamani, D. A. Bluemke, D. R. Jacobs, D. A. Duprez, R. Kronmal, S. M. Lilly, V. A. Ferrari, R. R. Townsend, J. A. Lima, M. Budoff, P. Segers, P. Hannan and J. A. Chirinos, 'Resistive and pulsatile arterial load as predictors of left ventricular mass and geometry the multi-ethnic study of atherosclerosis', *Hypertension*, vol. 65, no. 1, pp. 85–92, 2015.
- [170] T. Weber, S. Wassertheurer, M. F. O'Rourke, A. Haiden, R. Zweiker, M. Rammer, B. Hametner and B. Eber, 'Pulsatile hemodynamics in patients with exertional dyspnea potentially of value in the diagnostic evaluation of suspected heart failure with preserved ejection fraction', *Journal of the American College of Cardiology*, vol. 61, no. 18, pp. 1874–1883, 2013.
- [171] T. Weber, M. F. O'Rourke, M. Ammer, E. Kvas, C. Punzengruber and B. Eber, 'Arterial stiffness and arterial wave reflections are associated with systolic and diastolic function in patients with normal ejection fraction', *Am J Hypertens*, vol. 21, no. 11, pp. 1194–202, 2008.
- [172] S. H. Sung, W. C. Yu, H. M. Cheng, C. W. Lee, M. M. Lin, S. Y. Chuang and C. H. Chen, 'Excessive wave reflections on admission predict post-discharge events in patients hospitalized due to acute heart failure', *Eur J Heart Fail*, vol. 14, no. 12, pp. 1348–55, 2012.
- [173] S. Kobayashi, M. Yano, M. Kohno, M. Obayashi, Y. Hisamatsu, T. Ryoke, T. Ohkusa, K. Yamakawa and M. Matsuzaki, 'Influence of aortic impedance on the development of pressure-overload left ventricular hypertrophy in rats', *Circulation*, vol. 94, no. 12, pp. 3362–8, 1996.

- [174] J. Hashimoto, B. E. Westerhof, N. Westerhof, Y. Imai and M. F. O'Rourke, 'Different role of wave reflection magnitude and timing on left ventricular mass reduction during antihypertensive treatment', *J Hypertens*, vol. 26, no. 5, pp. 1017–24, 2008.
- [175] T. C. Gillebert and W. Y. Lew, 'Influence of systolic pressure profile on rate of left ventricular pressure fall', *Am J Physiol*, vol. 261, no. 3 Pt 2, H805–13, 1991.
- [176] J. A. Chirinos, P. Segers, D. A. Duprez, L. Brumback, D. A. Bluemke, P. Zamani, R. Kronmal, D. Vaidya, P. Ouyang, R. R. Townsend and D. R. Jacobs, 'Late systolic central hypertension as a predictor of incident heart failure: The multi-ethnic study of atherosclerosis', *Journal of the American Heart Association*, vol. 4, no. 3, 2015.
- [177] J. A. Chirinos, J. G. Kips, J. Jacobs D. R., L. Brumback, D. A. Duprez, R. Kronmal, D. A. Bluemke, R. R. Townsend, S. Vermeersch and P. Segers, 'Arterial wave reflections and incident cardiovascular events and heart failure: Mesa (multiethnic study of atherosclerosis)', *J Am Coll Cardiol*, vol. 60, no. 21, pp. 2170–7, 2012.
- [178] M. Guerra, C. Bras-Silva, M. J. Amorim, C. Moura, P. Bastos and A. F. Leite-Moreira, 'Intraventricular pressure gradients in heart failure', *Physiological Research*, vol. 62, no. 5, pp. 479–487, 2013.
- [179] T. Ohara, C. L. Niebel, K. C. Stewart, J. J. Charonko, M. Pu, P. P. Vlachos and W. C. Little, 'Loss of adrenergic augmentation of diastolic intra-lv pressure difference in patients with diastolic dysfunction evaluation by color m-mode echocardiography', *Jacc-Cardiovascular Imaging*, vol. 5, no. 9, pp. 861–870, 2012.
- [180] J. D. Thomas, 'Flow propagation analysis computer or eyeball?', *Jacc-Cardiovascular Imaging*, vol. 4, no. 1, pp. 47–49, 2011.
- [181] H. Iwano, D. Kamimura, E. Fox, M. Hall, P. Vlachos and W. C. Little, 'Altered spatial distribution of the diastolic left ventricular pressure difference in heart failure', *Journal of the American Society of Echocardiography*, vol. 28, no. 5, 597–U185, 2015.
- [182] B. Baccani, F. Domenichini, G. Pedrizzetti and G. Tonti, 'Fluid dynamics of the left ventricular filling in dilated cardiomyopathy', *Journal of Biomechanics*, vol. 35, no. 5, pp. 665–671, 2002.
- [183] M. Nakamura, S. Wada, T. Mikami, A. Kitabatake and T. Karino, 'Computational study on the evolution of an intraventricular vortical flow during early diastole for the interpretation of color m-mode doppler echocardiograms', *Biomechanics and modeling in mechanobiology*, vol. 2, no. 2, pp. 59–72, 2003.

-
- [184] J. N. Oshinski, W. J. Parks, C. P. Markou, H. L. Bergman, B. E. Larson, D. N. Ku, J. Mukundan S. and R. I. Pettigrew, 'Improved measurement of pressure gradients in aortic coarctation by magnetic resonance imaging', *Journal of the American College of Cardiology*, vol. 28, no. 7, pp. 1818–26, 1996.
- [185] J. H. Seo, V. Vedula, T. Abraham and R. Mittal, 'Multiphysics computational models for cardiac flow and virtual cardiography', *International journal for numerical methods in biomedical engineering*, vol. 29, no. 8, pp. 850–69, 2013.
- [186] X. Zheng, J. H. Seo, V. Vedula, T. Abraham and R. Mittal, 'Computational modeling and analysis of intracardiac flows in simple models of the left ventricle', *European Journal of Mechanics B-Fluids*, vol. 35, pp. 31–39, 2012.
- [187] G. Pedrizzetti and F. Domenichini, 'Left ventricular fluid mechanics: The long way from theoretical models to clinical applications', *Annals of biomedical engineering*, vol. 43, no. 1, pp. 26–40, 2015.
- [188] G. Pedrizzetti, A. R. Martiniello, V. Bianchi, A. D'Onofrio, P. Caso and G. Tonti, 'Cardiac fluid dynamics anticipates heart adaptation', *Journal of biomechanics*, vol. 48, no. 2, pp. 388–91, 2015.
- [189] J. L. Rojo-Alvarez, J. Bermejo, A. B. Rodriguez-Gonzalez, A. Martinez-Fernandez, R. Yotti, M. A. Garcia-Fernandez and J. Carlos Antoranz, 'Impact of image spatial, temporal, and velocity resolutions on cardiovascular indices derived from color-doppler echocardiography', *Medical image analysis*, vol. 11, no. 6, pp. 513–25, 2007.
- [190] B. I. Gardner, S. E. Bingham, M. R. Allen, D. D. Blatter and J. L. Anderson, 'Cardiac magnetic resonance versus transthoracic echocardiography for the assessment of cardiac volumes and regional function after myocardial infarction: An intrasubject comparison using simultaneous intrasubject recordings', *Cardiovascular ultrasound*, vol. 7, no. 1, p. 38, 2009.
- [191] R. Krishnamurthy, B. Cheong and R. Muthupillai, 'Tools for cardiovascular magnetic resonance imaging', *Cardiovascular diagnosis and therapy*, vol. 4, no. 2, pp. 104–25, 2014.
- [192] F. Buyens, O. Jolivet, A. D. Cesare, J. Bittoun, A. Herment, J.-P. Tasu and E. Mousseaux, 'Calculation of left ventricle relative pressure distribution in mri using acceleration data.' *Magnetic Resonance in Medicine*, vol. 53, no. 4, pp. 877–884, 2005.

- [193] R. Yotti, J. Bermejo, J. Antoranz, J. é Luis Rojo-Álvarez, C. Allue, J. Silva, M. Desco, M. Moreno and M. A. García-Fernández, 'Non-invasive assessment of ejection intraventricular pressure gradients', *Journal of the American College of Cardiology*, vol. 43, no. 9, pp. 1654–1662, 2004.
- [194] A. Pasipoularides, 'Right and left ventricular diastolic flow field: Why are measured intraventricular pressure gradients small?', *Revista Espanola De Cardiologia*, vol. 66, no. 5, pp. 337–341, 2013.
- [195] S. S. Mitter, S. J. Shah and J. D. Thomas, 'A test in context: E/a and e/e' to assess diastolic dysfunction and lv filling pressure', *Journal of the American College of Cardiology*, vol. 69, no. 11, pp. 1451–1464, 2017.
- [196] J. H. Park and T. H. Marwick, 'Use and limitations of e/e' to assess left ventricular filling pressure by echocardiography', *Journal of Cardiovascular Ultrasound*, vol. 19, no. 4, pp. 169–173, 2011.
- [197] T. Edvardsen, B. D. Rosen, L. Pan, M. Jerosch-Herold, S. Lai, W. G. Hundley, S. Sinha, R. A. Kronmal, D. A. Bluemke and J. A. Lima, 'Regional diastolic dysfunction in individuals with left ventricular hypertrophy measured by tagged magnetic resonance imaging - the multi-ethnic study of atherosclerosis (mesa)', *American Heart Journal*, vol. 151, no. 1, pp. 109–114, 2006.
- [198] H. Fok, A. Guilcher, Y. Li, S. Brett, A. Shah, B. Clapp and P. Chowienczyk, 'Augmentation pressure is influenced by ventricular contractility/relaxation dynamics: Novel mechanism of reduction of pulse pressure by nitrates', *Hypertension*, vol. 63, no. 5, pp. 1050–5, 2014.
- [199] T. W. Latson, W. C. Hunter, N. Katoh and K. Sagawa, 'Effect of nitroglycerin on aortic impedance, diameter, and pulse-wave velocity', *Circ Res*, vol. 62, no. 5, pp. 884–90, 1988.
- [200] D. H. Fitchett, G. J. Simkus, J. P. Beaudry and D. G. Marpole, 'Reflected pressure waves in the ascending aorta: Effect of glyceryl trinitrate', *Cardiovasc Res*, vol. 22, no. 7, pp. 494–500, 1988.
- [201] T. Yaginuma, A. Avolio, M. O'Rourke, W. Nichols, J. J. Morgan, P. Roy, D. Baron, J. Branson and M. Feneley, 'Effect of glyceryl trinitrate on peripheral arteries alters left ventricular hydraulic load in man', *Cardiovasc Res*, vol. 20, no. 2, pp. 153–60, 1986.
- [202] G. S. Stokes, E. S. Barin and K. L. Gilfillan, 'Effects of isosorbide mononitrate and aii inhibition on pulse wave reflection in hypertension', *Hypertension*, vol. 41, no. 2, pp. 297–301, 2003.

-
- [203] A. Heart Failure Society Of, 'Evaluation and management of patients with heart failure and preserved left ventricular ejection fraction', *J Card Fail*, vol. 12, no. 1, e80–5, 2006.
- [204] S. A. Hunt, W. T. Abraham, M. H. Chin, A. M. Feldman, G. S. Francis, T. G. Ganiats, M. Jessup, M. A. Konstam, D. M. Mancini, K. Michl, J. A. Oates, P. S. Rahko, M. A. Silver, L. W. Stevenson and C. W. Yancy, '2009 focused update incorporated into the acc/aha 2005 guidelines for the diagnosis and management of heart failure in adults: A report of the american college of cardiology foundation/american heart association task force on practice guidelines: Developed in collaboration with the international society for heart and lung transplantation', *Circulation*, vol. 119, no. 14, e391–479, 2009.
- [205] M. M. Redfield, K. J. Anstrom, J. A. Levine, G. A. Koepp, B. A. Borlaug, H. H. Chen, M. M. LeWinter, S. M. Joseph, S. J. Shah, M. J. Semigran, G. M. Felker, R. T. Cole, G. R. Reeves, R. J. Tedford, W. H. Tang, S. E. McNulty, E. J. Velazquez, M. R. Shah and E. Braunwald, 'Isosorbide mononitrate in heart failure with preserved ejection fraction', *The New England journal of medicine*, vol. 373, no. 24, pp. 2314–24, 2015.
- [206] P. Zamani, S. Akers, H. Soto-Calderon, M. Beraun, M. R. Koppula, S. Varakantam, D. Rawat, P. Shiva-Kumar, P. G. Haines, J. Chittams, R. R. Townsend, W. R. Witschey, P. Segers and J. A. Chirinos, 'Isosorbide dinitrate, with or without hydralazine, does not reduce wave reflections, left ventricular hypertrophy, or myocardial fibrosis in patients with heart failure with preserved ejection fraction', *J Am Heart Assoc*, vol. 6, no. 2, 2017.
- [207] P. Zamani, B. French, J. A. Brandimarto, P. T. Doulias, A. Javaheri, J. A. Chirinos, K. B. Margulies, R. R. Townsend, N. K. Sweitzer, J. C. Fang, H. Ischiropoulos and T. P. Cappola, 'Effect of heart failure with preserved ejection fraction on nitric oxide metabolites', *Am J Cardiol*, 2016.
- [208] P. Zamani, D. Rawat, P. Shiva-Kumar, S. Geraci, R. Bhuvu, P. Konda, P. T. Doulias, H. Ischiropoulos, R. R. Townsend, K. B. Margulies, T. P. Cappola, D. C. Poole and J. A. Chirinos, 'Effect of inorganic nitrate on exercise capacity in heart failure with preserved ejection fraction', *Circulation*, vol. 131, no. 4, 371–80, discussion 380, 2015.
- [209] J. Eggebeen, D. B. Kim-Shapiro, M. Haykowsky, T. M. Morgan, S. Basu, P. Brubaker, J. Rejeski and D. W. Kitzman, 'One week of daily dosing with beetroot juice improves submaximal endurance and blood pressure in older patients with heart failure and preserved ejection fraction', *JACC. Heart failure*, vol. 4, no. 6, pp. 428–37, 2016.

- [210] J. A. Chirinos and P. Zamani, 'The nitrate-nitrite-no pathway and its implications for heart failure and preserved ejection fraction', *Curr Heart Fail Rep*, vol. 13, no. 1, pp. 47–59, 2016.
- [211] R. Vanderpool and M. T. Gladwin, 'Harnessing the nitrate-nitrite-nitric oxide pathway for therapy of heart failure with preserved ejection fraction', *Circulation*, vol. 131, no. 4, pp. 334–6, 2015.
- [212] S. A. Omar, H. Fok, K. D. Tilgner, A. Nair, J. Hunt, B. Jiang, P. Taylor, P. Chowienczyk and A. J. Webb, 'Paradoxical normoxia-dependent selective actions of inorganic nitrite in human muscular conduit arteries and related selective actions on central blood pressures', *Circulation*, vol. 131, no. 4, 381–9, discussion 389, 2015.
- [213] C. H. Chen, C. T. Ting, A. Nussbacher, E. Nevo, D. A. Kass, P. Pak, S. P. Wang, M. S. Chang and F. C. Yin, 'Validation of carotid artery tonometry as a means of estimating augmentation index of ascending aortic pressure', *Hypertension*, vol. 27, no. 2, pp. 168–75, 1996.
- [214] P. Segers, E. Rietzschel, S. Heireman, M. De Buyzere, T. Gillebert, P. Verdonck and L. Van Bortel, 'Carotid tonometry versus synthesized aorta pressure waves for the estimation of central systolic blood pressure and augmentation index', *Am J Hypertens*, vol. 18, no. 9 Pt 1, pp. 1168–73, 2005.
- [215] W. Nichols, M. O'Rourke and C. Vlachopoulos, 'McDonald's blood flow in arteries: theoretical, experimental and clinical principles'. CRC Press, 2011.
- [216] N. Westerhof, P. Sipkema, G. C. van den Bos and G. Elzinga, 'Forward and backward waves in the arterial system', *Cardiovasc Res*, vol. 6, no. 6, pp. 648–56, 1972.
- [217] J. A. Chirinos and P. Segers, 'Noninvasive evaluation of left ventricular afterload: Part 2: Arterial pressure-flow and pressure-volume relations in humans', *Hypertension*, vol. 56, no. 4, pp. 563–70, 2010.
- [218] A. Swillens, L. Lanoye, J. De Backer, N. Stergiopoulos, P. R. Verdonck, F. Vermassen and P. Segers, 'Effect of an abdominal aortic aneurysm on wave reflection in the aorta', *IEEE transactions on bio-medical engineering*, vol. 55, no. 5, pp. 1602–11, 2008.
- [219] J. O. Lundberg, E. Weitzberg and M. T. Gladwin, 'The nitrate-nitrite-nitric oxide pathway in physiology and therapeutics', *Nature reviews. Drug discovery*, vol. 7, no. 2, pp. 156–67, 2008.

-
- [220] M. F. Montenegro, M. L. Sundqvist, F. J. Larsen, Z. Zhuge, M. Carlstrom, E. Weitzberg and J. O. Lundberg, 'Blood pressure-lowering effect of orally ingested nitrite is abolished by a proton pump inhibitor', *Hypertension (Dallas, Tex. : 1979)*, vol. 69, no. 1, pp. 23–31, 2017.
- [221] M. Thavasoathy, M. Broadhead, C. Elwell, M. Peters and M. Smith, 'A comparison of cerebral oxygenation as measured by the niro 300 and the invos 5100 near-infrared spectrophotometers', *Anaesthesia*, vol. 57, no. 10, pp. 999–1006, 2002.
- [222] J. A. Chirinos, P. Segers, T. C. Gillebert, A. K. Gupta, M. L. De Buyzere, D. De Bacquer, M. St John-Sutton, E. R. Rietzschel and I. Asklepios, 'Arterial properties as determinants of time-varying myocardial stress in humans', *Hypertension*, vol. 60, no. 1, pp. 64–70, 2012.
- [223] B. A. Borlaug, K. E. Koepp and V. Melenovsky, 'Sodium nitrite improves exercise hemodynamics and ventricular performance in heart failure with preserved ejection fraction', *Journal of the American College of Cardiology*, vol. 66, no. 15, pp. 1672–82, 2015.
- [224] T. S. Phan, J. K. Li, P. Segers and J. A. Chirinos, 'Misinterpretation of the determinants of elevated forward wave amplitude inflates the role of the proximal aorta', *J Am Heart Assoc*, vol. 5, no. 2, 2016.
- [225] J. A. Chirinos, P. Segers, T. C. Gillebert, M. L. De Buyzere, C. M. Van Daele, Z. A. Khan, U. Khawar, D. De Bacquer, E. R. Rietzschel and I. Asklepios, 'Central pulse pressure and its hemodynamic determinants in middle-aged adults with impaired fasting glucose and diabetes: The asklepios study', *Diabetes Care*, vol. 36, no. 8, pp. 2359–65, 2013.
- [226] G. F. Mitchell, M. A. van Buchem, S. Sigurdsson, J. D. Gotlib, M. K. Jonsdottir, O. Kjartansson, M. Garcia, T. Aspelund, T. B. Harris, V. Gudnason and L. J. Launer, 'Arterial stiffness, pressure and flow pulsatility and brain structure and function: The age, gene/environment susceptibility–reykjavik study', *Brain*, vol. 134, no. Pt 11, pp. 3398–407, 2011.
- [227] D. J. Penny, J. P. Mynard and J. J. Smolich, 'Aortic wave intensity analysis of ventricular-vascular interaction during incremental dobutamine infusion in adult sheep', *Am J Physiol Heart Circ Physiol*, vol. 294, no. 1, H481–9, 2008.
- [228] J. A. Cannon, J. J. McMurray and T. J. Quinn, '“hearts and minds”: Association, causation and implication of cognitive impairment in heart failure', *Alzheimers Res Ther*, vol. 7, no. 1, p. 22, 2015.

- [229] P. Cermakova, M. Eriksdotter, L. H. Lund, B. Winblad, P. Religa and D. Religa, 'Heart failure and alzheimer's disease', *J Intern Med*, vol. 277, no. 4, pp. 406–25, 2015.
- [230] Y. N. V. Reddy, G. D. Lewis, S. J. Shah, M. LeWinter, M. Semigran, V. G. Davila-Roman, K. Anstrom, A. Hernandez, E. Braunwald, M. M. Redfield and B. A. Borlaug, 'Indie-hfpef (inorganic nitrite delivery to improve exercise capacity in heart failure with preserved ejection fraction): Rationale and design', *Circ Heart Fail*, vol. 10, no. 5, 2017.
- [231] P. J. Rix, A. Vick, N. J. Attkins, G. E. Barker, A. W. Bott, J. Alcorn H., M. T. Gladwin, S. Shiva, S. Bradley, A. Hussaini, W. L. Hoye, E. L. Parsley and H. Masamune, 'Pharmacokinetics, pharmacodynamics, safety, and tolerability of nebulized sodium nitrite (airoo1) following repeat-dose inhalation in healthy subjects', *Clin Pharmacokinet*, vol. 54, no. 3, pp. 261–72, 2015.
- [232] V. Kapil, A. B. Milsom, M. Okorie, S. Maleki-Toyserkani, F. Akram, F. Rehman, S. Arghandawi, V. Pearl, N. Benjamin, S. Loukogeorgakis, R. Macallister, A. J. Hobbs, A. J. Webb and A. Ahluwalia, 'Inorganic nitrate supplementation lowers blood pressure in humans: Role for nitrite-derived no', *Hypertension*, vol. 56, no. 2, pp. 274–81, 2010.
- [233] A. C. Guyton and J. Hall, 'Text book of medical physiology 8th ed', *VVB Saunders, Philadelphia*, pp. 159–169, 1991.
- [234] E. P. Delaney, J. L. Greaney, D. G. Edwards, W. C. Rose, P. J. Fadel and W. B. Farquhar, 'Exaggerated sympathetic and pressor responses to handgrip exercise in older hypertensive humans: Role of the muscle metaboreflex', *American journal of physiology. Heart and circulatory physiology*, vol. 299, no. 5, H1318–27, 2010.
- [235] E. E. Benarroch, 'The arterial baroreflex: Functional organization and involvement in neurologic disease', *Neurology*, vol. 71, no. 21, pp. 1733–8, 2008.
- [236] T. J. Ebert, 'Baroreflex responsiveness is maintained during isometric exercise in humans', *Journal of applied physiology (Bethesda, Md. : 1985)*, vol. 61, no. 2, pp. 797–803, 1986.
- [237] P. B. Raven, P. J. Fadel and S. Ogoh, 'Arterial baroreflex resetting during exercise: A current perspective', *Experimental physiology*, vol. 91, no. 1, pp. 37–49, 2006.

-
- [238] Q. Fu, B. D. Levine, J. A. Pawelczyk, A. C. Ertl, A. Diedrich, J. F. Cox, J. H. Zuckerman, C. A. Ray, M. L. Smith, S. Iwase, M. Saito, Y. Sugiyama, T. Mano, R. Zhang, K. Iwasaki, L. D. Lane, J. Buckley J. C., W. H. Cooke, R. M. Robertson, F. J. Baisch, C. G. Blomqvist, D. L. Eckberg, D. Robertson and I. Biaggioni, 'Cardiovascular and sympathetic neural responses to handgrip and cold pressor stimuli in humans before, during and after spaceflight', *The Journal of physiology*, vol. 544, no. 2, pp. 653–64, 2002.
- [239] R. G. Victor, J. Leimbach W. N., D. R. Seals, B. G. Wallin and A. L. Mark, 'Effects of the cold pressor test on muscle sympathetic nerve activity in humans', *Hypertension (Dallas, Tex. : 1979)*, vol. 9, no. 5, pp. 429–36, 1987.
- [240] L. A. Mitchell, R. A. MacDonald and E. E. Brodie, 'Temperature and the cold pressor test', *The journal of pain : official journal of the American Pain Society*, vol. 5, no. 4, pp. 233–7, 2004.
- [241] J. W. Williamson, P. J. Fadel and J. H. Mitchell, 'New insights into central cardiovascular control during exercise in humans: A central command update', *Experimental physiology*, vol. 91, no. 1, pp. 51–8, 2006.
- [242] F. Iellamo, 'Neural mechanisms of cardiovascular regulation during exercise', *Autonomic neuroscience : basic & clinical*, vol. 90, no. 1-2, pp. 66–75, 2001.
- [243] S. Castellani, M. Bacci, A. Ungar, P. Prati, C. Di Serio, P. Geppetti, G. Masotti, G. G. Neri Serneri and G. F. Gensini, 'Abnormal pressure passive dilatation of cerebral arterioles in the elderly with isolated systolic hypertension', *Hypertension (Dallas, Tex. : 1979)*, vol. 48, no. 6, pp. 1143–50, 2006.
- [244] G. G. Neri Serneri, S. Castellani, L. Scarti, F. Trotta, J. L. Chen, M. Carnovali, L. Poggesi and G. Masotti, 'Repeated sympathetic stimuli elicit the decline and disappearance of prostaglandin modulation and an increase of vascular resistance in humans', *Circulation research*, vol. 67, no. 3, pp. 580–8, 1990.
- [245] T. Sadamoto, Y. Mutoh and M. Miyashita, 'Cardiovascular reflexes during sustained handgrip exercise: Role of muscle fibre composition, potassium and lactate', *European journal of applied physiology and occupational physiology*, vol. 65, no. 4, pp. 324–30, 1992.

- [246] D. Mahieu, J. Kips, E. R. Rietzschel, M. L. De Buyzere, F. Verbeke, T. C. Gillebert, G. G. De Backer, D. De Bacquer, P. Verdonck, L. M. Van Bortel, P. Segers and i. Asklepios, 'Noninvasive assessment of central and peripheral arterial pressure (waveforms): Implications of calibration methods', *Journal of hypertension*, vol. 28, no. 2, pp. 300–5, 2010.
- [247] K. F. Reid and M. A. Conway, 'Haemodynamic determinants of elevated pulse wave velocity during acute isometric handgrip exercise', *Irish Journal of Medical Science*, vol. 175, no. 3, pp. 13–19, 2006.
- [248] S. Ogoh, J. P. Fisher, E. A. Dawson, M. J. White, N. H. Secher and P. B. Raven, 'Autonomic nervous system influence on arterial baroreflex control of heart rate during exercise in humans', *Journal of Physiology-London*, vol. 566, no. 2, pp. 599–611, 2005.
- [249] J. Liu, T. S. Cao, Y. Y. Duan, Y. L. Yang and L. J. Yuan, 'Effects of cold pressor-induced sympathetic stimulation on the mechanical properties of common carotid and femoral arteries in healthy males', *Heart and Vessels*, vol. 26, no. 2, pp. 214–221, 2011.
- [250] L. Mourot, M. Bouhaddi and J. Regnard, 'Effects of the cold pressor test on cardiac autonomic control in normal subjects', *Physiological Research*, vol. 58, no. 1, pp. 83–91, 2009.
- [251] K. Matsukawa, K. Ishii, A. Kadowaki, N. Liang and T. Ishida, 'Differential effect of central command on aortic and carotid sinus baroreceptor-heart rate reflexes at the onset of spontaneous, fictive motor activity', *American Journal of Physiology-Heart and Circulatory Physiology*, vol. 303, no. 4, H464–H474, 2012.
- [252] J. P. Fisher, S. Ogoh, C. N. Young, D. M. Keller and P. J. Fadel, 'Exercise intensity influences cardiac baroreflex function at the onset of isometric exercise in humans', *Journal of Applied Physiology*, vol. 103, no. 3, pp. 941–947, 2007.
- [253] K. Moriyama and H. Ifuku, 'Increased cardiovascular reactivity to the cold pressor test is not associated with increased reactivity to isometric handgrip exercise', *European Journal of Applied Physiology*, vol. 108, no. 4, pp. 837–843, 2010.
- [254] C. W. Myers, W. B. Farquhar, D. E. Forman, T. D. Williams, D. L. Dierks and J. A. Taylor, 'Carotid distensibility characterized via the isometric exercise pressor response', *American Journal of Physiology-Heart and Circulatory Physiology*, vol. 283, no. 6, H2592–H2598, 2002.

-
- [255] E.-R. Rietzschel, M. L. De Buyzere, S. Bekaert, P. Segers, D. De Bacquer, L. Cooman, P. Van Damme, P. Cassiman, M. Langlois, P. van Oostveldt *et al.*, 'Rationale, design, methods and baseline characteristics of the asklepios study', *European Journal of Cardiovascular Prevention & Rehabilitation*, vol. 14, no. 2, pp. 179–191, 2007.
- [256] A. Swillens, L. Taelman, J. Degroote, J. Vierendeels and P. Segers, 'Comparison of non-invasive methods for measurement of local pulse wave velocity using fsi-simulations and in vivo data', *Annals of biomedical engineering*, vol. 41, no. 7, pp. 1567–78, 2013.
- [257] A. B. Lafleche, B. M. Pannier, B. Laloux and M. E. Safar, 'Arterial response during cold pressor test in borderline hypertension', *The American journal of physiology*, vol. 275, no. 2 Pt 2, H409–15, 1998.
- [258] P. Segers, A. Swillens, L. Taelman and J. Vierendeels, 'Wave reflection leads to over- and underestimation of local wave speed by the pu- and qa-loop methods: Theoretical basis and solution to the problem', *Physiological measurement*, vol. 35, no. 5, pp. 847–61, 2014.
- [259] R. V. for Arterial Stiffness' Collaboration, 'Determinants of pulse wave velocity in healthy people and in the presence of cardiovascular risk factors: 'establishing normal and reference values'', *European heart journal*, vol. 31, no. 19, pp. 2338–2350, 2010.
- [260] L. Engelen, J. Bossuyt, I. Ferreira, L. M. van Bortel, K. D. Reesink, P. Segers, C. D. Stehouwer, S. Laurent, P. Boutouyrie, R. V. for Arterial Measurements Collaboration *et al.*, 'Reference values for local arterial stiffness. part a: Carotid artery', *Journal of hypertension*, vol. 33, no. 10, pp. 1981–1996, 2015.
- [261] J. Bossuyt, L. Engelen, I. Ferreira, C. D. Stehouwer, P. Boutouyrie, S. Laurent, P. Segers, K. Reesink, L. M. Van Bortel, R. V. for Arterial Measurements Collaboration *et al.*, 'Reference values for local arterial stiffness. part b: Femoral artery', *Journal of hypertension*, vol. 33, no. 10, pp. 1997–2009, 2015.
- [262] L. M. Van Bortel, S. Laurent, P. Boutouyrie, P. Chowienczyk, J. Cruickshank, T. De Backer, J. Filipovsky, S. Huybrechts, F. U. Mattace-Raso, A. D. Protogerou *et al.*, 'Expert consensus document on the measurement of aortic stiffness in daily practice using carotid-femoral pulse wave velocity', *Journal of hypertension*, vol. 30, no. 3, pp. 445–448, 2012.
- [263] S. A. Huybrechts, D. G. Devos, S. J. Vermeersch, D. Mahieu, E. Achten, T. L. de Backer, P. Segers and L. M. van Bortel, 'Carotid to femoral pulse wave velocity: A comparison of real travelled aortic path lengths determined by mri and superficial measurements', *Journal of hypertension*, vol. 29, no. 8, pp. 1577–1582, 2011.

- [264] F. Faita, V. Gemignani, E. Bianchini, C. Giannarelli, L. Ghiadoni and M. Demi, 'Real-time measurement system for evaluation of the carotid intima-media thickness with a robust edge operator', *Journal of ultrasound in medicine*, vol. 27, no. 9, pp. 1353–1361, 2008.
- [265] F. J. Londono-Hoyos, 'Characterization and optimization of a semi-automatic algorithm for imt measurement in ultrasound carotid imaging', Master's thesis, Politecnico di Torino, 2010.
- [266] J. S. Suri, R. M. Haralick and F. H. Sheehan, 'Greedy algorithm for error correction in automatically produced boundaries from low contrast ventriculograms', *Pattern Analysis & Applications*, vol. 3, no. 1, pp. 39–60, 2000.
- [267] E. Van der Wall, 'Milestones in cardiovascular medicine: 10 or more?', *Netherlands Heart Journal*, vol. 21, no. 12, pp. 527–529, 2013.
- [268] S. J. Al'Aref, K. Anchouche, G. Singh, P. J. Slomka, K. K. Kolli, A. Kumar, M. Pandey, G. Maliakal, A. R. van Rosendael, A. N. Beecy *et al.*, 'Clinical applications of machine learning in cardiovascular disease and its relevance to cardiac imaging', *European heart journal*, vol. 40, no. 24, pp. 1975–1986, 2018.
- [269] J. P. Amezcua-Sanchez, M. Valtierra-Rodriguez, H. Adeli and C. A. Perez-Ramirez, 'A novel wavelet transform-homogeneity model for sudden cardiac death prediction using ecg signals', *Journal of medical systems*, vol. 42, no. 10, p. 176, 2018.
- [270] P. S. Addison, 'Wavelet transforms and the ecg: A review', *Physiological measurement*, vol. 26, no. 5, R155, 2005.
- [271] Y. Iñer and M. Kuntalp, 'Combining classical hrv indices with wavelet entropy measures improves to performance in diagnosing congestive heart failure', *Computers in biology and medicine*, vol. 37, no. 10, pp. 1502–1510, 2007.
- [272] Z. Lai, X. Qu, Y. Liu, D. Guo, J. Ye, Z. Zhan and Z. Chen, 'Image reconstruction of compressed sensing mri using graph-based redundant wavelet transform', *Medical image analysis*, vol. 27, pp. 93–104, 2016.
- [273] F. Ong, M. Uecker, U. Tariq, A. Hsiao, M. T. Alley, S. S. Vasanawala and M. Lustig, 'Robust 4d flow denoising using divergence-free wavelet transform', *Magnetic resonance in medicine*, vol. 73, no. 2, pp. 828–842, 2015.
- [274] C. Santelli, M. Loecher, J. Busch, O. Wieben, T. Schaeffter and S. Kozerke, 'Accelerating 4d flow mri by exploiting vector field divergence regularization', *Magnetic resonance in medicine*, vol. 75, no. 1, pp. 115–125, 2016.

-
- [275] M. Lustig, D. Donoho and J. M. Pauly, 'Sparse mri: The application of compressed sensing for rapid mr imaging', *Magnetic Resonance in Medicine: An Official Journal of the International Society for Magnetic Resonance in Medicine*, vol. 58, no. 6, pp. 1182–1195, 2007.
- [276] M. De Melis, U. Morbiducci, E. R. Rietzschel, M. De Buyzere, A. Qasem, L. Van Bortel, T. Claessens, F. M. Monteverchi, A. Avolio and P. Segers, 'Blood pressure waveform analysis by means of wavelet transform', *Medical & biological engineering & computing*, vol. 47, no. 2, pp. 165–173, 2009.
- [277] A. Khatami, A. Khosravi, T. Nguyen, C. P. Lim and S. Nahavandi, 'Medical image analysis using wavelet transform and deep belief networks', *Expert Systems with Applications*, vol. 86, pp. 190–198, 2017.
- [278] S. F. Weng, J. Reys, J. Kai, J. M. Garibaldi and N. Qureshi, 'Can machine-learning improve cardiovascular risk prediction using routine clinical data?', *PloS one*, vol. 12, no. 4, e0174944, 2017.
- [279] B. A. Goldstein, A. M. Navar and R. E. Carter, 'Moving beyond regression techniques in cardiovascular risk prediction: Applying machine learning to address analytic challenges', *European heart journal*, vol. 38, no. 23, pp. 1805–1814, 2016.
- [280] A. Alyass, M. Turcotte and D. Meyre, 'From big data analysis to personalized medicine for all: Challenges and opportunities', *BMC medical genomics*, vol. 8, no. 1, p. 33, 2015.
- [281] D. Cirillo and A. Valencia, 'Big data analytics for personalized medicine', *Current opinion in biotechnology*, vol. 58, pp. 161–167, 2019.
- [282] P. P. Sengupta, Y.-M. Huang, M. Bansal, A. Ashrafi, M. Fisher, K. Shameer, W. Gall and J. T. Dudley, 'Cognitive machine-learning algorithm for cardiac imaging: A pilot study for differentiating constrictive pericarditis from restrictive cardiomyopathy', *Circulation: Cardiovascular Imaging*, vol. 9, no. 6, e004330, 2016.
- [283] J. Mantilla, M. Garreau, J.-J. Bellanger and J. L. Paredes, 'Machine learning techniques for lv wall motion classification based on spatio-temporal profiles from cardiac cine mri', in *2013 12th International Conference on Machine Learning and Applications*, IEEE, vol. 1, 2013, pp. 167–172.
- [284] Y. Luo, B. Yang, L. Xu, L. Hao, J. Liu, Y. Yao and F. van de Vosse, 'Segmentation of the left ventricle in cardiac mri using a hierarchical extreme learning machine model', *International Journal of Machine Learning and Cybernetics*, vol. 9, no. 10, pp. 1741–1751, 2018.

- [285] P. Colletti, 'Deep learning for cardiac mri: The time has come.' *Radiology*, vol. 290, no. 1, pp. 89–89, 2019.
- [286] I. Goodfellow, Y. Bengio and A. Courville, 'Deep Learning'. MIT Press, 2016, <http://www.deeplearningbook.org>.
- [287] P. Radau, Y. Lu, K. Connelly, G. Paul, A. Dick and G. Wright, 'Evaluation framework for algorithms segmenting short axis cardiac mri', *The MIDAS Journal-Cardiac MR Left Ventricle Segmentation Challenge*, vol. 49, 2009.
- [288] A. Suinesiaputra, B. R. Cowan, J. P. Finn, C. G. Fonseca, A. H. Kadish, D. C. Lee, P. Medrano-Gracia, S. K. Warfield, W. Tao and A. A. Young, 'Left ventricular segmentation challenge from cardiac mri: A collation study', in *International Workshop on Statistical Atlases and Computational Models of the Heart*, Springer, 2011, pp. 88–97.
- [289] C. Petitjean, M. A. Zuluaga, W. Bai, J.-N. Dachet, D. Grosgeorge, J. Caudron, S. Ruan, I. B. Ayed, M. J. Cardoso, H.-C. Chen *et al.*, 'Right ventricle segmentation from cardiac mri: A collation study', *Medical image analysis*, vol. 19, no. 1, pp. 187–202, 2015.
- [290] Kaggle. (2015). Second annual data science bowl kaggle. B. A. H. Inc., Ed. Accessed: 03.10.2019, [Online]. Available: <https://www.kaggle.com/c/second-annual-data-science-bowl>.
- [291] O. Bernard, A. Lalande, C. Zotti, F. Cervenansky, X. Yang, P.-A. Heng, I. Cetin, K. Lekadir, O. Camara, M. A. G. Ballester *et al.*, 'Deep learning techniques for automatic mri cardiac multi-structures segmentation and diagnosis: Is the problem solved?', *IEEE transactions on medical imaging*, vol. 37, no. 11, pp. 2514–2525, 2018.
- [292] P. V. Tran, 'A fully convolutional neural network for cardiac segmentation in short-axis mri', *arXiv preprint arXiv:1604.00494*, 2016.
- [293] M. Avendi, A. Kheradvar and H. Jafarkhani, 'A combined deep-learning and deformable-model approach to fully automatic segmentation of the left ventricle in cardiac mri', *Medical image analysis*, vol. 30, pp. 108–119, 2016.
- [294] Q. Tao, W. Yan, Y. Wang, E. H. Paiman, D. P. Shamonin, P. Garg, S. Plein, L. Huang, L. Xia, M. Sramko *et al.*, 'Deep learning-based method for fully automatic quantification of left ventricle function from cine mr images: A multivendor, multicenter study', *Radiology*, vol. 290, no. 1, pp. 81–88, 2018.

-
- [295] G. Yang, S. Yu, H. Dong, G. Slabaugh, P. L. Dragotti, X. Ye, F. Liu, S. Arridge, J. Keegan, Y. Guo *et al.*, ‘Dagan: Deep de-aliasing generative adversarial networks for fast compressed sensing mri reconstruction’, *IEEE transactions on medical imaging*, vol. 37, no. 6, pp. 1310–1321, 2017.
- [296] B. Kaplan, ‘How should health data be used?: Privacy, secondary use, and big data sales’, *Cambridge Quarterly of Healthcare Ethics*, vol. 25, no. 2, pp. 312–329, 2016.
- [297] W. N. Price and I. G. Cohen, ‘Privacy in the age of medical big data’, *Nature medicine*, vol. 25, no. 1, p. 37, 2019.
- [298] K. Shameer, K. W. Johnson, B. S. Glicksberg, J. T. Dudley and P. P. Sengupta, ‘Machine learning in cardiovascular medicine: Are we there yet?’, *Heart*, vol. 104, no. 14, pp. 1156–1164, 2018.
- [299] P. J. Slomka, D. Dey, A. Sitek, M. Motwani, D. S. Berman and G. Germano, ‘Cardiac imaging: Working towards fully-automated machine analysis & interpretation’, *Expert review of medical devices*, vol. 14, no. 3, pp. 197–212, 2017.

